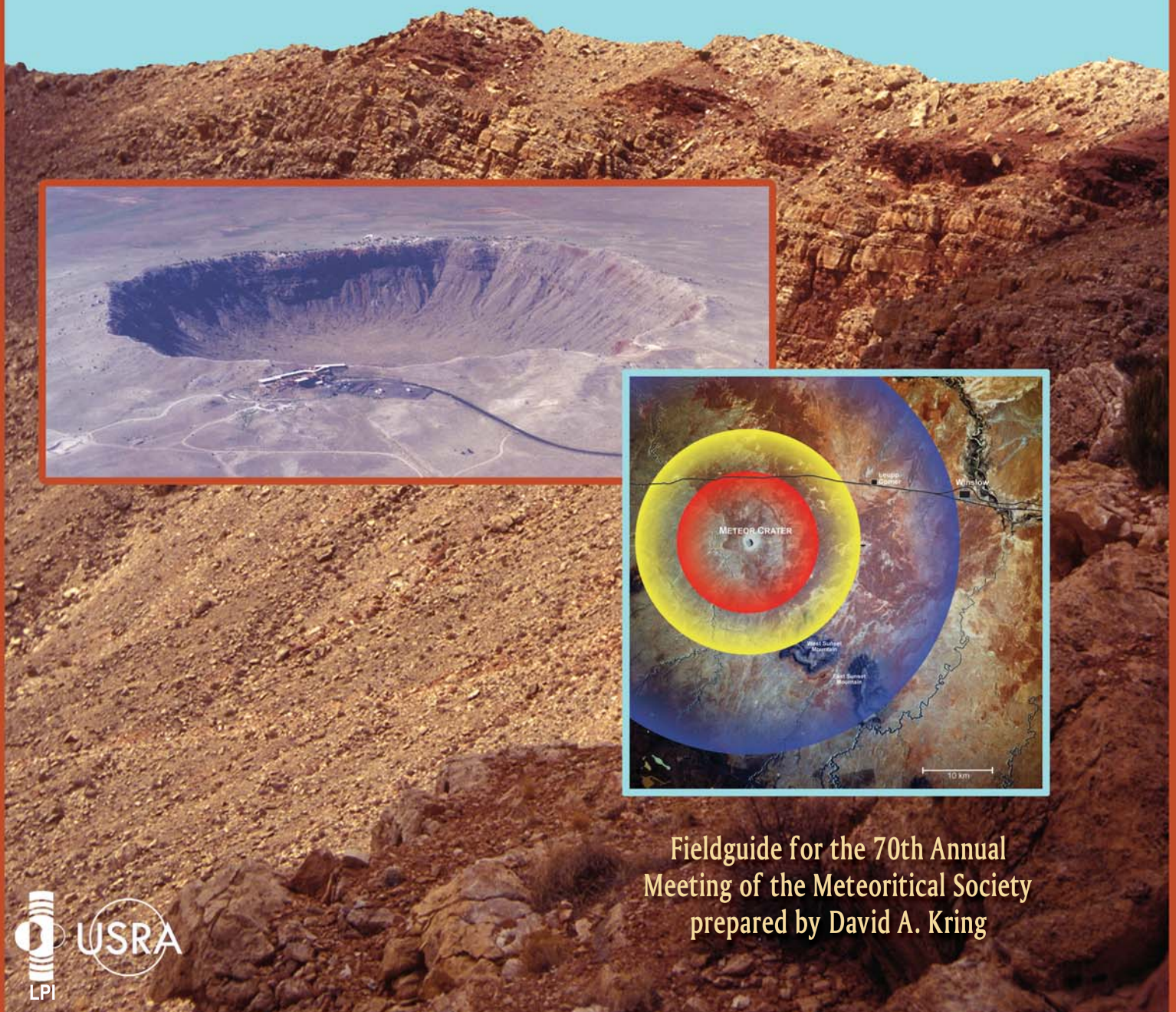


GUIDEBOOK TO THE GEOLOGY OF BARRINGER METEORITE CRATER, ARIZONA

(a.k.a. Meteor Crater)



Fieldguide for the 70th Annual
Meeting of the Meteoritical Society
prepared by David A. Kring

Guidebook to the Geology of Barringer

Meteorite Crater, Arizona

(*a k a* Meteor Crater)

Prepared by

David A. Kring

for the

70th Annual Meeting

of the

Meteoritical Society

August 2007

Copyright © 2007

Single copy academic use of this material can be made as long as appropriate acknowledgment of the source is maintained. Republication of any portion of the guidebook or any commercial use requires written permission from the author (David A. Kring) or the Lunar and Planetary Institute, in addition to appropriate acknowledgment of the source.

Table of Contents

Title Page	i
Table of Contents	ii
Preface and Acknowledgments	iii
Chapter 1 Introduction	1
Chapter 2 Target Sequence	6
Chapter 3 Barringer Meteorite Impact Crater	24
Chapter 4 Shock Metamorphism	39
Chapter 5 Crater Rim Uplift and Crater Wall Collapse	47
Chapter 6 Overturned Rim Sequence	53
Chapter 7 Distribution of Ejecta	59
Chapter 8 Projectile	67
Chapter 9 Trajectory	74
Chapter 10 Energy of Impact	77
Chapter 11 Age of the Crater	79
Chapter 12 Environmental Effects of the Impact	81
Chapter 13 Post-Impact Lake	86
Chapter 14 Crater Rim East Trail Guide	89
Chapter 15 Crater Floor Trail Guide	113
Bibliography	139

❖ Preface and Acknowledgments

The geological guidebook that follows has been prepared for the occasion of the 70th Annual Meeting of The Meteoritical Society in Tucson, Arizona, and a society field trip to the crater. The society last visited the crater in 1974 on a trip led by the late Eugene M. Shoemaker and one of his former students, Susan W. Kieffer, who is now the distinguished Charles R. Walgreen Jr. Chair at the University of Illinois. Like their guidebook, the following document provides a trail-oriented geological tour of the crater. The current guidebook relies heavily on the work of these authors, for which I thank them, but also incorporates lessons learned about impact cratering during the intervening 30+ years.

In addition, the geological processes involved in the formation of the crater have been broken down into a series of discrete topics. The goal is to illustrate how our understanding of those topics has evolved over the past 100+ years of study at the crater and how observations at the crater have influenced them. While our understanding of the processes involved in the crater's formation have grown, there are also a great number of topics that still need further research. In each section of the guidebook, I will try to identify those unresolved issues with the hope that those comments will spawn new studies.

I want to thank Drew Barringer, President of the Barringer Crater Company, and Brad Andes, President of Meteor Crater Enterprises, for their patience and response to countless questions and for agreeing to host The Meteoritical Society at the crater. I thank Carleton Moore for his insights about the crater, Canyon Diablo meteorites, and access to samples in the Nininger Collection at Arizona State University. I thank Carolyn Shoemaker for her insights about the crater and those of her husband. Both Carleton Moore and Carolyn Shoemaker are treasured colleagues who have guided many of the activities at the crater for many years. I also thank Bevan French for kindly stepping in to assist with a tour of the crater rim, while I lead a tour of the crater walls and crater floor. I thank Linda Chappell at the Lunar and Planetary Institute (LPI) for helping me obtain copies of some of the older publications about the crater. I thank Leanne Woolley and Ronna Hurd at LPI for their assistance with some of the illustrations in the guidebook. I thank the entire Publications and Program Services Department staff at the LPI for helping organize the field trip. Likewise, I thank the organizing committee of the 70th Annual Meeting of The Meteoritical Society for promoting the field trip.

As some of you may know, the Barringer family asked me to assume Gene Shoemaker's responsibilities at the crater after we lost him. At the time, David Roddy, who was another long-time advisor to the family, kindly tramped up and down the crater walls with me, providing a running commentary of crater lore. Unfortunately, we have since lost David too. I want to take this opportunity to thank both Gene and David for the insights they shared with me.

Finally, I thank the late Daniel Moreau Barringer, for without his work and insights we may not be here today, and members of the entire Barringer family, who have dedicated themselves to the preservation of this impact site for education and scientific research.

David A. Kring
Houston

1. Introduction



Science does not always move forward in a straight line and rarely at a constant cadence. Studies of Barringer Meteorite Crater (*a.k.a.* Meteor Crater) is a classic example. Although an immense collection of meteorites of undisputable extraterrestrial origin was gathered at northern Arizona's crater (Foote, 1891), the association was considered coincidental by many (e.g., Gilbert, 1896) and nearly fifteen years passed before a serious case linking the meteorites to the impact origin of the crater was presented (Barringer 1905; Tilghman 1905). That latter effort was part of an intense mining operation at the crater to recover the suspected projectile. The works were extensive, including a reservoir in the distant Canyon Diablo, a pipeline to the crater, and camps on both the crater rim and crater floor. Sadly for investors, economically viable deposits of metal were never recovered. Sadly for science, decades passed before the implications of Barringer's work were appreciated.

There are many ways to trace the path of this story, but perhaps the best place to begin is with the mineralogist A. E. Foote, who published the first scientific report about the crater and meteorites found there. Foote's interest was piqued by a railroad executive who sent him a sample of native iron and requested an analysis. Foote deduced the sample was a fragment of a meteorite and, having been told more material existed in northern Arizona ("185 miles due north from Tucson"), promptly traveled to the site from Philadelphia. Foote and his team collected several large masses (201, 154, and 40 lbs), 131 smaller masses (ranging from 1/16 oz to 6 lbs 10 oz), and 200 lbs of oxidized meteorite fragments. After returning to Philadelphia, he received three additional large masses (632, 506, and 145 lbs). Several of the larger samples were perforated with cavities similar to the one in the spectacular Tucson ring meteorite ("Signet Iron"). The iron meteorites also contained troilite, daubréelite, carbon, and diamonds (up to 1/8 inch diameter), the latter of which were described as being mostly black and of little commercial value.

The purpose of Foote's paper was to describe the diamond-bearing iron meteorites, but he was clearly impressed with the "Crater Mountain," where the samples were found and provided the scientific community with its first geologic description. He noted an uplifted rim of sandstone and limestone dipping 35 to 40° that stood 432 ft above the surrounding plain. The crater floor appeared to be 50 to 100 ft below the surrounding plain. He further noted that he could not locate any "lava, obsidian or other volcanic products," and, thus, concluded that he was "unable to explain the cause of this remarkable geological phenomenon." He did not recognize any genetic association between the crater and meteorite irons. Nor did he add any remarks about the unusual quantity of iron meteorites. With regard to the iron oxide fragments, however, he concluded that a large iron meteorite of 500 to 600 pounds "had become oxidized while passing through the atmosphere and was so weakened in its internal structure that it had burst into pieces not long before reaching the earth."

Foote presented his paper at a meeting of the Association for the Advancement of Science (AAAS) in Washington DC. Sitting in the audience was the chief geologist of the United States Geological Survey, Grove Karl Gilbert. Gilbert developed an immediate interest in the crater and its association with meteoritic iron. Having also recently heard T. C. Chamberlin's (1890) proposal for a new scientific method of "multiple working hypotheses," Gilbert decided to apply the principle to the origin of the crater. He posited two origins: (1) that the crater was produced by the impact of a large iron mass from space and (2) that the crater was produced by a volcanically-driven steam explosion, in which case the fall of meteoritic irons at that locality was coincidental and had nothing to do with the formation of the crater. He reasoned that if the impact of a "stellar body" occurred, it must still lay beneath the crater floor, but would be absent if the crater was produced by a volcanic steam explosion. To determine if a meteoritic mass lay beneath the crater floor and, thus, test the hypotheses, he devised several measurements that

were conducted during a two week stay at the crater in November, 1891. He measured the volume of the crater and ejected material contained in the rim: if the volumes are equal, he reasoned, then a mass did not lie buried beneath the crater floor. He also measured the magnetic field in the vicinity of the crater, assuming that a buried mass of iron would deflect magnetic instruments. While making those measurements, he also made notes about uplifted strata in the upper crater walls and the distribution of ejected sedimentary blocks and iron masses around the crater.

To compare the volume of the crater cavity and crater rim, Gilbert's team generated a topographic map with a contour interval of 10 feet, which is a remarkable achievement. It is a higher resolution topographical result than that currently available on the USGS Meteor Crater 7.5 minute quadrangle, which has a 20 ft contour interval. Unfortunately, Gilbert's map has not resurfaced and is only available in a small reproduction in his 1896 paper. (About 100 years later, David Roddy developed another 10 ft contour map of the crater that he informally distributed to some investigators. The map is available from the present author.) Using the 1891 map, Gilbert calculated that the crater cavity and the ejected rim material had the same volume, from which he concluded a buried mass could not be partially filling the crater volume. Interestingly, Gilbert did not recognize the lake sediments that partially filled the crater or discuss the change in density between the original target strata and the rim deposits, both of which affect this type of calculation. Nor does he describe the red Moenkopi Formation in the walls of the crater. His team's measurements of magnetism at the crater were negative: they did not reveal any variations in direction or intensity inside or outside the crater, leading Gilbert to conclude that a mass did not exist beneath the crater floor.

Thus, the tests of the meteoritic impact theory as envisioned by Gilbert failed. Consequently, he turned to the other hypothesis and observed that Arizona's crater "is in the midst of a great volcanic district." He then drew comparisons between Arizona's crater and several volcanic vents around the world, including the maars in Germany that would again draw attention during the Apollo era. Interestingly, he also referred to Lonar Crater of India, which, because it occurs within the Deccan Traps, he concluded also had a volcanic origin. As we now know, Lonar Crater has an impact origin. Based on these comparisons, Gilbert erroneously concluded that of the two hypotheses the steam explosion origin for northern Arizona's crater was the correct solution. Having applied Chamberlin's principle of multiple working hypotheses, Gilbert concluded his report with a principle of his own, one that remains a benchmark of comparative planetology today (although it has an echo of uniformitarianism): "tentative explanations are always founded on accepted explanations of similar phenomena," in this case referring to the similarities he believed existed between Arizona's crater and the volcanic ones to which he alluded.

Gilbert's (1896) conclusion that the crater was produced by a steam explosion greatly influenced the geologic community, because he was one of the nation's most eminent geologists. He had already been the chief geologist at the USGS for eight years and would continue in that post for many more years. At the time of his report, he was also President of the Geological Society of Washington. Indeed, he presented his report in the form of the annual presidential address to the society, which was then published in *Science*.

Quite unaware of Gilbert's work (at least initially), Daniel Moreau Barringer independently heard about the crater and its meteoritic irons from S. J. Holsinger on the veranda of the San Xavier Hotel in Tucson (Fig. 1.1). Barringer was entranced, particularly with the potential wealth associated with a source of metallic iron and nickel. He was well-schooled in the mining industry, having already made a fortune with silver. He quickly obtained the crater property and began a series of investigations of the structure with his business partner, Benjamin Chew Tilghman. Barringer was soon in a position to challenge the conclusions of Gilbert and he produced a series of reports over a 25 year period, beginning with his first report to The Academy of Natural Sciences of Philadelphia in 1905.

Barringer obtained the property in 1903, formed the Standard Iron Company to extract the metal, and immediately began a survey and drilling operation (Fig. 1.2 and 1.3). By the time Barringer prepared his 1905 report, he had made more than ten trips to the crater.

In comparison to Gilbert's report, Barringer's paper provides a much better description of the stratigraphic units and their regional context. He also provides a series of observations that are relevant to the structure's formation. He points out that meteoritic irons are concentrically distributed around the crater, suggesting the occurrence is not coincidental, but rather tied directly to the formation of the crater. (In a later paper (1910), he also observes that the concentration of irons increases towards the rim of the crater.) He describes uplifted strata in the crater walls, which he argues were "turned out bodily by the force which produced this enormous hole." He describes a mix of underlying strata in a breccia at the crater surface and, in one location, correctly notes the inverted stratigraphy of ejected material. Barringer found that some of the meteoritic irons are buried within the ejecta and, thus, both must have formed at the same time. He notes that the largest ejected blocks are distributed east and west, indicating a plane of symmetry that he would later map to the trajectory of an impacting object. Barringer focused a lot of attention on pulverized silica that he found beneath lake sediments and in ejected material. He noted that individual grains are sharply fractured, which is inconsistent with a sedimentary origin, and inferred the silica is crushed target sandstone. In some cases, he wrote, the silica was powdered so completely that no silt or sand grittiness was detectable with one's teeth. In a companion paper, his partner, Tilghman (1905), makes similar arguments. Importantly, Tilghman also describes three boreholes that encountered iron masses buried 300, 400, and 480 ft below the crater floor, which, like irons buried within the ejecta blanket, illustrated the simultaneous fall of the irons and production of the crater.

In counterpoint to Gilbert's findings, Barringer also wrote that he was unable to find any eruptive rock or any other evidence of volcanic-related activity. He organized eight arguments against a volcanic steam explosion hypothesis and three additional arguments against any other type of volcanic action. Barringer bluntly criticized Gilbert and his conclusion of a volcanic steam explosion, writing that if Gilbert "examined the surface carefully, it does not seem possible to me that any experienced geologist could have arrived at such a conclusion." Barringer's geologic and petrologic methods trumped Gilbert's geophysical techniques and he wanted it well known. Tilghman (1905), in his companion paper, emphasized that the drilling did not encounter any volcanic material beneath the crater to a depth of 1400 ft relative to the surrounding plane, thus demonstrating there is no magmatic conduit that could have fed a volcanic steam explosion.

For Barringer and his heirs, the issue was settled: Arizona's crater was produced by a meteoritic impact. The geologic community was less receptive. In general, processes that could be described as catastrophic were ignored or abandoned in favor of uniformitarian concepts. The problem continues to plague geology, although progress is being made (Marvin, 1990).

One of the most significant series of events to affect the scientific community's perception of Barringer's thesis was a re-examination of the problem by Gene Shoemaker (1960) and the Apollo exploration of the heavily cratered lunar surface. Shoemaker drew upon new observations of crater excavation associated with nuclear explosions and developed an analytical model for the penetration mechanics of hypervelocity impact events. One of the strengths of his work was the superb geologic description he provided of diagnostic features at Meteor Crater and nearly identical features that he found at the nuclear Teapot Ess Crater: crater rims overturned in synclinal folds, upper fold limbs composed of debris that preserves an inverted stratigraphic sequence, glass in the uppermost components of the debris, and crater floors covered with breccia lenses. With Ed Chao, he later discovered evidence of the shock-metamorphic transformation of quartz in target sediments to coesite and stishovite (Chao *et al.*, 1960, 1962).

Collectively, the work of Barringer, Tilghman, Shoemaker, and Chao demonstrated the impact origin of Barringer's crater and also provided the diagnostic geologic and petrologic tools needed to recognize structures formed by similar processes elsewhere on Earth and in the Solar System. We now understand that impact cratering is one of (if not the) dominant geologic process affecting planetary surfaces.

For students interested in additional details about the early exploration of the crater, I recommend the following primary references: Barringer (1910, 1914, 1924), Fairchild (1907), and Merrill (1908). I also recommend a very nice and pleasantly concise review written by Brandon Barringer (1964) and a longer, book-length review written by William Hoyt (1987). Both of the latter reviews include details of the mining operations associated with studies of the crater's origin. For an intimate portrait of Barringer and his enterprise, the best source is a small book written by Nancy Southgate and Felicity Barringer (2002).



Fig. 1.1. View of the San Xavier Hotel, Tucson, where S. J. Holsinger told D. M. Barringer about northern Arizona's crater and its meteoritic irons. This photograph (c. 1893) was taken approximately a decade before that conversation in 1902. Arizona was a territory at the time, not receiving statehood until 1912. The photograph appears courtesy of the George Mason University and should not be reproduced further without permission.

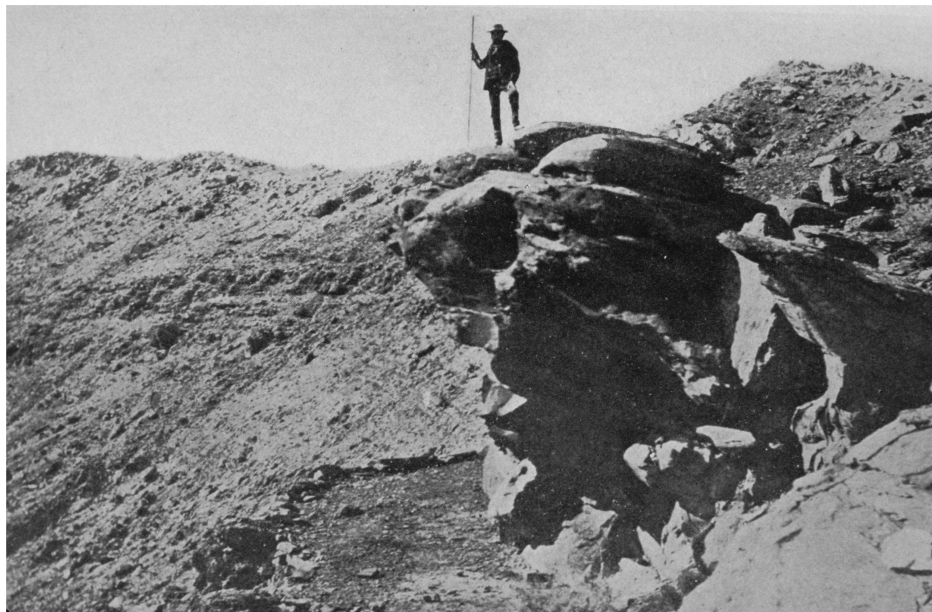


Fig. 1.2. View of the upper crater wall and crater rim, with uplifted (tilted) red Moenkopi in foreground. (Bottom panel of Plate VIII in Barringer, 1910.)

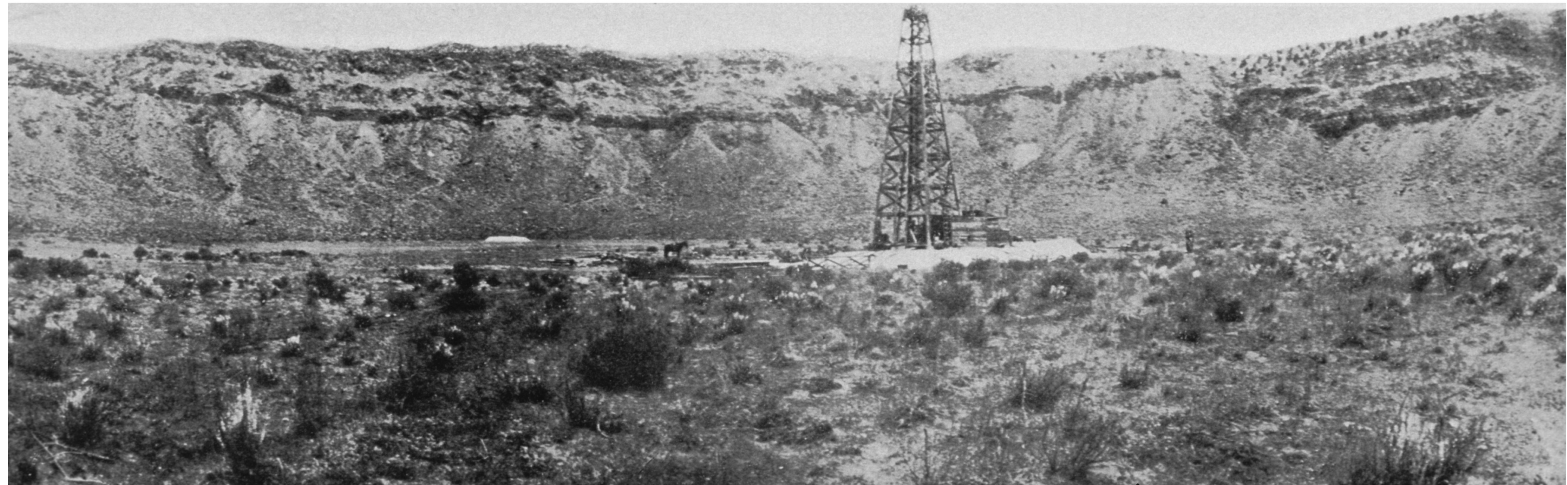


Fig. 1.3. (below) View of crater floor and a drilling unit near crater center. (Bottom panel of Plate IV in Barringer, 1910.)

2. Target Stratigraphy



The impact event excavated material from the Colorado Plateau, which is a broad region in the Four Corners area that is composed of relatively flat lying sedimentary rocks. A flat-lying, multi-layered sedimentary target has made Barringer Meteorite Crater a particular important impact site, because the structural deformation created by the impact is relatively easy to observe.

Plateau sediments in the vicinity of the crater are ~1070 m (~3510 ft) thick and overlie a crystalline basement of continental crust (Fig. 2.1). The Devonian Martin Formation unconformably overlies the basement, which is, in turn, unconformably covered by the Mississippian Redwall Formation. These units are covered by a Permian section that is poorly sampled in the immediate vicinity of the crater. A small amount of the Molas Formation may occur at the base of the Permian section, followed by the Naco Formation. The thickness of the latter is not well-known and is inferred on the basis of a seismic refraction horizon (Ackerman *et al.*, 1975) believed to occur between the Naco and the overlying Supai Formation (Roddy, 1978). The Supai is the thickest sedimentary unit in the section. It is covered by the Coconino Formation, Toroweap Formation, Kaibab Formation, and Moenkopi Formation, all of which are exposed in the crater walls. These units represent the upper portion of the well-known Grand Canyon sequence and are the critical units involved in the impact event (Fig. 2.1). Detailed descriptions of these latter units follow.

Coconino Sandstone. The Coconino sandstone is white, fine-grained, and saccharoidal (*i.e.*, a granular texture similar to loaf sugar) quartzose sandstone that occurs in massive beds with cross-stratification. The unit was defined in the plateau province by Darton (1910) and subsequently described in greater detail by Noble (1914) in the Grand Canyon, where outcrops of the sandstone are particularly spectacular. Sets of cross-stratified units are sometimes 30 m (100 ft) thick. The sedimentary environment was controversial for several decades, but an aeolian environment was the eventual consensus (McKee, 1934, and Reiche, 1938; *cf.*, Schuchert, 1918, and Read, 1950). Thus, the Coconino's high-angle cross-bedded laminae are fossilized sand dune slopes produced when northern Arizona was covered by a huge sand dune field similar to the modern Sahara. The Coconino thickens to the south, where it has a maximum thickness of 330 m (1000 ft ; Kieffer, 1974). In the vicinity of the impact, the Coconino is 210 to 240 m (700 to 800 ft) thick (Shoemaker, 1974). It is the basal unit excavated by the impact event. Only the upper portions of the Coconino Formation, however, are exposed in the crater walls.

The sandstone is >95% quartz. Grains are well-rounded and have dimensions that are 0.1 to nearly 4 mm, with an average length of 0.1 to 0.2 mm (Table 2.1). The sandstone is porous, but the porosity is heterogeneously distributed. Samples may have <10% porosity, but can also have 25% porosity, a variation that can influence the propagation of a shock wave and shock-metamorphic effects.

Chemical analyses of Coconino sandstone exposed in the crater walls reflect the high concentration of quartz (See *et al.*, 2002). Silica (SiO_2) totals range from 96.99 to 97.54%, with an average value of 97.03 wt% (Table 2.2). The dominant impurity is Al_2O_3 .

Because the Coconino sandstone is such an important target component (representing ~70% of the stratigraphic depth of the excavation cavity; calculated from reconstruction by Roddy 1978), its physical properties have been investigated experimentally (Table 2.1). Microscopic radial fracturing of Coconino occurs at tensile stresses of 30 MPa, which is a factor of 10 less than that of crystalline rocks (Ai and Ahrens, 2004) and approximately a factor of 10 higher than that measured in Kaibab samples that were recovered from the uplifted rim of the crater (Watkins and Walters, 1966).

Toroweap Formation. The Toroweap is a thin (10 ft or 3 m) layer of sandstone and dolomite at the crater. Elsewhere in northern Arizona the unit can be thicker and composed of limestone with substantial amounts of yellow sandstone and reddish mudstone. The Toroweap formed on the floor of a shallow sea that migrated into the area from the west. The sandy portions represent a fluctuating ancient shoreline of western North America during the Permian.

Much more is known about the Toroweap (*e.g.*, McKee, 1938) than will be summarized here, because the formation is such a thin unit at the crater. In other areas of northern Arizona, the limited stratigraphic extent of the Toroweap is partly the result of erosion, because the contact between the Toroweap and overlying Kaibab is normally unconformable (McKee, 1938). At the crater, however, the limited stratigraphic thickness appears to reflect limited sedimentation, because Shoemaker (1974) describes the contact between the Toroweap and Kaibab as conformable.

The Toroweap is not quite as pure a quartz sandstone as the Coconino (Table 2.2). It contains additional Al_2O_3 and probably carbonate (reflected by enhanced Mg, Ca, and LOI abundances). The average silica abundance is 93.34 wt%.

Kaibab Formation. The Kaibab Formation at the crater is 260 to 265 ft (79 to 81 m) thick and composed of dolomite, dolomitic limestone, and thin calcareous sandstone horizons. Fossil shells are apparent (Fig. 2.2), although preservation is often poor because of diagenesis. One also finds preserved burrows of marine organisms that lived and fed in the sea-floor sediments. The Kaibab was deposited in a low-energy marine environment during the Permian over 250 million years ago.

The first report of a thick magnesian limestone (dolomite) was provided by Jules Marcou in a report from the 1853-54 expedition across northern Arizona that was led by Lieutenant Whipple (and, hence, popularly known as the Whipple Survey). Once called the Aubrey limestone, the unit was renamed the Kaibab limestone in 1910 when the USGS assigned the term Aubrey to a larger group of rocks that contained the magnesian limestone. A formal description of the Kaibab Formation was produced by McKee (1938), who measured sections throughout the region, including several sections in the vicinity of Meteor Crater. These sections occur in Walnut Canyon, in Padre Canyon at Hwy 66, at an outcrop ~10 miles southwest of Winslow, and at several locations along Clear Creek. McKee (1938, p. 8) briefly describes 150 ft of Kaibab at Meteor Crater, although Shoemaker (1960) measured 260 to 265 ft (79 to 81 m). In general, the Kaibab thins regionally from the north to south or northwest to southeast.

The Kaibab has three members that are designated alpha (α), beta (β), and gamma (γ) from the top to the bottom of the sequence (Fig. 2.1). The oldest member (γ) represents a time of advancing seas, the middle member (β) the time with the most extensive seas, and the youngest member (α) a time of receding seas. Sand units mixed with the uppermost (α) dolomite beds have been interpreted as a shoreline facies. They also erode in different fashions, as illustrated in the crater walls. The α and γ members form cliffs, whereas the β member often erodes to form a slope. In outcrop, one finds that diagenesis and weathering have conspired to produce a distinctive vuggy texture (Fig. 2.2) that is commonly called tear-pants for obvious reasons.

The Kaibab varies horizontally (geographically), which McKee (1938) divided into several facies. Facies 3 of the α member, facies 4 of the β member, and facies 3 of the γ member of the Kaibab occur at Barringer Crater (Fig. 2.3). Facies 3 of the α member contains trilobites (*Ditomopyge*), brachiopods (*Chonetes*, *Marginifera*, and *Productus bassi*), cephalopods (*Orthoceras* and *Plagioglypta*), gastropods (*Pleurotomaria*, *Euphemus*, *Bellerophon*, *Euomphalus*, *Bucanopsis*, and *Naticopsis*), and pelecypods (*Allorisma*, *Leda*, *Astartella*, *Pleurophorus*, *Nucula*, and *Schizodus*). Facies 4 of the β member contains brachiopods (*Pugnoides* and *Hustedia*), pelecypods (*Schizodus*, *Leda*, *Pleurophorus*, *Deltpecten*, and *Myalina*), and a long-stem echinoid (*Archaeocidaris*).

Because the Kaibab Formation is an important target unit at the crater, a NASA-sponsored drilling project recovered several cores from the rim of the crater and one core from a distant site unaffected by the impact event (Watkins, 1966). The latter was analyzed to provide pre-impact properties of the Kaibab (Watkins and Walters, 1966), which are summarized in Table 2.3 (drill core hold KC-2). These samples were recovered from Kaibab that was buried by a basalt lava flow associated with the SP cinder cone north of Flagstaff. This hole penetrated the same Kaibab α and β facies as those exposed at the impact site (Fig. 2.3). Measurements of recovered sample include porosity, permeability, compressive strength, tensile strength, Poisson's ratio, Young's modulus, the shear modulus, bulk modulus, and compressional and shear velocities.

Five boreholes were drilled along the southern crater rim. Two of the holes (MCC-3 and MCC-4) provide most of the data. The MCC-3 hole is located about 150 m south of the modern topographic rim of the crater. Drill core hole MCC-4 is located 10 m south of the modern topographic rim of the crater. These holes penetrated impact ejecta, Moenkopi, and Kaibab, although physical measurements were not always tied to these lithologies. Physical properties from a depth of 21 to 31 m (69 to 102 ft) in MCC-3 are listed in Table 2.4. Abrupt changes in Young's, shear, and bulk moduli suggest a lithologic change at a depth of ~29 m. Samples in the 29 to 31 m interval may be tied to Kaibab, because those values in the MCC-3 data (Table 2.4) are similar to those of Kaibab in the KC-2 data (Table 2.3).

Lithological control in borehole MCC-4 is better than that in MCC-3, as shown in Tables 2.5 and 2.6. In this hole, the Kaibab begins at a depth of 21 m and continues to the bottom of the hole at 106 m. The thickness of the Kaibab in the core (~85 m) is similar to that measured in outcrop (79 to 81 m). The porosity in core samples ranges from ~2% (in dolomite) to ~30% (in some sandstone horizons). The permeability is equally variable.

Because Kaibab is composed of both dolomite and sandstone, carbonate fractions range from 20 to 97 vol% with quartz being responsible for most of the remaining material (Table 2.6; Haines, 1966). The carbonate fractions generally increase with stratigraphic height. Petrographically, dolomite occurs as (i) a microcrystalline matrix with smaller fraction of subangular to subrounded quartz grains, the latter of which are well sorted with an average diameter of 0.1 mm; (ii) microcrystalline clasts, in which grain diameters are ~0.01 mm and clast diameters range from 0.5 to 7 mm, with an average of 2.5 mm diameter; (iii) as anastomosing stringers, and (iv) coarse anhedral grains with diameters of 0.5 to 4 mm (Haines, 1966). The unit also contains minor plagioclase, microcline, and opaque minerals. Sericite occurs at one specific stratigraphic interval.

The composition of the Kaibab varies with stratigraphic position as the beds vary between different mixtures of sand and dolomite. Silica in 12 stratigraphic subdivisions of the Kaibab ranges from 16.36 to 57.43 wt%, with an average of 38.32 wt% (Table 2.2; See *et al.*, 2002). Dolomite (MgO , CaO , and CO_2) dominate the remainder of the material in the samples, but ~2 wt% Al_2O_3 and Fe_2O_3 also occur in the unit.

Moenkopi Formation. The strikingly red Moenkopi is the lower of two Triassic sedimentary sequences that dominate the Painted Desert province. Interestingly, the Moenkopi and the underlying yellowish Kaibab span the Permian-Triassic boundary, which represents the largest mass extinction event in the marine record during the Phanerozoic. The contact between these two formations is unconformable, however, so sediments deposited precisely at the P-T boundary do not exist and the sequence cannot be used to determine the cause of the P-T mass extinction event. One hypothesis being explored elsewhere in the world is that the P-T mass extinction, like the Cretaceous-Tertiary (K-T) event that claimed dinosaurs and 75% of the species on Earth, was caused by an impact event far larger in scale than that represented by Barringer Crater.

In the vicinity of the crater, the Moenkopi Formation is composed of two members: Wupatki and Moqui (McKee, 1954). An uppermost Holbrook Member and the overlying Chinle Formation do not occur in the vicinity of the crater, although the latter is abundant to the east, northeast, and north. Where covered by the Chinle (and, thus, not eroded), the Moenkopi can reach a thickness of 600 to 700 feet (183 to 213 m). In the walls of the crater, however, the Moenkopi ranges from only 7 to 30 ft (2 to 10 m).

Some of the beds of Moenkopi are a calcareous siltstone with an iron-rich matrix. Within the MCC-4 core, quartz content of the siltstone varied from 55 to 80%, the remainder being composed of carbonate (Table 2.6). Porosity ranged from 7.5 to 18.2% and the permeability is low. Quartz is subrounded, equant, and well-sorted, with an average diameter of 0.1 mm (Haines, 1966). Some of the quartz recovered in the MCC-4 core has wavy extinction. Calcite is typically coarser (0.2 mm average) than the quartz. It also envelopes quartz and has anhedral margins, indicating a secondary origin. Diagenetic growth of calcite nodules, up to 6 mm, with embedded quartz occurs in some intervals (Haines, 1966). Other detrital grains include feldspar and unidentified opaque material in trace amounts. The matrix is very fine-grained and not well-characterized, but is stained by iron. The Moenkopi also contains fissile intervals that contain abundant sericite and muscovite (Haines, 1966).

Those mineral assemblages produce strata with compositions that are moderately silicious (averaging 65.30 wt% SiO_2) and also contain significant quantities of CaO (and presumably CO_2), Al_2O_3 , Fe_2O_3 , FeO , and K_2O (Table 2.2).

Moenkopi sediments were deposited on a coastal floodplain at the edge of a sea, similar to modern Louisiana. Many of the beds were deposited on intertidal mud flats, where several sedimentary features were produced (Fig. 2.4): dessication (mud) cracks, longitudinal and interference ripple marks (the latter indicating conflicting current directions), sole marks, worm and shrimp burrows that wander across slabs, raindrop impressions, reptile and amphibian trackways, and abundant fossils. One of the most important fossil quarries in the Moenkopi is located at the crater (Camp et al., 1947; Peabody, 1948; Welles and Cosgriff, 1965).

A University of California excavation team worked the site in the 1930's. The finds include tetrapod tracks with beaded skin surfaces and over 20 skulls. Track ways produced by multiple species of amphibians and reptiles were recovered (Fig. 2.5). Some of the skulls represented a new species of capitosaurid amphibian (Fig. 2.6). The type specimen from the quarry is called *Parotosaurus peabodyi* (Welles and Cosgriff, 1965).

The basal Wupatki Member begins with a red, thin (~1 ft thick) fissile shale, although this shale does not outcrop in all locations around the crater. The Wupatki Member is dominated by a cross-bedded, but relatively massive unit that outcrops as a rounded pink ledge-forming unit that often erodes into a series of orbicular knobs. The unit is 2 to 6 m (7 to 20 ft) thick. Outcrops of the Wupatki Member form a veneer on the landscape in the immediate vicinity of the crater.

Stratigraphically above the Wupatki Member is a dark red siltstone and sandstone unit about 8 m (25 ft) thick that is called the Moqui Member of the Moenkopi (Shoemaker and Kieffer, 1974). This unit is very fissile compared to the Wupatki member. The overturned sequence usually occurs in this unit, which, because of its fissile nature, makes it difficult to put one's finger on the contact between upright and overturned Moenkopi in the rim sequence. (See discussion in Chapter 6).

The Moenkopi is a well-known building stone at the crater and elsewhere in the region. The first museum at the crater (on northwest crater rim) and another building (on southwest ejecta blanket) were built of the stone, as was Harvey Nininger's American Meteorite Museum that existed along Highway or Route 66 from 1946 through 1953. In Flagstaff, the Babbitt Brothers Building (built between 1888 and

1891), Atlantic and Pacific Railroad Depot (1889), Old Main at Northern Arizona University (1894), and the Coconino County Courthouse (1894-95) are built with blocks of Moenkopi, which is often called Arizona Red Sandstone.

Pre-impact Structure

The impact occurred in a relatively flat lying sequence of these Permian and Triassic sediments. Folds in the region are evident, but subtle. Synclines and anticlines occur within a few kilometers of the crater and the impact occurred on a gentle monoclinal fold (Fig. 2.7; Shoemaker, 1960). Although a thin-veneer of Moenkopi occurs at the crater, it is absent around Canyon Diablo and over a vast region to the west of the crater. The presence of Moenkopi at the impact site is fortuitous, however, because it greatly assists in interpretation of crater formation (as discussed in Chapter 6). Target sediments are also cross-cut by NW-SE trending normal faults (Fig. 2.7) that may be many kilometers long, but only have offsets of a few to about 30 m (Shoemaker, 1987). The region is also cross-cut by a strong set of joints that can extend for hundreds of meters (Kelley and Clinton, 1960), with pre-impact orientations of that seem to have formed a conjugate NW-SE and weaker SW-NE. Roddy (1978) measured the joints within a few kilometers of the crater and found the most prominent orientations in Moenkopi are 293° (with a range of 290 to 297°) and in Kaibab are 304° (with a range of 301 to 308°). A secondary set is oriented 23° (with a range of 10 to 32°) in the Moenkopi and 30° (with a range of 17 to 36°) in the Kaibab. As Roddy (1978) describes, these joints remain vertical in canyon walls down to depths of 100 m in the region and have been implicated in the unusually square shape of the impact crater (Shoemaker, 1960, 1987), as discussed further in the next chapter.

Topography at the time of impact

Pre-impact topography can be inferred from the existing topography, because the crater is so young and erosion may have been small. (See Chapter 7 for discussion of post-impact erosion.) A better measure of the topography at the time of impact, however, can be made using the topography visible in the crater walls and buried beneath impact ejecta. As discussed above, the Moenkopi in the crater walls varies in thickness from 2 to 10 m, implying topography up to 8 m. A drilling campaign through the ejecta blanket revealed buried topography with an average relief of 5 to 10 m and a maximum of 23 m (Roddy *et al.*, 1975). Grant and Schultz (1993) used ground-penetrating radar to image the subsurface on the west side of the crater. They found Moenkopi ridges beneath the ejecta blanket that were approximately 200 m wide and 5 m high. Gilbert (1896) also tried to reconstruct the topography before the crater formed. He extended existing topographic contours beyond the crater ejecta blanket towards crater center. His method assumes there has been little erosion since the crater formed. His restored topographic map suggests variation of about 3 m and the possibility of a small SW-NE stream channel at the point of impact.

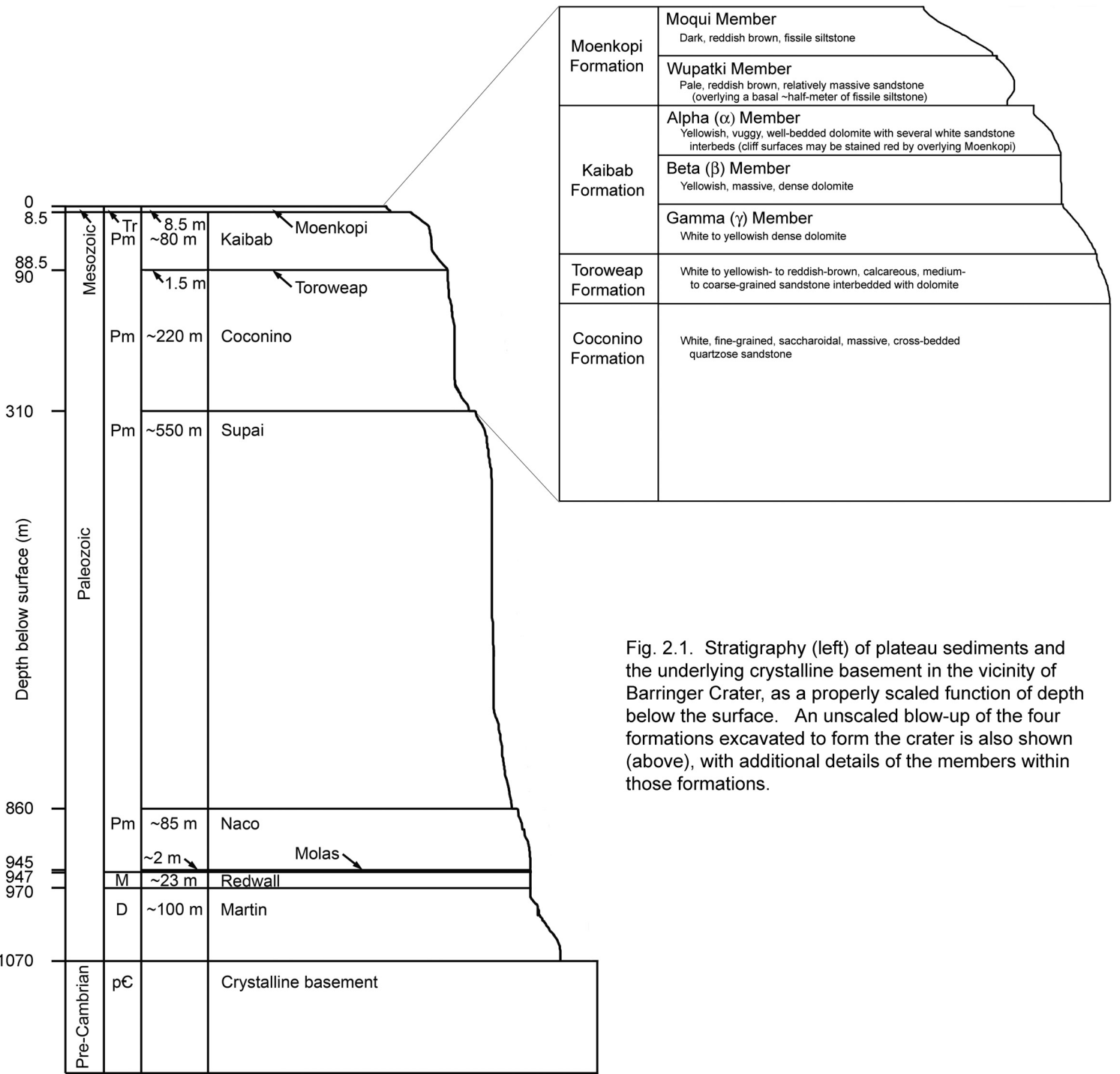


Fig. 2.1. Stratigraphy (left) of plateau sediments and the underlying crystalline basement in the vicinity of Barringer Crater, as a properly scaled function of depth below the surface. An unscaled blow-up of the four formations excavated to form the crater is also shown (above), with additional details of the members within those formations.

Table 2.1. Physical properties of the Coconino Formation

Bulk density (g/cm ³)	Grain density (g/cm ³)	Quartz (vol%)	Feldspar (vol%)	Other minerals	Average grain size (mm)	Modal grain size (mm)	Porosity (%)	Crushing strength dry (dynes/cm ²) (10 ⁸)	Crushing strength H ₂ O sat. (dynes/cm ²) (10 ⁸)	Tensile strength (MPa)	Cp (km/s)	Cs (km/s)	Reference
1.99	-	97	3	-	0.12-0.15	-	24-25	-	-	-	-	-	1
1.98	2.67	97	3	tr	0.117	0.149	25	3.14	3.64	-	-	-	2
-	-	>95	<1	<4	0.19	-	9-18*	-	-	-	-	-	3
-	-	>95	<1	<4	0.19	-	<10**	-	-	-	-	-	3
2.08	-	-	-	-	-	-	-	-	-	17***	2.81	1.82	4
2.08	-	-	-	-	-	-	-	-	-	20****	2.81	1.82	4

* for massive Coconino sandstone beds

** for laminated Coconino sandstone beds

*** for strain rate of 1/2.4 x 10⁶/s

**** for strain rate of 1/1.4 x 10⁶/s

Data tabulated as published. To compare the crushing and tensile strengths, 3.14 and 3.64 x 10⁸ dynes/cm² = 31.4 and 36.4 MPa

References: (1) Ahrens and Gregson, 1964; (2) Shipman *et al.*, 1971; (3) Kieffer, 1971; (4) Ai and Ahrens, 2004

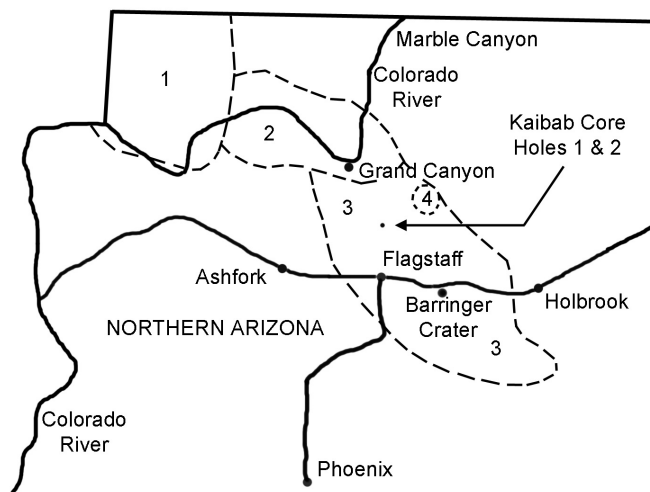
Table 2.2. Compositions of target lithologies at Barringer Meteorite Crater*

Formation	Stratigraphic thickness (m)	Cumulative target rock thickness (m)	SiO ₂	TiO ₂	Al ₂ O ₃	Fe ₂ O ₃	FeO	MnO	MgO	CaO	Na ₂ O	K ₂ O	P ₂ O ₅	LOI	Total
Moenkopi	12.3	12.3	65.30	0.43	7.67	2.63	1.88	0.06	0.99	10.17	0.02	1.42	0.11	11.05	99.10
Kaibab	73	85.3	38.32	0.12	2.02	2.05	0.16	0.03	11.57	19.31	0.03	0.51	0.19	27.29	99.57
Toroweap	1.4	86.7	93.34	0.08	2.02	0.73	0.17	0.01	0.88	1.07	0.00	0.38	0.06	2.14	100.16
Coconino	34.4	121.1	97.03	0.07	1.49	0.67	0.05	0.00	0.06	0.12	0.00	0.19	0.03	0.51	99.55

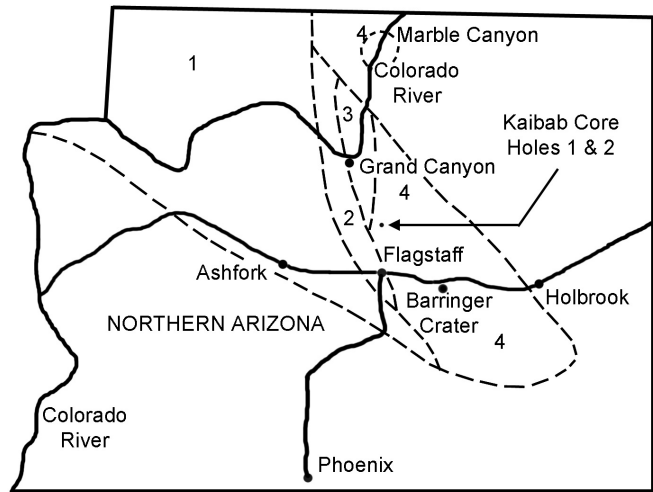
* See *et al.* (2002); analyses of individual stratigraphic intervals can also be found in that source.



Fig. 2.2. Fossils (a-c) and diagenetic features (d) in the Kaibab Formation. Fossils are apparent in the unit, but are often poorly preserved because of diagenetic alteration (a). Better examples can be found, albeit rarely, as illustrated by the two specimens (b-c) recovered by Meteor Crater Enterprises staff. Tear-pants weathering of Kaibab surfaces (d) reflects the mix of carbonate, sulphate, and silica fluids involved in the formation of the dolomite. In the alpha member of the Kaibab, a prominent diagenetically-altered bed is often described as the yellow vuggy unit or yellow vuggy dolomite. It is a useful marker bed.



Kaibab Fm.; Alpha (α) Member; Facies 1, 2, 3, and 4



Kaibab Fm.; Beta (β) Member; Facies 1, 2, 3, and 4

Fig. 2.3. The geographic distribution of facies within the Kaibab Formation of northern Arizona. Barringer Meteorite Crater occurs in Facies 3 of the Alpha Member (left panel) and Facies 4 of the Beta Member (right panel) of the Kaibab Formation. Drill core samples of Kaibab dolomite unaffected by the impact event were recovered in the vicinity of SP cinder cone, northwest of the crater. The Kaibab at that location represents the same facies as that at the impact crater. (Map modified from McKee, 1938.)

Table 2.3. Physical properties of the Kaibab Formation recovered from a site unaffected by impact event*

Drill core hole KC-2 (to represent unshocked Kaibab)

Located ~1 km west of the SP Crater Lava Flow

Depth (m)	Dry Bulk Density (g/cm ³)	Grain Density (g/cm ³)	Porosity (%)	Permeability (millidarcies)	Unconfined Compressive Strength (10 ³ dyne/cm ²)	Tensile Strength (10 ⁷ dyne/cm ²)	Poisson's Ratio	Young's Modulus (dynes/cm ²) (10 ¹¹)	Shear Modulus (dynes/cm ²) (10 ¹¹)	Bulk Modulus (dynes/cm ²) (10 ¹¹)	V _p (mps)	V _s (mps)
Static Measurements												
2.5	2.49	2.88	13.5	-	-	6.21	0.316	7.16	2.83	6.28	-	-
5	2.18	2.87	24	-	8.54	-	0.264	4.45	1.76	3.14	-	-
7.2	2.29	2.66	13.9	-	-	1.57	0.192	1.65	0.70	1.00	-	-
8.3	2.08	2.85	27	-	6.6	-	0.249	4.12	1.65	2.74	-	-
11.2	2.49	2.85	12.6	-	9.89	-	0.326	6.33	2.39	6.07	-	-
15.2	2.18	2.72	19.9	-	-	3.03	0.125	2.42	1.08	1.08	-	-
17.9	2.23	2.85	21.8	-	4.08	-	0.157	3.32	1.44	1.62	-	-
18.7	2.16	2.69	19.7	-	-	1.2	0.088	1.28	0.59	0.87	-	-
22.3	2.09	2.78	24.8	-	8.54	-	0.155	2.60	1.12	1.25	-	-
Avg	2.24	2.79	19.69	-	7.53	3.00	0.21	3.70	1.51	2.67	-	-
Std Dev	0.15	0.08	5.30	-	2.26	2.28	0.08	2.02	0.75	2.14	-	-
#	9	9	9	-	5	4	9	9	9	9	-	-
Pulse Measurements												
2.5	2.49	2.88	13.5	-	-	-	0.254	7.03	2.80	4.77	5800	3400
5	2.18	2.87	24	-	-	-	0.198	4.42	1.85	2.44	4800	2900
7.2	2.29	2.66	13.9	-	-	-	0.131	1.61	0.71	0.72	2700	1700
8.3	2.08	2.85	27	-	-	-	0.205	3.82	1.58	2.16	4500	2800
11.2	2.49	2.85	12.6	-	-	-	0.237	6.63	2.68	4.20	5600	3300
15.2	2.18	2.72	19.9	-	-	-	0.147	2.85	1.24	1.34	3700	2400
17.9	2.23	2.85	21.8	-	-	-	0.245	2.91	1.16	1.90	3900	2300
18.7	2.16	2.69	19.7	-	-	-	0.06	1.45	0.69	0.55	2600	1800
22.3	2.09	2.78	24.8	-	-	-	0.209	2.78	1.15	1.60	3900	2300
Avg	2.24	2.79	19.69	-	-	-	0.187	3.72	1.54	2.19	4167	2544
Std Dev	0.15	0.08	5.30	-	-	-	0.063	1.99	0.77	1.45	1129	602
#	9	9	9	-	-	-	9	9	9	9	9	9
Avg	2.24	2.79	19.69	-	7.53	3.00	0.198	3.71	1.52	2.43	4167	2544
Std Dev	0.15	0.08	5.30	-	2.26	2.28	0.073	1.95	0.74	1.79	1129	602
#	9	9	9	-	5	4	18	18	18	18	9	9

* Watkins and Walters (1966); Core type NX, which produces a 75 mm diameter hole and a 54.8 mm diameter core

Data is tabulated as originally published. However, to convert to modern units: 1 dyne/cm² = 0.1 pascals;

thus, a tensile strength of 3.00×10⁷ dyne/cm² = 3.00×10⁶ pascals = 3.00 M Pa

Table 2.4. Physical properties of crater lithologies

Drill core hole MCC-3*

South side of crater, 150 meters from topographical crater rim

Depth (m)	Dry Bulk Density (g/cm ³)	Grain Density (g/cm ³)	Porosity (%)	Permeability (millidarcies)	Unconfined Compressive Strength (10 ⁸) (dynes/cm ²)	Tensile Strength (10 ⁷) (dynes/cm ²)	Poisson's Ratio	Young's Modulus (10 ¹¹) (dynes/cm ²)	Shear Modulus (10 ¹¹) (dynes/cm ²)	Bulk Modulus (10 ¹¹) (dynes/cm ²)	Vp (mps)	Vs (mps)				
Static Measurements																
21.1	1.98	2.70	26.8	-	Sample too soft for testing											
23.4	2.30	2.69	14.5	-	6.37	-	0.118	0.98	0.43	0.44	-	-				
24.1	2.28	2.71	15.8	-	5.55	-	0.195	0.48	0.26	0.20	-	-				
28.1	2.22	2.65	16.3	-	-	0.47	0.165	0.60	0.30	0.33	-	-				
29.0	2.49	2.81	12.1	-	Sample too small for testing											
29.8	2.30	2.81	18.1	-	8.68	-	0.172	3.83	1.95	1.63	-	-				
30.0	2.14	2.90	26.3	-	-	2.16	0.220	1.88	1.12	0.77	-	-				
30.3	2.41	2.82	14.6	-	6.44	-	0.197	4.55	2.50	1.90	-	-				
30.4	2.44	2.80	12.9	-	-	2.94	0.135	6.23	2.84	2.74	-	-				
Avg	2.28	2.77	17.5		6.76	1.86	0.172	2.65	1.34	1.14	-	-				
Std Dev	0.16	0.08	5.4		1.34	1.26	0.036	2.24	1.09	0.96	-	-				
#	9	9	9		4	3	7	7	7	7	-	-				
Pulse Measurements																
21.1	1.98	2.70	26.8	-	-	-	0.239	0.37	0.14	0.23	1470	860				
23.4	2.30	2.69	14.5	-	-	-	0.235	1.01	0.41	0.64	2260	1330				
24.1	2.28	2.71	15.8	-	-	-	0.194	1.98	0.83	1.07	2180	1340				
28.1	2.22	2.65	16.3	-	-	-	0.052	1.28	0.61	0.47	2410	1660				
29.0	2.49	2.81	12.1	-	-	-	-	-	-	-	3850	-				
29.8	2.30	2.81	18.1	-	-	-	0.179	3.75	1.59	2.98	4210	2630				
30.0	2.14	2.90	26.3	-	-	-	0.304	3.06	1.17	2.59	4940	2620				
30.3	2.41	2.82	14.6	-	-	-	0.222	0.71	0.29	0.43	1840	1100				
30.4	2.44	2.80	12.9	-	-	-	0.143	5.23	2.28	2.45	4750	3060				
Avg	2.28	2.77	17.5				0.196	2.17	0.92	1.36	3101	1825				
Std Dev	0.16	0.08	5.4				0.075	1.70	0.73	1.13	1331	825				
#	9	9	9		4	3	8	8	8	8	9	9				
Avg	2.28	2.77	17.5	-	6.8	1.86	0.185	2.40	1.11	1.26	3101	1825				
Std Dev	0.16	0.08	5.4	-	1.3	1.26	0.059	1.91	0.91	1.02	1331	825				
#	9	9	9		4	3	15	15	15	15	9	9				

* Watkins and Walters (1966); Core type NX, which produces a 75 mm diameter hole and a 54.8 mm diameter core

Data is tabulated as originally published. However, to convert to modern units: 1 dyne/cm² = 0.1 pascals;

thus, a tensile strength of 1.86×10^7 dyne/cm² = 1.86×10^6 pascals = 1.86 MPa

Table 2.5. Physical properties of crater lithologies and a lithologic assessment

Drill core hole MCC-4*

South side of crater, 10 meters from topographical crater rim

Depth (m)	Sub-surface elevation (m)	Dry Bulk Density (g/cm ³)	Grain Density (g/cm ³)	Porosity (%)	Permeability (millidarcies)	Lithologic Assessment**
8.2	1731.8	2.18	2.85	23.5	17.3	Ejecta - Sandstone
9.3	1730.7	2.17	2.93	25.9	2.5	Ejecta - Sandstone
10.7	1729.3	2.19	3.63	18.2	1.3	Moenkopi - Sandstone
16.0	1724.0	2.44	2.89	15.6	<0.4	Moenkopi - Sandstone
20.0	1720.0	2.48	2.68	7.5	<0.4	Moenkopi - Shaly Sandstone
21.0	1719.0	2.68	2.73	1.8	<0.4	Kaibab - Dolomite
21.4	1718.6	2.63	2.74	4.0	<0.4	Kaibab - Calc-dolomite
22.0	1718.0	2.61	2.68	2.6	<0.4	Kaibab - Dolomite
29.5	1710.5	2.44	3.04	20.0	<0.4	Kaibab - Dolomite
34.0	1706.0	2.18	2.81	23.2	26.8	Kaibab - Dolomite
37.5	1702.5	2.22	3.03	26.7	4.7	Kaibab - Dolomite
47.6	1692.4	2.39	2.99	20.1	3.8	Kaibab - Sandstone and Dolomite
54.4	1685.6	2.15	3.05	29.5	25.1	Kaibab - Sandstone and Dolomite
61.0	1679.0	2.33	2.74	15.0	1.5	Kaibab - Sandstone and Dolomite
68.0	1672.0	2.17	2.89	24.9	16.8	Kaibab - Sandstone and Dolomite
75.8	1664.2	2.14	2.72	21.3	16.7	Kaibab - Sandstone and Dolomite
81.7	1658.3	2.12	2.82	24.8	30.6	Kaibab - Sandstone and Dolomite
87.5	1652.5	2.15	3.02	28.8	37.6	Kaibab - Sandstone and Dolomite
91.5	1648.5	2.24	2.68	16.7	4.2	Kaibab - Sandstone and Dolomite
94.8	1645.2	2.35	2.91	19.2	1.7	Kaibab - Dolomite
98.3	1641.7	2.13	2.87	25.8	33.3	Kaibab - Sandstone
101.9	1638.1	2.12	2.65	22.0	80.7	Kaibab - Sandstone
105.9	1634.1	2.18	2.65	18.3	15.5	Kaibab - Sandstone
Avg		2.29	2.87	18.9	~13.9	
Std Dev		0.18	0.21	8.1	~19.1	

* Watkins and Walters (1966); core type NX, which produces a 75 mm diameter hole and a 54.8 mm diameter core

** Haines (1966); the elevation data for these lithologies are also calculated from a 1,740 m collar height provided by this author

Table 2.6. Physical and mineralogical properties of the Moenkopi and Kaibab formations.

Moenkopi Properties

Drill core hole MCC-4* **

South side of crater, 10 meters from topographical crater rim

Depth (m)	Sub-surface elevation (m)	Carbonate (vol%)	Quartz (vol%)	Cavities (vol%)	Insoluble residue (mostly qtz) (wt%)	Dry Bulk Density (g/cm ³)	Grain Density (g/cm ³)	Porosity (%)	Permeability (millidarcies)
10.7	1729.3	-	-	-	-	2.19	3.63	18.2	1.3
11.4	1728.6	25	75	-	71.7	-	-	-	-
16.0	1724.0	-	-	-	-	2.44	2.89	15.6	<0.4
16.1	1723.9	45	55	-	-	-	-	-	-
20.0	1720.0	-	-	-	-	2.48	2.68	7.5	<0.4
20.1	1719.9	20	80	-	-	-	-	-	-

* Haines (1966); vol% determined visually in thin-section; wt% insoluble residue after acid dissolution of carbonate

** Watkins and Walters (1966)

Kaibab Properties

Drill core hole MCC-4*, **, ***

South side of crater, 10 meters from topographical crater rim

Depth (m)	Sub-surface elevation (m)	Carbonate (vol%)	Quartz (vol%)	Cavities (vol%)	Insoluble residue (mostly qtz) (wt%)	Dry Bulk Density (g/cm ³)	Grain Density (g/cm ³)	Porosity (%)	Permeability (millidarcies)
21.0	1719.0	97	3	Tr	-	2.68	2.73	1.8	<0.4
21.4	1718.6	95	2	3	-	2.63	2.74	4.0	<0.4
22.0	1718.0	95	5	-	-	2.61	2.68	2.6	<0.4
22.6	1717.4	-	-	-	24.6	-	-	-	-
22.7	1717.3	65	35	-	-	-	-	-	-
23.3	1716.7	40	60	-	-	-	-	-	-
29.5	1710.5	-	-	-	-	2.44	3.04	20.0	<0.4
29.9	1710.1	75	10	15	-	-	-	-	-
30.2	1709.8	-	-	-	5.1	-	-	-	-
32.6	1707.4	70	10	20	-	-	-	-	-
34.0	1706.0	-	-	-	-	2.18	2.81	23.2	26.8
37.5	1702.5	75	25	-	-	2.22	3.03	26.7	4.7
45.5	1694.5	75	20	5	-	-	-	-	-
45.5	1694.5	-	-	-	41.4	-	-	-	-
47.6	1692.4	-	-	-	-	2.39	2.99	20.1	3.8
53.4	1686.6	75	10	15	-	-	-	-	-
54.4	1685.6	-	-	-	-	2.15	3.05	29.5	25.1
61.0	1679.0	35	65	-	-	2.33	2.74	15.0	1.5
61.0	1679.0	-	-	-	73.7	-	-	-	-
67.5	1672.5	75	10	15	-	-	-	-	-
68.0	1672.0	-	-	-	-	2.17	2.89	24.9	16.8
69.8	1670.2	55	45	-	-	-	-	-	-
75.6	1664.4	-	-	-	69.6	-	-	-	-
75.7	1664.3	44	55	1	-	-	-	-	-
75.8	1664.2	-	-	-	-	2.14	2.72	21.3	16.7
81.7	1658.3	-	-	-	-	2.12	2.82	24.8	30.6
81.8	1658.2	55	43	2	-	-	-	-	-
87.4	1652.6	60	40	-	-	-	-	-	-
87.5	1652.5	-	-	-	-	2.15	3.02	28.8	37.6
91.5	1648.5	-	-	-	-	2.24	2.68	16.7	4.2
91.5	1648.5	-	-	-	48.5	-	-	-	-
91.6	1648.4	60	35	5	-	-	-	-	-
94.8	1645.2	-	-	-	-	2.35	2.91	19.2	1.7
95.0	1645.0	25	75	-	-	-	-	-	-
95.0	1645.0	-	-	-	76.4	-	-	-	-
98.3	1641.7	-	-	-	-	2.13	2.87	25.8	33.3
98.5	1641.5	40	60	-	-	-	-	-	-
98.5	1641.5	-	-	-	66	-	-	-	-
101.5	1638.5	-	-	-	71.5	-	-	-	-
101.9	1638.1	-	-	-	-	2.12	2.65	22.0	80.7
103.0	1637.0	20	75	5	-	-	-	-	-
105.9	1634.1	-	-	-	-	2.18	2.65	18.3	15.5
106.0	1634.0	40	60	-	-	-	-	-	-
106.0	1634.0	-	-	-	56.5	-	-	-	-

* Haines (1966); vol% determined visually in thin-section; wt% insoluble residue after acid dissolution of carbonate

** Watkins and Walters (1966)

*** Kaibab is logged from 21 to 106 m for a total of 85 m, which is comparable to Shoemaker's measured thickness of 79-81 m.

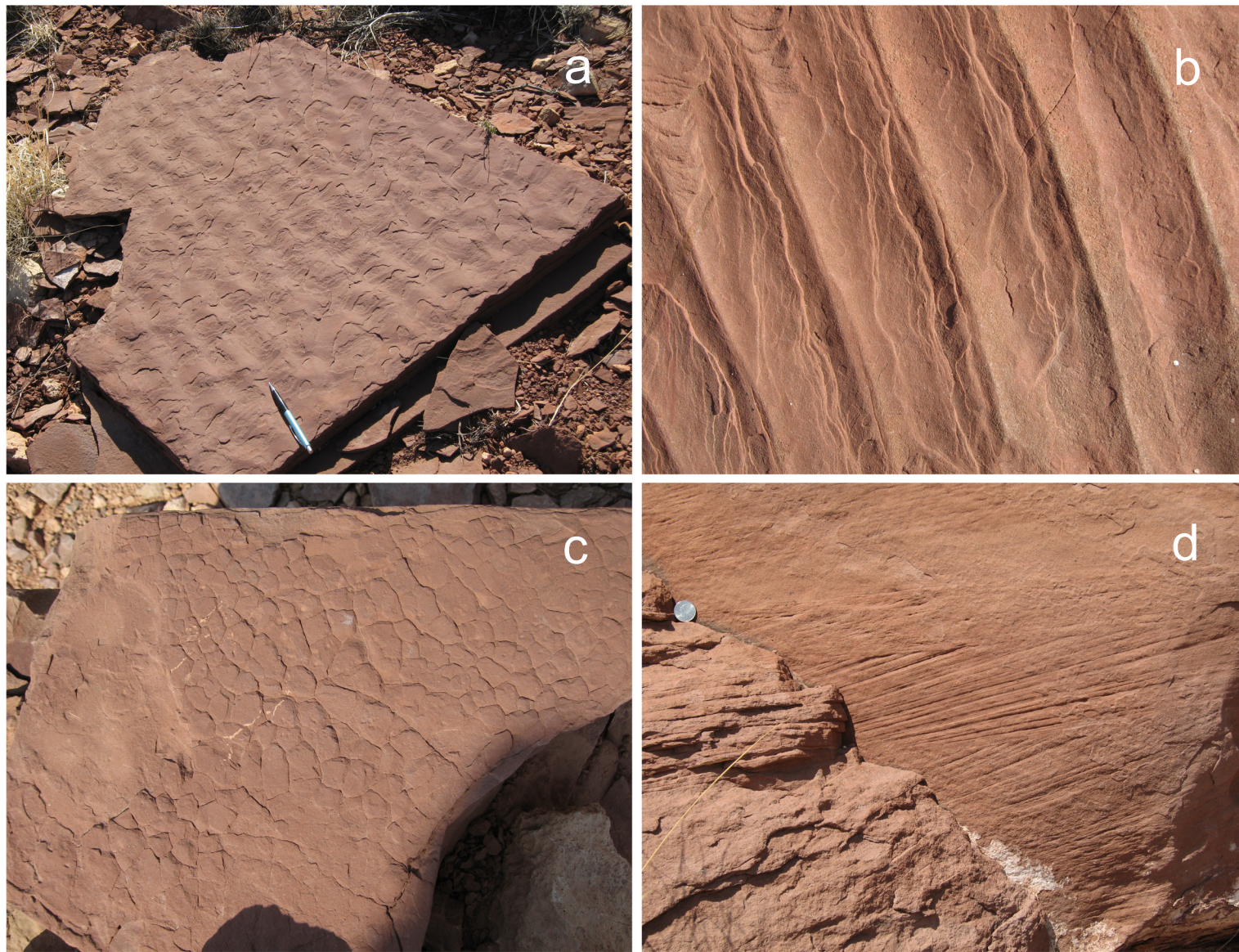
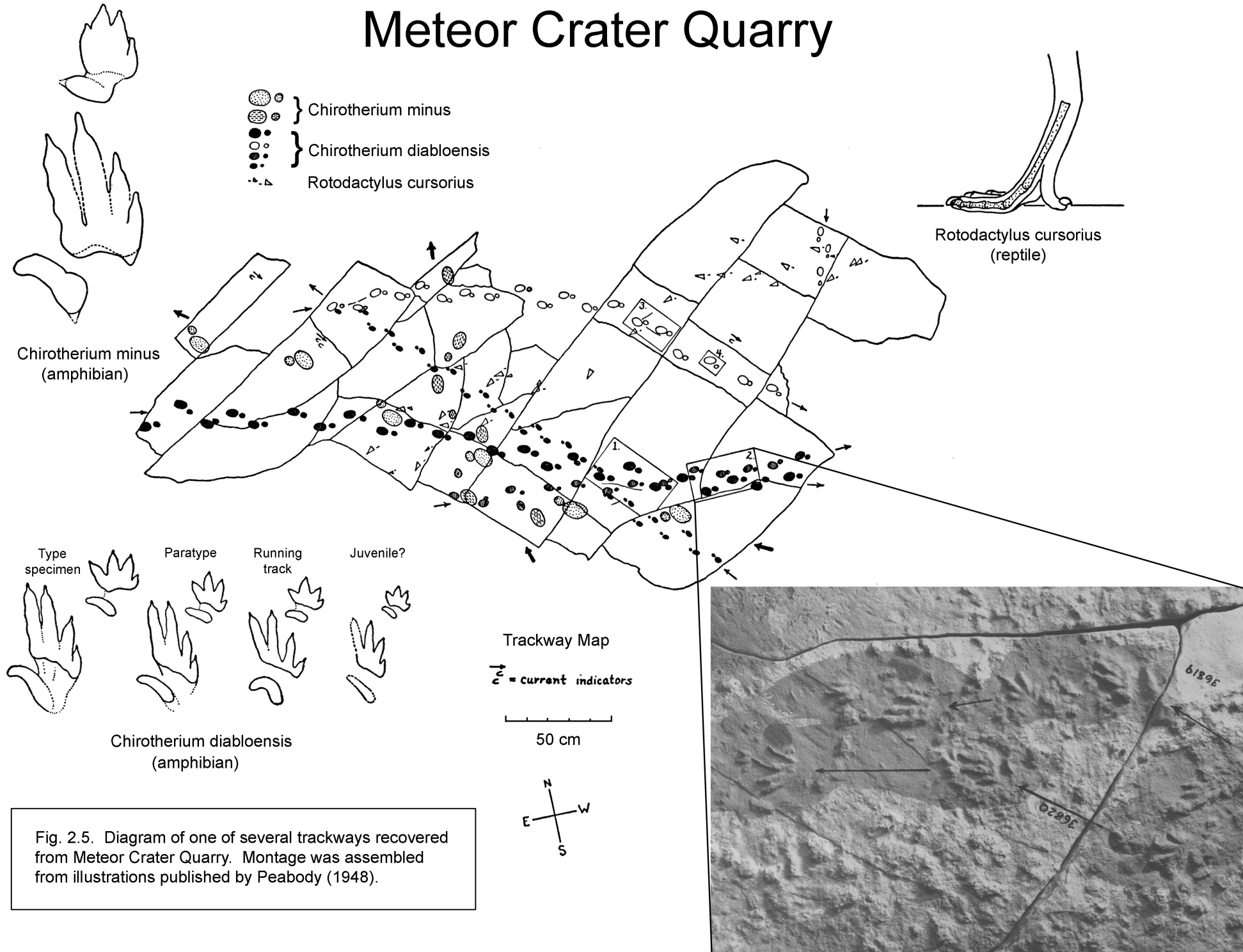


Fig. 2.4. Moenkopi sediments were deposited in a shallow-water coastal environment that was above wave base. A variety of wave-driven ripple marks, representing several types of current velocities, occur in the Moenkopi as illustrated in an oblique view of a slab (a) and an overhead view of another slab (b). Water often receded, producing dessication or mud cracks (c). Particularly important for the interpretation of the crater rim structure is the geopetal nature of cross-bedding exposed in the Moenkopi (d). This particular block is oriented normally, although the cross-beds in other blocks in the crater rim may be overturned.

Meteor Crater Quarry



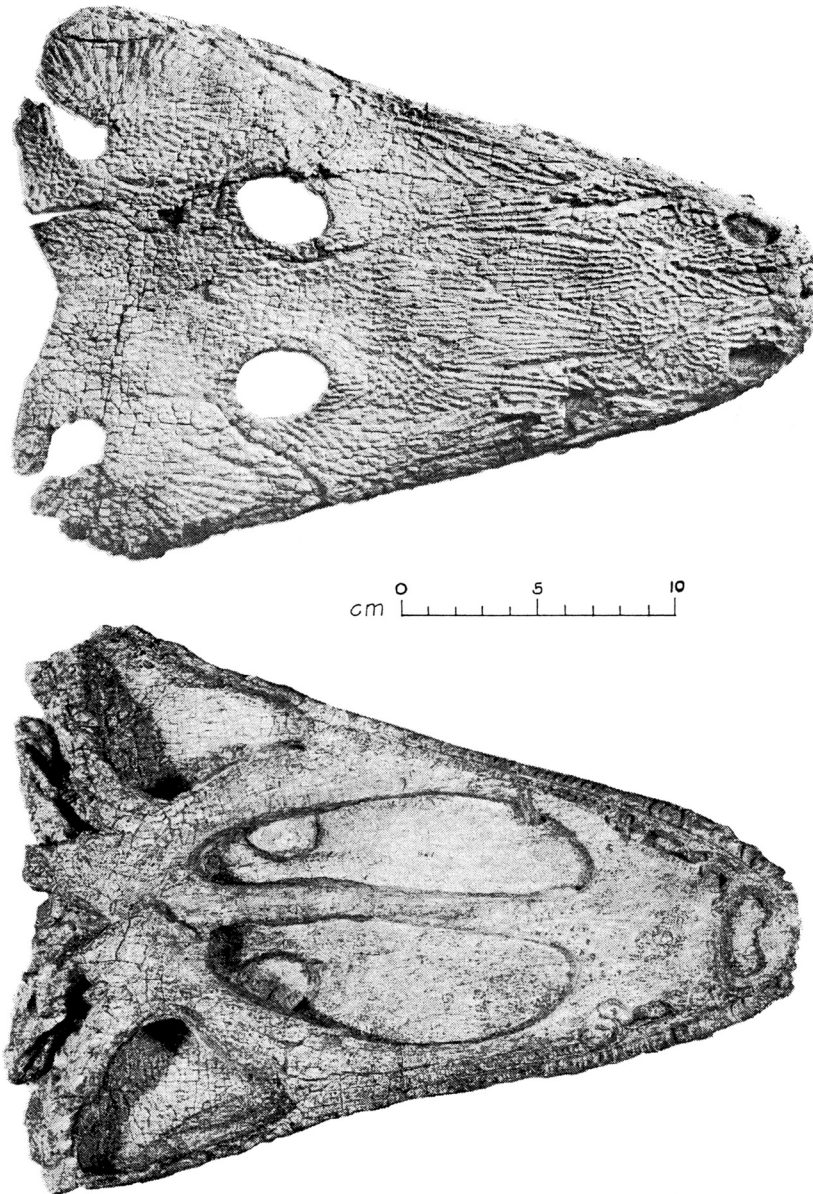
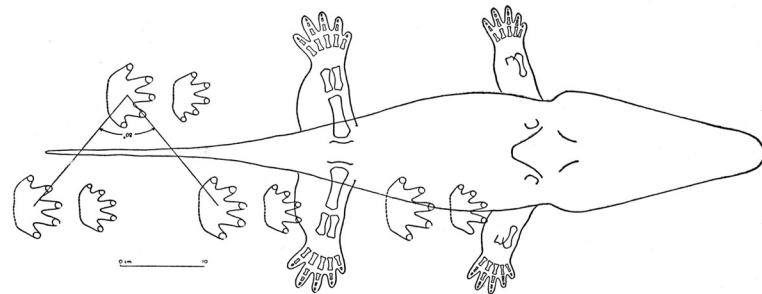
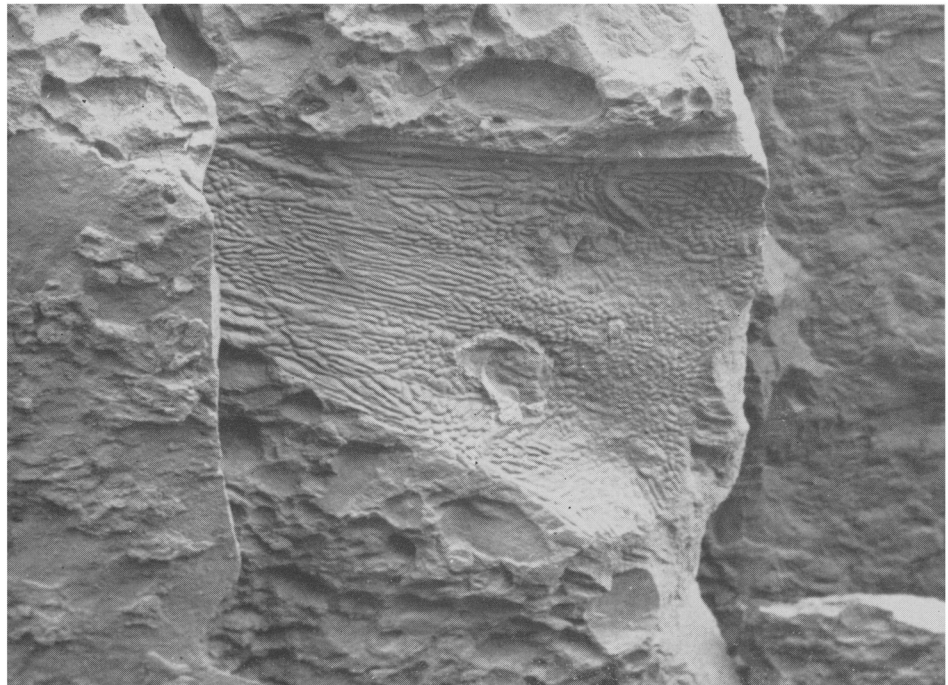


Fig. 2.6. A nearly complete skull of a new species of Labyrinthodont Family Capitosauridae that was recovered from the Moenkopi Formation in the Meteor Crater Quarry. This new species, *Parotosaurus peabodyi*, was described by Welles and Cosgriff (1965). The midline length of the skull is 28.3 cm (11.1 in). Teath are 6 mm long. There is room for 80 teeth in the peripheral row on each side of the maxillary, although Welles and Cosgriff suggest only half these were functional on the living animal. This is the type specimen for the species, but more than 20 skulls were recovered from the quarry, the largest of which had a midline length of 43.8 cm (17.2 in).



Impressions of capitosaurid skulls were also recovered a neaby quarry in Moqui Wash, including an example that occurs with shale pebbles in a fluvial foreset bed (top photograph from Peabody 1948). A sketch of a capitosaurid and the tracks it produced at Moqui Wash is also shown (bottom illustration, also from Peabody 1948).

Meteor Crater Quarry

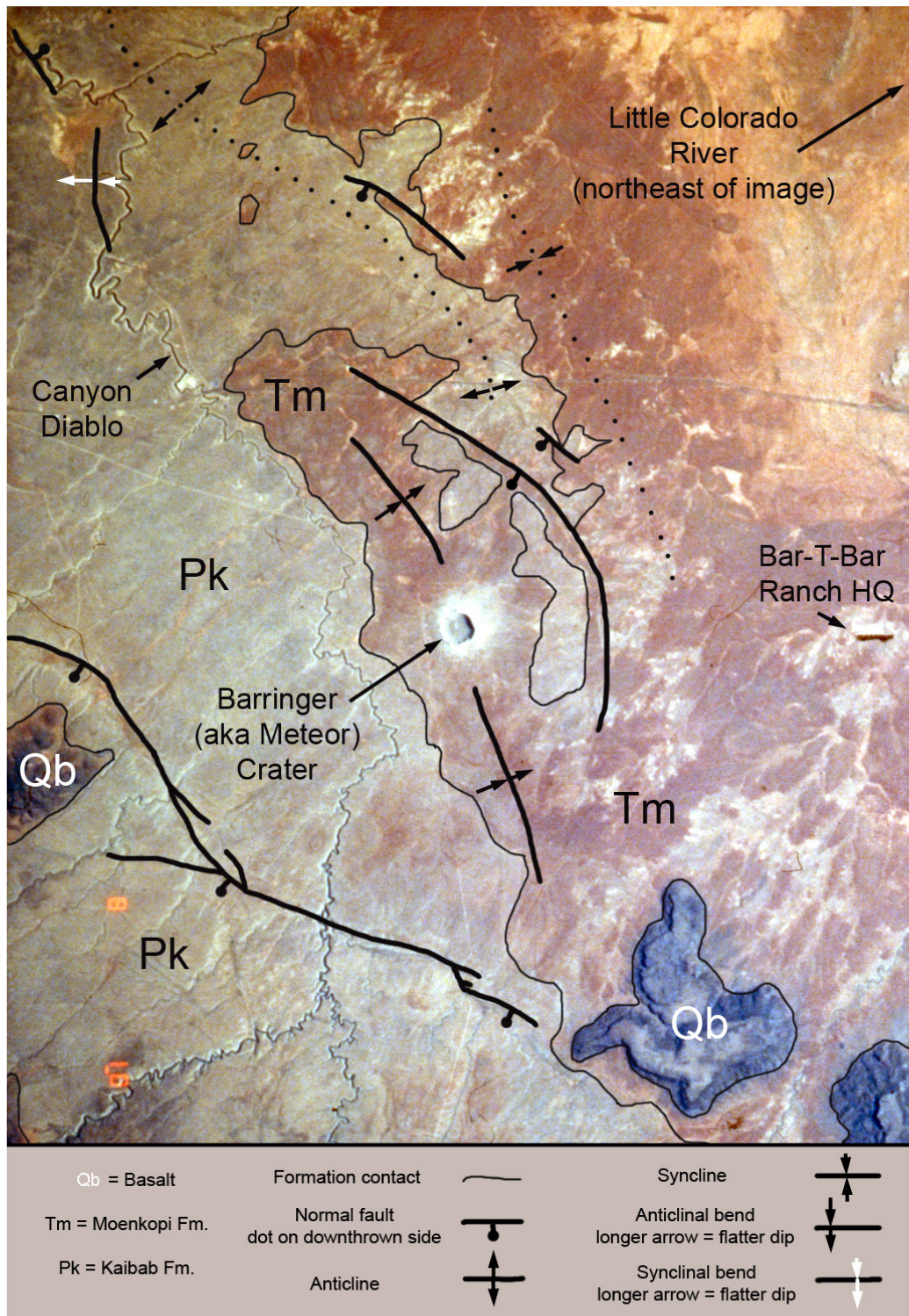


Fig. 2.7. Bedrock geologic map for the region around Barringer Meteorite Crater (*a k a* Meteor Crater) imprinted on an image taken from Space Shuttle Columbia (a cropped version of image #STS040-614-058). The formation contacts of Moenkopi (Tm) and Kaibab (Pk) are approximate, because Moenkopi is thin and becomes patchy in the vicinity of the crater. No effort was made to represent Pleistocene and Holocene alluvium or to distinguish Quaternary basalt (Qb) from talus derived from the basalt. Pleistocene impact ejecta and older subsurface lithologies exposed in the crater walls are also not mapped at this scale. Solid-line normal faults are mapped as seen in the image. Solid-line anticlines are inferred from geologic exposure and are consistent with the geologic map of Shoemaker (1958, as published in 1960). Anticlinal and synclinal bends are taken from Shoemaker (1960); solid lines represent more precise location of axes than do dotted lines.

3. Barringer Meteorite Impact Crater



Barringer Meteorite Crater has a diameter of ~1.2 km (Fig. 3.1 and 3.2). It is topographically defined by a rim that rises 30 to 60 m above the surrounding plain and a bowl-shaped depression that is ~180 m deep. The upper crater walls have average slopes of ~40 to ~50°, although they also include vertical to near-vertical cliffs. The crater floor is below the surrounding plain, which is a feature that distinguishes Barringer Crater from most volcanic structures where craters are perched on volcanic summits (*e.g.*, cinder cones, shield volcanoes, and stratovolcanoes). Volcanic maars are the principal exception.

The crater has a simple bowl-shaped morphology, which is the classic “simple” crater morphology that characterizes impact craters that are ≤ 2 km diameter in sedimentary targets and ≤ 4 km diameter in crystalline targets (under Earth’s gravity). In contrast, larger “complex” craters may have central peaks, central peak rings, modification zones where the crater walls extensively collapse, and possibly external structural deformational rings.

Tear faults cross-cut the crater in four areas, producing “corners” that give the crater a squared shape in plan view, rather than a circular one. The region was cross-cut by a strong set of SE-NW joints and a weaker set of SW-NE joints prior to impact (Shoemaker, 1960; Roddy, 1978), which are generally thought to have been activated into tear faults during the excavation phase of the crater forming event.

Shoemaker (1960) produced the definitive geologic map of the crater (Fig. 3.3), which illustrates the target lithologies in the crater walls and the redistribution of target lithologies in a surrounding ejecta blanket. It also shows that the upper crater walls and uplifted crater rim are composed of Coconino, Toroweap, Kaibab, Moenkopi, and debris from those units. Debris also occurs within the crater in the form of complex breccia deposits that Shoemaker (1960) mapped as three units: authigenic breccia, allogenetic breccia, and mixed debris.

Authigenic breccias are monomict, intraformational breccias that are caused by disruptive shear within formations (*e.g.*, Kaibab). This type of breccia is present along faults that cross-cut the crater walls and crater rim.

Allogenetic breccias are sometimes dominated by components from a single formation, but in other cases are composed of fragments from multiple formations. These breccia deposits are displaced, however, having flowed down crater walls. They also contain shock-melted Coconino (lechatelerite) and meteoritic debris. Remnants of these breccias occur on upper crater walls, but they also flowed downward to form a thick breccia lens at the bottom of the crater (Fig. 3.4). Shoemaker (1974) suggested that downward flows of allogenetic breccia converged on the crater floor to form a “central peak” beneath Silica Hill. Where exposed in crater walls, the allogenetic breccia is dominated by debris from the Kaibab Formation. In the breccia lens on the crater floor, however, the breccia is dominated by fragments from the Coconino Formation. As illustrated in the W-E cross-section of Fig 3.4, the lens of allogenetic breccia on the crater floor is generally believed to conform to a hemispherical transient crater. As discussed below, however, the subsurface extent of the breccia is still uncertain.

Stratigraphically above and resting on the allogenetic breccia is a unit Shoemaker (1960) called “mixed debris.” This unit contains material from all four formations, including all five stages of shocked Coconino sandstone (as defined by Kieffer, 1971), plus meteoritic debris. In one of the deposits that outcrops along the east crater wall, Shoemaker (1974) also described lapilli of shock-melted Kaibab dolomite. Although not described by Shoemaker, I have also found fragments of vesicular mixed melts in that breccia. Shoemaker interpreted this mixed debris unit to be fall-out material. That is, material

blasted into the atmosphere above the crater and then re-deposited on top of the crater after it was excavated. Shoemaker (1960) only found this material within the crater. Exposed patches are found along the upper crater walls and a 10.5 m (35 ft) thick layer sits on top of the allogenetic breccia on the crater floor. This latter unit appears to be normally size-sorted (*i.e.*, coarse fragments on the bottom of unit and finer fragments at top of unit; Shoemaker, 1974). Mixed debris was probably deposited beyond the crater rim on top of the ejecta blanket, although it has since been stripped away by erosion. Fragments of the type of material found in the mixed debris unit are found in younger (post-impact) alluvium terraces that surround the crater.

Post-impact erosion and sedimentation has modified the crater interior, which is evident in both the aerial image of the crater (Fig. 3.1) and the geologic map (Fig. 3.3). Talus and finer debris components have collected at the base of the crater walls, greatly reducing the steepness of the crater walls. Although the topography of the crater is still dramatic, erosional reduction of the rim height, shallowing of the crater wall slope, and sediment filling of the crater floor has reduced the observable size of the crater.

A ~30 m (100 ft) section of lake sediments cover the allogenetic breccia in the center of the crater. Moving radially outward from crater center, these lake sediments are interfingered with alluvium being shed from the crater walls. After the impact event the climatic conditions became increasingly arid and the lake evaporated, producing a ~1.6 m (10 ft) thick sequence of playa beds (Shoemaker, 1974).

The erosional processes that produced the talus and alluvium deposits continue today, as evident from the large Kaibab boulders strewn about the crater floor and continuous loss of the fragile allogenetic and mixed breccia deposits that cling to the crater walls. Multiple cubic yards of these scientifically valuable breccias are sometimes lost each year.

To help readers correlate the surface geologic units described above with the observable landscape, I have produced an overlay (Fig. 3.5) of Shoemaker's geologic map and an aerial photograph.

Our ability to extend this surface geology downward into the subsurface is greatly enhanced by extensive drilling and deep shafts that were excavated during mining operations at the crater, augmented by later subsurface imaging using several geophysical techniques.

Between 1903 and 1908, the Standard Iron Company drilled 28 holes in the crater floor (maximum depth 1,085 ft or 323 m), excavated 7 shafts on the crater floor (maximum depth of 222 ft or 68 m), excavated 6 shafts on the southern ejecta blanket, excavated 1 shaft on the northern ejecta blanket, excavated 1 shaft just beyond the northern ejecta blanket, and excavated several trenches in the ejecta blanket at sites distributed around the entire crater (Barringer, 1910). Fairchild (1907) reports there were more than 50 pits and trenches on the external slopes of the crater.

Many of the boreholes were reamed with a toothed, hardened steel bit that produced a 2 ½ inch core, if the rock had sufficient structural integrity (Fairchild, 1907). Because of its inherent weakness, most material in the breccia lens was washed upward by flowing water in the form of disaggregated chips and sand. Only large boulders in the breccia lens and bedrock below the breccia lens were recovered in core form (*e.g.*, in holes 4, 6, 7, and 8). Unfortunately, none of that core material survives.

The boreholes drilled in the crater floor indicate the breccia lens bottoms at a depth of 600 to 700 ft (180 to 210 m) (Table 3.1), which corresponds to the base of the Coconino (Shoemaker, 1960; Roddy, 1978). These boreholes provided the data used to estimate the depth of the breccia lens in Shoemaker's cross-section of the crater (Fig. 3.4). According to Shoemaker (1974), the Supai Formation was recovered at depths exceeding 700 ft (210 m), whereas Fairchild (1907) reports red beds of the Supai were encountered at depths of 830, 860, and 870 ft (253, 262, and 265 m) beneath the crater floor.

Seismic refraction data (Ackermann *et al.*, 1975) is consistent with a breccia lens that bottoms ~190 m beneath the crater floor. The seismic refraction data also suggest the target rocks are fractured beneath the ejecta blanket to distances of 900 m beyond the crater rim and to a depth of at least 800 m below the crater floor and possibly to the crystalline basement.

Holsinger wrote in a letter (as reported by Fairchild, 1907) that a large slab of Coconino slumped down the crater wall during the formation of the breccia lens. Several boreholes northeast of the main shaft encountered a block of the sandstone at depths ranging from 160 to 200 ft before punching through it. The slab is 250 to 400 ft (76 to 122 m) thick, dips at an angle of 40°, and covers 4 to 5 acres (1.6 to 2.0 $\times 10^4$ m²). Approximately 100 ft of breccia is above the slab and more than 100 ft is below it. Meteoritic material occurs in the breccia beneath the slab.

The United States Refining, Smelting, and Mining Company drilled the deepest exploration hole at the crater on the south rim in 1920-1922 and drove a nearly 400-ft long adit or drift into the wall of the crater when the drill stem broke and drill tools were lost at a depth of 311 ft. After the drilling tools were recovered at the end of the adit, drilling continued until a final depth of 1,376 ft (419 m) was reached, which is approximately 827 ft (252 m) (per Hager, 1953) beneath the level of the crater floor. Not only did the adit solve the drilling problem, it also penetrated meteorite-bearing mixed debris between the talus and crater wall, suggesting additional mixed breccia may survive beneath a protective sheath of talus if needed for future research.

Interestingly, the deep borehole encountered several hundred feet of breccia with Ni traces and an apparent concentration of meteoritic debris in the final 30 feet of the hole (Barringer, 1924; see also Table 3.2, which is a log of this borehole). If the borehole was plumbed vertically, then this breccia lies far outside the transient crater. Thus, there is a discrepancy between the symmetrical view of the breccia lens represented by Fig. 3.4 and the borehole data of Barringer. Shoemaker was aware of the drill hole data and the discrepancy it represented, but was unable to resolve the conundrum.

Some possible solutions: (a) breccias and the transient cavity extend beneath the south rim, which, as interpreted by Barringer, might imply something about the trajectory of the impacting asteroid; (b) the drill hole may have curved towards the crater center while descending and essentially intersected a crater cavity with a geometry similar to that inferred by Shoemaker in Fig. 3.4; or (c) a vein, network of veins, or some other horizon of meteoritic debris and/or breccia was injected into the wall of the transient crater cavity and into the surrounding Coconino bedrock. The first solution defies our current understanding of transient crater cavities, unless strong asymmetry was caused by an oblique impact. The second solution is uncomfortable, because the adit that intersects the drill hole at a depth of 311 feet suggests the hole is vertical. The hole would have had to curve tremendously at greater depths to pierce the breccia lens depicted in Shoemaker's cross-section. The third option is also uncomfortable, because the breccia beneath the rim is several hundred feet thick, which, if taken at face value, implies an injection of material far larger than that considered feasible in the past.

Seismic refraction (Ackermann *et al.*, 1975) and gravity (Regan and Hinze, 1975) data paint an independent image of the breccia zone. A model derived from the seismic refraction data suggests the breccia lens is symmetrical, concentrated in the center of the crater, and does not, at depth, extend to the diameter of the crater (Fig. 3.6). A model of the gravity at the crater also suggests the breccia lens is concentrated in the center of the crater and does not, at depth, extend to points beneath the crater rim (Fig. 3.6). An asymmetric feature is recognized on the south side of the crater, but it suggests the breccia lens is less wide (not wider) towards the south. Thus, these geophysical models are generally consistent with Shoemaker's cross-section through the breccia lens.

The seismic refraction data, however, also suggests a possible explanation for the breccia and

meteoritic components in the 1,376 ft borehole. It is clear that the walls of the transient crater (that is, the bedrock beyond the breccia lens) was highly fractured by the impact event. The seismic model includes fractured bedrock to within ~150 m of the bottom of the 1,376 ft borehole. It is possible that the breccia encountered in the borehole represented fractured wall rock, rather than the breccia lens. It is also possible that the traces of meteoritic material represent veins of material injected into that crater wall, producing the Ni-traces seen several times while the drill passed through the fractured wall rock. This requires, however, the injection of meteoritic material nearly 300 m beyond the walls of the transient crater with a radius of ~500 m and depth of ~300 m. The magnitude of brecciation may have been greater than that depicted in Fig. 3.6, if either the zone of fracturing was wider than in the model or if the drill curved towards the crater center. Thus, one might be able to explain the occurrence of breccia and meteoritic material in the hole and still be consistent with estimated dimensions of the breccia lens. The remaining problem is the rather thick (Barringer estimated 30 ft thick) zone of oxidized asteroid at the bottom of the hole. This would seem to require an unusually large vein of injected material in the crater wall. A completely satisfying explanation will probably escape us, unless a series of new boreholes, with coring capabilities, are drilled on the crater floor and crater rim.

Additional drilling occurred after the 1,376 ft hole was completed, but it did not resolve this issue. In 1928, the Meteor Crater Exploration and Mining Company began the final phase of mining operations with three more drill holes (maximum depth 721 feet) in the same area as the 1,376 ft hole. The company then sank a final shaft at the crater from June 1928 through mid-July 1929, when the shaft reached a final depth of 713 ft. Operations stopped there because of flooding. Further exploration of the meteoritic debris beneath the south rim was never pursued further.

Drilling operations were renewed several decades later, but in this case for scientific purposes in support of the Apollo program. The USGS, under contract to NASA, drilled 5 holes on the south rim in 1965-1966 (maximum depth of 366 ft) and excavated a single trench to provide physical information for lunar analogue studies. The USGS also drilled 116 holes through the ejecta blanket and 45 holes beyond the ejecta blanket in the early 1970's. Some of this latter material survives and is available for credible research projects; see the author for details.

Roddy (1978) collated the above drilling and geophysical data and converted the structural depths to values relative to the pre-impact surface. He determined that the average pre-impact surface elevation was 1683 ± 2 m. He estimated the distances from that surface to the top of the fallout, top of breccia lens, base of breccia lens, and base of fractured rock are ~150, ~160, ~310, and 990 m, respectively. He also estimated the average height of the structural uplift in the rim is ~47 m above the pre-impact surface and that the pre-erosion thickness of ejecta on the rim was $\sim 20 \pm 5$ m, with the caveat that the latter was variable.

Beginning with Shoemaker's (1960) comparison of Meteor Crater with nuclear explosion craters, a picture of the processes involved in the crater's formation has matured. Details about the trajectory, energy, and several other parameters are still being debated in the community, but several general attributes of the processes that created the crater can be summarized with two generic graphics (Fig. 3.7 and 3.8). The impacting asteroid penetrated the Moenkopi surface to a depth approximately equal to its diameter and, in an explosive release of its kinetic energy, generated a downward and laterally radiating shock wave. As that shock wave radiated through an increasingly larger volume of rock in the Earth's crust, peak shock pressures declined. Thus, the highest, vapor- and melt-producing shock pressures occurred near the point of impact.

A shock wave simultaneously radiated upward through the projectile, producing a reflected rarefaction wave that then radiated downward into the target. After the shock wave and rarefaction wave passed through a section of the Earth's crust, a residual particle velocity was imparted on the material.

The effect of that velocity was to establish a flow of rock that initially moved downward and radially outward, before moving upward and outward. This is the flow of material that excavated the crater cavity and ejected debris onto the surrounding landscape. Material remaining along the crater walls slumped inward, forming a breccia lens. Depending on the energy of an event, that breccia lens may incorporate impact melt fragments. In the case of Barringer Crater, which is one of the smallest hypervelocity impact craters, very little melt appears to have been incorporated into that breccia lens. The total time involved in this dramatic re-organization of rock, melt, and vapor was only a few seconds.

A discussion of the details involved in this generalized impact cratering scenario, like the trajectory and energy of impact, are discussed in later chapters.

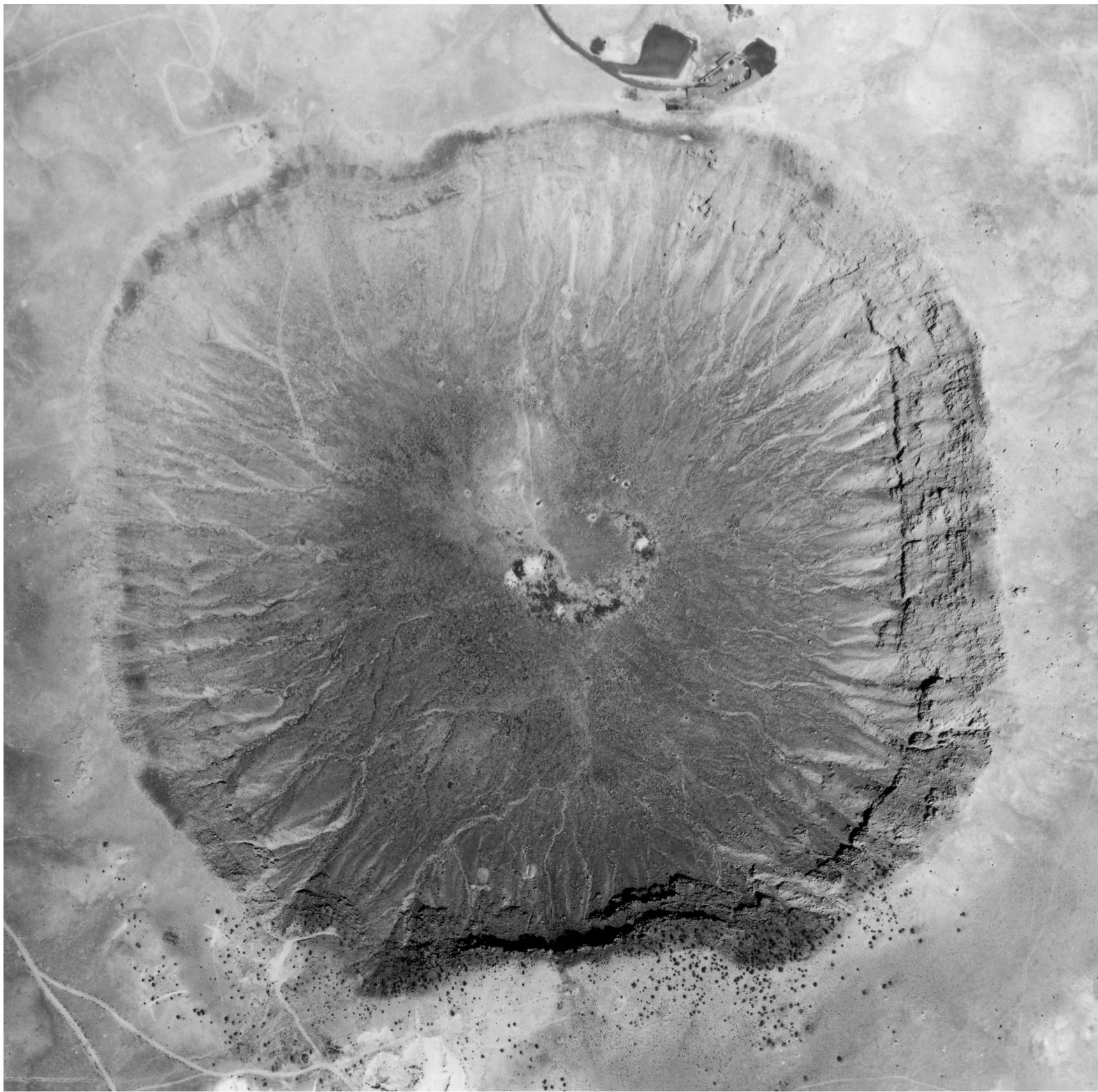
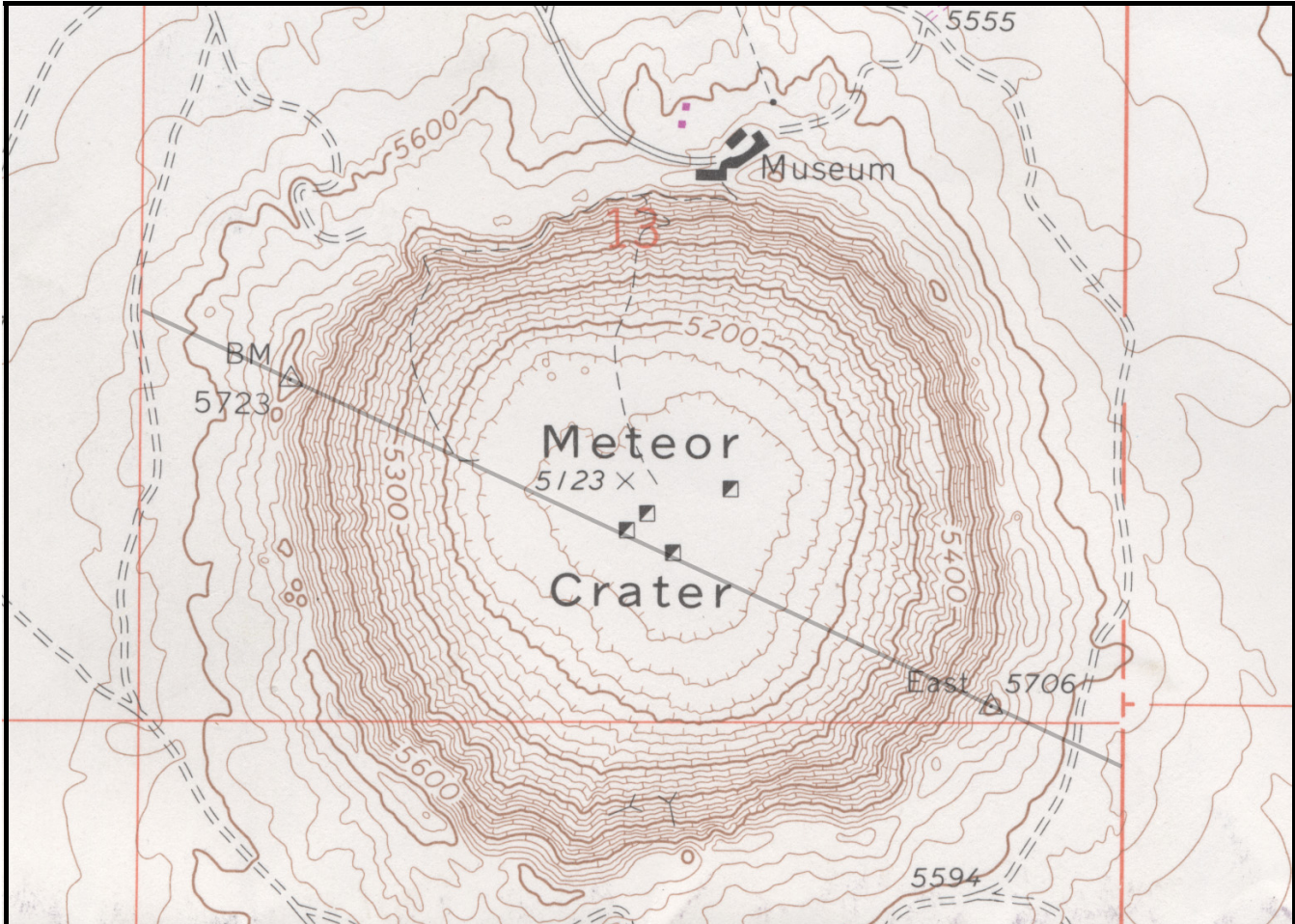


Fig. 3.1. Overhead aerial view of Barringer Meteorite Crater. The crater is ~1.2 km in diameter. The central depression is ~180 m deep and the crater rim rises 30 to 60 m above the surrounding plain. North is at the top of the image and the sun is illuminating the crater from the SSE, creating shadows beneath the cliffs in the southern crater wall and, to a lesser extent, beneath the cliffs in the eastern crater wall. The current museum complex is located on the NNE crater rim. Remnants of mining operations are visible on the crater floor, the south crater wall, and on the SW flank of the crater. Two-needle pinyon pine and juniper dot the southern flank of the crater and the uppermost southern crater wall. Several faults cut through the crater wall and rim sequence. The crater is a modified circle, with slightly squared corners that are associated with those tear faults. The faults may have been activated along pre-existing joints in this portion of the Colorado Plateau (e.g., Shoemaker, 1960).



Barringer Crater Profile (NW-SE)

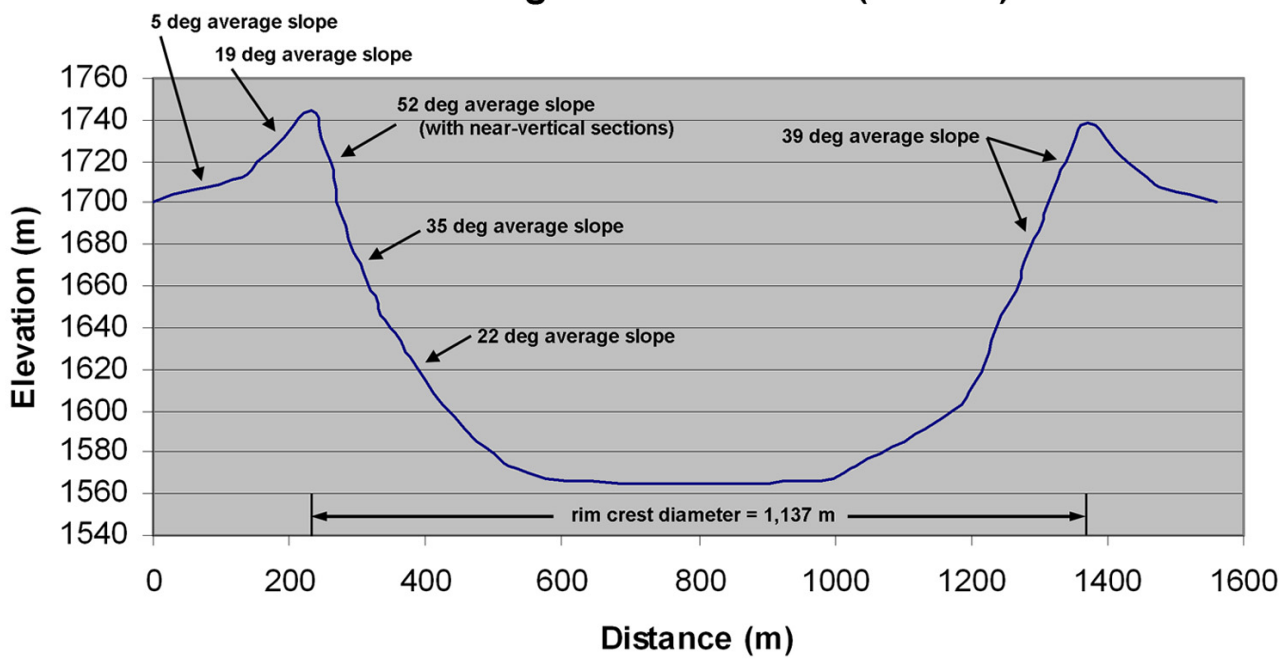


Fig. 3.2. Topographic map of the crater (top panel) as presented on the current USGS 7.5 minute quadrangle for Meteor Crater. The map is contoured in 20 ft intervals. Barringer Point (5723 ft) is the highest location on the crater rim. A line drawn across the map from NW to SE indicates the location of a cross-section through the crater (bottom panel). The cross-section is calibrated in meters and is vertically exaggerated. Slopes in the upper crater wall average ~50 degrees and include near vertical cliffs.

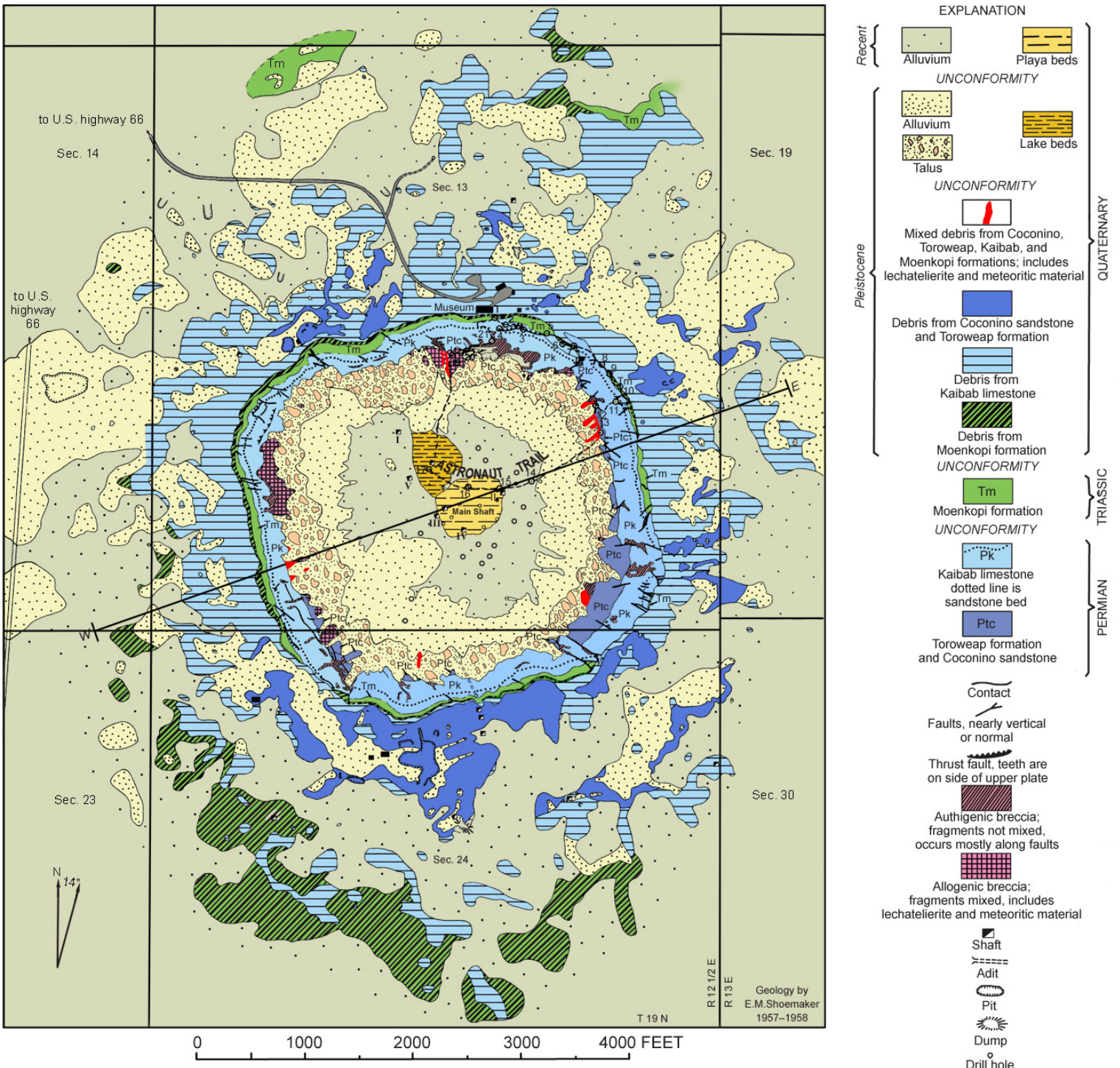


Fig. 3.3. Geologic map of Meteor Crater, Arizona, produced by Eugene M. Shoemaker (1960). In addition to locating the bedrock lithologies (Coconino-Toroweap, Kaibab, and Moenkopi Formations), he also mapped the interior breccia deposits, exterior debris deposits, and faults that cross-cut the crater walls. Many of the features represented by this map had previously been identified by Barringer (e.g., 1905), but Shoemaker mapped them in exquisite detail and provided useful comparisons to geologic features produced in a nuclear explosion crater. This figure is a colorized version of Shoemaker's original map. Target lithologies visible in the crater walls are the Permian Toroweap and Coconino Formations (undivided, Ptc), Permian Kaibab Formation (Pk), and Triassic Moenkopi Formation (Tm). Overturned and ejected Quaternary debris from those units are identified with diagonal hatching (Moenkopi ejecta), horizontal hatching (Kaibab ejecta), and a different shade of color (Coconino ejecta). Impact-generated breccias are identified with different shades of red and pink. A west-east cross-section across the structure is shown in Fig. 3.4.

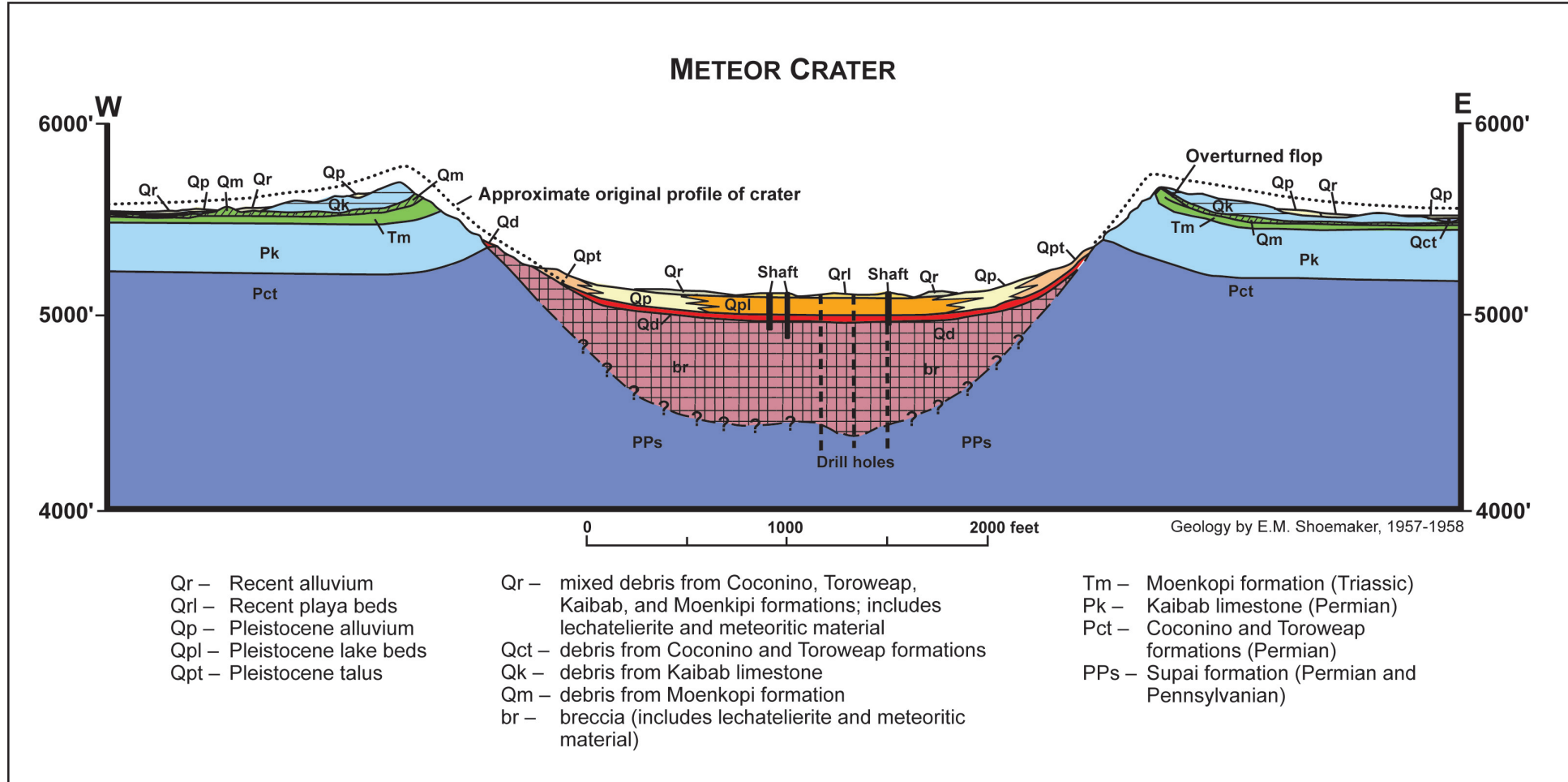


Fig. 3.4. Structural and lithological cross-section through Meteor Crater along a W-E axis. See Fig. 3.3 for the location of the W-E axis and Shoemaker (1960) for the original presentation of this cross-section. The breccia (Br) refers to the allogenic breccia described in the text. The mixed debris unit (Qd) refers to the mixed debris unit or fall-back breccia described in the text. Although not precisely defined in drill core and, thus not marked in the cross-section, the boundary between the Coconino Formation (Pct) and underlying Supai Formation (PPs) is near the bottom of the breccia lens. The cross-section has been redrawn from Shoemaker (1974) and keyed in color.

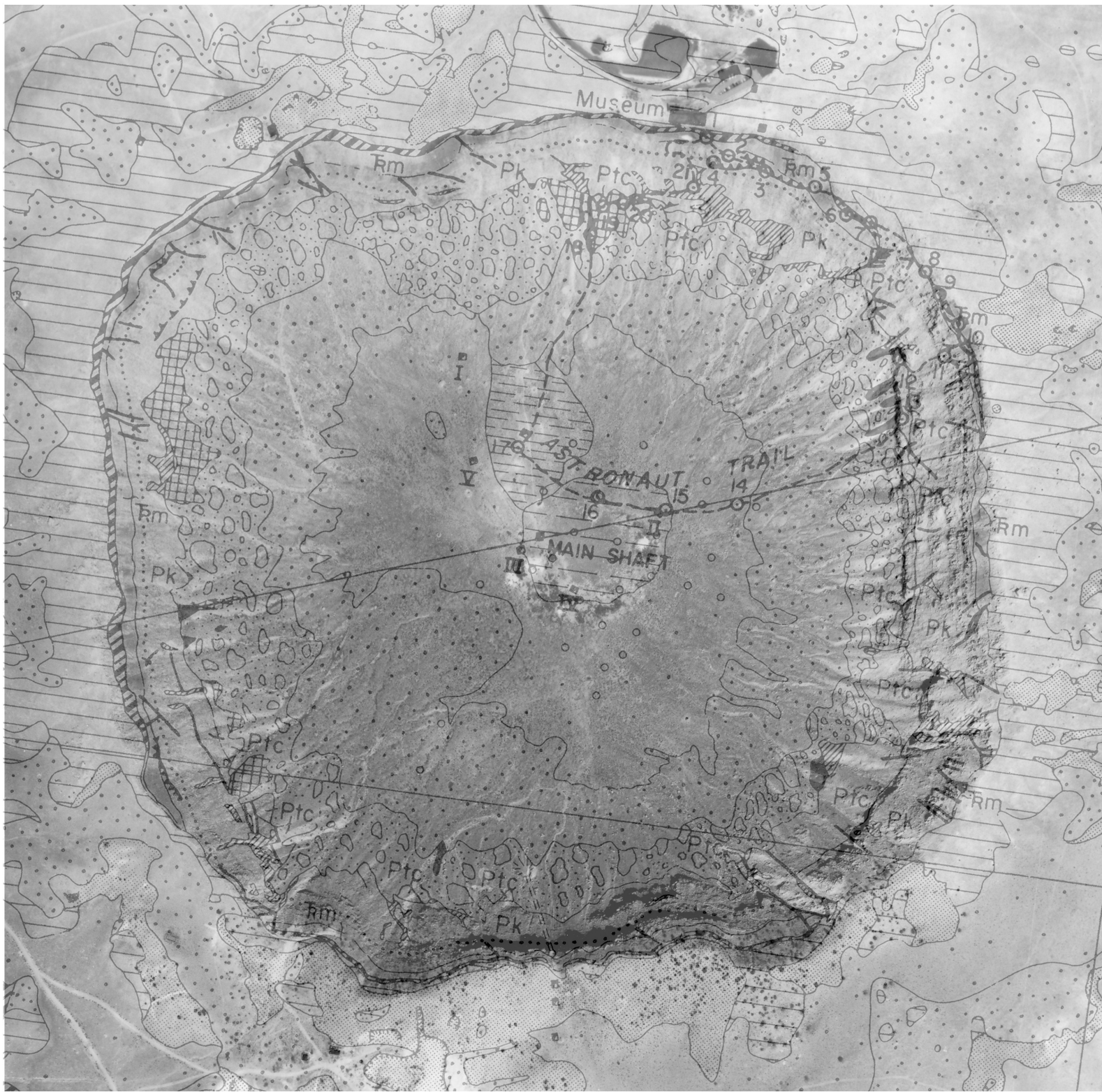


Fig. 3.5. An overlay of Shoemaker's 1960 map and an overhead aerial photograph of the crater. The Astronaut Trail is the route featured during the 1974 Meteoritical Society field trip to the crater, but is severely degraded and no longer functional. The approximate locations of some of the mining features (e.g., main shaft, several smaller shafts, and borehole locations) are marked on the crater floor. See Fig. 3.3 for key to map symbols.

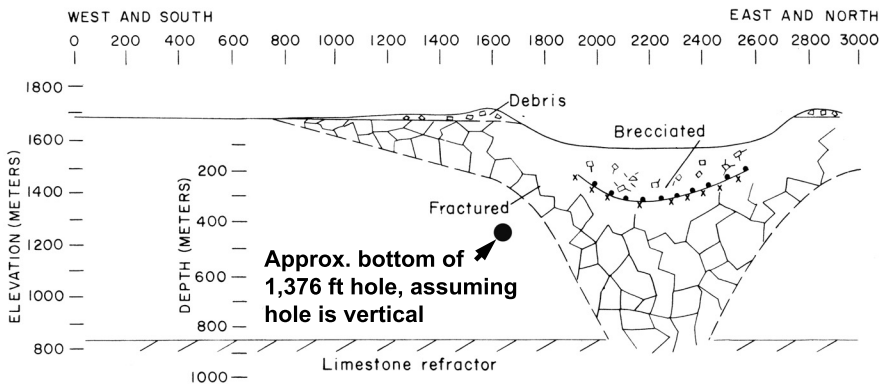
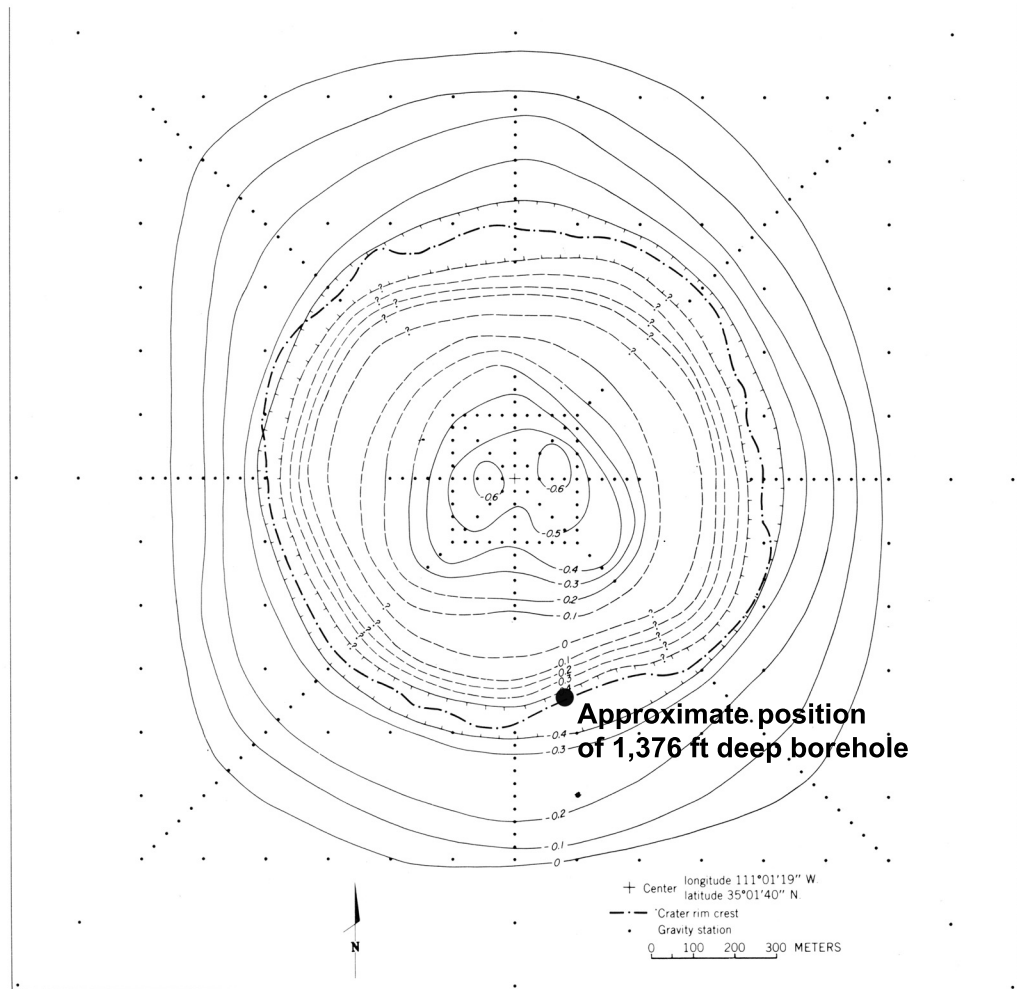
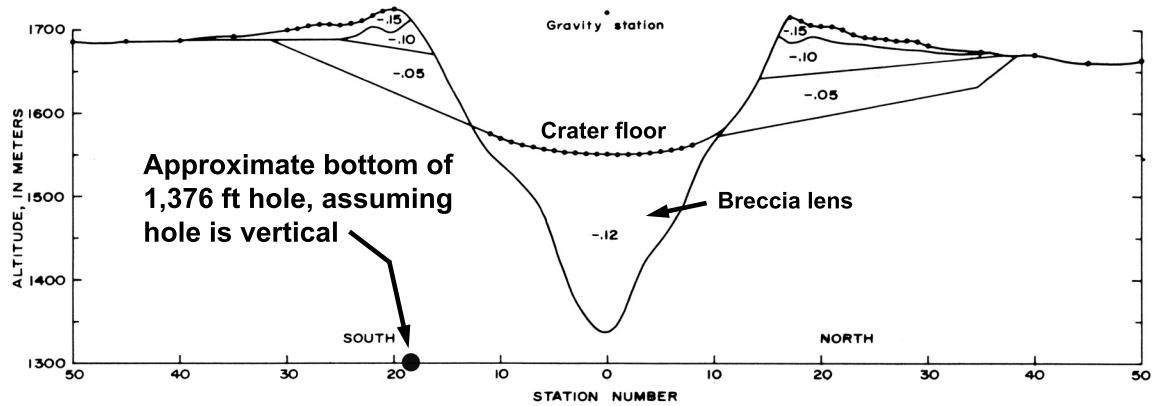


Fig. 3.6. Models of the subsurface structure of Barringer Crater. Model based on seismic refraction data illustrates the extent of ejected debris, the breccia lens, and fractured walls of the crater (top panel). Model based on gravity anomalies illustrates the floor of the breccia lens in a south-north cross-section (middle panel) and in plan view (bottom panel). (Composite illustration based on Ackermann et al., 1975, and Regan & Hinze, 1975.)



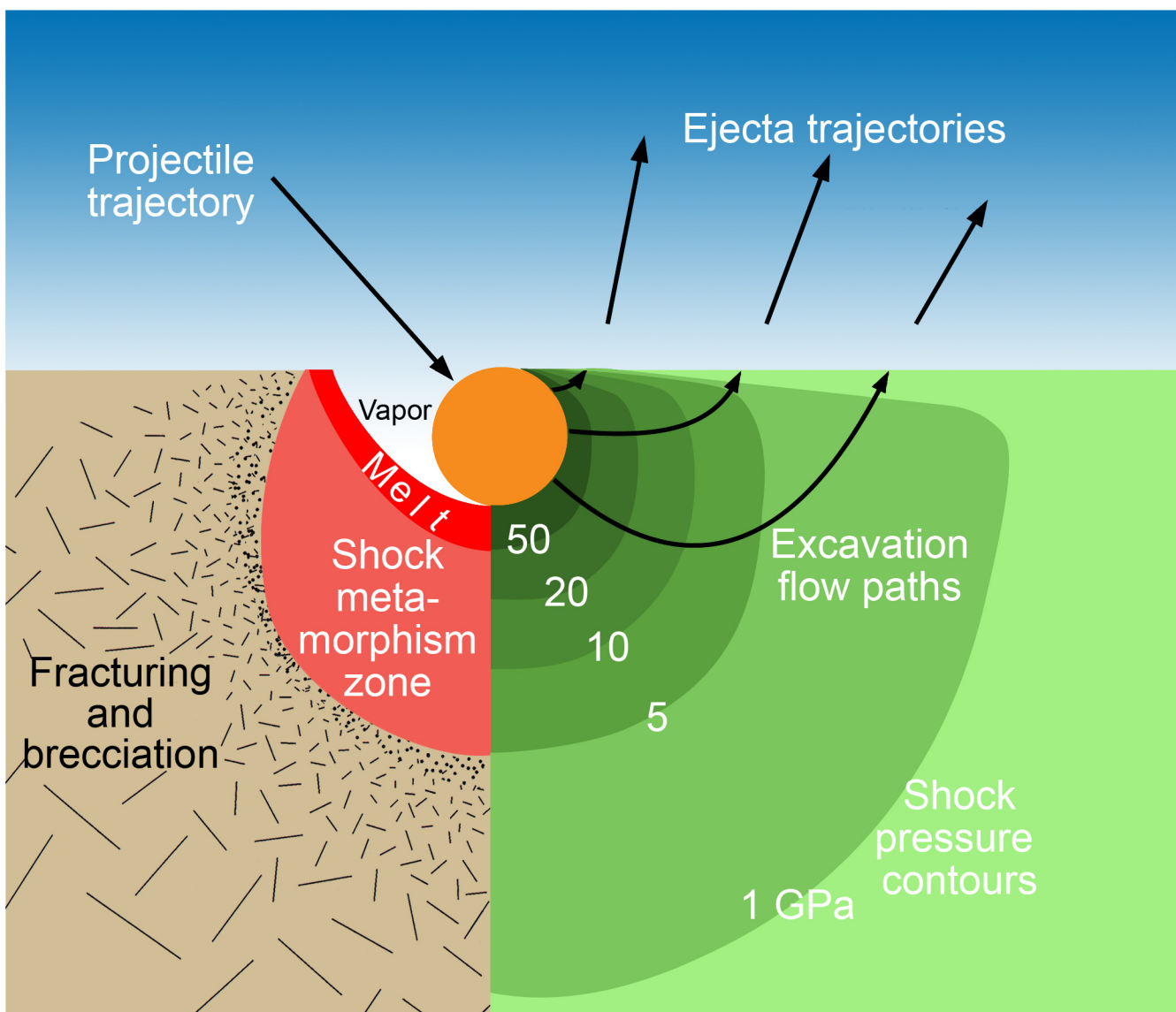


Fig. 3.7. Schematic diagram of the peak shock pressure contours generated during an impact event (right side of diagram) and the type of deformation generated by those shock conditions (left side of diagram). The projectile penetrates to a depth approximately equivalent to its diameter or slightly deeper. The projectile is largely transformed to melt and vapor (the relative proportions of which depend on the energy of the impact event), although a small (<10%) fraction of it may survive as solid fragments. Some of the melted projectile will be mixed with a zone of molten target material (shocked to pressures >50 GPa), but a fraction of it will also be ejected with the vaporized components of the projectile. Shock pressures in the target decrease with distance. Beyond the regions where the target is vaporized and melted, target material will undergo a series of solid state transformations (between shock pressures of ~5 to ~50 GPa), including the production of planar fractures, planar deformation features (or shock lamellae), higher-pressure polymorphs, and diaplectic glasses. At the greatest distances (and lowest shock pressures), the bedrock may be sculpted into shatter cones and fractured. The vaporized, melted, and otherwise shock-metamorphosed material within the transient cavity will flow downward and outward and then upward and outward on paths perpendicular to the shock isobars and ejected into the atmosphere before falling back to the surface on ballistic trajectories. The flow and ejection processes mix material of several different shock levels (including completely unshocked material) and produce complex breccias. (Illustration from an educational poster, *Geological Effects of Impact Cratering*, David A. Kring, NASA Univ. Arizona Space Imagery Center, 2006. Modified from a figure in *Traces of Catastrophe*, Bevan M. French, 1998.)

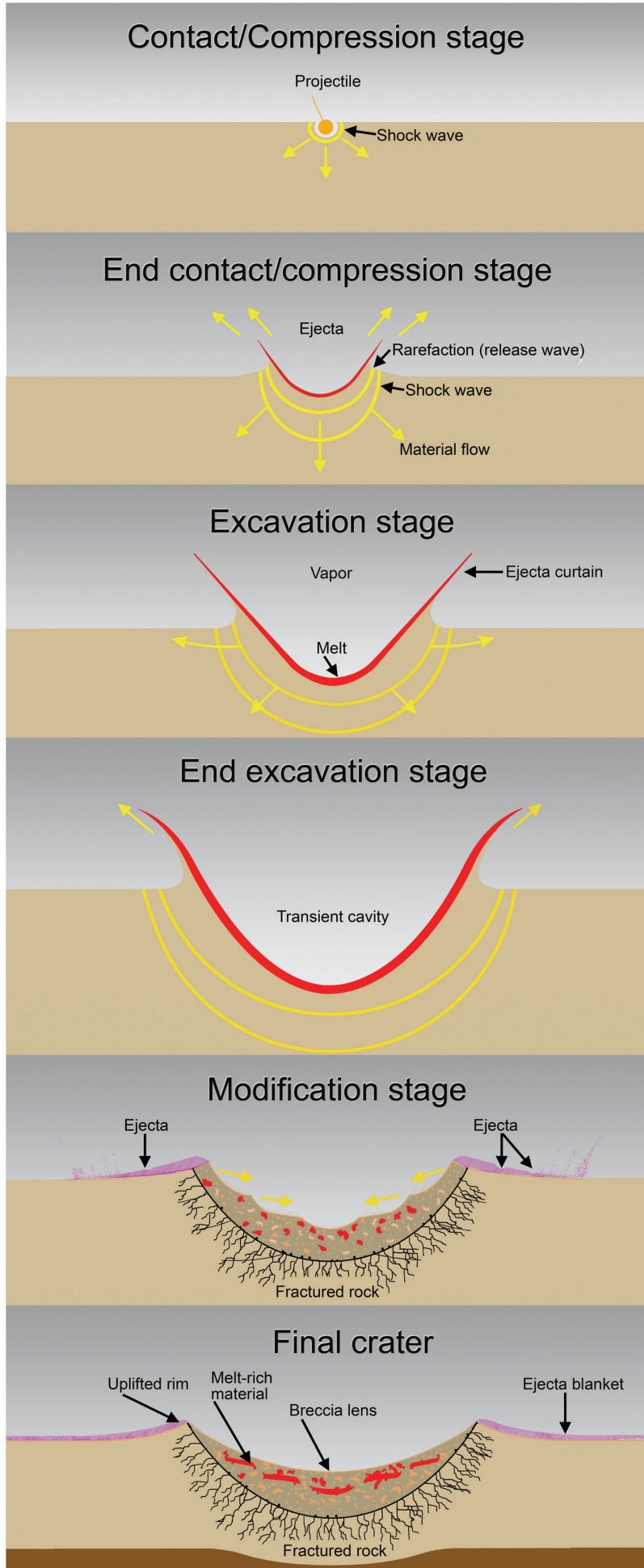


Fig. 3.8. Six views of simple crater formation (generic and schematic). Projectile penetrates the surface and generates a shock wave. A transient crater begins to grow as excavation begins. The transient crater reaches its maximum depth before reaching its maximum radius. When excavation is complete, any remaining debris on the crater walls slump inward to form a breccia lens. Melt will be distributed in the ejecta and any material that falls back on top of the breccia lens. If the crater-forming event is energetic enough, then melt will also be incorporated into the breccia lens. (Illustration from an educational poster, *Geological Effects of Impact Cratering*, David A. Kring, NASA Univ. Arizona Space Imagery Center, 2006. Modified from a figure in *Traces of Catastrophe*, Bevan M. French, 1998.)

Table 3.1. Partial summary of exploration boreholes and shafts produced by Standard Iron Company on the crater floor

Hole No. or Shaft No.	Radial distance from Main Shaft	Approx. bearing of hole or shaft from crater center	Approx. elevation at top of hole	Total depth of hole	Depth of hole normalized to 5135 ft datum	Thickness of lake sediments	Depth to Variety A sandstone	Range of Ni-bearing material	Depth to solid rock
Main Shaft	0	-	5135	222	222	-	-	-	-
2	80	230	-	-	-	-	-	-	-
8	90	125	5135	1085	1085	-	-	-	1030
Shaft III	100	230	5135	-	-	-	-	-	-
1	110	235	-	-	-	-	-	-	-
4	120	180	-	-	-	-	-	-	-
3	130	185	-	-	-	-	-	-	-
23	160	65	-	800	-	-	40	520-620	660
6	200	0	5135	1059	1059	-	-	-	1030
5	250	230	5140	1003	998	-	-	-	-
Shaft IV	250	135	5135	>15	-	-	-	-	-
22	300	45	-	860	-	-	30	600-620	650
7	320	135	5135	960	960	-	-	450-550	-
Shaft VI	320	345	5140	36	31	35	-	-	-
20	330	75	5135	780	780	-	40	640-680	720
12	380	110	5135	881	881	60	60	595-640	700
11	440	165	5135	830	830	-	-	-	640
14	460	125	5135	780	780	-	50	540-620	670
13	480	100	5135	740	740	-	20	598-660	640
21	500	75	-	760	-	-	20	620-640	660
Shaft II	510	70	5135	145	145	100	-	-	-
16	570	110	-	750	-	-	20	540-620	640
9	590	140	5140	670	665	-	-	-	-
Shaft V	600	310	5140	>15	-	-	-	-	-
15	620	125	5140	750	745	-	50	590-600	650
10	650	155	5150	745	730	-	-	-	640
17	650	100	5140	720	715	61	40	520-580	600
19	730	85	5140	680	675	-	-	-	620
Shaft I	740	330	5155	>15	-	-	-	-	-
18	800	100	5150	660	645	-	-	-	630
24	-	-	5140	-	-	-	-	550-650	-
1**	1750	-	5684	1376	827	-	-	? - 1376	-

Sources: Merrill (1908) and Hager (1953) for borehole data; elevations at top of holes determined by correlating numbered hole positions on Barringer's (1910) map with un-numbered hole positions on a current USGS 7.5 min quadrangle topographic map

* Merrill provides a range from 450 to 584 ft, whereas Hager provides range of 550 to 584 ft; Merrill's value of 450 ft is consistent with Barringer (1910)

** Hole drilled by U. S. Smelting, Refining, and Mining Company on south crater rim

Table 3.2. Log of 1,376 foot deep churn drill hole on south rim of Meteor Crater*

Drilling by U. S. Smelting, Refining, and Mining Company

L. F. I. Holland, drilling superintendent to 326 ft; C. W. Plumb, drilling superintendent to 1,376 ft

Drilling began November 1920; drilling completed November 1922

Depth from (ft)	to (ft)	Description
0	174	Limestone. Many crevices in limestone
174	195	{Interval not logged}
195	200	Sandstone. Lighted center goes out of sight. White, loose
200	250	Limestone. Drilling past broken cores
250	257	Limestone. Particles of shale ball
257	283	Limestone
282	288	Limestone. Sand commenced to show in bailings
288	290	Brown and yellow stained saccharoidal sand. Much iron and steel, no nickel
290	311	Sand
311	312	Lost hole. Underreamer at bottom
312	326	In tunnel 71—vesicular sandstone
326	380	White sandstone, very quick. 375' hard material dropped in hole
380	384	Drill twisted off
390	425	White sandstone
425	460	White sandstone
460	464	Red cong. Or coarse red sandstone. Small shells, 1/8" long
464	468	Red clay—streaks of white calcite
468	480	Red or cong. or coarse red sandstone
480	500	Red sandstone or conglomerate. Steel
500	520	White sandstone
600	603	White sandstone
603	605	Hard conglomerate
605	607	Hard conglomerate
607	615	Possibly white sandstone with reddish streaks
615	620	Hard conglomerate
620	627	Whitish sandstone
627	669	White sandstone
669	684	White sandstone (?), red sandstone at bottom
684	725	Red sandstone. Hard to get samples
725	750	Crevice. Coarse grains of limestone, sandstone, and silica
750	801	Red mud or clay, white streaks
801	820	Red clay with calcite streaks
820	876	Large crevice. Rounded pebbles of limestone, silica, and sandstone. Iron nodules, all cemented
876	930	Same conglomeratic material
930	940	Conglomerate as above
940	942	Red clay
942	953	Red clay
953	957	Iron nodule. No nickel
957	1096	Alternating layers of white and gray sandstone. Drilled easily
1096	1100	Hard drilling, iron nodule, no nickel
1100	1130	Hard nodules, similar to 958. Segregations from sandstone, filled with small black particles—silicon, effervesces readily
1130	1287	Hard boulders in siliceous white sandstone. 1" to 6". Some nodules show nickel reaction—perhaps shale balls. Some greenish material, looks like clay
1130	1134	4' very hard, like rest of boulders
1134	1145	Soft sandstone. Small greenish pieces of metal or slag in sample. Slight show of nickel
1145	1168	Hard and soft material, slight nickel, layers 6 inches to one-foot layers
1168	1187	Very soft, white silica sand. Then hard and white like silica sand found in crater
1187	1188	Five hours, sample very black, heavy, greenish pieces of metal, very strong nickel
1188	1190	Same as above
1190	1208	First foot hard. Then alternate hard and soft in 6 inches to one foot
1208	1228	Very soft for 15', then hard and rough. Good test of nickel. Silica sand almost transparent
1228	1251	2' hard, rough. Five hours on last foot, stray nickel
1231	1235	4' hard, rough
1235	1249	Silica sand, medium soft. Slight nickel
1249	1271	Soft, white sandstone. Hard nodules at 1,255', 1,260', 1,270'. No nickel
1271	1276	Hard and rough. Like nest of hard boulders. Fine nickel test
1276	1287	Easier for 5 feet. Then harder and rough, fine nickel test
1287	1293	Drilled very hard 4', hard to get samples. Then easier, good nickel
1293	1311	Hard few inches. Then very soft. Fair nickel test
1311	1323	Easy drilling 10', then very rough. Samples quite black. White sandstone and black material about 50 per cent each. Few pieces red sandstone showing. Shells. White sandstone getting harder. Samples show good nickel test
1323	1335	Drilling rough for 7 feet. Then smooth and very hard. Many pieces of <i>hard red sandstone</i> . Also many shells 1/8" long. Fine nickel test
1335	1339	Reamed very hard, like in boulders size of baseball. Drillings looked very black. Samples all gave fine nickel test, about 75 per cent mineral
1339	1350	Drilling hard but smooth. Some red sandstone but mostly black or brownish pieces of material, very magnetic. Best nickel test yet
1350	1352	Hard for 2 feet. Lost sludge at once. Lost circulation. From 1,095' to 1,352' black mineral particles, plentiful
1352	1360	Formation about as last 250 feet. Nickel about same
1360	1370	Formation hard and rough. Shale ball appearance. Last 2500 feet
1370	1376	Extremely hard and rough. Strong nickel test. Samples look as if we are passing through a recemented mass of conglomerate as we find shells, rounded pebbles of red sandstone and of limestone, and also a great many small brown pieces resembling shale balls. Stuck and had to abandon at 1,376 feet. Bit appears to have wedged under boulders

* Hager (1953), who obtained access to drilling record from R. N. Hunt, chief geologist for the U. S. Smelting, Refining, and Mining Company in Salt Lake City, Utah

4. Shock Metamorphism



Shock-metamorphic products have become one of the diagnostic tools of impact cratering studies. They have become the main criteria used to identify structures of impact origin. They have also been used to map the distribution of shock-pressure throughout an impact target. The diverse styles of shock metamorphism include fracturing of crystals, formation of microcrystalline planes of glass through crystals, conversion of crystals to high-pressure polymorphs, conversion of crystals to glass without loss of textural integrity, conversion of crystals to melts that may or may not mix with melts from other crystals.

Shock-metamorphism of target lithologies at the crater was first described by Barringer (1905, 1910) and Tilghman (1905), who recognized three different products. The first altered material they identified is rock flour, which they concluded was pulverized Coconino sandstone. Barringer observed that rock flour was composed of fragmented quartz crystals that were far smaller in size than the unaffected quartz grains in normal Coconino sandstone. Most of the pulverized silica he examined passed through a 200 mesh screen, indicating grain sizes $<74 \mu\text{m}$ (0.074 mm), which is far smaller than the 0.2 mm average detrital grain size in normal Coconino (Table 2.1). Fairchild (1907) and Merrill (1908) also report a dramatic comminution of Coconino, although only 50% of Fairchild's sample of rock flour passed through a 100 mesh screen, indicating grain sizes $<149 \mu\text{m}$. Heterogeneity of the rock flour is evident in areas where sandstone clasts survive within the rock flour. The rock flour is pervasive and a major component of the debris at the crater. Barringer estimated that 15 to 20% of the ejecta is composed of rock flour.

He also noted that surviving rock fragments of Coconino in the debris deposits are altered, describing a Variety A sandstone (which is lightly to moderately shocked sandstone with a greater density than unaffected Coconino) and a Variety B sandstone (which was melted, is vesicular, and will float on water). Variety A sandstone is distributed within the rock flour. According to Tilghman (as recorded by Merrill, 1908), it constitutes ~2% of the sandstone debris and ranges in size from fractions of an inch to blocks 10 to 12 ft in diameter. One of the boreholes apparently penetrated a 50 ft block 500 ft below the crater floor. Barringer (1910) noted that Variety A shock-metamorphosed sandstone is far more abundant than the pumiceous Variety B sandstone, but also suggests that Variety B material may have decomposed over time and be partly responsible for rock flour. As far as I know, a quantitative microscopic study of the rock flour and the relative proportions of different types of silica components in it has not been done to evaluate this suggestion.

Based on a microscopic examination of crater lithologies in thin-section, Merrill (1908, after Diller) began to augment Barringer's shock-classification of the sandstone. The initial phase of shock crushed the sandstone, reduced porosity, and created fractures in quartz grains where they collided. In a second phase of shock-metamorphism, the interlocking of the quartz is so complete that the sandstone resembles a holocrystalline rock. The quartz also often has undulatory extinction. He suggests the quartz was altered under intense pressure and deformed "in an almost putty-like or plastic condition." Rocks shocked to this state also have interstitial pockets of a nearly isotropic, fibrous, and scaly material that has the composition of opal (silica with water). In the third stage of shock-metamorphism, the rocks become increasingly vesicular or pumiceous glass with relict grains of unaltered quartz. Merrill wrote that the damage was limited to samples of the Coconino. He could not find any deformation in cores of the underlying Supai sandstone, recovered beneath the breccia lens, that were available at the time. He wrote that "in no instance did they show any signs whatever of the shattering, fusion, or metamorphism so characteristic of the overlying white sandstone [Coconino]."

The next contribution to the study of shock metamorphism at the crater was provided by Rogers (1928) in his Presidential Address to The Mineralogical Society of America. He recognized that some of the silica glass (lechatelierite) in Variety B shock-metamorphosed sandstone has the same texture as quartz in unaffected sandstone, writing that “Lechateliérite (silica glass) ... retains the granular texture from which it was derived” and that the lechateliérite grains are “paramorphs ... after quartz.” This characteristic shock-metamorphic material is generically called *thetamorphic* or *diaplectic* glass today (*e.g.*, Chao, 1967; Stöffler, 1972).

In some of the dominantly sheared, yet granular Coconino, it was eventually realized that some pockets of suspected glass or devitrified glass (the nearly isotropic pockets of Merrill) were instead coesite, a high-pressure polymorph of silica. Indeed, the first natural occurrence of coesite was found at Meteor Crater (Chao *et al.*, 1960) and has become another important criterion for identifying an impact crater. Soon thereafter, another high-pressure polymorph of silica, stishovite, was also found at the crater (Chao *et al.*, 1962). Chao and his colleagues reported that both phases occur in Variety A sandstones and survive as a minor constituent in the melted Variety B sandstone.

Kieffer (1971, 1976) continued the detailed examination of shocked Coconino in an effort to expand upon the shock-metamorphic sequence that occurs in the rocks and, where possible, interpret them in the context of the mechanics of the rock’s interaction with a passing shock wave. She divided shocked samples into the five classes recognized today:

Class 1. Initially, the porosity of the rocks was reduced, largely by grain rotation, but no fracturing of quartz grains occurs (Class 1a). At slightly higher shock conditions, the grains began to fracture and may have small amounts of plastic deformation (Class 1b). The fractures appear to have been produced by concussion when neighboring grains collide, because the fractures often radiate from the point of contact between grains. Class 1a rocks have remnant porosity, but Class 1b rocks do not. Class 1 rocks do not contain any higher pressure silica polymorphs.

Class 2. The porosity of the Coconino was completely consumed as grains deformed plastically, forming a puzzle-like fabric. Sympelitic pockets occur between grains where pores once existed. Coesite formed in the symplectic regions. These rocks will be 80 to 95% quartz, 2 to 5% coesite, 3 to 10% glass, and have no detectable stishovite.

Class 3. Like class 2 rocks, plastic flow of quartz collapsed the pore space. Coesite is abundant in cryptocrystalline pockets and stishovite begins to appear in opaque regions that surround the coesite-bearing cryptocrystalline pockets. Estimates for the amount of coesite range from 18 to 32% in these rocks, in addition to 0 to 20% glass and traces of stishovite.

Class 4. Vesicular glass formed adjacent to coesite-rimmed quartz grains. Only 15 to 45% of the original quartz survives. These samples have abundant coesite (10 to 30%) and glass (20 to 75%). They do not have any detectable stishovite using optical microscope techniques.

Class 5. This is an extreme version of class 4, where the glass and vesicles dominate the rock and only a few quartz relicts survive. These samples are 80 to 100% glass, with 0 to 15% quartz and 0 to 5% coesite. Most samples that can still be recovered at the surface are only 1 to 5 centimeters thick, although I have seen blocks of this glass that are ~15 cm thick.

Unlike quartz-bearing crystalline target rocks (*e.g.*, granites and gneisses), the shocked Coconino sandstone has very few planar shock features (either fractures or closer-space lamellae). Typically less than 5% of the grains in Class 2 or 3 rocks have planar features. This reflects one of the important differences between impact cratering events in crystalline targets and sedimentary targets. In the latter, a

greater fraction of the impact energy is consumed closing pore space, so that there are fewer solid state transformations and higher post-shock temperatures than similar impacts into crystalline targets.

Increasing shock pressures also destroyed fluid inclusions that occurred in the Coconino sandstone (Elwood Madden *et al.*, 2006). Two-phase inclusions begin to disappear under Class 1 conditions and are completely gone in Class 3 samples. The number of inclusions in Class 1 and 2 samples, however, remains the same, as the two-phase inclusions are transformed into single-phase inclusions. The total number of inclusions in Class 3 and 4 rocks are lower, indicating that fluid inclusions are destroyed by the plastic deformation and phase changes that occur under those shock conditions. Very few one-phase inclusions survive in Class 4 and 5 samples. Thus, crystal components in the sandstone are dehydrated by shock-metamorphism.

In contrast to these extensive studies of Coconino sandstone, very little is known about the effects of solid phase shock transformation in the Moenkopi and Kaibab Formations. The Moenkopi shales and siltstones are so fine-grained that optical microscope identification of any shock transformation that may have occurred is difficult. The Moenkopi also represents the free surface of the impact site, which would have reduced the volume that saw peak shock pressures in excess of 5 GPa (Fig. 3.7). Shock-metamorphism in the carbonate fraction of the Kaibab is a challenge to study, because it is difficult to discriminate shock-induced deformation from other types of geologic deformation in that type of material. Carbonate is too easily deformed to be used routinely for shock-metamorphic studies. Nonetheless, samples from Barringer Crater probably offer one of the best opportunities to document the progression of deformation that occurs in dolomite; it may be worth further study. It might also be interesting to determine how the quartz fraction within the Kaibab has been affected by shock (both where it is embedded within carbonate and where it occurs in isolated beds of sandstone).

At higher shock levels, target rocks are melted. Melts from individual phases are mixed, producing “normal melts” or “mixed melt,” that are distributed in deposits of mixed debris inside the crater and deposits of alluvium on the outermost flanks of the crater. Some of these mixed melts also entrain fractions of the impacting asteroid.

Impact-generated melts at the crater were first described by Nininger (1954, 1956). The melts range in morphology from melt splashes that encompass clasts of target rock (Fig. 4.1) to a variety of isolated aerodynamic forms, although most specimens are irregularly shaped with pitted (and often vesicular) surfaces. The largest clasts found with melt splashes were 5 to 6 cm in length and composed of Coconino sandstone. Molten particles collided with each other in flight, because some melt fragments have compound droplet morphologies. Melt particle colors have many different colors, although they are usually shades of gray, brown, and red-stained brown in bulk form. Yellow and bright red colors are often evident in thin-section. The melt particles (or, at least those that are easily recoverable) range in size from a millimeter to a few centimeters. The volume of total melt produced is still debated and is hard to evaluate now because of the extensive effects of erosion (which stripped the fall-out unit around the crater) and previous collections of melt. Nininger (1956) reported that most melts were within 1,500 ft (~460 m) of the crater rim and that none were found beyond 1 ½ mi (2.4 km) from the crater rim.

Before describing the Barringer Crater melts further, it might be useful to make some general comments about impact melts. One of the oft-spoken attributes of impact melts is their homogeneity. In large complex craters with substantial impact melt sheets, the melt is often a homogenized mixture of the complex target lithologies that were melted. Only subtle compositional variations have been reported. There must always be an exception to prove the rule and that exception is Sudbury. In that case the melt sheet is heterogeneous, because of post-impact igneous differentiation.

In contrast, melts that are ejected from a crater are often incompletely mixed. For example, in the

case of Chicxulub, which involved a diverse target assemblage of carbonates and silicates, a range of Ca-rich to Ca-poor melt droplets were deposited in moderately distal ejecta deposits.

In simple impact craters, like Barringer, there is not sufficient molten material to form a coherent melt sheet. Even in the larger (4 km diameter) Brent simple crater in Canada, only sufficient melt to form pods within a breccia lens was generated. In Barringer Crater, there is no detectable melt pods within the breccia lens. Nor are there any significant melt pools on the crater walls and in the ejecta blanket. There was either an insufficient volume of melt produced by the impact event and/or it was too finely disseminated (possibly because of a relative high volatile content in the target rocks; Kieffer and Simonds, 1980) to produce those types of deposits. Melts were locally produced within the transient cavity and not well mixed. In addition, a highly disparate proportion of projectile material was added to the melts. A relatively large range of melt compositions is the result.

A preliminary petrographic study of Barringer Crater melts was generated during the Apollo era by Greenwood and Morrison (1969), who reported that Fe,Ni-metal was entrained in the melt and that the silicate fraction of the melt precipitated olivine, actinolite, and magnetite. Much more detail, however, was recently revealed by Hörz *et al.* (2002) and See *et al.* (2002), who thoroughly studied the chemical compositions of target strata and 80 melt particles generated from them. They confirmed that the melts contain immiscible Fe-Ni metal alloys and sulfides from the projectile, although they also noted that the metal and sulfide often have chemically fractionated compositions. Nickel is enhanced in the metal and sulfide. The abundance of FeO from target lithologies is on the order of 2 wt%, yet FeO contents of the silicate portions of the melts are often 25 to 30 wt%. The enhanced FeO is attributed to oxidation of meteoritic iron component from the projectile, which is consistent with the Ni/Fe fractionation in the metal and sulfide. In principal, it is possible that some of the FeO in the silicate impact melts came from silicate inclusions within the type IAB iron asteroid. Inclusions in type IAB meteorites are generally about 70% mafic silicates (olivine and pyroxene), 10% sodic plagioclase, 10% metal, 10% sulfide. However, in the specific case of the Canyon Diablo meteoritic fragments, silicates are usually associated with troilite-graphite nodules, which represent about 8.5% of the meteorites (Buchwald, 1975). Silicates in Canyon Diablo specimens are much less common than in other type IAB meteorites, so they are not likely to be a significant source of FeO. Hörz *et al.* (2002) found that the projectile component is greater in melts that have a significant Kaibab component and less in those that have a larger Moenkopi component. This is consistent with models in which the projectile passes through the thin Moenkopi cover and penetrates the underlying Kaibab.

A significant fraction of the projectile-derived FeO was incorporated into olivine and pyroxene that precipitated from the impact melt. Olivine and pyroxene compositions vary considerably between melt particles (and within some melt particles). These two phases are not in equilibrium with each other, nor with the surviving metal alloys entrained in the melts. The crystallization of olivine and pyroxene in a sedimentary province or, in this case, in melts generated from sedimentary siltstone, dolomite, and sandstone, is unusual. It appears that CO₂ in the target carbonate was driven off, forming refractory (Ca, Mg, and Fe-rich) residues that mixed with Si and meteoritic components. Most of the melts are highly vesicular, which is further testament to the thorough loss of target volatiles. A preliminary study of impact melts by another group (Kargel *et al.*, 1996) also reported 100% decarbonation of melted Kaibab.

Many of the melt particles have regions that produce low analytical totals (typically 70 to 90 wt%), implying a volatile component (*e.g.*, H₂O, OH, CO, or CO₂) exists within them. Hörz *et al.* (2002) and See *et al.* (2002) heated several representative samples to drive off any gases and analyze them. Only water vapor was detected, which is probably the result of post-impact oxidation and hydration rather than an inherent property of the melts. No CO or CO₂ was detected, indicating that component of the target carbonates was thoroughly excised during the formation of the large collection of melts studied.

Although almost all melts studied suggest strong degassing, small amounts of CO₂-charged impact melt appear to have also been produced. Thin-layers and veneers of melts with carbonate-like compositions have been recovered (Fig. 4.2 and 4.3). Although a direct detection of CO₂ has not yet been reported, analytical totals are consistent with a CO₂ rather than H₂O component. The presumed CO₂-charged melts are in direct contact with refractory olivine and pyroxene-bearing melts that are highly vesiculated and that were obviously degassed. Although the silicate-dominated melts were thoroughly degassed, the splashes of CO₂-charged melts imply there were small batches of melts that did not degas. Presumably, they were heated to temperatures needed for melting, but not hot enough to degas or were quenched before degassing could occur.

Interestingly, a quench zone of carbonate crystals along the boundary of the carbonate-dominated melt in Fig. 4.2 suggests an un-degassed molten sample collided with a previously degassed melt that had already solidified. This illustrates the complexity and speed with which material is affected by the impact event and mixed.

Observations at Barringer Crater, in addition to those at craters with larger melt volumes, imply a two-step mixing process for crater melts: (1) mixing of projectile material with local (stratigraphically-limited) target melts and (2) mixing of those melts along the crater wall to produce a homogeneous melt composition. In the case of Barringer Crater, step (1) occurred, but (2) did not occur or only partially occurred, because there is tremendous heterogeneity among silicate melt compositions, in addition to the sharp contrast between silicate-dominated and carbonate-dominated melts. Either there was not sufficient melt volume along the crater wall to facilitate homogenizing melt mixing or the material was ejected before that mixing could occur. The high volatile content of the target lithologies (11 wt% for Moenkopi and 27 wt% for Kaibab; See *et al.*, 2002) may have triggered an early and/or particularly violent disruption of melt volumes and expansion out of the crater.

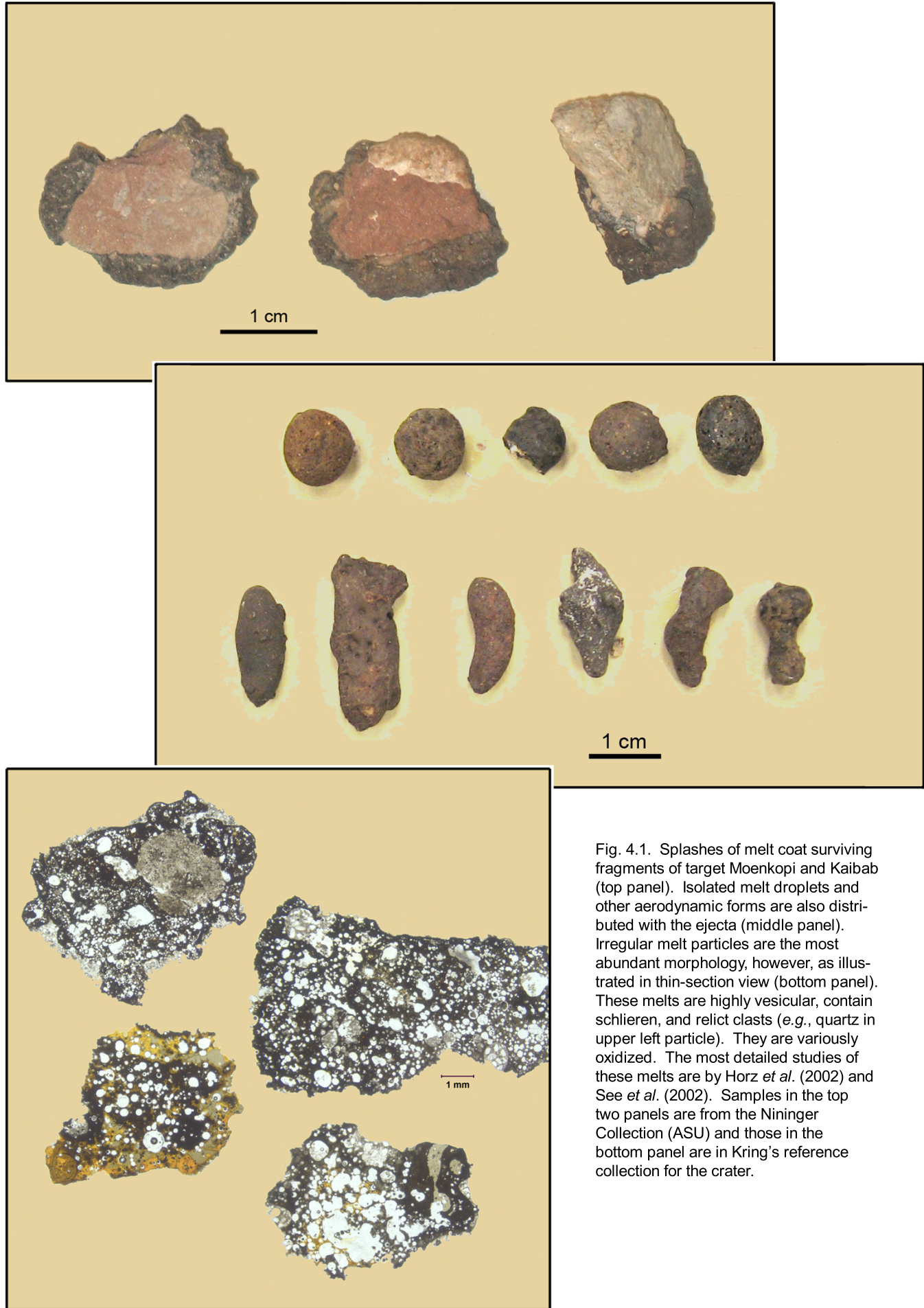


Fig. 4.1. Splashes of melt coat surviving fragments of target Moenkopi and Kaibab (top panel). Isolated melt droplets and other aerodynamic forms are also distributed with the ejecta (middle panel). Irregular melt particles are the most abundant morphology, however, as illustrated in thin-section view (bottom panel). These melts are highly vesicular, contain schlieren, and relict clasts (e.g., quartz in upper left particle). They are variously oxidized. The most detailed studies of these melts are by Horz *et al.* (2002) and See *et al.* (2002). Samples in the top two panels are from the Nininger Collection (ASU) and those in the bottom panel are in Kring's reference collection for the crater.

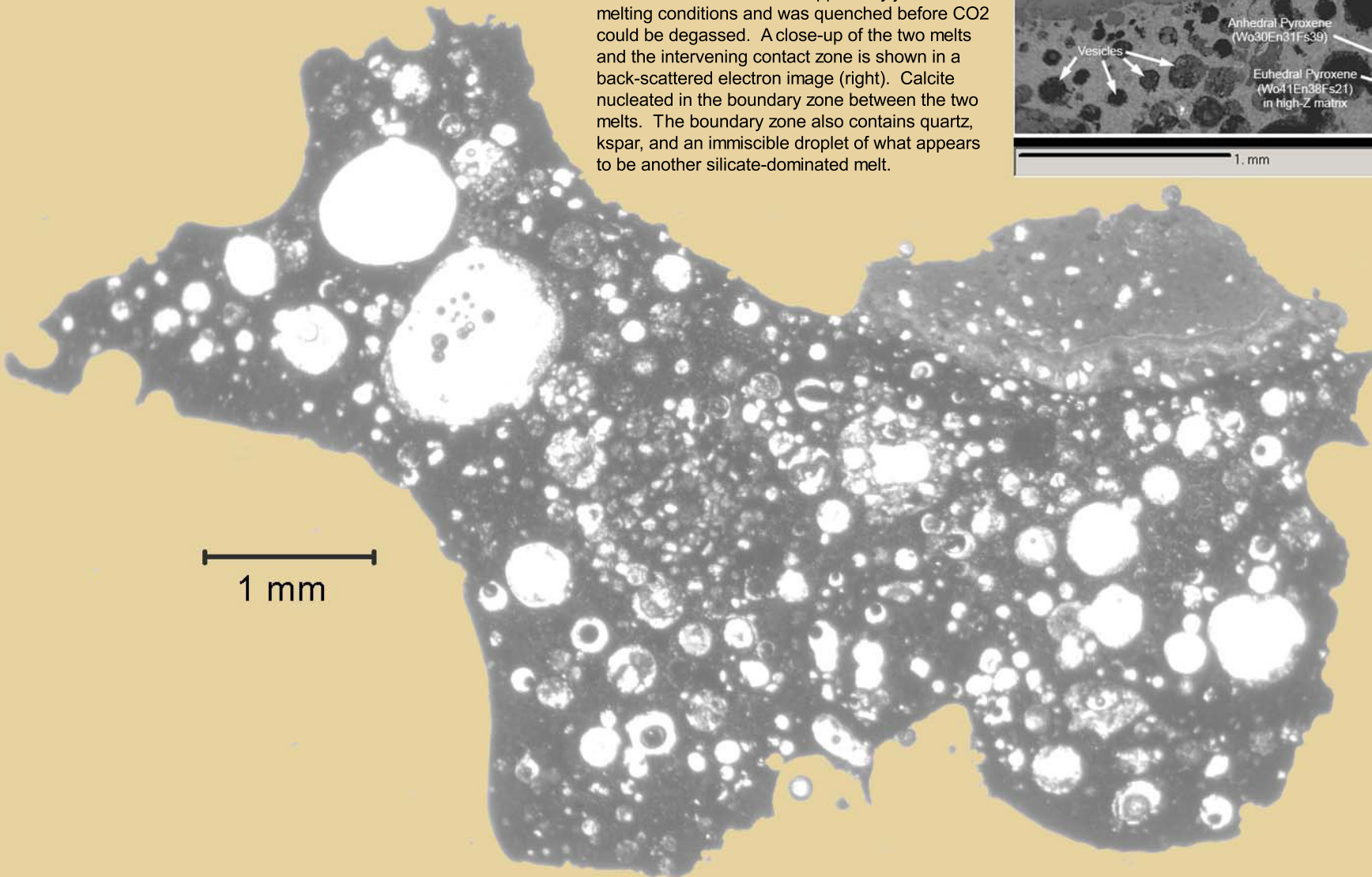
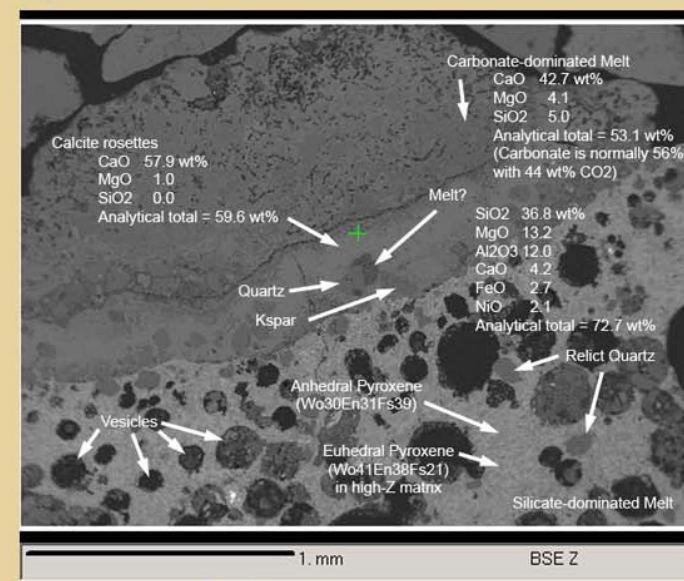
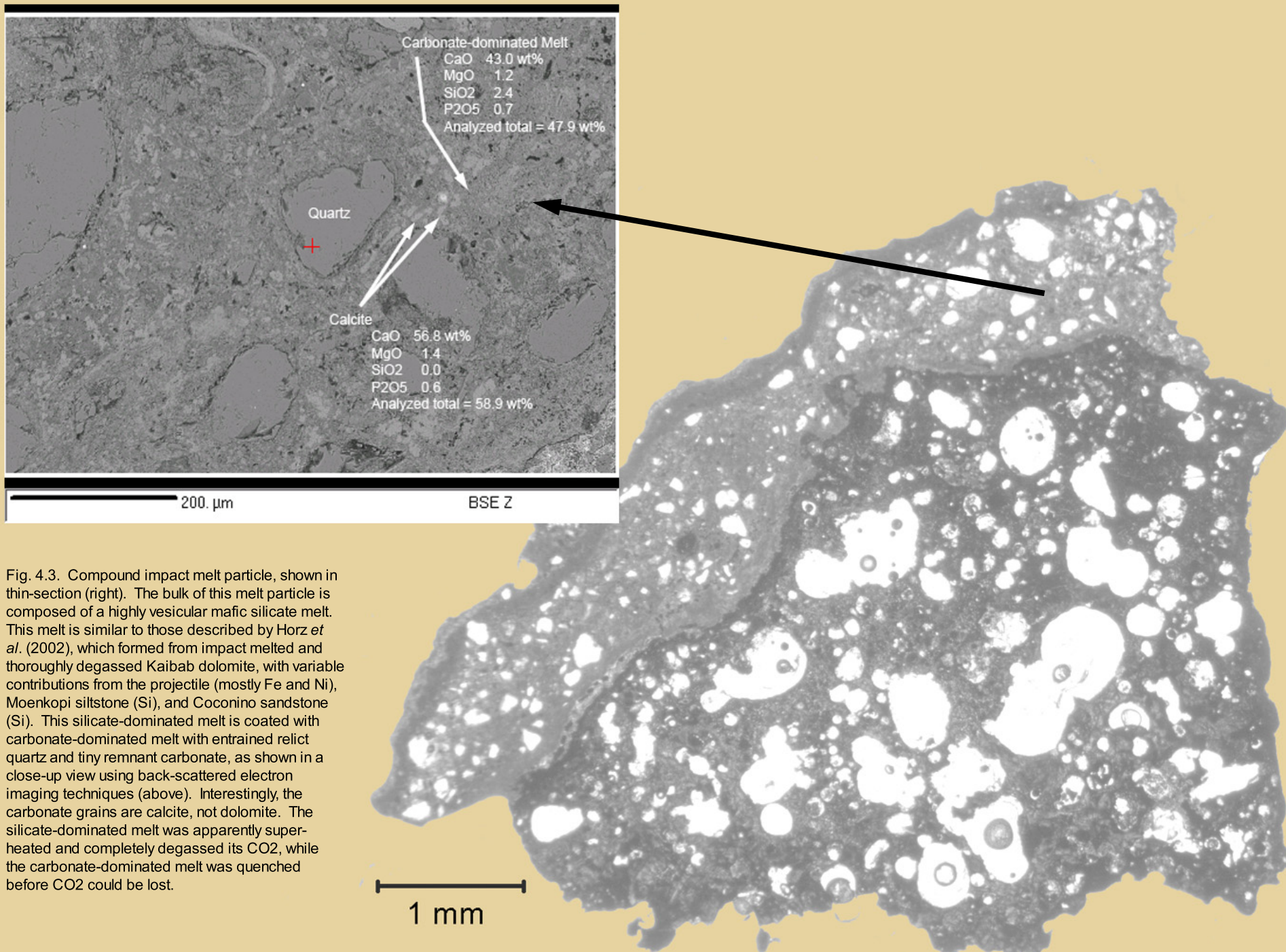


Fig. 4.2. Compound impact melt particle, shown in thin-section (below). The bulk of this melt particle is composed of a highly vesicular mafic silicate melt with relict quartz grains. Pyroxene crystallized from the melt while it was cooling from its initial superheated state. The melt is similar to those described by Horz *et al.* (2002), which formed from impact melted, and thoroughly degassed Kaibab, with variable contributions from the projectile (mostly Fe, Ni), Moenkopi (Si) and Coconino (Si). This silicate-dominated melt collided with a carbonate-dominated melt. The carbonate-dominated melt apparently just reached melting conditions and was quenched before CO₂ could be degassed. A close-up of the two melts and the intervening contact zone is shown in a back-scattered electron image (right). Calcite nucleated in the boundary zone between the two melts. The boundary zone also contains quartz, kspar, and an immiscible droplet of what appears to be another silicate-dominated melt.





5. Crater Rim Uplift and Crater Wall Collapse



The basic processes involved in crater rim uplift are understood, but there is a lot of evidence at the crater that has not been fully explored and may eventually paint a better picture of the processes that occur at the margins of transient craters.

It is clear from almost all vantage points that the horizontal strata in the pre-impact target were uplifted and now have outward dipping orientations. Pre-impact dips are estimated to have generally been <3 or 4°. The regional dip of the underlying Supai is 0.7° to the northeast (Roddy, 1978). Strata in the crater walls, however, typically dip 30 to 40°. The unusual outward dipping strata were noted by all of the early geologic explorers (*e.g.*, Foote, 1891; Gilbert, 1896; Barringer, 1905; Tilghman, 1905).

The uplift in the crater walls is a continuation of the processes that excavated the crater. Within the crater cavity, that flow was sufficient to uplift and launch material, producing the cavity that we now observe. The capacity to eject material decreased with radial distance. Immediately beyond the margins of the transient cavity, there was sufficient energy to generate flow and, hence, uplift of material, but not sufficient energy to eject it. Thus, we see uplift in the crater walls. Similar uplift occurs in the walls of chemical and nuclear explosion craters.

The uplifted walls did not collapse into their pre-impact horizontal positions after the excavation flow ceased. The uplift is preserved for several reasons, including intense fracturing in the crater walls that “bulk up” the rock, the injection of breccia into the crater walls from the crater cavity, and fault-facilitated stratigraphic thickening within the crater walls.

Estimates for the amount of bulking in the walls of Barringer Crater are sketchy, but some insights are available from experimental explosion craters. For example, in the walls of a ~230 ft diameter crater produced by an 85 ton chemical explosion in volcanic rock (Pre-Schooner II; Frandsen, 1967), the bulk density declined by 27, 37, and 47% in three trenches cut through the crater wall. The average (37%) bulking factor measured in the crater walls is similar to the bulking factor measured in ejecta on the crater’s flanks (38%) and in fallback ejecta within the crater (37%). These are generally higher values than those used by investigators at Barringer Crater. Regan and Hinze (1975) estimated a 5% density decrease (*e.g.*, 2.18 vs. 2.30 g/cm³) in the crater breccia lens relative to pre-impact rock, based on a gravity study. This 5% bulking factor has been applied by others (Roddy *et al.*, 1975). A similar bulking value (6 to 10%) was obtained with a single direct density measurement of crater rim ejecta (Walters, 1966). If these bulking values for the breccia lens and ejecta are approximately the same as that in the crater wall, then part of the uplift at Barringer Crater is due to bulking. However, bulking is apparently a smaller component of rim uplift at Barringer Crater than it is around some experimental explosion craters.

The only other data point we have thus far for the amount of brecciation in the crater walls is an observation made by Haines (1966). In core recovered from one of the NASA-sponsored boreholes (MCC-4; Chapter 3), he logged 1,059 fractures in 107.4 m. These were horizontal fractures with an average spacing of 2 to 3 inches. Having examined material from other sites in that particular drilling campaign, he apparently believed the fractures were a property of the rock, rather than a drilling artifact.

In addition to this *in situ* brecciation and bulking of the crater walls, injected breccias from the crater cavity have also been proposed as a mechanism for maintaining crater rim uplift. Barringer (1905) was the first person to articulate the idea, suggesting that the crushed silica he observed beneath lake sediments and in ejecta was also propelled beneath the uplifted limestone and red sandstone walls. As

discussed in Chapter 3, a deep borehole into the crater wall from the south crater rim encountered injected material, including fragments of the asteroid.

Structural uplift has also been attributed to a variety of faults (*e.g.*, Shoemaker, 1960; Shoemaker and Kieffer, 1974; Roddy, 1977). They are often called “thrust” faults, to capture the idea that material is thrust into the crater walls or up the crater walls. The faults are not, however, always technically thrust faults. The term overthrust has also been used to describe structural features at craters, particularly around experimental explosion craters, but this term is applied to an overturned sequence of debris on the crater rim, not structure within the crater wall. The overturned sequence on the crater rim will be discussed in the following chapter.

Interpreting structure in crater walls is complicated, because the crater wall has been rotated during uplift, in addition to being faulted. The relative timing of faulting and rotation still needs to be examined along many of the faults now exposed in the crater walls. Some options include (Fig. 5.1): (a) An apparent thrust fault, produced by a normal fault along which the foot-wall moved up and outward from the crater, which was then rotated during crater wall uplift. (b) Reverse or thrust fault along which lower strata were moved down and outward from the crater and then rotated during crater wall uplift, possibly forming an anticline with a radially-directed plunge line at the top of the crater wall. (c) Thrust fault produced after crater wall uplift and outward dipping rotation; in this case there should be a rupture of the Moenkopi beneath the ejecta blanket. (d-e) High-angle thrust fault or reverse fault that essentially moves material up the crater wall, possibly forming an anticline with a radially-directed plunge line at the top of the crater wall. This type of fault would be produced during crater flow uplift, although it is unclear whether it would occur early, late, or throughout the uplift process. We (Thomas Kenkmann, Michael Poelchau, and I) have observed a fault within one ejected block of debris near the museum complex. Assuming the block was excavated during crater formation (rather than museum construction), the block indicates that thrusting occurs during the compression and excavation phases, not during a modification phase of crater formation.

Good structural descriptions of the most faults and their orientations relative to bedding do not yet exist. The best described fault occurs in the north-northeast wall of the crater, within the Kaibab-Alpha (Shoemaker and Kieffer, 1974). In this case, the fault dips about 45° , while the beds in the upper plate dip 30° . The sequence is thickened and forms a wedge that produces an anticline in the uppermost Kaibab, Moenkopi, and impact ejecta. This forms one of the highest uplifted points along the crater rim. (See Chapter 14 for a trail guide to this portion of the crater.) These observations are consistent with Fig. 5.1b. Two other options (a and c) do not satisfy observations, because they thin the sequence and also have faults with shallower dips than bedding. For this particular location, options (d-e) are also not appropriate, because the fault dips away from crater center, not towards crater center. However, Roddy (1977) indicates that (d-e) occur elsewhere in the crater. It is also possible that complex (multi-)fault systems were activated. For example, a wedge shaped block might be thrust into the expanding wall of the crater, bounded by a thrust fault on top and a normal fault on the base, that then maintains crater wall uplift after excavation flow has ceased.

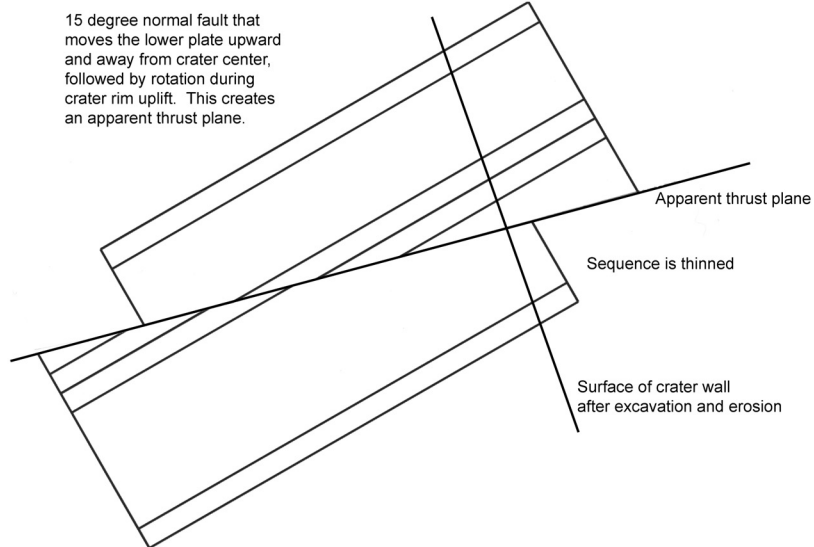
Thrust faulting is evident along the crater walls, with offsets of fractions of a meter to several meters. They cross-cut strata in both the Kaibab-Alpha and Kaibab-Beta. It is unknown if additional fault-bounded repetition of strata occurs in the lower crater walls of the covered Coconino. The faults, however, are poorly described and a much better structural description is needed. Qualitatively, a significant fraction of crater rim uplift is attributable to thrust faults. More work is needed to quantify this contribution.

One of the attributes of a fault-thickened section is an anticline in the overlying crater wall bedrock and overlying ejecta. These are particularly evident at Barringer Point and Moon Mountain, two of the

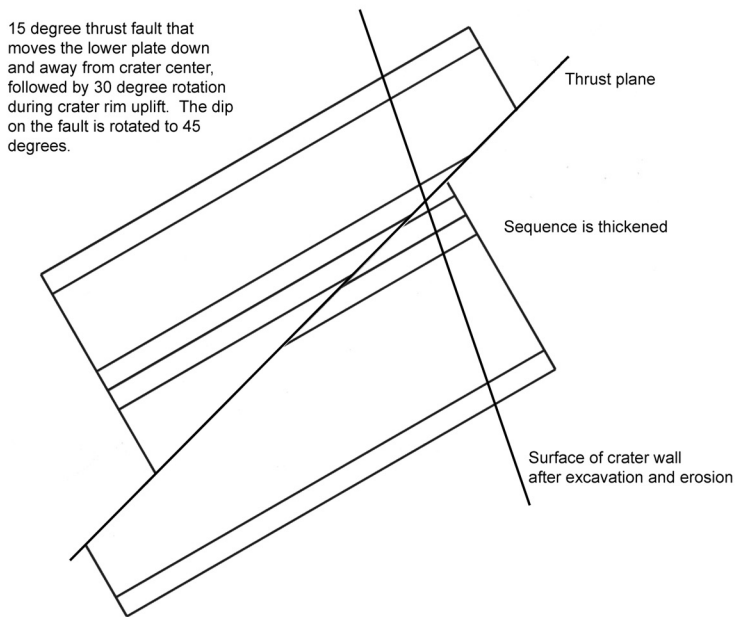
highest topographic points around the rim of the crater. Both are illustrated in the trail guides to the crater (Chapters 14 and 15). The thrust wedges created a circumferentially-distributed series of alternating anticlines and synclines. These structures were also cross-cut by tear faults in some portions of the crater walls. Drag folds along those tear faults accentuated the anticline-syncline structure (*e.g.*, in the northwest corner of the crater).

All of these structures were produced during the excavation phase of crater formation, which moved material upward along the crater wall. In contrast, the subsequent modification stage provided an opportunity for material to begin moving down along the crater wall. This is the source of the breccia lens on the crater floor. Large slabs of bedrock also slumped down the crater walls. Drilling revealed that at least one large slab of Coconino was incorporated into the breccia lens. Other fragments of slumped rock were left hanging on the crater walls, bounded by authigenic breccias that were created by shear while they moved. Neither the blocks or the authigenic breccias exposed in the crater walls are well-documented. (To be clear, some authigenic breccias were produced during the thrusting described above. Thus, there are two generations of authigenic breccias.)

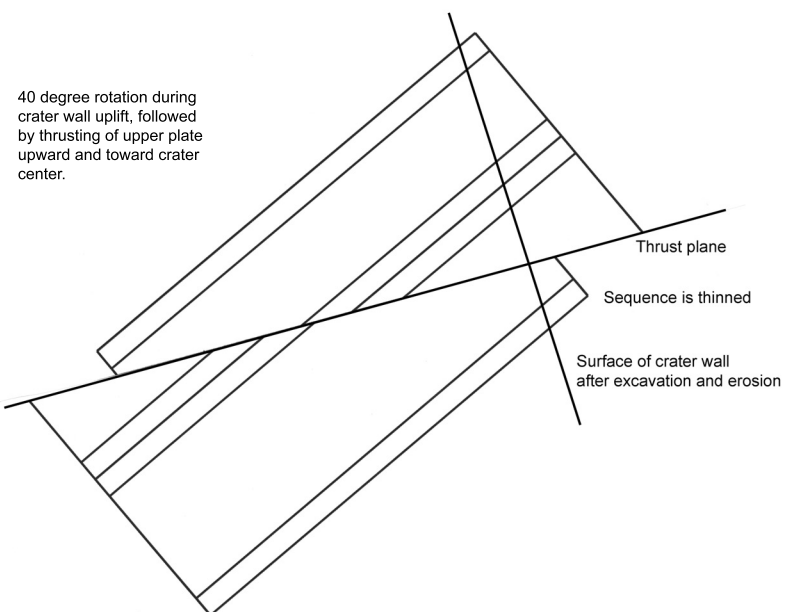
Other types of shear within and between strata generated during crater excavation and modification are preserved in blocks that bound the crater wall. “Chatter” marks are found within blocks of Kaibab (Fig. 5.2). These chatter marks may be small drag folds that were created along a shear plane; they have been observed at other craters in sedimentary targets (Thomas Kenkmann, personal communication, 2007). Slippage lineations created when rock broke along shear planes have also been found (with Michael Poelchau and Thomas Kenkmann). The direction of shear is indicated by a sharp leading edge where the rock popped apart (Fig. 5.2). After further study, it is hoped that these newly identified structures will assist with an enhanced description of crater flow.



(a)



(b)



(c)

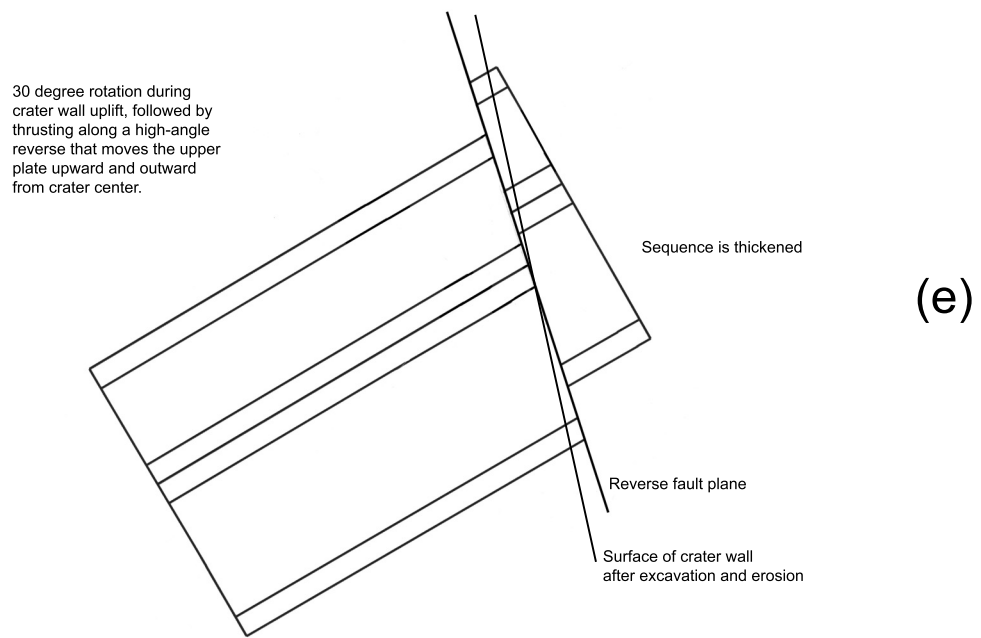
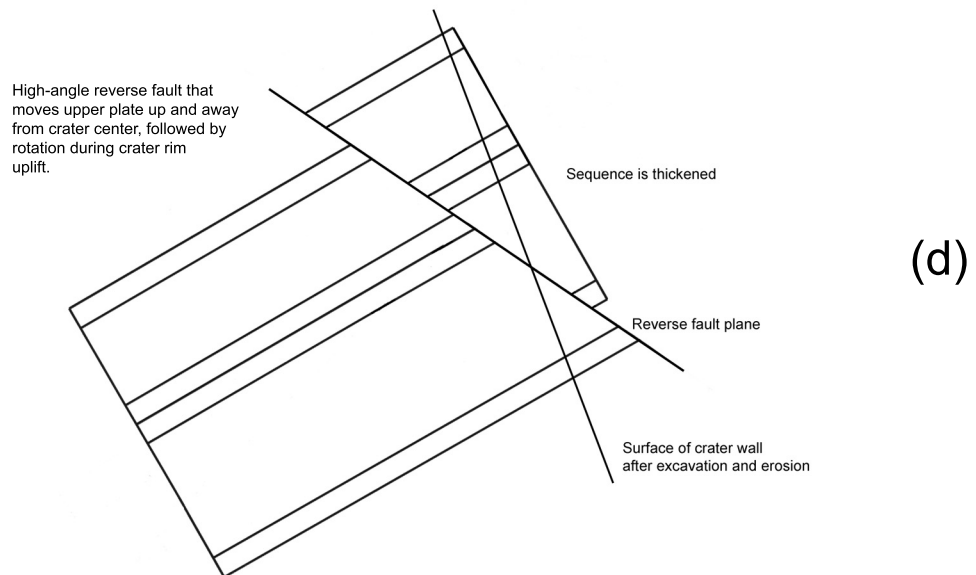


Fig. 5.1. Schematic block diagrams of possible fault movements and rotation during crater excavation and rim uplift (a-c, previous page; d-e, this page). A thrust fault (b) that moves the lower plate down and away from crater center, followed by rotation during rim uplift, is consistent with observations in the north-northeast crater wall. High-angle thrusts or reverse faults (d-e) that move the upper plate up and away from crater center have also been proposed for some of the features at the crater (Roddy, 1977).

Fig. 5.2. Elements of shear in blocks of Kaibab dolomite. "Chatter" marks are visible on some surfaces. In the upper right panel, the marks occur on top of an outcrop. They are located between and are oriented perpendicular to the arrows. In the middle panel (below), the marks are visible on a near-vertical block of dolomite along the crater wall; the chatter marks trend horizontally across the image. Slippage lineations also occur along shear planes (lower right panel), in this case indicating upward shear.



6. Overturned Rim Sequence



Shock pressures overwhelm the material strength of rock in the immediate vicinity of an impact event. Thus, rock under the influence of shock does not behave in the immovable, brittle fashion that we normally assign to it. The excavation flow (Fig. 3.7 and 3.8) that generated the crater produced a nearly instantaneous folding of the bedrock in the rim of the crater, which is partly responsible for the height of the rim above the surrounding plain. Structural overturning of the strata was noted by Barringer (1910) in the northwest corner of the crater: "... the strata exposed in the walls of the crater gradually increase from 5 degrees up to vertical and in one place they are slightly overturned." In that same paper, he also characterizes the stratigraphic consequences, writing that a deeper sandstone is on top of shallower sandstone, which is on top of even shallower limestone. Shoemaker (1960) pointed out that similar overturned sequences are produced in the rims of nuclear explosion craters (*e.g.*, the crater produced by the ~1 kt Ess or Teapot Ess explosion in 1955). An overturned rim sequence is now recognized as one of the hallmarks of an impact crater.

Traditionally, students are introduced to this overturning in a study of the Moenkopi in the northeast rim of the crater, where cross-bedded laminae within the siltstone can be used to identify the overturned sequence. Additional details of those outcrops are provided in the trail guide for the east crater rim (Chapter 14). The overturned sequence can, however, be seen around the entire crater. For example, on the south rim of the crater, one finds the Wupatki and Moqui members of the Moenkopi repeated and overturned (Fig. 6.1).

Before examining another example of the overturned sequence, it is perhaps useful to first examine a schematic diagram that illustrates the structural and stratigraphic context of the overturned rim sequence. In structural terms, the overturned rim is a syncline with a circumferential axial trace or compound syncline, because there are actually two folds involved. The first is associated with the uplift and outward tilting of the beds in the crater walls (as described in the last chapter) and the second is with the complete overturning of those strata. With regard to the latter, there are actually two types of overturning evident in the crater rim (Fig. 6.2). Structural overturning occurs when the dips of the beds pass a vertical plane (and, thus, have dips exceeding 90°). Stratigraphic overturning occurs when the dips of the beds are rotated 90° beyond the outward dip of the lower limb of the fold. Thus, if the outward dip of the rim strata are, say, 35°, stratigraphic overturning occurs when the beds exceed dips of 125° (90° + 35°). Indeed, some strata will dip 215° (180° + 35°) on the overturned upper limb of that fold, relative to their pre-impact orientation.

Several locations exist on the east side of the crater where erosion reveals the fold hinge in the Kaibab and Moenkopi units. An example of a fold hinge in Moenkopi is shown in Fig. 6.3. The axial plane is within the fissile Moqui Member of the Moenkopi. In overturned sequences where the hinge is not exposed, it is often difficult to identify the axial plane because of the fissile nature of the Moqui. One often has to rely on the geopetal characteristics of the Wupatki Member to demonstrate the overturned stratigraphic context. This and other fold hinges are included in the trail guide for the east crater rim.

The Moenkopi is not everywhere exposed along the upper crater walls, because it is buried within the overturned Kaibab and Coconino. Access to the Moenkopi is facilitated by rim erosion, as illustrated in a series of time-steps in Fig. 6.4. As erosion cuts back into the crater walls, it removes fold hinges in the deeper layers (*e.g.*, Kaibab) and reveals overturned sequences in the shallower layers (*i.e.*, Moenkopi). Folds in both the Kaibab and Moenkopi are evident along the east crater rim. As discussed further in the next chapter, the amount of erosion is still being debated, but Shoemaker (1974) argued that 40 ft (12 m) occurred on the outer flank of the northeast corner of the crater, which suggests a cut back of the inner

crater wall probably also occurred in that area.

The Moenkopi exposed in upper crater walls will not everywhere be the same thickness. This partly reflects pre-impact topographical relief that existed on the Moenkopi, because it was the eroding surface unit on the landscape. It also is partly the result of structural thinning that occurred during the overturning process, which is manifest in a series of small faults in the overturned rim sequence.

The views in Fig. 6.4 are idealized. Hummocky ejecta and crater rays will modify the distribution, which will be discussed further in the next chapter. The amount of erosion that occurs is also variable. Consequently, as one circumnavigates the crater rim, one might be walking on Coconino (as in top panel of Fig. 6.4) or on Kaibab (as in bottom panel of Fig. 6.4). The amount of overturned debris on the rim crest varies accordingly. Roddy (1978) estimated the original rim was covered with $\sim 20 \pm 5$ m of debris, which is a structurally-thinned remnant of an excavated stratigraphic thickness of at least 88 m (corresponding to Kaibab and Moenkopi, which dominate the exposed rim sequence) and also much less than a total excavated stratigraphic thickness of 300 to 310 m (corresponding to Coconino, Toroweap, Kaibab, and Moenkopi). Currently, 0 to ~ 20 m of ejected debris survives on the current rim crest, depending on location around the crater. A greater fraction of the uplifted rim is the result of the uplifted strata beneath the overturned debris sequence, which is responsible for ~ 47 m of the uplift (Roddy, 1978).



Fig. 6.1. Stratigraphic overturning of the Moenkopi Formation in the upper crater wall. The characteristic orbicular outcrops of the Wupatki Member sits on top of the Kaibab Formation (lower far right). Above the Wupatki is the fissile Moqui Member. The Wupatki-Moqui sequence is repeated, but overturned (center). Kaibab debris (upper far left) sits on top of the overturned Wupatki Member. Outcrop is on the south side of the crater. View is looking west.

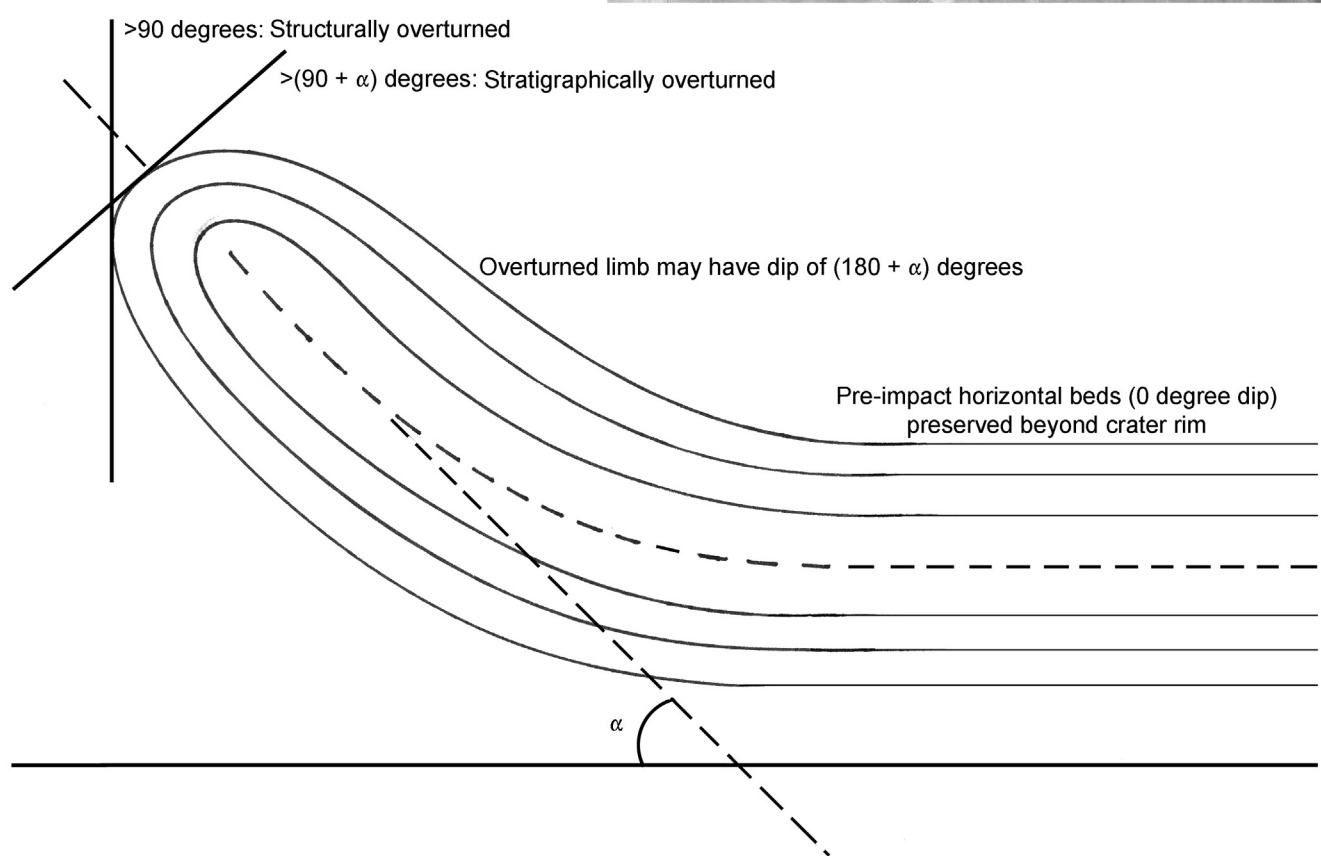
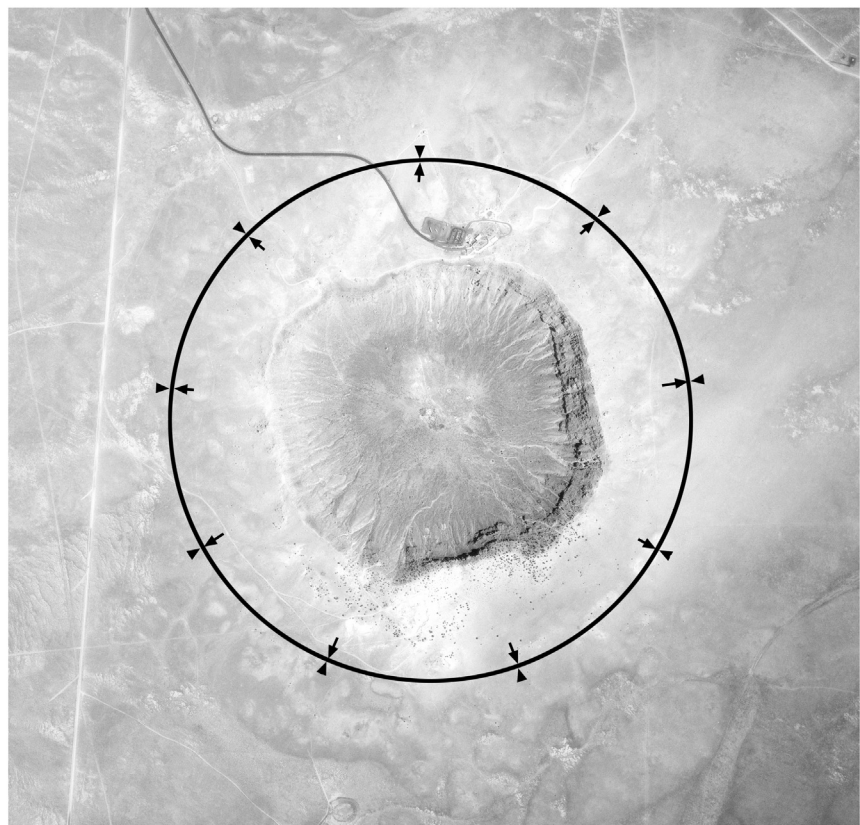


Fig. 6.2. Schematic diagram of the structural and stratigraphic overturning that occurs in the ring syncline of an impact crater (bottom). The axis of the ring syncline is not shown in the schematic diagram; it is perpendicular to the page and would trace a circle around the crater in a plan or map view. At Barringer Crater, the amount of uplift in the crater walls typically corresponds to an α of 35 to 40 degrees. The axial trace of the ring syncline at Barringer Crater is ~900 m from crater center or slightly more than 300 m beyond the crater rim (inset, upper right), based on the results of an intense drilling program (Roddy et al., 1975) that penetrated the ejecta blanket and determined the elevation of subsurface bedrock. An independent measurement using ground-penetrating radar (Pilon et al., 1991) suggests the axial trace may be slightly farther, ~400 m beyond the crater rim.



Fig. 6.3. Structurally and stratigraphically overturned Kaibab and Moenkopi, with an exposed hinge within the Moenkopi. Crater center is to left and the ejecta blanket lies beyond the top of the crater rim on the right. As can be seen in the lower left (above), the crater wall rocks have been uplifted so that they have an outward dipping slope. The top of the Kaibab reaches near vertical dips. The hinge within the Kaibab is eroded, but a trace of the fold is indicated with a dashed line. At the upper far right, the Kaibab is overturned. Within that Kaibab fold is a Moenkopi fold. Erosion has exposed the hinge in the Moenkopi fold. The location of the hinge within the overturned rim is shown above and a close-up of that hinge is shown to the right. This outcrop is located on the east side of the crater, slightly north of House or Monument Rock.



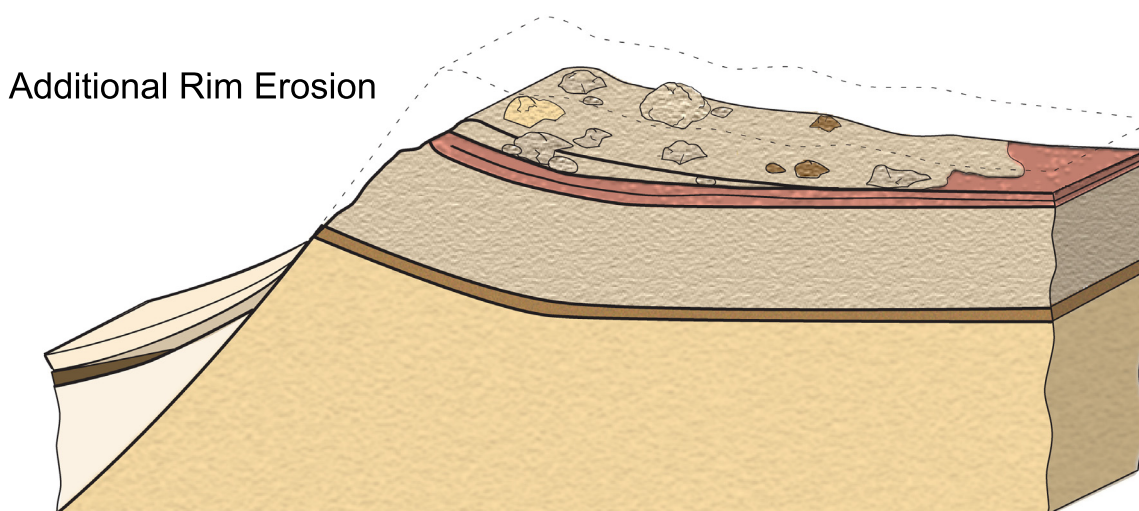
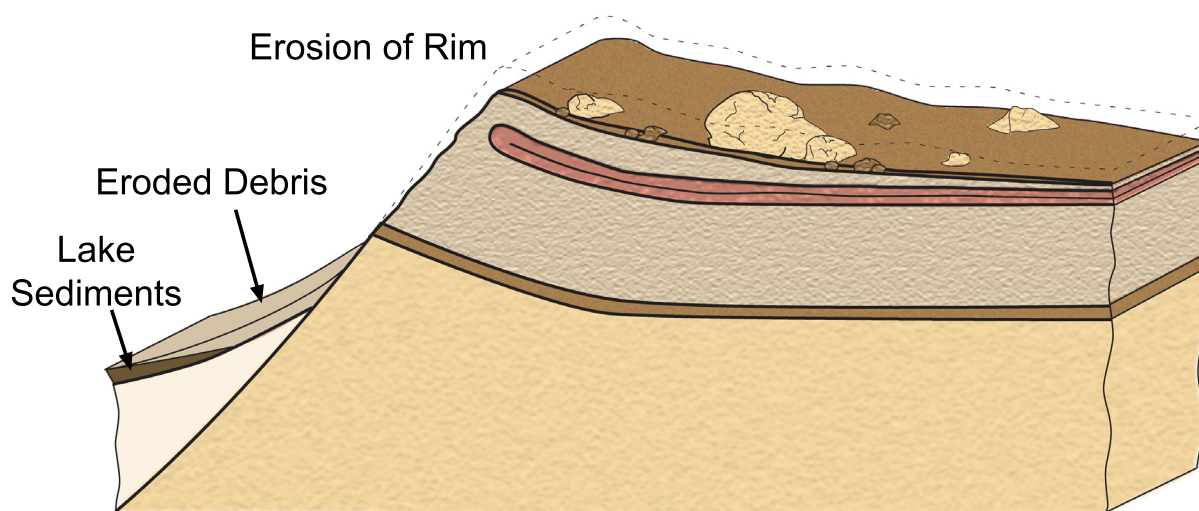
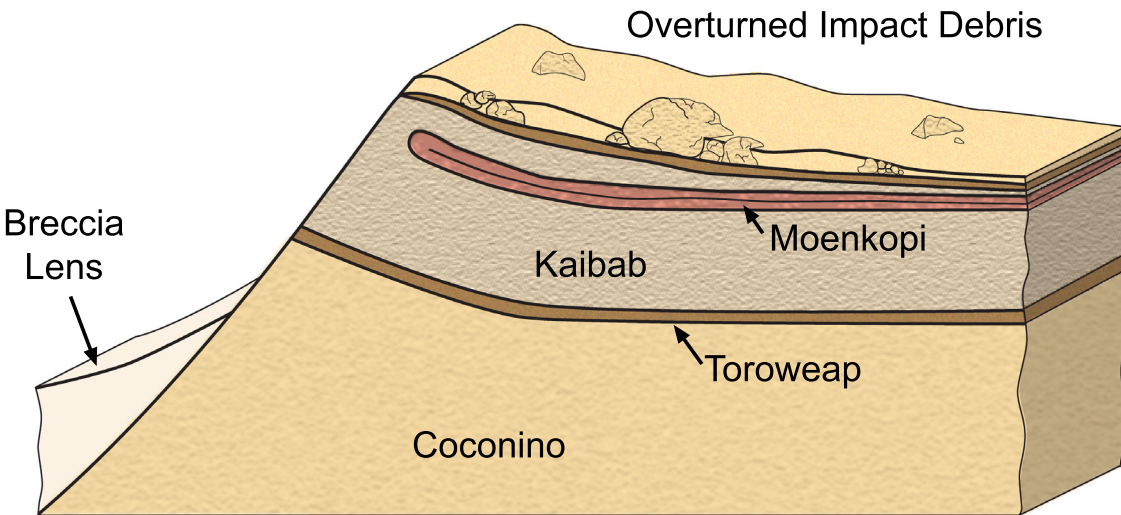


Fig. 6.4. Schematic illustration of the overturned rim sequence and its evolution during subsequent erosion. Immediately after impact, the rim is at its maximum height. The rim and ejecta blanket contain a complete overturned sequence of Moenkopi, Kaibab, Toroweap, and Coconino (top panel). This is an idealized view. Hummocky ejecta distribution and crater rays will modify this distribution. A breccia lens partially fills the crater. Over time, erosion of the rim exposes deeper levels in the upper crater wall and impact ejecta blanket (middle panel). Eroded debris falls to the crater floor. Coarse talus deposits interfinger with finer-grained lake sediments being deposited at the same time. Additional debris is washed down the flanks of the ejecta blanket towards the surrounding plain, where it collects in alluvium terraces (not shown). Additional erosion (bottom panel) exposes a Moenkopi fold hinge in the upper crater wall. It also creates an eroded pavement on the flank of the crater that is dominated by Kaibab. Erosion on the crater rim is not everywhere the same. Consequently, along the trail that circumnavigates the crater rim, one might be walking on Coconino (top panel) or on Kaibab that sits above an exposed Moenkopi hinge (bottom panel).

7. Distribution of Ejecta



The overturned rim sequence described in the previous chapter is part of a larger extended blanket of debris. A nearly continuous layer of rubble radiates outward over distances in excess of a kilometer beyond the crater rim. An extensive rotary drilling campaign helped map out the extent of this unit, its thickness, and internal structure (Roddy *et al.*, 1975). Along several transects across the ejecta blanket, debris extends from 1,341 to 1,860 m from crater center, with an average radial distance of 1,543 m (Fig. 7.1). Roddy (1978) estimates the original extent of the continuous ejecta blanket was \approx 2,500 to 3,000 m.

Previously, mapping by Barringer and Shoemaker (*e.g.*, Fig. 3.2) showed that Coconino debris is prevalent on the south side of the crater and forms patches around the east and north sides of the crater. It is absent on the west side of the crater. Drilling of the ejecta blanket showed further that the thickness of the ejecta blanket is greatest on the south side (see, for example, the lower panel of Fig. 7.1), with some blocks of Kaibab visible in the field at distances of 1.5 km from crater center.

Barringer (1910) argued that a deeper unit of the Coconino (a browner sandstone) is deposited on the southeast side of the crater and, thus, that the deepest units excavated were ejected to the southeast. I do not recall Shoemaker or Roddy reporting a similar distribution, nor have I yet had time to confirm it.

Roddy *et al.* (1975) examined the contact between the bedded Moenkopi and overlying debris to determine if there was any erosion, brecciation, and mixing when the ejected material landed, similar to the process that generated the Bunte Breccia around the Ries Crater. No significant effects were found. Above normally-bedded Moenkopi, drilling routinely encountered a well-defined overturned sequence of the target lithologies: Moenkopi, Kaibab, Toroweap, and Coconino.

The thickness of the debris, however, is substantially thinner than the pre-impact sequence (*e.g.*, \sim 20 m on the crater rim versus \sim 300 m in the walls of transient crater). It is also distributed laterally over greater distances. The existing ejecta blanket beyond the crater rim is 1.6 to 2.6 times wider than the crater radii (from data in Roddy *et al.*, 1975) and distributed over \sim 7.5 km² or \sim 1,850 acres. In other words, the debris now covers an area \sim 9 times larger than the crater. This thinning is also apparent in the rotary drill data of Roddy *et al.* (1975), who noted that the Moenkopi becomes thin to discontinuous with increasing distance from the crater. In addition, deeper lithologies (*e.g.*, Coconino) are concentrated on the crater rim, while shallower lithologies (*e.g.*, Moenkopi) occur at greater distances. Thus, the stratigraphy in the pre-impact target is preserved as one walks down slope from the crater rim.

The coarsest material within the ejecta blanket is concentrated near the crater rim. Gilbert (1896), for example, reported blocks of limestone up to 60 ft in diameter (probably Monument Rock) and sandstone up to 100 ft in diameter (the location of which is uncertain) near the crater rim. These are immense blocks of debris. A carbonate boulder 60 ft in diameter, with a density of 2.24 g/cm³ (Table 2.3), has an approximate mass of 7.2×10^9 g or over 7,000 metric tons. Monument Rock also sits more than 50 m above its pre-impact position and several tens of meters beyond the crater rim. Barringer (1905) described ejected blocks of debris with masses up to 5,000 tons. These early explorers were particularly impressed with two boulder fields, dominated by Kaibab blocks, that were distributed roughly symmetrically, occurring on both the east and west sides of the crater (Fig. 7.2). As discussed further in Chapter 9, Barringer used these boulder fields in his assessment of the impacting projectile's trajectory.

Although we often idealize the continuous ejecta blanket as a well-ordered set of inverted target strata, local complexities exist within the debris blanket. For example, along the north rim of the crater, the surface of Kaibab ejecta was undulating or hummocky, forming a depression that was filled with

Coconino debris (Fig. 7.3). This particular deposit was described by Barringer (1910) as one of the “spurts or jets” of sandstone that surround the crater, thinking they were akin to crater rays. The ejected strata have also been fragmented, so that the overturned units are better described as partially-disrupted, semi-coherent sheets. The degree of disruption increases towards the surface of the ejecta blanket. Overturned Moenkopi is very coherent, Kaibab less so, and Coconino sandstone on top of the debris blanket has been fractured much more severely (Fig. 7.4). A nearly 20 metric ton sample of overturned Coconino demonstrated that fragments had been reduced to $40 \times 40 \times 90$ cm and smaller (Walters, 1966), far smaller than many of the Kaibab boulders in the underling layer of ejected debris. The additional disruption may reflect the inherent structural integrity of the pre-impact lithologies. It may, however, also be a function of the material’s position in the overturned sequence. Moenkopi and Kaibab were contained within additional debris, whereas the ejected and overturned Coconino represented an unbounded free surface.

Not surprisingly, the density of material incorporated into the ejecta blanket is less than that of the original target rocks. In a NASA-sponsored study during the Apollo era, 19,320 kg or 10.31 m^3 of ejecta were excavated at the surface to a depth of 2 m. The ejecta was excavated on the overturned flap of the southern rim of the crater, where it is dominated by loose sand and platy blocks of Coconino-Toroweap sandstone. The bulk density of the ejecta was 1.87 g/cm^3 (Walters, 1966), which is 6 to 10% lower than that (1.98 to 2.08 g/cm^3 ; Table 2.1) of isolated Coconino sandstone fragments that have been used for shock experiments (Ahrens and Gregson, 1964; Shipman et al., 1971; Ai and Ahrens, 2004). A decrease in density is a general property of impacts into consolidated lithologies like those at Barringer Crater. It may not apply, however, to unconsolidated sediments. Following a nuclear test explosion in alluvium (Sedan), an ejecta density identical to pre-shot target density (1.5 g/cm^3) was measured (Carlson and Roberts, 1963). In some cases, shock may even compress and cement unconsolidated target materials, effectively increasing density in both crater walls and ejecta.

The continuous ejecta blanket represents the bulk of excavated debris, but there are other ejecta components. Isolated blocks of debris were flung far beyond the continuous ejecta blanket. These are sometimes called missile debris and, around experimental explosion craters, have produced secondary craters. Barringer (1910) reported fragments of Kaibab that were ejected $2 \frac{1}{2}$ to 3 miles (4 to 5 km) in blocks weighing 50 to several hundred pounds. In addition, Gilbert (1896) found at least one Kaibab block $3 \frac{1}{2}$ miles beyond the crater rim. As far as I know, no secondary craters associated with these blocks have been described.

There were probably two other debris components beyond the rim of the crater: a fall-out unit and a base-surge unit. Neither of these units exist today, but they are inferred from observations within Barringer Crater and around experimental (particularly nuclear) explosion craters. A fall-out debris deposit on top of the overturned ejecta blanket is inferred from fall-out debris that is observed within the crater (Chapter 3). It is likely to have covered the crater rim, but its radial extent is unknown. Did it, for example, cover all of the overturned ejecta blanket? Or could it have extended even farther? An important component of the fall-out unit within the crater walls is meteoritic material and may have also been an important component of the fall-out unit beyond the crater rim. Barringer (1910) reported fragments of meteoritic material out to distances of $\sim 5 \frac{1}{2}$ mi (Chapter 8). Gilbert (1896) reported on meteoritic mass 8 mi (nearly 12.8 km) east of the crater, which is more than twice the distance of the farthest Kaibab block he observed. In addition, Nininger (1956) reported impact-melted spherules of projectile material out to a distance of 5 mi (8 km) from the crater rim, although erosional transport may have modified their distribution.

Impact melt fragments are another component of fall-out debris. Unfortunately, a good survey of its distribution has not been published. Nininger (1956) reported that melt fragments were abundant within 1,500 ft (~ 0.46 km) of the crater rim, but decreased rapidly at greater radii to a maximum extent of $1 \frac{1}{2}$

miles (2.4 km). Taken at face value, this suggests the impact melt in a fall-out debris unit extended to greater radii than the continuous overturned ejecta blanket. This is consistent with observations around the Sedan nuclear test explosion in alluvium, which distributed fused material beyond the continuous overturned ejecta blanket, but not as far as some missile ejecta. Unfortunately, erosional transport may have modified the distribution of melt fragments around Barringer Crater, so it is difficult to make an independent assessment of the distribution.

A base-surge deposit likely formed on top of the fall-out unit. A base-surge unit is produced from a collapsing column of the finest components in up-thrown ejecta. It has been observed around several experimental nuclear explosion craters. Unfortunately, no remnant of this unit survives at Barringer Crater, so we can only crudely estimate its distribution. In the case of the Sedan nuclear explosion crater in alluvium, isolated blocks of debris (missiles) landed up to 3 times farther than the continuous ejecta blanket and the base surge deposit extended more than 5 times farther than the continuous ejecta blanket (Carlson and Roberts, 1963). Thus, using Roddy's measurements of the existing continuous ejecta blanket around Barringer Crater, a base-surge deposit may have radiated outward for distances of 7.5 to 15 km (and possibly farther). Fine-grained base surge deposits are susceptible to wind and can be redistributed within days of crater formation. This unit was probably stripped from the region around the crater very quickly.

Estimates of the total mass of ejected material have varied. Barringer (1910) estimated more than 300 million tons of rock were ejected from the crater. A modern value derived by Roddy *et al.* (1975) is 175 million metric tons, which includes 60, 113.8, and 1.2 million metric tons from the Coconino-Toroweap, Kaibab, and Moenkopi, respectively. Not all of this mass, however, can be accounted for in existing debris deposits. They estimate 100 million metric tons survive in the overturned rim sequence and continuous ejecta blanket; 22.2 million metric tons were redeposited inside the crater; and 5.6 million metric tons were deposited as fall-back ejecta. Thus, 27% of the ejected mass is missing. These mass estimates utilized a volume bulking factor of 5% in ejected units, which is based on geophysical estimates of 2.30 g/cm³ for an average density of undisturbed bedrock and 2.18 g/cm³ for the density of the breccia lens. This may be a slightly low correction, given that analyses of the ejected material suggest a 6 to 10% density decrease (1.87 vs. 1.98 to 2.08 g/cm³) measured on the south crater rim (above). Roddy *et al.* (1975) also suggested that the missing mass can be accounted for as (a) material ejected beyond the continuous ejecta blanket, (b) material distributed in fine particles that were lofted high by the impact and carried away by wind, and (c) erosion that has stripped material from the ejecta blanket. They estimate that (a) and (b) explain 5 to 10% of the mass deficit and that the remainder is an erosional loss.

Shoemaker and Kieffer (1974) measured 40 ft (12 m) of erosion on the northeast crater flank. They argue that this is a minimum number and estimate that total rim erosion is 50 to 75 ft (15 to 20 m). They also suggest that erosion may be as much as 100 ft (30 m), assuming Coconino debris was deposited and subsequently eroded where Kaibab ejecta is currently exposed. This result also implies that the outer flank of the crater rim was originally steeper than now observed, because the alluvium and colluvium that covers the Coconino sandstone ejecta pediment softened the slope. It is worth noting that erosion has been more severe in some areas around the crater than in others. Barringer (1910) reported that the silica pits on the southwest side of the crater were a natural arroyo when he arrived, having an expanse of 200 to 300 yds and a depth of 10 to 12 feet. Thus, some sections of the ejecta blanket were severely dissected before any mining operations disturbed them.

While analyzing samples to determine the age of the impact event, Nishiizumi *et al.* (1991) also measured the exposure ages at several different levels along an ~10 m-tall Kaibab boulder (Whale Rock) on the west side of the crater. Their analyses suggest the uppermost 8 m of the boulder were uncovered in ~27,000 yrs at an average rate of 30 cm/1000 yrs, and 1.2 m were uncovered in the last 23,000 yrs at an average rate of 5 cm/1000 yrs. Thus, at least where Whale Rock is located, 9 m of finer-grained ejecta

has apparently been eroded.

In contrast, Grant and Schultz (1993) reported smaller amounts of erosion around the crater, although they focused their studies on debris farther from the rim crest and on shallower slopes. They based their estimate on the production of coarse erosional lag deposits and the sediment budgets of multiple drainage systems on the flank of the crater. They estimated <1 m of erosion beyond 1/4-1/2 crater radii from the crater rim, although loss of 2 to 3 m of material occurred in small areas. These estimates of erosion are smaller than those in previous studies, but Grant and Schultz (1993) suggest that there are true variations with radial distance from the crater rim: Higher erosional rates determined by Shoemaker and Kieffer (1974), Roddy *et al.* (1975), and Nishiizumi *et al.* (1991) reflect erosional conditions on or near the steep rim crest, whereas their results reflect erosional conditions on the shallower flanks of the ejecta blanket.

Table 7.1. Radial extent of impact components

Ejecta Component	Distance from Crater Rim (km)	Distance from Crater Rim (crater radii)	Distance from Crater Center (km)	Distance from Crater Center (crater radii)	References
Continuous Overturned Ejecta Blanket					
Observed Range	0.748-1.267	1.46-2.48	1.341-1.860	2.62-3.64	1
Average of Observed Range	0.95	1.86	1.543	3.02	1
Estimate of Average Pre-erosional Extent	1.9-2.4	3.7-4.7	2.5-3.0	4.89-5.87	2
Isolated Blocks of Kaibab					
Observed Maximum	5.6	11	6.2	12	3
Impact Melt Fragments					
Observed Maximum	2.4	4.7	3.0	5.9	4
Meteoritic Fragments of Asteroid					
Observed Maximum	8.8	12	9.3	12	5
	13	25	13.5	26	3
Melted Meteoritic Spherules					
Observed Maximum	8.0-9.6	16-19	8.6-10	17-20	4,6

(1) Roddy *et al.*, 1975; (2) Roddy, 1978; (3) Gilbert, 1896; (4) Nininger, 1956; (5) Barringer, 1910; (6) Rinehart, 1958
Value for crater radii is based on a 1022 m estimate of a pre-erosional crater diameter measured at the pre-impact elevation (Roddy, 1978). The current average crater rim diameter is taken to be 1186 m (Roddy, 1978).

I emphasize that the values above are observed distances. Erosion may have affected the distribution of ejecta components.

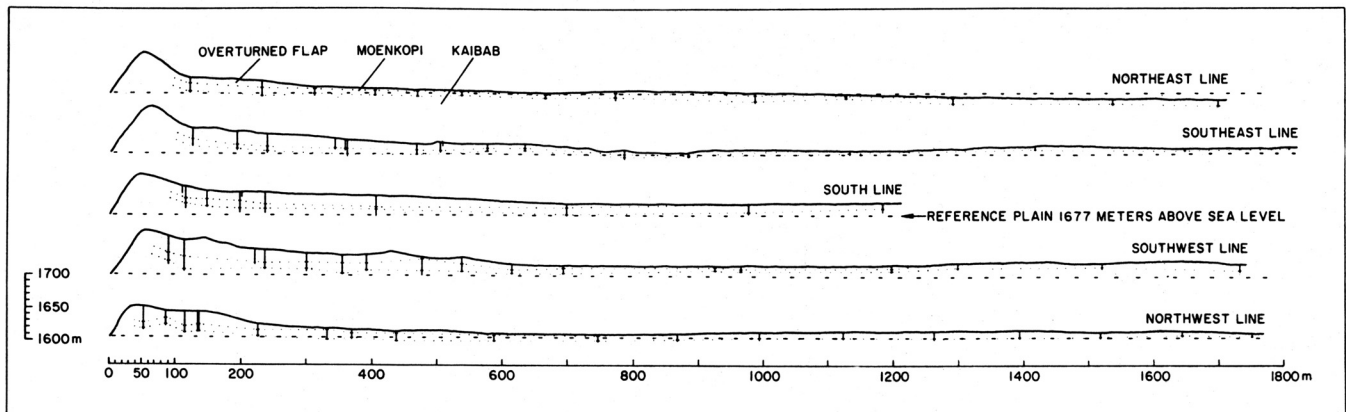
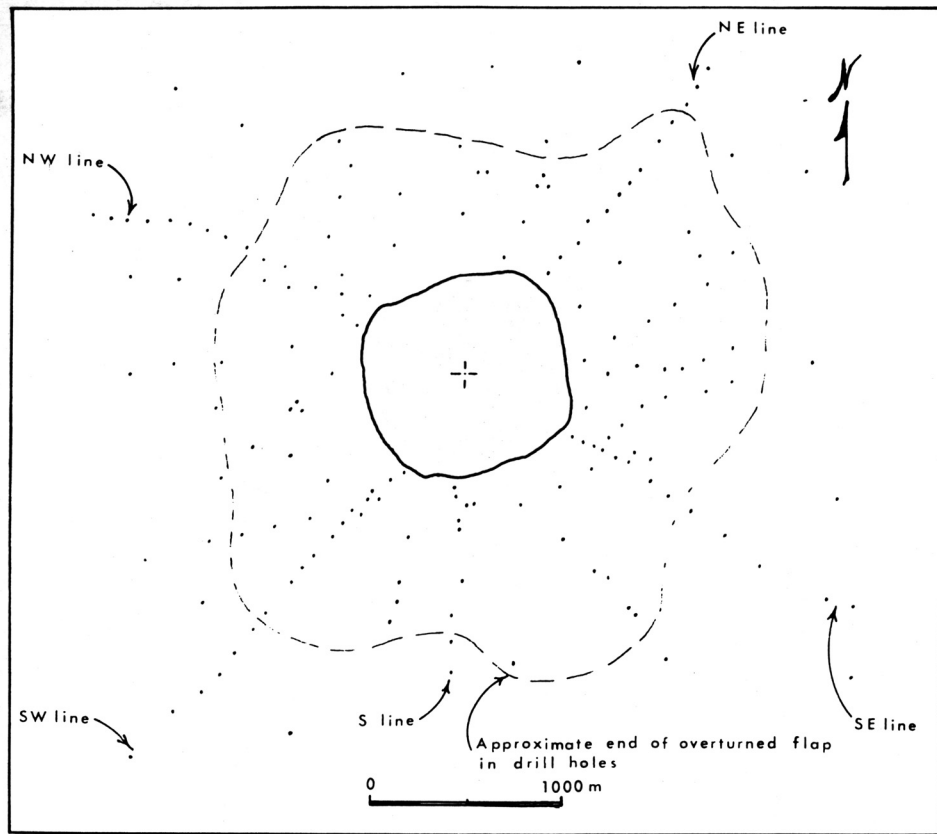


Fig. 7.1. Locations of rotary drill holes around Meteor Crater (top panel) and generalized geologic cross-sections along five transects (bottom panel). Both panels are from Roddy *et al.* (1975). The lateral extent of the ejecta blanket is mapped in the plan view and illustrates slight asymmetry. The average radial extent of the ejecta blanket around the crater is 1,543 m from crater center. In the cross-sections, the locations of the drill holes are indicated by vertical lines. Subtle dotted lines within each profile also indicate the top and bottom of Moenkopi encountered in the drill holes. These symbols are poorly expressed in the original figure and have not (yet) been redrawn.



Fig. 7.2. One of two boulder-rich fields within the continuous overturned ejecta blanket. This deposit of boulders is exposed on the west side of the crater, south of Barringer Point. The boulder field contains Whale Rock, which was originally buried within the ejecta blanket. Erosion of finer-grained and more friable ejecta components has exposed the boulders. The inset shows the same boulder field from a southeast-looking vantage point with a slightly different illumination angle. The surface of the surviving ejecta blanket is much steeper on the rim crest than it is at greater radii from crater center.

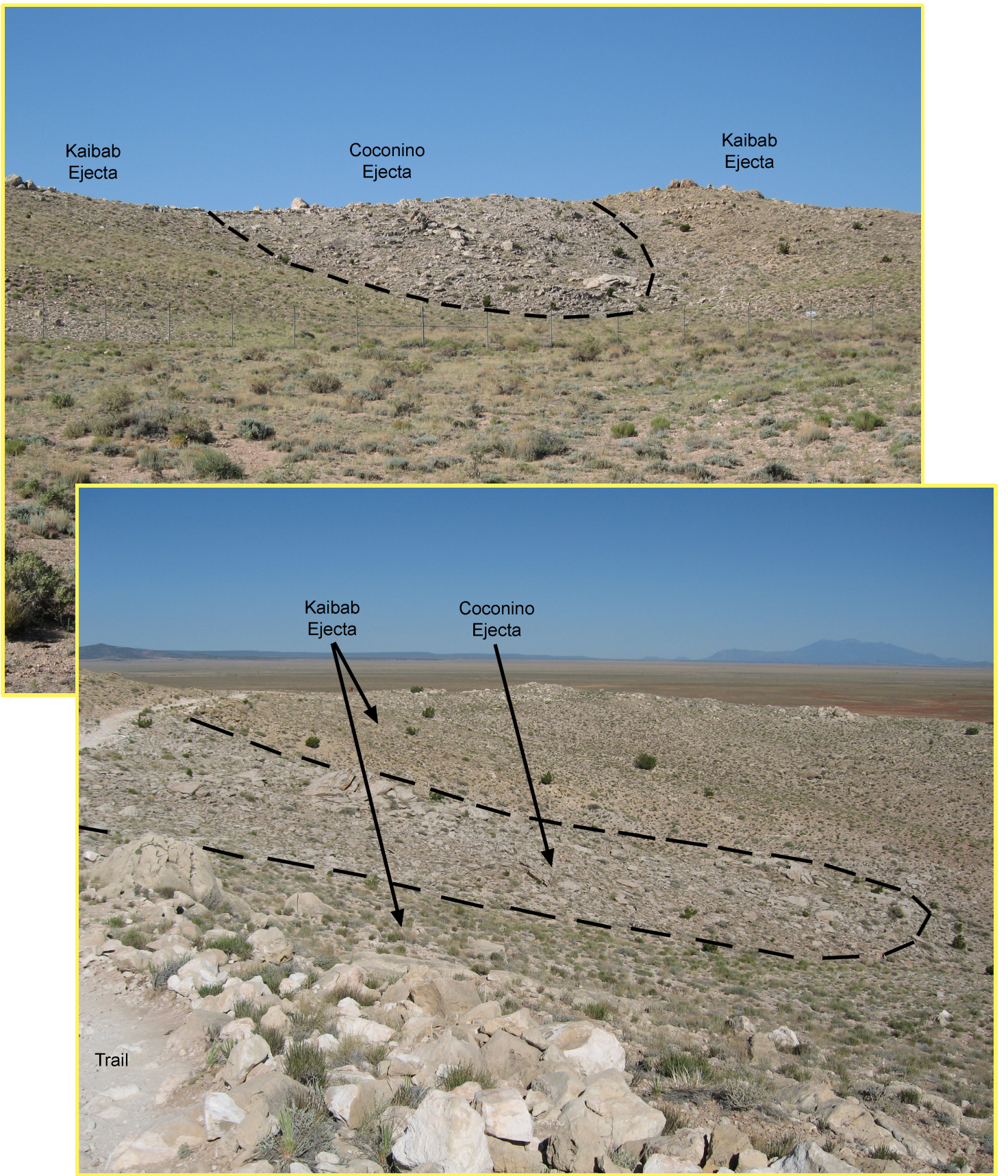


Fig. 7.3. The surface of ejected Kaibab debris was irregular, forming a depression in this location (top panel) that was filled with a wedge of Coconino sandstone debris (top and bottom panels). The deposit is on the north side of the crater. The view of the top panel (looking south) is from the road that leads up to the museum complex. The view in the bottom panel (looking northwest) is from the trail along the north rim, between the current museum complex and remnants of an old museum building.



Fig. 7.4. Examples of Moenkopi, Kaibab, and Coconino-Toroweap ejecta in the continuous overturned ejecta blanket. Overturned and ejected Moenkopi is relatively unfractured and forms a coherent unit below a more disrupted layer of Kaibab debris (top panel). This view is along the north wall of the crater. Overturned Coconino-Toroweap ejecta is disrupted even further (bottom panel), with boulders often limited to diameters of only a few tens of centimeters. This view is on the south side of the crater, beyond the crater rim.

8. Projectile



Meteoritic remnants of the impacting asteroid that produced Barringer Crater littered the landscape when exploration began ~115 years ago. As described in Chapter 1, meteoritic irons are what initially captured Foote's interest and spurred Barringer's interest in a possibly rich natural source of native metal. After Foote's description was published, samples were collected by F. W. Volz at a nearby trading post and sold widely. Gilbert (1896) estimated that 10 tons of meteoritic debris had already been recovered by the time of his visit. Similarly, Barringer (1905) estimated that 10 to 15 tons of it were circulating around the world by the time his exploration work began. Fortunately, he tried to document the geographic and mass distribution of that debris in a detailed map, which is reproduced in Fig. 8.1. The map indicates that meteoritic irons were recovered from distances approaching 10 km. Gilbert (1896) apparently recovered a sample nearly 13 km beyond the crater rim. A lot of the meteoritic material was oxidized. It is sometimes simply called oxidized iron, but large masses are also called shale balls. A concentrated deposit of small oxidized iron fragments was found northeast of the crater, although those types of fragments are distributed in all directions around the crater. The current estimate of the recovered meteoritic iron mass is 30 tons (Nininger, 1949; Grady, 2000), although this is a highly uncertain number. Specimens were transported in pre-historical times and have been found scattered throughout Arizona (see, for example, Wasson, 1968). Specimens have also been illicitly removed in recent times, without any documentation of the locations or masses recovered.

These iron fragments are collectively called the Canyon Diablo meteorite, whose namesake is a sinuous canyon west of the crater. This meteorite is a coarse octahedrite with a bandwidth of 1.2 to 2.2 mm. It is chemically classified as a Group IA iron (or Group IAB iron). This is a non-magmatic type of iron meteorite. I refer readers to the literature for more details about the petrogenesis of these irons.

The asteroid was dominated by Fe,Ni-alloys, particularly kamacite, reflecting a bulk chemical composition with 6.91 to 7.10 wt% Ni (Moore *et al.*, 1967; Wasson and Ouyang, 1990). The mineralogical diversity, however, is large (Table 8.1). As noted in Chapter 1, diamond is one of the mineralogical components of Canyon Diablo specimens. The interpretation of the diamond-bearing specimens led to a firestorm of controversy. Urey (1956) suggested the diamonds were produced in hydrostatic equilibrium and, thus, came from a planet of sufficient size to produce very high pressures. That implies a planetesimal in excess of 2020 km. Indeed, on the basis of diamonds, Urey postulated a series of Moon-sized bodies as the source of meteoritic material. Lipschutz and Anders (1961a,b) correctly argued that the diamonds were formed from carbon-graphite-troilite nodules by high shock pressures generated by the impact. Not everybody was immediately convinced. Carter and Kennedy (1964) were critical, which generated an interesting exchange (Anders and Lipschutz, 1966).

An analysis of meteorites from the crater rim and surrounding plain indicated the rim samples are much more strongly reheated than the plains samples and saw much higher shock pressures. Thus, the diamond-bearing specimens are concentrated on the crater rim (Nininger, 1956; Moore *et al.*, 1967). Heymann *et al.* (1966) conducted a detailed study of 56 Canyon Diablo specimens distributed from the crater rim to distances of about 4 mi (6 ½ km) and used cosmogenic nuclides to determine their original depth in the parent asteroid. Moderately- to severely-shocked specimens came from greater depths (*e.g.*, a mean of 132 cm vs 72 cm). Diamond-bearing and rim specimens came from greater mean depths (135 and 127 cm, respectively) than plains specimens (81 cm). They noted that the severely shocked specimens were recovered on top of the NE and SE portions of the continuous ejecta blanket, suggesting a ray-like distribution pattern and preferential distribution of material from slightly deeper levels of the asteroid in those directions.

Table 8.1. Minerals in the Canyon Diablo Meteorite

Mineral Name	Chemical Formula	Type of Mineral
kamacite	Fe,Ni-alloy	metal
taenite	Fe,Ni-alloy	metal
troilite	FeS	sulfide
daubreelite	FeCr ₂ S ₄	sulfide
sphalerite	(Fe,Zn)S	sulfide
mackinawite	(Fe,Ni)S _{0.9}	sulfide
chalcopyrrhotite	(Cu,Fe)S	sulfide
schreibersite	(Fe,Ni) ₃ P	phosphide
cohenite	(Fe,Ni,Co) ₃ C	carbide
haxonite	(Fe,Ni) ₂₃ C ₆	carbide
graphite	C	carbon
diamond	C	carbon
lonsdaleite	C	carbon
olivine	(Mg,Fe) ₂ SiO ₄	silicate
pyroxene	(Mg,Fe,Ca) ₂ Si ₂ O ₆	silicate
plagioclase	(Ca,Na)(Si,Al) ₄ O ₈	silicate
ureyite	NaCrSi ₂ O ₆	silicate
krinovite	NaMg ₂ Cr ₂ Si ₃ O ₁₀	silicate
chromite	FeCr ₂ O ₄	oxide
rutile	TiO ₂	oxide

Additional details about the Canyon Diablo meteorite appear in V.F. Buchwald's volumes about iron meteorites (1975).

In addition to meteoritic fragments, isolated opaque melt droplets were showered around the crater, either as a direct impact melt product or as a molten condensate from an impact-generated vapor cloud. In an early survey, Nininger (1951) reported a recovery rate of 100 g/ft³ of ejecta and/or alluvium derived from ejecta, which is 3,000 tons of spherules per square mile. He says the total area covered by the spherules is unclear, although there is a "sparse sprinkling...over 100 sq mi." Nininger (1956) later amended these estimates, reporting that 4,000 to 8,000 tons of spherules exist in the upper 4 inches of soil, based on measurements in 60 locations. From these data, he suggests the original asteroid had a mass of 100,000 to 200,000 tons. Most of the spherules are found within 1 ½ mi (2.4 km), although they have been found as far away as 5 mi (8 km) from the crater rim.

The spherules do not have the same composition as Canyon Diablo meteorites and were, thus, somehow fractionated during their formation. The compositional disparity was detected by Nininger (1951), who reported spherules with 17% Ni. Blau *et al.* (1973) found that the spherules are also enriched in S and P. They suggested the spherules formed by preferential shock melting of sulfide-rich portions of the asteroid, rather than oxidation of Fe. Using the dimensions of dendritic crystalline texture in the spherules, they calculated that the 1 mm spherules cooled between 500 and 30,000 °C/sec. They further argued that unshocked "plains" specimens spalled off the asteroid as it approached the surface, that shocked "rim" specimens were blasted off the trailing edge or backside of the asteroid, and that the remainder of the asteroid was dispersed in vapor cloud.

More recently, cosmogenic nuclides have been used to determine the source depths of the spherules on the asteroid. Surprisingly, this signature is preserved, despite the fractionation of the principal siderophile elements. Xue *et al.* (1995) examined the cosmogenic nuclides ¹⁰Be and ²⁶Al in 17 spherules

and compared them to meteorite fragments. They concluded that the spherules come from a greater depth than meteorites (or that Al and Be is lost during the spherule-forming process). Leya *et al.* (2002) pursued more cosmogenic noble gases. They also concluded that the spheroids come from a deeper depth than meteorites, but still from within a distance of 2.3 m from the pre-atmospheric asteroid surface.

Other isotope systems were employed to independently assess the relative depths of meteorite and spherule production. Schnabel *et al.* (1999) found that a group of spherules contains 7 times less ^{59}Ni than meteorite specimens, implying the spherules came from a depth that is 0.5 to 1.0 m deeper in the impactor than the meteorites. In absolute terms, their results suggest the spherules came from a region that was 1.3 to 1.6 m beneath the pre-atmospheric surface. A model simulation of the impact event in that same study suggested that 1.5 to 2 m of the backside of asteroid (assuming spherical symmetry, 30 m diameter asteroid, and a 20 km/s impact velocity) survives as solid material. This represents 16% of asteroid. The remainder was obliterated and these authors suggest that the bulk of that material was dispersed in a spray of fine molten material and did not involve a significant vapor component. They also argued that the Ni isotope data are consistent with 20 km/s impact simulation, not a slower, 15 km/s simulation; I refer the reader to their paper for details of that discussion.

A crude schematic of the asteroid that summarizes these data is shown in Fig. 8.2. The schematic diagram illustrates a perfectly spherical asteroid. In reality, the asteroid probably had an irregular surface and may have been significantly elongated. To illustrate a possible morphology, model images based on radar data are also included in Fig. 8.2 courtesy of Steve Ostro. The model images are of near-Earth asteroid (29075) 1950 DA, which is a suspected metallic asteroid. These images were selected rather than those of metallic main belt asteroids, because the Canyon Diablo asteroid was truly a near-Earth asteroid. The other candidate near-Earth metallic asteroid that has been imaged with radar is 1986 DA (Ostro *et al.*, 1991). Two previously imaged metallic asteroids in the main asteroid belt are 216 Kleopatra and 16 Psyche.

As the model images suggest, metallic asteroids can have irregular surfaces that reflect their collisional evolution. In the case of the Canyon Diablo asteroid, cosmic ray exposure ages suggest the object was liberated in a planetesimal breakup event ~540 million years ago and was subsequently involved in a secondary collision ~170 million years ago (Heymann *et al.*, 1966; Michlovich *et al.*, 1994).

It is not yet clear how surface irregularities or the shape of the asteroid may have affected the excavation of the crater and distribution of debris around the crater (including the distribution of projectile components). This is an area of study that has become approachable only recently with the advent of new computational codes that permit 3-D simulations with asymmetrical components.

The size of (29075) 1950 DA is ~1 km in diameter, which is far larger than the Canyon Diablo asteroid. Previous estimates of its diameter generally fall within the range of 10 to 50 m, but the exact size is still uncertain. To help readers link a discussion of proposed masses with asteroid diameters, I built a table (Table 8.2) of hypothetical spherical projectiles with radii from 5 to 25 m (and, thus, diameters of 10 to 50 m). As noted above, a recent simulation of the impact event assumed a 30 m diameter object, which corresponds to a mass of 1.1×10^8 kg or 110,000 metric tons assuming a density of 7.8 g/cm³. Other mass estimates include 400,000 tons (Magie, 1910); 10,000,000 tons (Barringer, 1914); 5,000 to 3,000,000 tons (Moulton, 1931; per Hoyt, 1987); 15,000 tons (Wylie, 1943a,b); 5,000,000 tons (Öpik, 1936; Rostoker, 1953); 100,000 to 200,000 tons (Nininger, 1956); 2,600,000 tons (Öpik, 1958); 30,000 to 194,000 tons (Bjork, 1961); 63,000 tons (corresponding to 25 m sphere; Shoemaker, 1963); and 500,000 to 1,000,000 tons (Shoemaker in Elston, 1990), as discussed in greater detail by Buchwald (1975) and Hoyt (1987). Only a small fraction of this mass survives. As described above, the current estimate of surviving meteoritic material is 30 tons. In addition, Rinehart (1958) estimates 8,000 tons survives as dispersed metallic particles.

Table 8.2. Masses of hypothetical iron asteroids

Radius (m)	Volume (m ³)	Density (g/cm ³)	Mass (kg)	Mass (metric ton)
5	524	7.8	4.08×10^6	4.08×10^3
6	905	7.8	7.06×10^6	7.06×10^3
7	1437	7.8	1.12×10^7	1.12×10^4
8	2145	7.8	1.67×10^7	1.67×10^4
9	3054	7.8	2.38×10^7	2.38×10^4
10	4189	7.8	3.27×10^7	3.27×10^4
11	5575	7.8	4.35×10^7	4.35×10^4
12	7238	7.8	5.65×10^7	5.65×10^4
13	9203	7.8	7.18×10^7	7.18×10^4
14	11494	7.8	8.97×10^7	8.97×10^4
15	14137	7.8	1.10×10^8	1.10×10^5
16	17157	7.8	1.34×10^8	1.34×10^5
17	20580	7.8	1.61×10^8	1.61×10^5
18	24429	7.8	1.91×10^8	1.91×10^5
19	28731	7.8	2.24×10^8	2.24×10^5
20	33510	7.8	2.61×10^8	2.61×10^5
21	38792	7.8	3.03×10^8	3.03×10^5
22	44602	7.8	3.48×10^8	3.48×10^5
23	50965	7.8	3.98×10^8	3.98×10^5
24	57906	7.8	4.52×10^8	4.52×10^5
25	65450	7.8	5.11×10^8	5.11×10^5

The fate of the missing material has been at the center of considerable debate. Barringer, of course, thought it was buried beneath the crater floor. He considered the alternative possibility that the object was vaporized (Barringer, 1910). In that case, he reasoned, the vaporized projectile and target materials would have re-condensed, producing a mass of material (perhaps similar to rock flour) that was stained with iron and nickel oxides. Since this is not observed, he argued the mass must still exist inside the crater. (At this point in the development of his model, he also thought the asteroid was a cluster of fragments rather than a solid mass.)

Others have argued that a large fraction of the object was obliterated, either in the form of a vapor or finely-dispersed molten mist. A quantitative assessment of that fraction and the amount of obliterated material that was truly ejected is still lacking. Or, rather, a consensus has not developed around one of the proposed answers. Shoemaker, for example, maintained that one-third to one-half of the projectile mass is dispersed in material that remains in the crater (Elston, 1990), consistent with his initial assessment of the impact event (Shoemaker, 1963). In contrast, others have suggested nearly all of the projectile was dispersed beyond the rim of the crater as melted and/or vaporized ejecta (*e.g.*, Blau *et al.*, 1973).

The size and strength of the Canyon Diablo asteroid affected the outcome of the impact event. Smaller and weaker objects are often unable to penetrate the atmosphere without catastrophically fragmenting far above the ground. For example, a 6 to 8 m diameter stony asteroid with L-chondrite affinities fell about ~15,000 years ago in northern Arizona, but fragmented into thousands of stones (the Gold Basin meteorites) that showered more than 225 km² of the Earth's surface rather than create a hypervelocity impact crater (Kring *et al.*, 2001). In the case of Barringer Crater, however, the asteroid was able to collide with the Earth's surface while still moving with a large fraction of its cosmic velocity.

As noted briefly above, Barringer wondered whether the impacting asteroid hit as a solid iron mass, a cluster of iron fragments, or as iron fragments within a stony or icy matrix. The impact cratering community continues to debate the first two options. Results are in considerable flux at the moment, so I will not try to capture them here and suggest instead that interested students watch the literature.

With regard to Barringer Crater and the projectile that produced it, there are two other observations worth noting. First, with a diameter of ~1 km, the crater approaches the lower limit of hypervelocity craters on Earth (Table 8.3). The atmosphere screens most objects that make smaller craters. That is, the atmosphere shields the surface from objects that are smaller or weaker. Because most small craters are associated with iron asteroids, they appear to be stronger than stony asteroids. Second, the number of craters produced by type IAB irons, relative to other irons, is higher than the ratio of those objects seen in the smaller meteorite population. At least 14 to 15 of the craters in Table 8.3 were generated by irons and, of these, 6 (or ~40%) were produced by type IAB irons. Also, at least 28% of all the small crater impacts were produced by type IAB iron asteroids. In contrast, only 10% of observed iron meteorite falls are type IAB (Grady, 2000). Even in a combined population of iron meteorite finds and falls, type IAB specimens constitute only 15% of the population. The data suggest one of three conclusions: (1) Type IAB asteroids are stronger than other irons and, thus, better able to penetrate the atmosphere; (2) Type IAB asteroids are less collisionally evolved than other irons and, thus, less populous among meteorite-size objects; or (3) we are falling prey to the vagaries of small number statistics.

Table 8.3. Small (≤ 1 km) diameter impact pits and impact craters.

Crater	Locality	Diameter (km)	Projectile	Age (Ma)
Haviland	Kansas, USA	0.011	Pallasite	0
Dalgaranga	Western Australia, Australia	0.021	Mesosiderite	0.025
Sikhote Alin	Primorskiy Kray, Russia	0.027	IIB	0
Campo del Cielo*	Gran Chaco Gualamba, Argentina	0.05	IAB	<0.004
Sobolev	Primorye Territory, Russia	0.053	Iron	0
Vevers	Western Australia, Australia	0.08	IIB	<1
Ilumetsa	Estonia	0.08	?	>0.002
Wabar*	Rub' al Khali, Saudi Arabia	0.097	IIIB	0.006 ± 0.002
Morasko*	Poznan, Poland	0.1	IAB	0.01
Kaalijarvi*	Saaremaa, Estonia	0.11	IAB	0.004 ± 0.001
Henbury*	Northern Territory, Australia	0.157	IIIB	<0.005
Odessa*	Texas, USA	0.168	IAB	<0.05
Boxhole	Northern Territory, Australia	0.17	IIIB	0.03
Macha*	Russia	0.3	Iron	<0.007
Aouelloul	Adrar, Mauritania	0.39	Iron or Pallasite	3.1 ± 0.3
Amguid	Algeria	0.45	?	<0.1
Monturaqui	Antofagasta, Chile	0.46	IAB	<1
Kalkkop	South Africa	0.64	?	<1.8
Wolfe Creek	Western Australia, Australia	0.87	IIIB	<0.3
Tswaing	South Africa	1.13	Chondrite	0.220 ± 0.052
Barringer	Arizona, USA	1.19	IAB	0.049 ± 0.003

From Grieve (1991), Grieve *et al.* (1995), Koeberl *et al.* (1994), and Koeberl *et al.* (1998).

*Crater field; diameter of largest crater listed.

DISTRIBUTION OF METEORITIC MATERIAL AROUND METEOR CRATER, COCONINO Co., ARIZONA



LEGEND

- Canyon Diablo iron meteorites from 10 to 547 lbs. Discovered by Standard Iron Company.
- ★ Canyon Diablo iron meteorites from 10 to 1000 lbs. Discovered by employees of F.W. Volz et al., previous to acquisition of property by S.I.Co.
- ▲ Small Canyon Diablo iron meteorites. Discovered by S.I.Co. The distribution of specimens is only approximated because thousands were found. Specimens are usually a few grains or ounces in weight; irons weighing from 1 to 10 lbs were only found occasionally.
- ✿ Large irregular masses of meteoritic iron oxide or large shale balls from 100 to 300 lbs in weight, due to oxidation of meteoritic iron rich in chlorine and sulphur or shale ball iron.
- Small broken fragments of meteoritic iron oxide or iron shale (a few grains or ounces, rarely a pound in weight). Thousands of such pieces found, hence distribution only approximated.

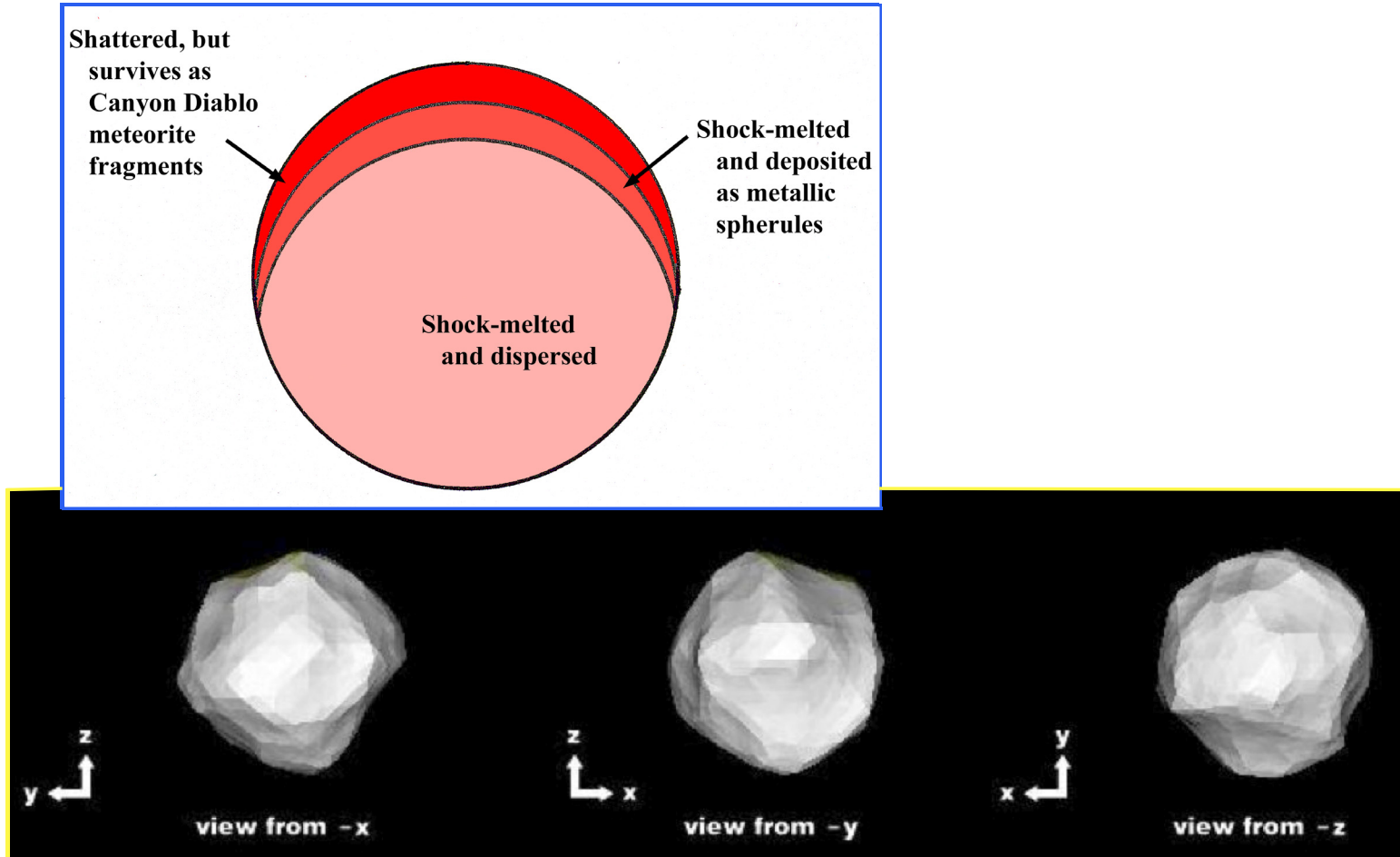


Fig. 8.2 Schematic diagram of the asteroid that produced Barringer Crater (upper left). Cosmogenic nuclides suggest the surviving meteoritic component of the asteroid was derived from a shallower depth (roughly 0.6 to 1.3 m) than molten metallic spherules (roughly 1.3 to 2.0 m depth). Furthermore, lightly-shocked meteorites appear to come from a shallower depth (mean of 0.8 m) than moderately- to heavily-shocked meteorites (mean of 1.3 m depth). The lightly-shocked meteorites are distributed on the plain surrounding the crater, while moderately- to heavily-shocked meteorites are concentrated near the crater rim. Almost all of the diamond-bearing specimens were found on the crater rim. The shape of the asteroid that produced Barringer Crater is unknown, but a suspected metallic near-Earth asteroid is shown (bottom panel) to provide an example of possible morphologies. Three model images based on radar data are shown for (29075) 1950 DA, which were kindly provided by Steve Ostro for our field guide. This object is far larger than the one that produced Barringer Crater (1 km versus 10 to 50 m), but it should help focus our discussion of projectile shape. I refer readers to a paper by Busch *et al.* (submitted to *Icarus*, 2007) for additional details about asteroid (29075) 1950 DA.

9. Trajectory



The trajectory of the impacting asteroid is another issue of considerable debate and still unresolved. Historically, circular plan views of impact craters confounded many investigators who assumed a circular crater requires a vertical impact. They wondered why more craters are not elliptical. Gilbert and Barringer both realized that 45 degree impacts are the most probable trajectories for meteoritic material. Yet Gilbert, like many of his contemporaries, mistakenly thought a 45 degree impact produces an oval crater (Hoyt, 1987). Barringer, on the other hand, realized that a 45 degree impact will produce a round crater (Hoyt, 1987). Despite this insight, Barringer, like Gilbert, initially assumed that the northern Arizona impact had been vertical or nearly vertical and that the asteroid was buried beneath the center of the crater floor.

When extensive drilling did not locate a main mass beneath the crater floor and instead only produced traces of the projectile, Barringer began to consider other options. He had already noted several features that seem to have a directional symmetry. In his 1905 paper, he observed that clusters of immense Kaibab boulders were deposited on the east and west sides of the crater. In his 1910 paper, he argued that the lowermost section of the Coconino only appears in the south-east section of the ejecta blanket and, thus, that the deepest units excavated by the impacting object were ejected in that direction. In that same paper, he also observed that the southern cliffs were uplifted as a single entity by 105 ft. He then suggested that the uplift was caused by a meteoritic mass moving from the north to the south and that the mass remained wedged beneath the cliffs along with a vast amount of shattered rock and Variety A and B shock-metamorphosed Coconino sandstone. He felt vindicated when drilling in 1920-1922 produced a 1,376 ft deep borehole on the southern crater rim that encountered ~30 ft of oxidized meteoritic material, Variety A and B shock-metamorphosed sandstone, and became stuck in what was interpreted to be the main asteroid mass. (See Table 3.2 for the driller's log of that hole.) He published a report (Barringer, 1924), concluding the "mass seems to have approached the earth at an angle of approximately 45°, and from a direction slightly west of north, and to have made a slight curve to the west in its slanting flight through more than 2500 feet or one half-mile of solid rock...."

Shoemaker, on the other hand, was impressed with thrust faults in the crater walls. (See Chapter 5 for more details about the faults.) These faults outlined wedges of rock that are thrust into crater walls, forming anticlines and enhancing crater rim uplift. He and Kieffer (1974) argued that they only occur on the north and west sides of the crater and that they were especially well-developed in the northwest corner. They suggested the features were produced by a bolide moving from the southeast to the northwest.

I agree that the thrust faults are impressive and seem to point to a flow of material through the transient crater margin into the surrounding crater wall in a rough south-to-north direction that encompasses flow towards the northwest and northeast. I have observed a few additional thrust faults along the east margin of the crater, so a purely southeast to northwest flow no longer seems plausible. Taken at face value, the thrusts seem to imply a trajectory roughly from the south to north, with variations to both the northwest and northeast possible. However, I can also imagine the same thrusts produced in reaction to an impact with a projectile trajectory in the opposite direction. I also worry that we are biased by what we can observe. If thrust-faulting occurs low on the hidden portions the crater walls, we are unable to factor that information into our analysis. The observations only seem truly inconsistent with an east to west or west to east trajectory. Thus, the thrust faults can possibly be reconciled with Barringer's proposed trajectory and the impressive amount of material that may have been injected beneath the rim along the south side of the crater. (See discussion of injected material in Chapter 3.) The uplift of the southern crater wall is a less convincing indicator, because the amount of uplift along the southern crater

wall is much less than that in the east-southeast corner of the crater, as shown in Fig. 14.6 and 14.9 in the trail guide chapters. If uplift is an indicator of trajectory, then the east-southeast corner seems to be at the end of the trajectory. Alternatively, crater wall uplift may be influenced as much by preferential movement along tear faults as trajectory and, thus, not a diagnostic indicator of trajectory.

Other directional indicators have been noted by several investigators: Barringer (1910) pointed to a concentration of iron oxide beyond the northeast corner of the crater; Nininger (1956) and Rinehart (1958) pointed to a concentration of meteoritic soil particles in that same direction; Heymann *et al.* (1966) pointed to a concentration of highly-shocked and diamond-bearing Canyon Diablo meteorite specimens near the northeast and southeast crater rims. Shoemaker and Kieffer (1974) suggested Silica Hill is a small uplift on the crater floor that is offset towards the north. The concentration of meteoritic oxide and iron-rich soil particles in the northeast is the most-often cited evidence beyond the crater rim. Rinehart (1958), for example, wrote that “a highly reasonable hypothesis is that the meteorite approached the earth from a south-westerly direction and, when it struck, pitched forward large quantities of meteoritic material to the position where it now rests.”

A more distant indicator of impact trajectory may be another young impact crater that some investigators speculate was produced at the same time at the Barringer Crater. This story, too, has its origins with a Barringer. In this case, D. Moreau Barringer Jr. had an opportunity to explore another crater-like structure near the west-Texas town of Odessa. Within a few hours, he found iron meteorites and shale balls and concluded that the structure was an impact crater with at least one satellite impact crater. He telegraphed the news to his father immediately. In private correspondence, Daniel Moreau Barringer wondered if his crater and the Odessa crater could have been produced at the same time by a pair of asteroids traveling together.

The possibility was further explored by Brandon Barringer in a paper presented to The Meteoritical Society in 1965 and published in 1967. Several hints seemed to link the two impact events. (1) Both were produced by similar types of iron asteroids. (2) Although the ages of the craters were imprecisely known, they were approximately similar. Estimated ages for Barringer Meteorite Crater and Odessa Crater were 20,000 and 25,000 years, respectively, at the time of Brandon Barringer’s report. (3) There were hints that both craters were produced by objects with roughly north to south trajectories.

Brandon Barringer recognized problems with some scenarios linking the two events, noting that it was “unlikely that they were formed by the decomposition of a single natural satellite” in the atmosphere. He left the door open, however, to other possibilities. In general, he recommended further study to resolve these and other issues regarding the origin of the craters.

Additional research and newer technology have shed light on the hypothesis. The chemical compositions of the iron asteroids that produced the craters have been analyzed in greater detail and the ages of the two craters have been better determined.

Wasson (1967, 1968) examined the trace element compositions of the iron meteorites at Barringer Crater and those at Odessa. Although both groups of meteorites are part of the same chemical class, there are subtle differences between the meteorites that led Wasson to suggest they formed from two unrelated iron asteroids.

The second set of studies began in the 1980's, when Sutton (1985) examined the crystalline damage caused by naturally occurring radioactive isotopes in crater rocks. Using the isotopes as a clock, he estimated the Barringer Crater was produced approximately 49,000 years ago. Nishiizumi *et al.* (1991) and Phillips *et al.* (1991) used different types of isotopic clocks in crater rocks. They too estimated the crater formed approximately 49,000 years ago. (See Chapter 11 for more information about estimates of

the crater's age.)

More recently, techniques similar to those of Sutton were applied by Holliday *et al.* (2005) to the Odessa impact site. They estimated the Odessa craters were produced approximately 63,000 years ago. Although the ages of Barringer and Odessa craters are still not precisely known, these approximate ages suggest Odessa formed earlier, with the caveat that the Barringer crater may be older than 49,000 yrs. (See discussion in Chapter 11). Thus, the two impact events may not be directly related and may not have any bearing on the issue of trajectory.

Nonetheless, several other potential indicators of trajectory survive (and even the Odessa connection might be revived). Unfortunately, these indicators cannot be reconciled at the present time and I think it fair to conclude that the trajectory of the impacting asteroid that produced Barringer Crater remains uncertain.

10. Energy of Impact



The kinetic energy of an impacting asteroid is one-half its mass times velocity squared. As discussed in the previous chapter, the projectile is usually assumed to have a pre-collisional diameter of roughly 10 to 50 m, which represents a mass of ~4,000 to 500,000 metric tons (Table 8.2.). The impact velocity is usually assumed to be between 11 and 20 km/s.

Those dimensions and velocities reflect a wide range of impact energy. Published estimates range from an impact energy equivalent to a few tens of kilotons of TNT to over 60 megatons of TNT (Table 10.1.). When Shoemaker (1960, 1963) published his classic study of the crater and analogies with nuclear explosion craters, he estimated an impact energy equivalent to ~1.4 to 1.8 MT. This estimate was based on a cube-root scaling law that he calibrated with the Teapot Ess nuclear explosion. Schmidt (1980) conducted centrifuge experiments, from which he derived a new set of scaling laws. Based on those results, he suggested much higher impact energies, ranging from 22 to 61 MT. At nearly the same time, Roddy *et al.* (1980) developed a new computer model of crater excavation and estimated a 15 MT blast for a vertical impact. Shoemaker (1987) concluded the energy was probably a little higher than 15 MT, because the impact was more likely to have had an oblique trajectory. Roddy and Shoemaker (1995) revised their computer simulations and suggested 20 to 40 MT is a better estimate, which is a rough average of Shoemaker's original estimate and Schmidt's estimates. Unfortunately, the details of those computer simulations only appeared in preliminary form and the details are now lost.

More recently, a family of estimates have been appearing that are dramatically lower and approach Shoemaker's original estimate of the impact energy. These calculations have been emphasizing three features of the impact process: atmospheric deceleration, disruption, and ablation. Before discussing the new results, it may be useful to digress a moment to discuss atmospheric deceleration, disruption, and ablation.

With regard to atmospheric deceleration, it may be best to begin with small isolated iron meteorites. These objects fall to Earth with the same range of velocities as larger, Canyon Diablo-size asteroids, when they first encounter the top of the atmosphere. These small objects are, however, completely decelerated in the atmosphere and eventually fall with a velocity governed by Earth's gravity. Larger impacting bodies with masses substantially greater than the mass of atmosphere they encounter will not be significantly decelerated and will then hit the Earth's surface with most of their cosmic velocity intact. The Canyon Diablo asteroid is at the small end of the range that produces impact craters, so it may represent an intermediate case. It may have been partially decelerated, but still able to maintain enough motion to generate a hypervelocity impact crater.

The Canyon Diablo asteroid is also at the small end of the range of objects that produce impact craters, as discussed briefly in Chapter 8. Smaller objects and weaker objects often catastrophically fragment in the atmosphere. A nearby example is the 6 to 8 m Gold Basin brecciated stony meteoroid that failed to reach the ground intact in northwestern Arizona (Kring *et al.*, 2001). A more recent example is the Tunguska impact blast, in which a stony impactor catastrophically fragmented above the Siberian taiga. Neither event produced an impact crater. Potentially, the Canyon Diablo asteroid began to fragment, but not catastrophically, and reached the ground with a sufficiently large main mass or with a sufficiently dense cluster, while maintaining a significant fraction of its cosmic velocity.

When meteoritic material enters the atmosphere, surfaces are heated dramatically, melt, and slough off. They are ablated. Radiating flow lines generated in the melt are often preserved in meteoritic fusion crusts. Because this is a surface phenomena, the effect is usually proportionally smaller for larger objects

that have larger volume to surface area ratios. However, if a larger object begins to fragment and greatly enlarge the amount of surface area, ablation may consume an increasingly large fraction of the original asteroid.

Calculations that explicitly examine atmospheric deceleration, disruption, and ablation processes are generating new estimates of the impact energy that fall in the range of ~1 to 10 MT (Melosh and Collins, 2005; Artemieva, 2006). Because the asteroid is being decelerated, a larger mass and diameter for the original asteroid are implied. For example, Artemieva (2006) calculates an ~40 m diameter coherent iron asteroid with an 18 km/s collisional velocity has sufficient energy to create the crater. However, if she allows for disruption and ablation, she requires a 57 m diameter asteroid that was decelerated to a final impact velocity of 11 km/s or a 46 m diameter asteroid that was decelerated to a final impact velocity of 15 km/s. Both generate about 10 to 11 MT, which her calculations suggest is sufficient to excavate the crater and fracture the surrounding wall rock.

This is an evolving subject. A consensus on the impact energy has not yet been reached, although the trend is towards smaller values (*i.e.*, 1 to 10 MT rather than 20 to 40 MT).

Table 10.1. Estimates of Impact Energy

Energy (MT TNT equivalent)	Source
38.8	Magie 1910 (per Hoyt 1987)
38	Moulton (per Hoyt 1987)
2.91	Moulton (per Hoyt 1987)
0.21	Wylie 1943 (per Hoyt 1987)
0.08	Baldwin 1949 (per Hoyt 1987)
4.8	Gilvarry and Hill 1956 (per Hoyt 1987)
64	Opik 1958 (per Hoyt 1987)
1.4 to 1.8	Shoemaker 1963
8.1	Baldwin 1963
4 to 5	Shoemaker 1974
22 to 61	Schmidt 1980
15	Roddy et al. 1980
15+	Shoemaker 1987
20 to 40	Roddy and Shoemaker 1995
5.3	Schnabel et al. 1999 (calc. for their 15 m radius & 20 km/s velocity)
0.44	Ai and Ahrens 2004 (calc. for their 9 m diameter & 33 km/s velocity)
2.5	Melosh and Collins 2005
10 to 11	Artemieva 2006 (calc. for her 46-57 m diameter & 15-11 km/s velocity)

For cases where kinetic energy is calculated from authors' estimates of projectile size and velocity, I assume a projectile density of 7.8 g/cm³.

11. Age of the Crater



As any visitor can see, the crater is exceptionally well-preserved. Although talus covers the lower slopes of the crater walls and finer-grained sediments cover the crater floor, the crater still has the sharp edges of a relatively unaltered structure. For that reason, a young age has always been assigned to it. Indeed, Barringer (1905) estimated the age to be 2,000 to 3,000 yrs, not much older than the 700 yr-old rim cedars (junipers). Likewise, Tilghman (1905) commented that the crater looked like it formed yesterday and that it must have an age less than 10,000 yrs and probably less than 5,000 yrs.

Measuring a precise age for the crater, however, was difficult. Even using modern techniques, the question of age was difficult to resolve. The impact did not produce huge volumes of impact melt that might be analyzed using the isotopic systems (*e.g.*, ^{39}Ar - ^{40}Ar) often applied to other igneous rocks, including impact melts. In addition, the crater is too young for many of those radiometric systems to be applied, because they involve half-lives that are too long. For that reason, many early attempts to determine the age of the crater relied on evaluations of erosion and sedimentation.

In a paper titled “The Age of Meteor Crater,” Blackwelder (1932) evaluated the thickness of lake sediments within the crater, the amount of alluvium and finer-grained debris on the crater slopes and crater floor, ravines cut into the crater deposits, and dissolution pitting of ejected limestone blocks. Based on those criteria, he estimated the crater was produced between 40,000 and 75,000 years ago. As described further below, this may be an incredibly accurate estimate.

At about the same time, Jakosky *et al.* (1932) conducted an electrical and magnetic survey of the crater. In the course of that investigation, they evaluated the thickness of lake beds on the crater floor, lag deposits of concretions on Coconino and Kaibab surfaces on the crater rim, and small basins filled with sediment from eroded ejecta. They argued that the “fresh looking cliffs” are not, in fact, fresh, but rather “the products of centuries of erosion.” They also pointed out that the thickness of Moenkopi buried beneath Kaibab and Coconino in the crater walls is much greater than the thickness of Moenkopi on the surrounding plains. They required sufficient time to erode up to 40 ft of Moenkopi on the plains. We now understand that this latter argument is flawed, because the Moenkopi is thickened by an overturned component in the crater walls and, thus, the discrepancy is not an erosional one. Nonetheless, based on all of these criteria, they concluded the crater formed tens of thousands of years ago and probably about 50,000 years ago.

Shoemaker (1960, 1974) compared the Pleistocene and Holocene alluvium that covers the ejecta blanket with deposits elsewhere on the Colorado Plateau. Drawing on those comparisons, he estimated (Shoemaker, 1974) the crater was produced “a few tens of thousands of years ago, as shown by the mid-Wisconsin age of the oldest sedimentary deposits on the rim and in the interior of the crater.” He quantified those words with estimates of 20,000 to 30,000 yrs and $25,000 \pm 5,000$ yrs (Shoemaker, 1983), which were numbers he used for over a decade. His estimate may have been influenced by the first radiometric age of material in the crater. Ives *et al.* (1964) obtained a radiocarbon age for shells from a dump around the crater’s main shaft. The measured age was $24,000 \pm 2,000$ yrs. The shells were believed to be from the basal portion of the lake sediments. Assuming the lake sediments were deposited immediately after the crater formed, the value indicated the age of the crater. However, if either the lake did not form immediately or the shells were from a higher level within the lake sediments, the date only represented a minimum age for the crater.

Those shells and other fossils deposited in lake sediments on the crater floor provide additional clues about the crater’s age through correlations with fossil assemblages in other localities and climatic events.

The results, however, are ambiguous (Reger and Batchelder, 1971; Forester, 1987) and will not be discussed in any detail here. In addition, a preliminary assessment of pollen from the base of the lake sediments (Davis and Kring, 2002) found an assemblage that is similar to those in 50 ka sediments in Walker Lake near Flagstaff. That, however, is more a measure of climatic conditions and not a diagnostic indicator of age.

Efforts to directly measure the age of the crater resumed in the mid-1980's, when Sutton (1985) measured thermoluminescence ages for shock metamorphosed rocks. He estimated an age of $49,000 \pm 3,000$ yrs for the crater. Similar ages were soon recovered using cosmogenic nuclides that measured the amount of time boulders on the rim of the crater had been exposed. In back-to-back papers, Phillips *et al.* (1991) and Nishiizumi *et al.* (1991) reported $49,700 \pm 850$ and $49,200 \pm 1,700$ yr ages, respectively. Based on the extraordinary agreement between these three independent studies, 49 or 50 ka is widely accepted to be the age of the crater.

The ages based on cosmogenic nuclides will be re-visited in the near future, because estimates of the production constants and scaling factors needed for the calculations have been improved. As I write this, a large project is underway to re-calibrate those systems, particularly for ^{36}Cl -based age determinations. Fred Phillips (of Phillips *et al.*, 1991) is leading this re-evaluation. It will be interesting to see if the re-calibrated system produces the same 49 to 50 ka age or a different age. Potentially, an improved set of production calculations may destroy the agreement that currently exists between ages determined using cosmogenic and thermoluminescence methods. At the moment, there are hints that the recalculated ^{36}Cl age will be older than 50 ka.

Plans for two other types of age determinations have been made. The first involves pack-rat middens that are scattered among the rocky clefts of the crater walls. Pack-rat middens have been excellent sources of both age and climate information elsewhere on the Colorado Plateau. Appropriate samples will be collected to determine an age for the deposits, which will provide an additional minimum age for the crater. In addition, the fossil sequence within the lake sediments will be resampled. This latter task, however, is delayed until the walls of Main Shaft and/or Shaft #2 in the crater floor can be stabilized. Efforts are underway to raise funds so that the shafts can be re-cribbed and converted into permanent research and educational facilities.

12. Environmental Effects of the Impact



The relationship between the Chicxulub impact event and a mass extinction at the Cretaceous-Tertiary boundary has promoted an assessment of the environmental effects of impacts of all sizes. Such studies have two components. First, they must reconstruct the environment at the time of impact. Second, they must determine the effects of the impact on that environment and the plants and animals within it. An initial attempt to resolve those issues at Barringer Crater appeared a decade ago (Kring, 1997) and will be summarized here. As discussed at the time, there were numerous uncertainties in the baseline data being used, so a discussion of possible permutations will also appear below.

Any age for the crater within 20,000 yrs of 50 ka places the impact event within the Wisconsin interstadial, which is a relatively warm interval during the Wisconsin period of glaciation. The topography was similar to that seen today. The average slope was ~0.5° to the northeast. Moenkopi ridges had an average relief of ~5 to 10 m and the maximum topographic high was no more than ~20 m. Drainage systems may have been more active than they are today, because the climate was wetter during the Wisconsin period. Gilbert (1896) even suggested the impact hit a small drainage system. Most of the volcanic features in the region were present, with the possible exception of three cinder cones with age comparable to or younger than that of the crater.

Currently, the vegetation around the crater is dominated by a grassland (Fig. 12.1). At lower elevations to the east, the grassland is replaced by a sagebrush ecosystem. At higher elevations to the west, the grassland is replaced sequentially by a woodland and pine forest. The woodland is dominated by juniper and pinyon, small patches of which can also be found on the south crater rim. The understory of the woodland is composed of grasses and shrubs. The pine forest is dominated by Ponderosa Pine at lower elevations and a mixture of Douglas-fir, White-fir, Limber Pine, and Aspen at higher elevations. Spruce-bearing conifer forests and alpine tundra occur at the highest elevations in the San Francisco Peaks, ~60 to 70 km northwest of the crater.

At the time of impact, these vegetation zones were shifted to lower elevations, because of climatic conditions during the interstadial. Pollen deposited in lake sediments throughout the region suggested woodlands may have been established near the crater and possibly at the impact site (Kring, 1997). Efforts to improve this floral reconstruction continue and have benefitted greatly from the expertise of Owen Davis, who is one of the leading palynologists in the American southwest. In a preliminary study (Davis and Kring, 2002), lake sediment deposited on top of the impact breccia lens was recovered ~30 m beneath the crater floor. Davis' pollen analysis confirms the climate favored the types of forests now restricted to the highlands of the Flagstaff area. However, the concentration and diversity of the pollen is low and dominated by wind-dispersed pollen types, suggesting long-distance transport and locally sparse vegetation at the crater. The impact may have occurred in a sagebrush community, bordered by a narrow woodland that transitioned to pine and spruce forests over short distances (Fig. 12.2).

The surrounding sagebrush steppe, woodland, and forest terrains were populated with mammoths, mastodons, large ground sloths, tapirs, bison, camels, and horses (Kring, 1997). Mammoths grazed on sagebrush and related vegetation, so they may have been in the immediate vicinity of the impact. They also migrated into nearby spruce forests. Mastodons preferred to browse in spruce forests, pine forests, and woodlands. Large ground sloths preferred to graze and browse in sagebrush and open woodlands, along with bison and camels.

In this type of environment, the most destructive components of the impact event were ejected debris, a fireball, a radiating shock wave, and a closely related air blast. These effects were confined to

the region. A small amount of seismic energy was generated and small amounts of climatically-active gases (*e.g.*, CO, CO₂, SO₂ and/or SO₃, H₂O, Cl, and Br) were released, but of little consequence.

The magnitude and radial extent of a radiating shock wave and air blast depends on the energy of the impact event. (It also depends on the trajectory, but that issue will be discussed separately.) At the time of Kring's initial study, Roddy and Shoemaker (1995) estimated the impact energy was equivalent to 20 to 40 MT of TNT. As discussed in Chapter 10, more recent calculations suggest lower energies. For purposes of discussion on the field trip, some of the effects are illustrated (Fig. 12.3) for a 20 MT blast, with the caveat that smaller radii may apply to the effects if lower impact energies are appropriate.

We do not yet know if the impact occurred during the day or night. Nonetheless, a relatively pastoral scene was disrupted when an iron asteroid came hurtling through the atmosphere. The meteor would have split the sky along a bright path of light before slamming into the ground. Plants and animals at ground zero were vaporized, while most of the asteroid and some of the underlying bedrock were obliterated. Bedrock below and around the vapor-melt zone was then ejected and overturned, burying the topography and any plants and animals not already swept away by an air blast.

The collision generated a shock wave, as described previously in Chapter 3. In addition to radiating into target bedrock and the asteroid, a shock wave radiated across the landscape. This created dramatic overpressures. It also generated an air blast. These winds were in excess of 1000 km/hr in the vicinity of the impact event (Fig. 12.3) and decreased with distance. The winds severely damaged trees in any forested area within a diameter of 32 km. Grass, small shrubs, and soil were probably stripped from the area near the crater by these high velocity winds. A small amount of material can potentially have been trapped beneath the overturned ejecta, because roots in soil were preserved in a similar position around the Sedan nuclear explosion crater (Carlson and Roberts, 1963). I have not yet found, however, any material sandwiched in Moenkopi hinges along the crater wall or in drill samples that penetrated that contact beneath the ejecta blanket. Shock overpressure and wind velocity diminished with distance, falling from 2200 km/hr at a radial distance of 3 km to 800 km/hr at a radial distance of 6 km, but remaining fairly large for distances approaching 30 km. Throughout a circular region up to 32 km in diameter, the large mammals described above would have been killed or wounded by the pressure pulse and air blast. Some of the injuries would have been directly caused by the pressure pulse. For example, it would have caused rapid pressure oscillations in air-containing organs and damaged areas between tissues of different densities (*e.g.*, near joints). This would have generated hemorrhaging and edema in the lungs that caused suffocation, air emboli that may have obstructed blood vessels in the heart and brain, and fibrin emboli in the blood that may have damaged the brain and other organs. In addition to these direct blast injuries, animals would have been injured when the blast wave hit them, accelerated their bodies to velocities on the order of a few to tens of kilometers per hour, and then slammed them back onto the ground or they collided with other objects. The air blast also picked up broken branches, rocks, and other types of missiles that created an fusillade of debris that impaled, lacerated, or otherwise traumatized animals.

These are the effects of the impact and crater-excavating blast. Additional damage was created by the ballistic shock wave. Because we do not yet know the trajectory of the object (Chapter 9), these effects are more difficult to quantify. However, it is likely that a ballistic shock expanded the region affected by many of the processes described above.

As far as we can tell, the northern Arizona impact was not witnessed by or involved any humans in the region. (It is more likely that the Gold Basin event was witnessed, because it occurred ~15 ka.) If a similar size impact were to occur over a modern city, however, that city would largely be destroyed. As an example, the effects above have been mapped to Kansas City (Kring, 1997).

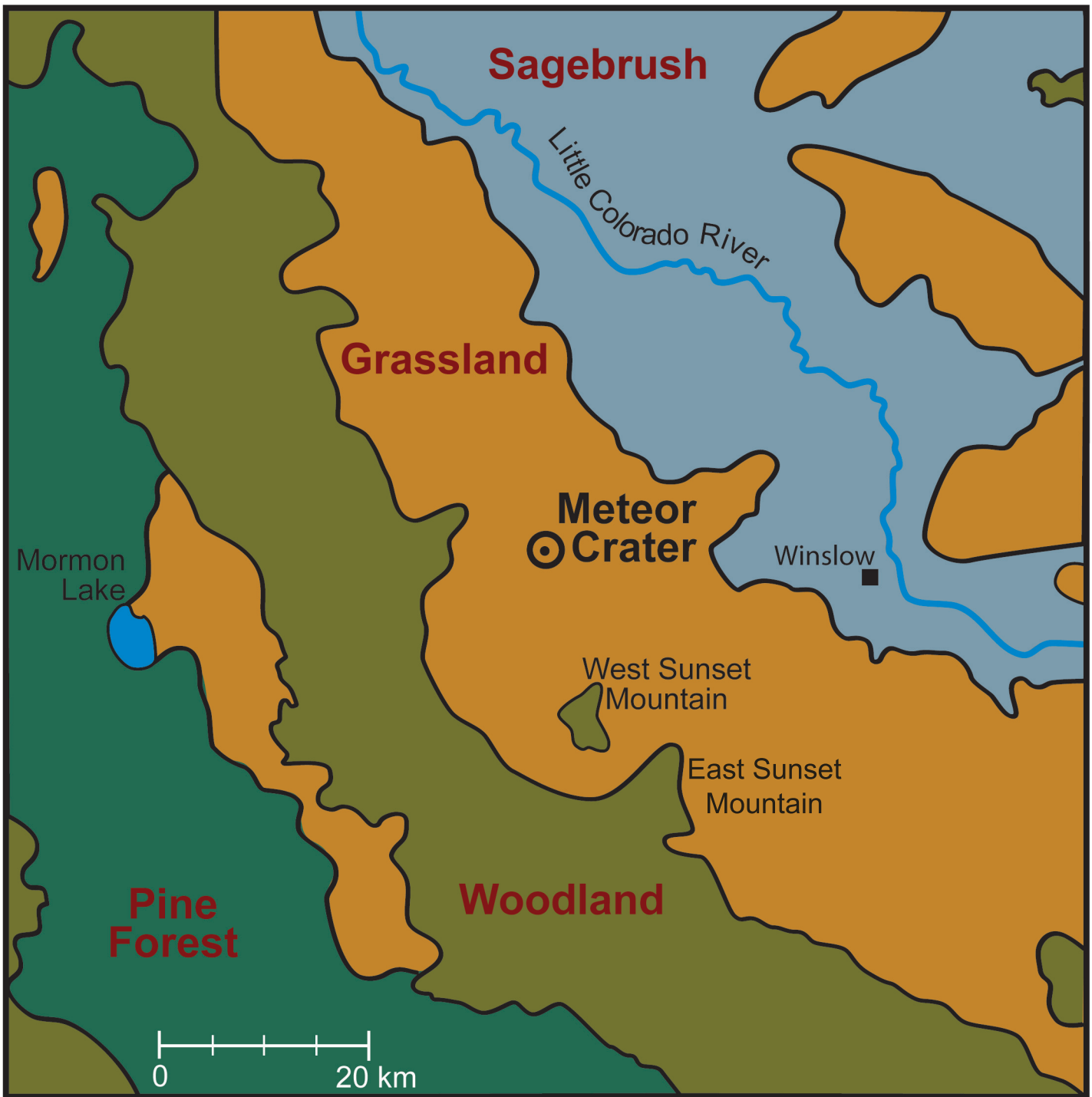


Fig. 12.1. Map showing the distribution of biotic communities in the area around Meteor Crater today. The zones of sagebrush, grassland, woodland, and pine forest are extracted from a map of southwestern biotic communities by Brown and Lowe (1980). This is a slightly simplified and colorized version of a map that appeared in Kring (1997), which should be consulted for additional details about the vegetation in the immediate vicinity of the crater.

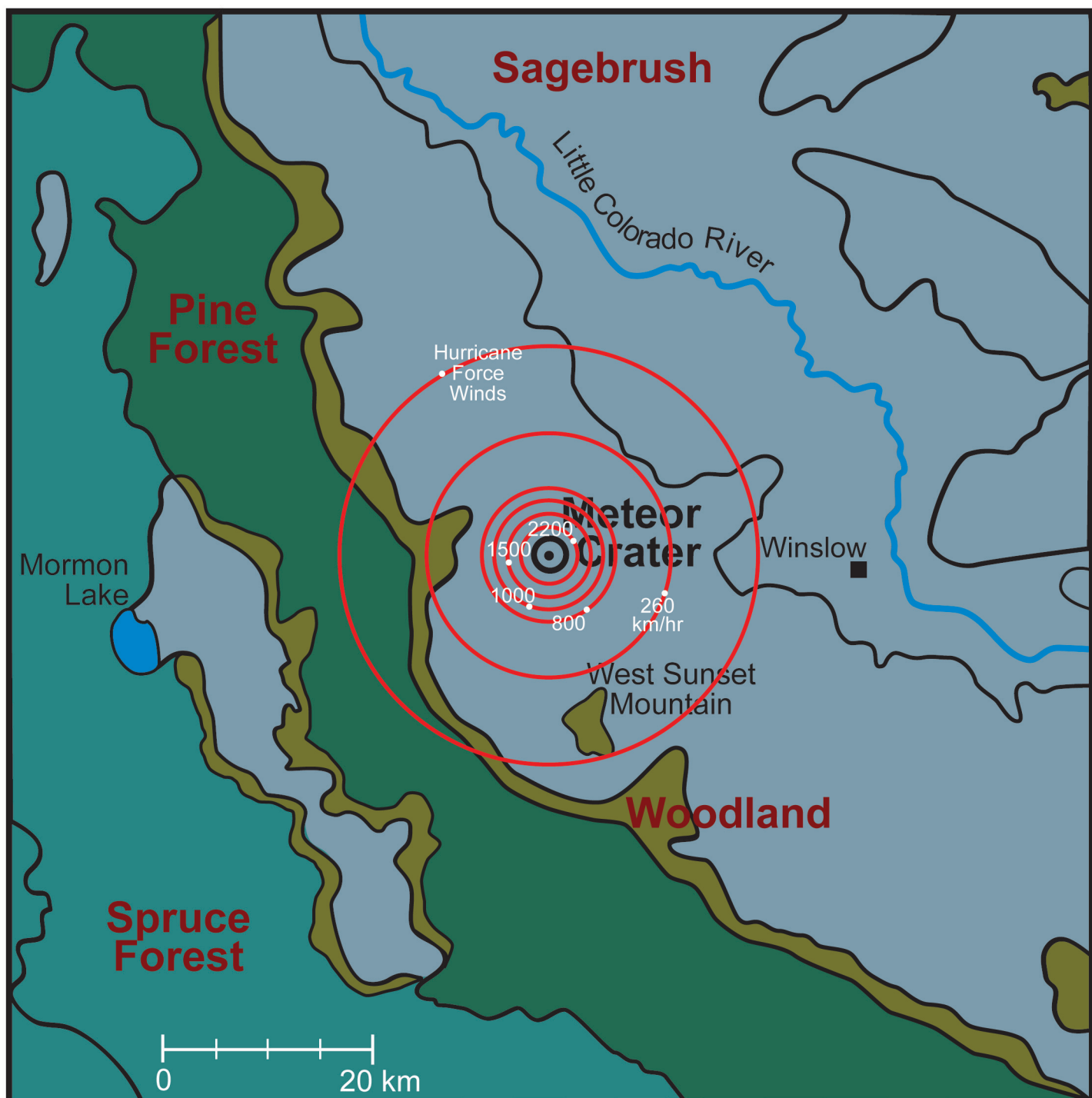


Fig. 12.2. A preliminary palynological study of sediments deposited immediately on top of the mixed debris unit on the floor of the crater has been used to reconstruct the vegetation zones that may have existed at the time of impact ~50,000 years ago (Davis and Kring, 2002). The climate at the time of impact favored the types of forests that are now restricted to the highlands of the Flagstaff area (Kring, 1997). The concentration and diversity of the pollen in the crater sediment is low and dominated by wind-dispersed pollen types, suggesting long-distance transport and locally sparse vegetation at the crater (Owen Davis, personal communication). Thus, upland vegetation near the crater was probably a conifer groveland, with stands of pine, spruce, and fir scattered along a sagebrush steppe. In contrast to a previous reconstruction (Kring, 1997), the new data suggest forests were a few kilometers west of the crater, rather than in the immediate vicinity of the crater at the time of impact. As the new study proceeds, additional samples will be analyzed to further refine our reconstruction of environmental conditions at the time of impact. Also indicated on the map are the wind velocities generated by the impact event, assuming an impact energy of 20 MT. Wind velocities at radial distances of 3, 4, 5, 6, and 12 kilometers were 2200, 1500, 1000, 800, and 260 km/hr (Kring, 1997). Category 3 hurricane-force winds existed at a radial distance of 20 km (outermost red circle). Although not shown, hurricane-force winds extended to a radial distance of 30 km.

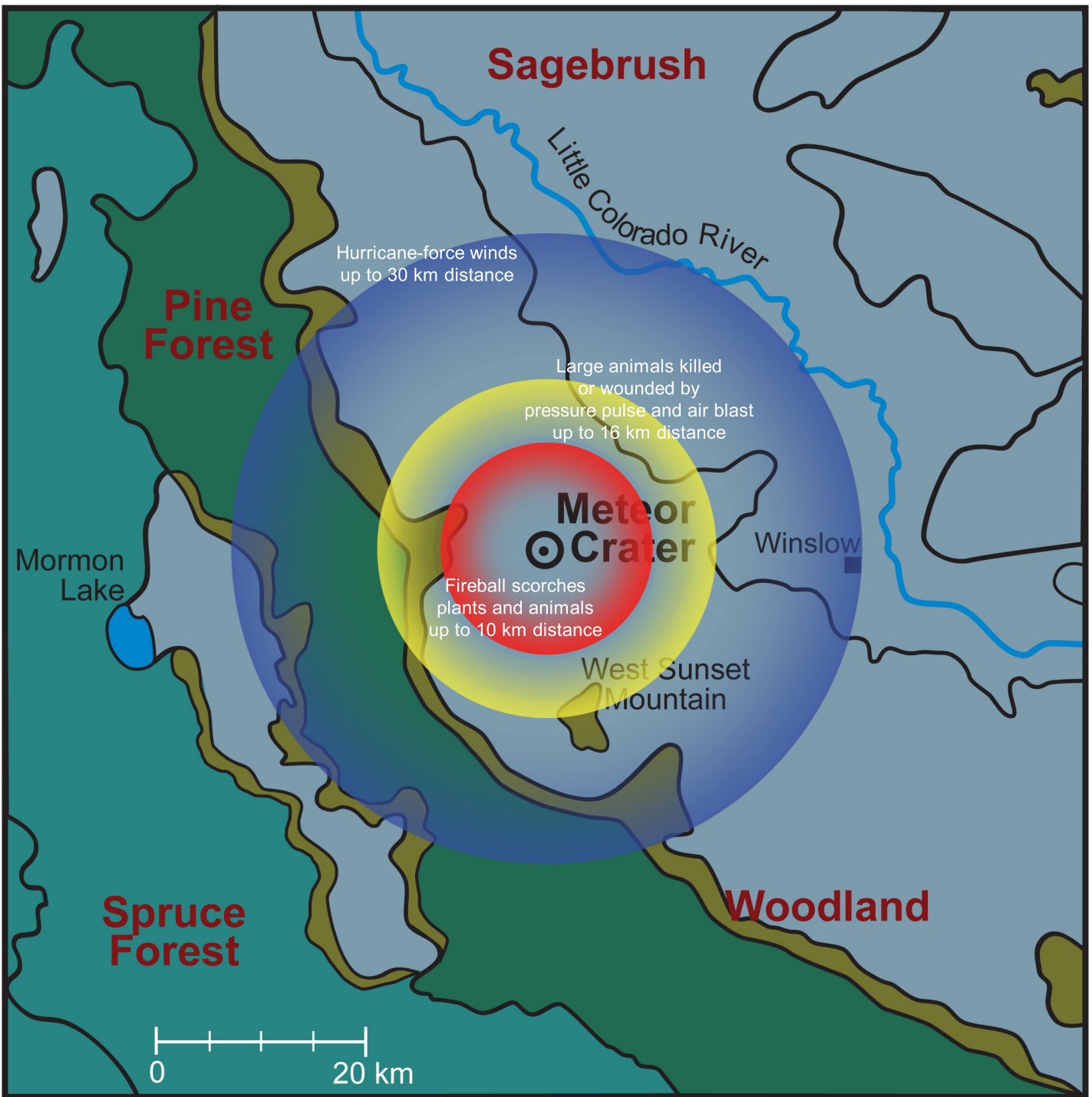


Fig. 12.3. The surrounding sagebrush, woodland, and forest terrains were populated with mammoths, mastodons, large ground sloths, tapirs, bison, camels, and horses. Mammoths grazed on sagebrush and related vegetation, so they may have been in the immediate vicinity of the impact. They also occasionally migrated into spruce forests. Mastodons preferred to browse in spruce forests, pine forests, and woodlands. Large ground sloths preferred to graze and browse in sagebrush and open woodland communities. Similarly, bison and camels migrated through both sagebrush and open woodland communities. Presumably horses did the same, but their distribution 50,000 years ago is less well-known. Shock pressures, wind velocities, and heating were greatest within a few kilometers of the impact. The fireball scorched plants and animals out to a maximum distance of 10 km (red circle). Large animals were killed or wounded by the pressure pulse and air blast out to a distance of 16 km (yellow circle). The air blast decelerated with distance from the crater. The maximum limit of hurricane force winds was 30 km (blue circle). These radial distances assume a 20 MT impact event.

13. Post-impact Lake



Barringer (1905) recognized ~70 ft of lake sediments on the crater floor and reported they contained fresh-water shells and microscopic organisms with siliceous skeletons. Sketchy reports of the lake sediments were included in several other papers about the crater (*e.g.*, Tilghman, 1905; Fairchild, 1907; Merrill, 1908; Barringer, 1910, 1914; and Jakosky *et al.*, 1932), including the work of Shoemaker (1960), who included them in his cross-section of the crater (Fig. 3.4).

The lake sediments indicate climatic conditions were wetter at some point in the past and potentially at the time of the impact. Today the water table is far below the crater floor. In the well for the museum complex, the water table is 186 m deep, which places it about 183 m beneath the average pre-impact surface. Based largely on the presence of lake sediments, Shoemaker and Kieffer (1974) estimated the water table was about 30 m higher at the time of impact, arguing further that the impact occurred during a pluvial period in the late Pleistocene.

They made two important observations: the lake sediments are deposited directly on the fall-out debris unit without any intervening alluvium; and there is a concentration of fragile, pumiceous lechatellierite in those basal lake sediments, as if it floated before being buried. They concluded the lake must have formed immediately after impact. Roddy (1978) concurred, suggesting the water table may have been as much as 43 m higher than it is today to generate a 10 m deep lake. This puts the water table well up into the walls of Coconino and one can envision a ring of artesian fed springs or water falls around the crater. These springs and the lake they created produced a new habitat in the region. They may have also begun to dissect impact breccias on the crater walls. The lake sediments are continuous laterally across the crater floor based on exploration shafts and drilling. They also are stratigraphically continuous, with breaks only composed of volcanic ash. The lake eventually disappeared as climatic conditions became arid and the water table fell. A series of playa deposits were produced during the transition.

I suspect these lake sediments may provide one of the best climatic records on the Colorado Plateau for the late Pleistocene, at least from the time the impact occurred (50 ka?) until the lake disappeared (11 ka?). For that reason, efforts are underway to restore access to the lake sediments in the two surviving shafts in the crater floor. Access will permit detailed sampling of macro- and micro-fauna and the rich stable isotope record that those types of specimens can provide.

Only a small amount of data exists from previous fossil collections and the documentation is poor. Many samples were collected from dumps around the shafts and without reliable stratigraphic control.

One of the most interesting reports was generated by Reger and Batchelder (1971) who re-examined the collection of fossils that Holsinger made for Barringer. They identified the species of molluscs in two shafts (#1 and #3), a pit and cut near Silica Hill, and drill hole number 28. They separated the molluscs into groups that inhabit terrestrial, fluctuating water, and perennial water environments. Molluscs that favor perennial water habitats were found at all stratigraphic depths, including the deepest level analyzed (73 ft in Shaft #3).

Another interesting report, albeit brief (3 paragraphs) was written by Forester (1987). He received a collection of lake sediments from Shoemaker, who is said to have collected them from the wall of one of the shafts. Unfortunately, no details about sample depths or sample density is available, nor do we even know if more than one shaft was sampled. Nonetheless, he tried to reconstruct the evolution of the lacustrine system based on available material. The samples contain a diverse assemblage of ostracodes (19 species) and diatoms. One sample also contained benthic foraminifera. He suggests that the earliest

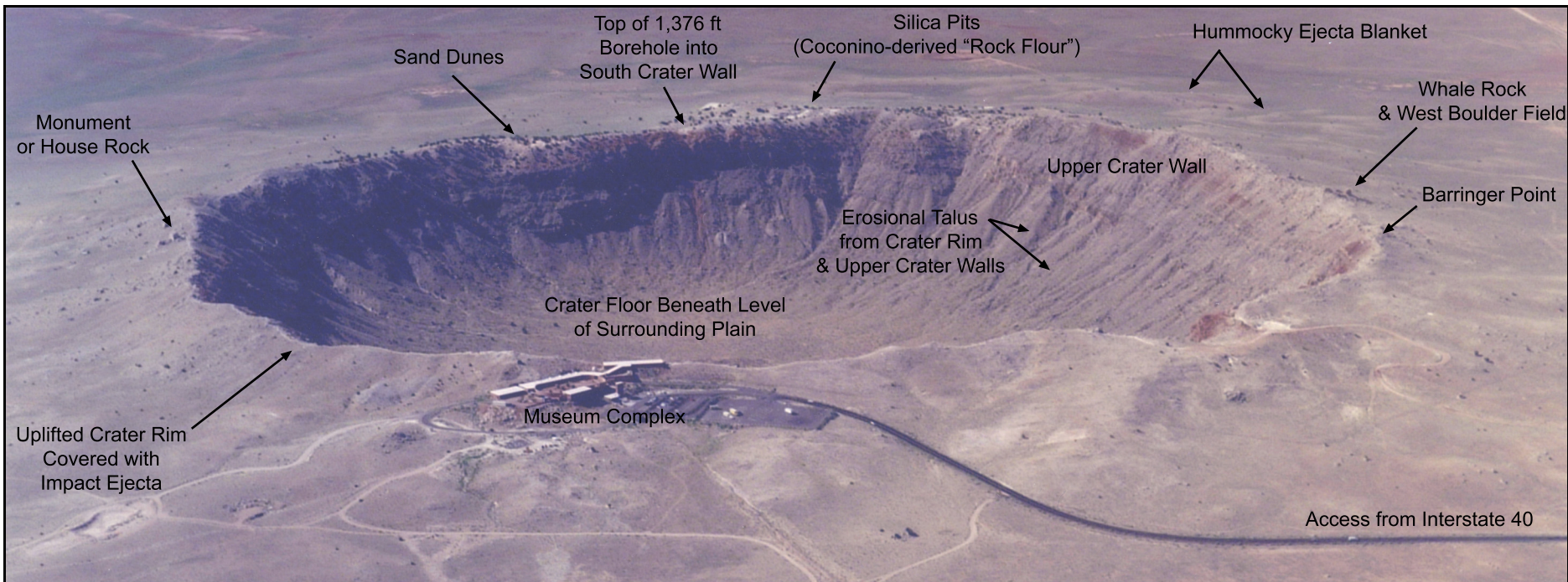
ostracodes are consistent with a saline lacustrine or spring environment, from which he infers the system was shallow. The water freshened resulting in a truly freshwater lake that hosted ostracodes that prefer cold water. He envisions the lake was fed by freshwater springs or seeps around the perimeter. The next ostracode assemblage is dominated by species that only inhabit freshwater springs or seeps, from which he suggests the lake had evolved into a marsh. This assemblage was eventually extinguished, when conditions became too arid to support any aquatic activity and, instead, transitioned to a dry playa environment.

It is unfortunate that the sample suite is not tied to the stratigraphy of the lake sediments. Taken at face value, the first assemblage suggests a lower water table than that inferred by Shoemaker and Kieffer (1974) and Roddy (1978). It is also seemingly inconsistent with the observations of Reger and Batchelder (1971). Because of the uncertainties involved in existing data and the importance of the issues involved, a new set of samples with good stratigraphic control is clearly needed. In addition, any new sampling should be coordinated with a large number of investigators to ensure that all fauna and flora in the samples are studied and integrated together to provide the best environmental and climatic reconstruction possible. A nascent team has been assembled, but we are still trying to secure funds to re-crib Shaft #2 and the Main Shaft so that the appropriate samples can be collected.

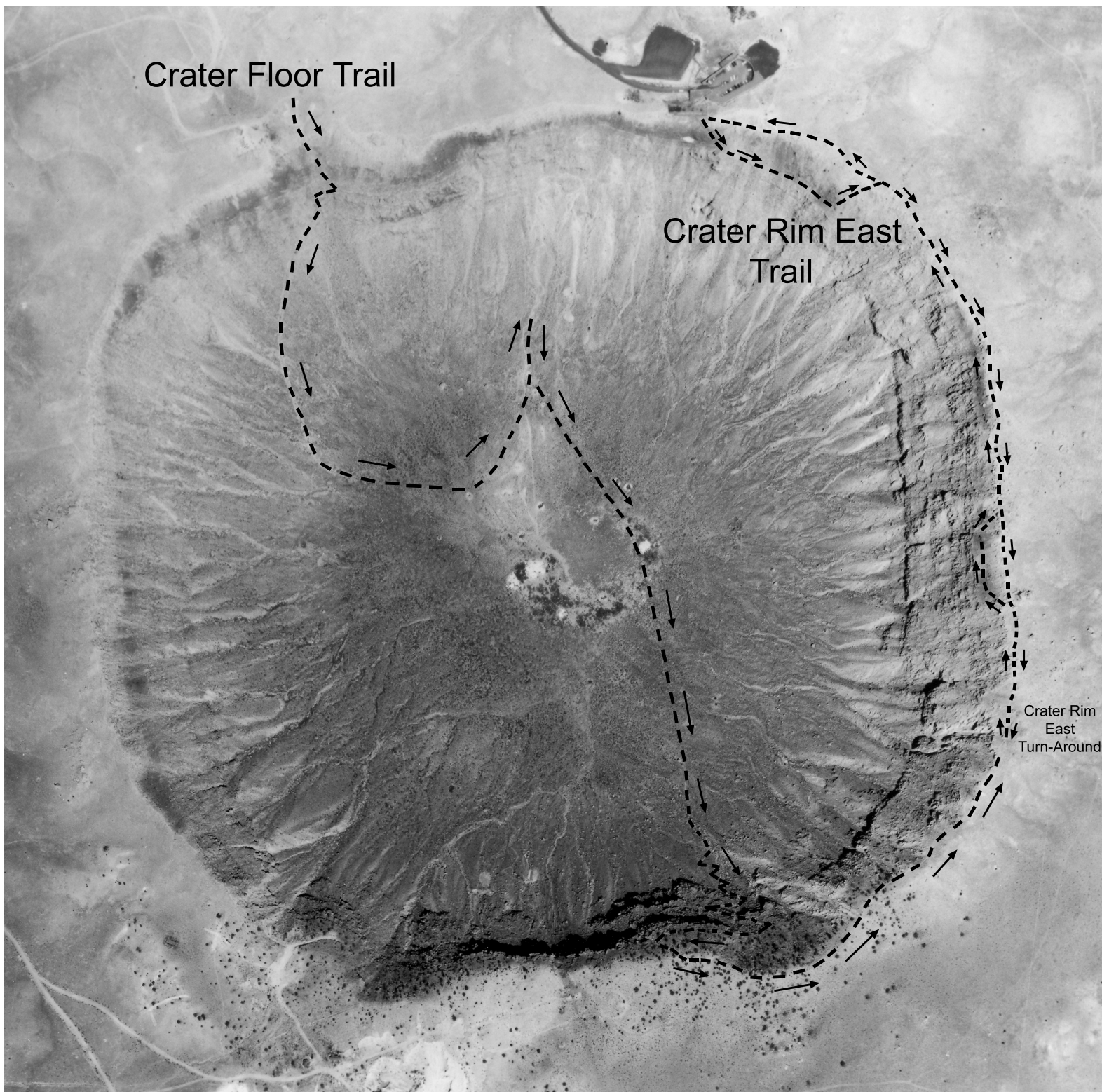
Trail Guides

Crater Rim East

Crater Floor



Aerial view of Meteor Crater with some of its features labeled. Photograph is provided courtesy of Meteor Crater Enterprises.



Trail Guide Routes

14. Trail Guide 1: Crater Rim East



We begin our excursion along a paved trail that leads to the museum's overlook platform. Walk down that trail and pause before walking out onto the platform. The bedrock adjacent to the paved trail is red Moenkopi siltstone. It has been uplifted from its pre-impact horizontal configuration. Moenkopi a few meters farther up the slope has been overturned and forms the base of the impact ejecta or debris unit. Overturned Kaibab debris rests on top of the Moenkopi debris. The precise location of the axis of the fold will be obscure here. We will revisit this overturned sequence at several other locations along the east wall of the crater.

With permission of crater staff, we will step from the paved trail onto the Moenkopi and then follow a faint trail (the Astronaut Trail), proceeding roughly east along this portion of the crater's north rim. The path drops down into the Alpha Member of the Kaibab Formation where we will have our first stop.

Crater Stratigraphy

Before taking a closer look at the rock beneath our feet, it will be useful to examine the crater stratigraphy in a dramatic exposure in the southern cliffs of the crater (Fig. 14.1). The basal Kaibab (or Gamma Mbr) outcrops as a cliff-forming unit immediately above lower, talus-covered slopes in the crater wall. The Gamma Mbr is a medium- to thick-bedded sandy dolomite that is normally gray to buff yellow in color. The cliff, however, is stained. A moderately bright red stain comes from the overlying Moenkopi. A dark, nearly black stain also coats large sections of the cliff-face. Although not visible from this vantage point, a small patch of the Toroweap Fm can be found in a cave at the base of the Gamma Mbr. Pleistocene talus and a small amount of mining debris covers the Gamma Mbr and Toroweap Fm to the right (west) of the cave.

The uneven slope above the Gamma Mbr is produced by the Beta Mbr of the Kaibab Formation. It is composed of sandy dolomite that does not outcrop around the crater as well as the underlying Gamma and overlying Alpha Mbrs. This tendency to be a poorly-outcropping and slope-forming unit can be seen particularly well on the slope with a stripe of red drilling mud.

The sharp, cliff-forming unit above the Beta Mbr is the Alpha Mbr. This unit is dominated by medium- to thick-bedded sandy dolomite at its base and an interbedded sequence of medium-bedded dolomite and sandstone at the top. A key marker bed within the Alpha Mbr is a 2-m-thick white sandstone, which Shoemaker traced around the crater and used extensively when identifying fault displacements in the crater wall. It is not the only sandstone horizon in the Alpha Mbr, however.

Although historically called the Kaibab Limestone, the formation is better described as a dolomite or interbedded sequence of sandy dolomites and sandstones. The entire formation is ~80 m thick in the crater walls. I refer readers to Chapter 2 for additional details.

Above the Kaibab is the red Moenkopi Formation. The basal Wupatki Mbr outcrops in relatively massive orbicular knobs and ledges. That unit is covered by a more fissile Moqui Mbr. There is also a very thin, ~30 cm-thick section of fissile Moenkopi at the base of the Wupatki Mbr, although it is not always visible in outcrop. These units formed the eroded, and, thus, uneven pre-impact surface. For that reason, they are not the same thickness in all locations around the crater, although they can be traced continuously along most of the southern crater wall. Additional details of these units can be found in Chapter 2.

Above this pre-impact stratigraphic sequence is a thick deposit of impact ejecta composed of Moenkopi, Kaibab, Toroweap, and Coconino. We will be taking a closer look at those units later in the field excursion.

Museum or Moon Mountain Anticline

The uppermost Kaibab unit in the walls of the crater is chaotic, irregular, and, in places, missing. Here one will find a dolomitic sandstone with individual sandstone and sandy dolomite clasts in a bed about 1 m thick. Shoemaker and Kieffer (1974) interpreted this to be a residual deposit formed on a karst surface. That is, it formed by partial solution of the Kaibab over a fairly long period of time. The unit is sometimes called the “leached Kaibab” unit. Below the unit is an ~4 meter-thick sequence of medium-bedded sandy dolomite, sandstone, and minor limestone. Below that interval is an important marker bed at the crater: the yellow vuggy dolomite. This unit can easily be traced around the uplifted crater walls and found in overturned ejecta debris.

In front of us (Fig. 14.2), two thrust faults cut through the Alpha Mbr, duplicating part of the section and enhancing the uplift of the crater rim. The yellow vuggy dolomite marker bed in the lower plate of the thrust plane is in contact with a duplicate of the same bed in the overlying plate. Fault gouge can be found along the thrust fault, particularly on the west (or left) side of the exposure in Fig. 14.2. The thickness of the gouge is variable, but ranges up to 15 cm thick. The contact is also covered in some places. Farther to the east, the fault and the yellow vuggy dolomite marker bed bend sharply and angle downward. These beds of the Alpha Mbr are arched over a wedge of additional Alpha Mbr rock about 15 m across. This wedge was thrust outward from the center of the crater during crater excavation and crater wall uplift. Shoemaker measured a 30° outward dip on the crest of the arch and estimated ~45° dip on the fault. He also measured 2 m of Kaibab that was repeated in the section, implying ~5 m of throw on the fault.

These types of faults occur in several locations around the crater, in both the Alpha and Beta Mbrs of the Kaibab, and are responsible for a significant portion of crater rim uplift. Shoemaker noted them on the west and north sides. Examples also occur on the east side. Multiple thrusts occur beneath the highest anticlines around the crater, which remain the topographical high-points on the crater rim, such as the northwest corner of the crater (*e.g.*, Barringer Point). The thrusts are often small (as here), but occur multiple times, producing a cumulative effect. Bedding within the Kaibab (particular the Beta Mbr) is often indistinct, so the amount of bedding repetition cannot always be measured quantitatively. Nonetheless, most of the uplift in the largest anticlines appears to be a direct consequence of the thrusts. Shoemaker suggested that the concentration of these thrusts to the northwest suggests the trajectory of the projectile may have been moving from southeast to northwest. I concur, although we are also studying other structural indicators to further test the trajectory.

If we turn around, a thrust fault can be followed down the crater wall to the west, passing beneath a prominent dolomite outcrop, from where it continues to a point beneath the observation platform (Fig. 14.3). Also visible in this section is the white marker sandstone in the middle of the Alpha Mbr of the Kaibab Fm and the yellow vuggy dolomite near the top of the Alpha Mbr of the Kaibab Fm. These previously horizontal units have been sharply uplifted in the walls of the crater and now dip outward. If the field party is small, it can follow the thrust fault to the west and peer beneath the observation deck. Erosion along the thrust fault has formed a chute. If the field party is large, this extra view should probably be avoided.

Next, we want to return to our trek to the east. Follow the trail, which should stay above a small section of near-vertical outcrops within the Alpha Mbr of the Kaibab. The trail will pass into a section of

Moenkopi that tracks across and diagonally down the crater wall (Fig. 14.4). We will stop here to discuss the Moenkopi.

Identifying Overturned Bedrock in the Crater Rim

As discussed in Chapter 2, Moenkopi siltstone was deposited in a coastal environment that was constantly being processed by water currents and wind. This generated cross-bedded laminae that can be used to separate uplifted strata and overturned strata. Normally-bedded units will be sitting on top of Kaibab-Alpha. Somewhere up-slope, those units are overturned and duplicated. We will use the cross-bedded laminae to identify that point.

Begin by examining large blocks of Moenkopi near the contact with the Kaibab-Alpha. The top of many cross-bed sets will be sharply truncated, typically at an angle of ~30° (see Fig. 2.4d for an example). At the base of these sets, however, the cross-bedded laminae are truncated at very shallow angles, typically less than 5°. The laminae will appear to tangentially or asymptotically approach the base of the set. The distinct difference between the base and top of a cross-bed set can be used to identify units that are oriented normally or overturned. A schematic illustration of these features and their relationship to parental dunes is also provided (Fig. 14.5).

I invite the group to migrate across the slope, moving increasingly upward in section, to study the cross-bedded laminae and identify the level where blocks have been overturned.

Not all blocks will have an unambiguous indicator of orientation. Some blocks of Moenkopi may have, for example, horizontal rather than cross-bedded laminae. In addition, some blocks have rotated and shifted slightly downhill, obscuring their original orientations. Nonetheless, with careful scrutiny, the duplicated and overturned sequence of the Moenkopi on this portion of the upper crater wall is identifiable.

After locating the overturned section of Moenkopi, follow the Moenkopi across the slope to the east with your eyes. You will see that the trace of Moenkopi disappears. It is replaced by yellow to buff-colored Kaibab. The Moenkopi in that section of crater wall is at a much higher elevation near the top of the crater rim. The jump from Moenkopi to Kaibab in this section of the crater wall was created by differential uplift along a tear fault. Shoemaker (1960) and Roddy (1978) argued that these tear faults formed along pre-existing sets of joints that are particularly prominent in the Kaibab and accentuated by dissolution along those joints.

Additional faults can be seen from this location along the east crater wall (Fig. 14.6). The relative structural displacements can best be seen by following the cliff-forming Kaibab-Gamma unit. The displacements are modest along the crater wall, but dramatic in the southeast corner of the crater where another large tear fault (or, rather, a complex set of tear faults) was produced during crater formation. The additional uplift generated on the north side of this tear fault provides the best exposure of the Toroweap and Coconino Fms in the entire crater. As the excursion proceeds, we will hike above those faults and it will be evident that they are easily eroded and an important structural source for major gully formation in the crater walls.

From this vantage point, we can also glimpse the path we will be taking along the remainder of our excursion (Fig. 14.7). We will be walking along the east rim of the crater. Similar outcrops of uplifted Kaibab-Alpha are visible along that portion of the crater wall. Also visible is a particularly large block of Kaibab ejecta called Monument or House rock. We will be visiting that location. We will also hike beyond that point to a location near a gate in a fence line that is visible slightly further to the south. We

will then turn around. Our hike to the southeast will utilize a trail on the rim of the crater. On the return, we will dip down the crater wall again.

From our current position in the field of Moenkopi blocks, the field party should climb up the slope of the crater wall to the crater rim trail that circumnavigates the crater.

If time allows, however, the field party can follow the Moenkopi to the tear fault before climbing to the rim. Exposures indicate the fault is complex, diverging into several sub-parallel faults, particularly as it cuts through the Moenkopi. Where the fault cuts through the Kaibab, gouge is visible in the walls of a ravine that has been eroded deeply into the fault.

Relative displacement on the tear fault along the gully is ~24 m (Shoemaker and Kieffer, 1974). It has juxtaposed the overturned Moenkopi debris layer (this side of fault) against the white marker sandstone in the middle of Kaibab-Alpha (far side of fault). Farther down the slope, it has juxtaposed the upper part of the Kaibab-Alpha (this side of fault) against the upper part of the Kaibab-Beta (far side of fault).

The group still needs to reach the trail on the crater rim before continuing the excursion. From the tear fault, the climb up to the crater rim is very steep and over unstable rock. It may be prudent to return to the Moenkopi boulder field and climb to the rim from that point.

Once on the rim trail, follow it to the southeast along the east wall of the crater.

Traversing Impact Ejecta

This portion of the rim trail weaves over and through blocks of Kaibab that were excavated from the crater. Roddy *et al.* (1975) calculated that 175 million metric tons of rock were deposited on the crater rim and the surrounding landscape. The debris is composed of angular to subangular blocks. The smallest debris components identifiable in the field are millimeter in scale and range to blocks that are several meters in size. Shoemaker and Kieffer (1974) report that the size frequency of this debris follows a classic fragmentation law, such that the cumulative mass of debris is a simple power function of the particle size. The exponent of this power function is such that 50% of the total mass falls in the largest 3 phi intervals. The data, however, appears to be lost. Size frequency data for the smallest size fractions (0.03 to 16 mm or +5 to -4 phi units) of Kaibab and Coconino ejecta were independently gathered by Grant and Schultz (1993). They found modes at 0.074 and 0.21 mm for Kaibab and Coconino samples, respectively, without any identifiable power-law distribution. The mode for this fine fraction of Coconino ejecta is approximately equal to the average grain size in the original Coconino target rock (~0.19 mm; Table 2.1).

A cursory comparison of the size-frequency data at the crater suggests the power law exponent may be different than that for ejecta observed around some experimental explosion craters. For example, less than 25% of the ejecta mass is in the 3 largest phi intervals (smallest grain sizes) at the ~230 m diameter Pre-Schooner II crater (Frandsen, 1967), compared to the 50% reported for Meteor Crater by Shoemaker and Kieffer (1974).

A careful examination of bedding features within the *in situ* Kaibab beds below and the Kaibab debris here on the crater rim can be used to demonstrate that the debris is largely overturned, although we will not take the time to repeat this exercise. It is, however, worth noting that additional rotation of some blocks can produce diverging orientations. We will be discussing other details of the ejecta blanket later in the excursion.

Additional Views of Crater Interior

Approximately mid-way to the fence line in the southeast corner of the crater, it is worthwhile to stop and re-examine the crater interior from this perspective. In the foreground, slightly south of our present position, we see that the Kaibab continues to sandwich red Moenkopi along the east wall of the crater (Fig. 14.8). All three members of the Kaibab are visible below the Moenkopi. The uplifted and outward dipping orientation of those strata are also clearly visible here. Keen-eyed observers may also spy small thrust faults in the Kaibab-Alpha.

Sweeping our gaze around the crater towards the south crater wall, we see that the Kaibab is truncated against a large tear fault (Fig. 14.9). This is the same section we examined earlier from our perspective on the north crater rim (Fig. 14.1 and 14.6). The Kaibab is uplifted much higher on our side of the tear fault. That additional uplift provides the best exposure of the Coconino Fm in the walls of the crater. Beyond the tear fault, all three members of the Kaibab can be traced across the face of the southern cliffs.

Looking across the crater to the west, we see the same simple Kaibab-Moenkopi-ejecta stratigraphic sequence repeated (Fig. 14.10). The lower crater walls are covered with Pleistocene talus, so very little exposure of the Toroweap and Coconino Fms are found there. Barringer Point is the highest point along the crater rim. From this vantage point, the anticlinal nature of that feature and underlying thrusts in the Kaibab-Beta are visible.

Remnants of mining operations are visible on the crater floor. White patches of disturbed debris mark the locations of several shafts and boreholes. The top of the Main Shaft is enclosed in a large fence, as is the nearby Shaft #3. The top of the East Shaft is covered. This shaft was crudely cribbed and has been used in the past for studies of the crater's subsurface. That is, for example, the source of the pollen being used to reconstruct the environment at the time of impact (Chapter 12). Collectively, the shafts reveal that ~30 m of lake sediments sit on top of an impact breccia lens. The breccia lens is ~175 m thick and was produced when the excavation flow stopped and remaining allogenic breccias along the transient crater wall collapsed. At the time of impact, the water table was within the Coconino, so artesian spring flow filled the crater with a small lake. As the climate became arid ~11,000 yrs ago, the lake dried and a small amount of playa sediments were deposited. Silica Hill is a small knoll on the crater floor with the highest level of lake sediments. Shoemaker and Kieffer (1974) hypothesized that the knoll of lake sediments is on top of a topographic high or "central peak" that formed when allogenic breccias collapsed.

Kaibab, Toroweap, and Coconino Ejecta on Crater Rim

In the east-southeast portion of the crater rim, one finds an immense block of uncovered Kaibab ejecta (Fig. 14.11) that Barringer called Monument Rock. The block is often called House Rock today. We approach this boulder from the north. We want to walk past the rock, turn around, and look at it from the south for the best view. While standing next to the rock, it is usually a worthwhile exercise to imagine the energy necessary to excavate it from the crater center, carry it upwards, and deposit it many meters beyond the crater rim. The block, however, is only one among countless numbers of blocks that were excavated, form a blanket of debris that was ~20 m thick on the crater rim, and that stretches from the rim of the crater to distances in excess of a kilometer. The enormity of the energy involved in crater formation often begins to become tangible at this location. This is also a region where some of the most heavily-shocked Canyon Diablo specimens were recovered (e.g., Heymann et al., 1966), including diamond-bearing meteorites that Nininger (1956) and Moore et al. (1967) found to be concentrated on the crater rim and virtually absent on the distant plains. See Chapter 8 for additional details.

A short distance south of Monument Rock we encounter additional mounds of impact debris (Fig. 14.12). The character of the debris changes, however. The trail crosses or passes adjacent to sandstone debris. This is our first encounter with sandstone from the Toroweap and Coconino Fms that underlie the Kaibab Fm. This material was excavated from a pre-impact depth of at least 80 m.

This material, and another patch of sandstone on the north rim, intrigued Barringer and his colleagues with the Standard Iron Company. He describes them as impact-ejected rays of material. He was essentially describing what we know understand to be instabilities that can develop in ejecta blankets, leading to hummocky ejecta blankets and concentrated rays of ejected debris. In some cases, however, a transition from Kaibab to Coconino debris can reflect erosional remnants of ejecta that was deposited on a topographically variable surface that was created by tear faults in the underlying crater walls. A clear map identifying the source of this type of ejecta patchiness has not been developed in past studies. An example of the first source of the patchiness, however, is visible on the north rim. Although we will not visit that locality on this excursion, it is illustrated in Chapter 7 (Fig. 7.3).

Tear Fault in Crater Wall

If we continue south on the rim trail and pass through a gate in the fence line, we encounter additional Toroweap-Coconino ejecta. Toroweap and Coconino lithologies are not easily separated in these deposits and were mapped together by Shoemaker. We will stop near a winch (Fig. 14.14) that was used to haul supplies to and from the crater floor during mining operations. It is a nice historical reminder of original focus of exploration activities at the crater and the impetus for understanding the structure's origins. The winch sits above the tear fault that is responsible for the dramatic off-set in the Kaibab-Gamma Mbr that we viewed from the north and east rims of the crater (Fig. 14.1 and 14.6). A tremendous amount of fault gouge is visible in a ravine below the rim that continues nearly all the way down to the crater floor. The structural complexity of the crater rim along tear faults will also be visible. A number of small faults, one of which may reflect the partial collapse of the crater rim, is visible in the flank of the ravine. A detailed structural map of this section of the crater wall and rim is still needed, with an interpretation of the kinematics implied by those structures.

This is also a useful vantage point for peering again at the northwest "corner" of the crater. That "corner" is also cut by a large tear fault. Slightly west of that tear fault the crater rim rises to Barringer Point. The thrusts in the Kaibab-Beta that underlie the anticline are sometimes easier to see here (Fig. 14.13) than from the stop earlier on our excursion.

From this point, we want to retrace our steps through the gate. When we reach Monument Rock, we will descend the crater wall in a diagonal line towards the north, until we reach outcrops of Moenkopi.

Fold Hinge in Moenkopi

Erosion and the angle of light hitting south-facing slopes makes a study of folds in the overturned rim sequence easier on our return hike. A good example of a hinge within the Moenkopi is visible on the slope north of our position (Fig. 14.15). The Moenkopi core is enveloped by a fold in Kaibab, whose apex is in the sky. Once the hinge has been located, we will walk to it. Please be careful when approaching the hinge. The fissile Moqui shale is fragile and we want to avoid damaging it so that its orientation will be apparent to future visitors. We also do not want to dislodge any of the adjacent blocks of vertical to near-vertical Kaibab limestone.

In the immediate vicinity of the Moenkopi hinge, we can see that the Moqui core is surrounded by

blocks of Wupatki, which is, in turn, surround by blocks of Kaibab-Alpha. As illustrated in a schematic diagram in Chapter 6 (Fig. 6.2), the units are both structurally and stratigraphically overturned.

Hinges in the Moenkopi are not everywhere visible around the crater. Indeed, in some sections of the crater wall, the Moenkopi is not exposed because it lies encased within folded Kaibab. Erosion after the impact has cut into the overturned sequence, however, and occasionally exposed Moenkopi cores. This is illustrated schematically in Fig. 6.4.

Next we want to hike up hill and return to the trail on the crater rim.

Kaibab Ejecta Beyond the Crater Rim

We return to the trail in the midst of a Kaibab boulder field that extends outward from the crater rim towards the surrounding plain (Fig. 14.16). Although this material was visible on the hike out, it is easier to appreciate with the sun behind us.

This is one of two boulder fields that impressed Barringer. The other boulder field sits on the west flank of the crater and contains the charismatic Whale Rock. The symmetry of these boulder fields is one of the reasons he favored a north to south trajectory for the impacting asteroid.

Beyond the immediate boulder field, one can also see isolated mounds of debris that are often pinnacled by a large block of Kaibab (Fig. 14.17). These features accentuate the hummocky topography of the ejecta blanket. In a larger impact event, ejected boulders like those visible will produce secondary craters.

We continue our return trek to the museum along the rim trail.

Fold Hinge in Kaibab

As we begin to turn the “corner” along the crater wall, another fold hinge is visible (Fig. 14.18). In this case, the fold hinge occurs in Kaibab, rather than Moenkopi. Beds on the lower limb of the fold have vertical dips. Tracing those beds around the hinge, they become increasingly overturned. Beds on the top of the slope mirror perfectly the beds on the lower limb and are clearly inverted or upside down. Within the Kaibab fold is a pale red core of Moenkopi. Erosion has barely reached that level, so very little of the Moenkopi is visible. Nonetheless, it nicely illustrates how Moenkopi is sandwiched within the overturned Kaibab sequence.

Breccia Deposits and Pleistocene Talus on Crater Walls

En route to the museum, we will have several opportunities to view the interior face of the crater’s north wall. Breccia deposits and post-impact alluvium are easily seen, particularly when highlighted by shadows in the late afternoon (Fig. 14.19). The upper portion of the crater wall is composed of near vertical cliffs. The lower 2/3 of the wall, however, have a much shallower slope. Those slopes are defined by Pleistocene talus, but they have a core of alloigenic and fall-out breccia. Lechatelierite and meteoritic debris is included within the fall-out breccia. Large blocks of debris that slid with the alloigenic breccias towards the crater floor during the modification stage can also be seen along the crater wall. Authigenic breccias along shear planes within and at the base of those blocks can be found when examined more closely. Ravines with a fairly regular spacing cut through the fall-out and alloigenic

impact breccias. Although that provides for good exposure of the breccias, erosion along the ravines is slowly destroying the deposits.

Hopi Buttes

Before climbing over Moon Mountain and returning to the museum, one has a good view of the Hopi Buttes northeast of the crater (Fig. 14.19). If we begin our scan directly to the east, we are peering towards the Painted Desert, which is dominated by the Chinle Fm, which sits on top of the Moenkopi Fm. Towards the north, sequentially younger Jurassic and Cretaceous strata are found. The highest and most-distant mesas towards the northeast are capped with Cretaceous bedrock, which records the recession of the Cretaceous Seaway that once cut through the middle of North America, connecting the Gulf of Mexico and Arctic Ocean. Many of the mesas and buttes towards the northeast are carved from the sandstones and shales of the Jurassic-Cretaceous sequence. However, a large number of the buttes are, instead, Tertiary diatremes, which are called the Hopi Buttes. These diatremes contain fragments of the mantle, lower crust, middle crust, and the sediments that encompass them, providing a fascinating cross-section of the Earth. Despite the diatremes' similarities to kimberlites in South Africa, they do not contain any diamonds. Those are only found in the shock-metamorphosed specimens of Canyon Diablo found here on the rim of Barringer Crater.

Unfortunately, samples of those meteorites and related shock-metamorphosed target rocks are not found (or no longer found) on the rim of the crater. They are, however, displayed in the museum and I invite everyone to examine them there.

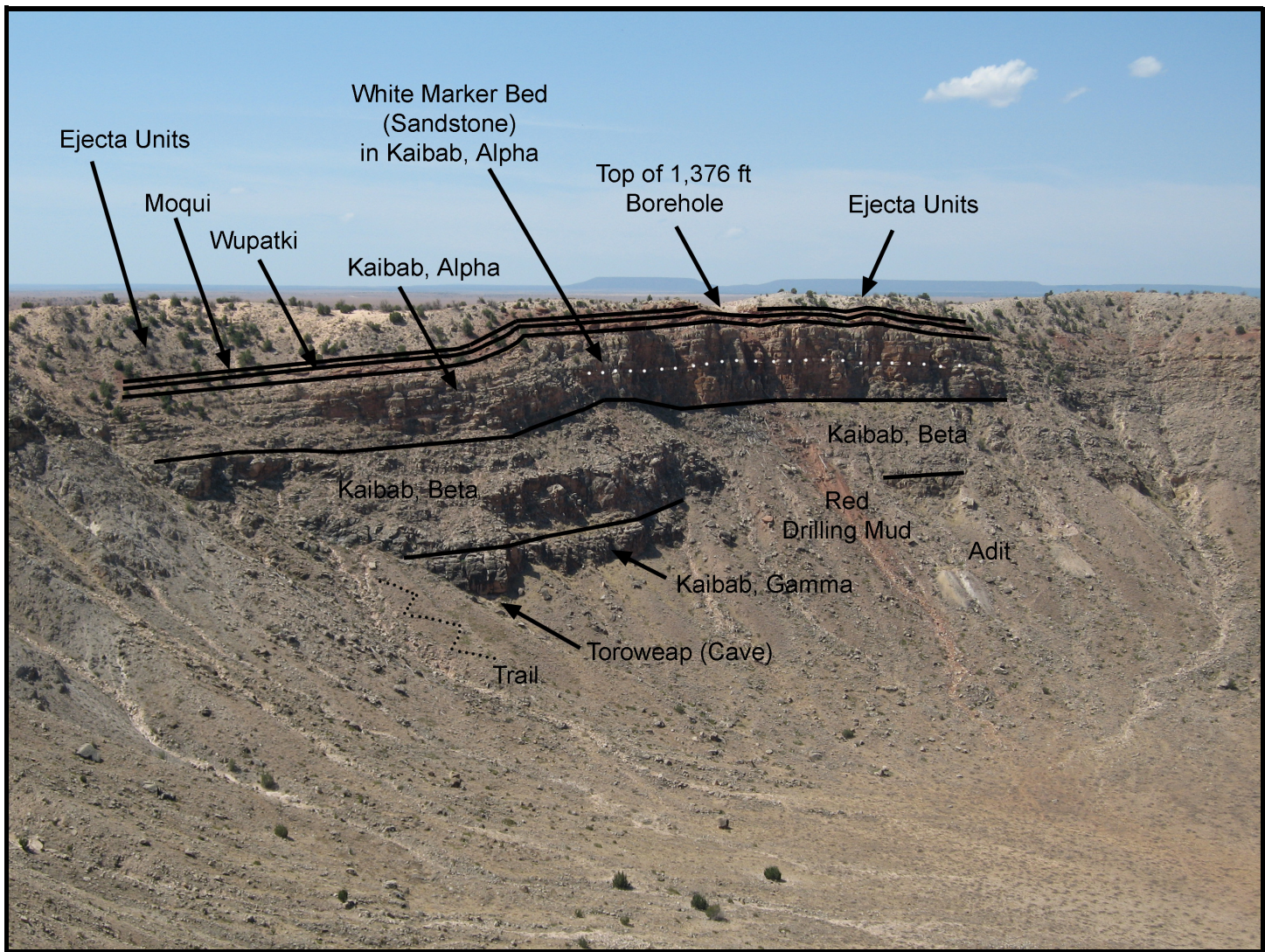


Fig. 14.1. Stratigraphy of the upper crater wall, as viewed towards the south. Target units shown are the Toroweap Fm, Gamma Mbr of the Kaibab Fm, Beta Mbr of the Kaibab Fm, Alpha Mbr of the Kaibab Fm, Wupatki Mbr of the Moenkopi Fm, and Moqui Mbr of the Moenkopi Fm. The Coconino Fm is not visible in this particular exposure (but is visible in the southeast corner of the crater). The position of a white marker sandstone bed in the middle of the Alpha Mbr of the Kaibab Fm is shown with a dotted white line. Ejecta from the target lithologies is visible on top of the Moenkopi beds. Also visible is the top of a 1,376 ft deep borehole through target lithologies on the south side of the crater. That borehole encountered fractured rock with meteoritic debris. See Chapter 3 for details.



Fig. 14.2. Museum or Moon Mountain thrust faults. Thrust faults within the Kaibab-Alpha duplicate part of the section, generating a wedge of material that creates an anticline and additional uplift of the crater rim. The thrust fault can be traced using the yellow vuggy dolomite unit within the Kaibab-Alpha (top panel). The wedge of material injected beneath the anticline is ~15 m across (bottom panel). The thrust fault was mapped by Shoemaker (1960) and described by Shoemaker and Kieffer (1974).



Fig. 14.3. View of outward-dipping beds in the wall of the crater and a thrust fault that cuts across a slope of Kaibab-Alpha towards the west. The yellow vuggy dolomite marker bed is visible in the upper plate (upper right of image) and the white marker sandstone bed is visible in the lower plate (lower center of image). The fault continues beyond the field of view and continues to cut down the slope beneath the observation deck of the museum complex.

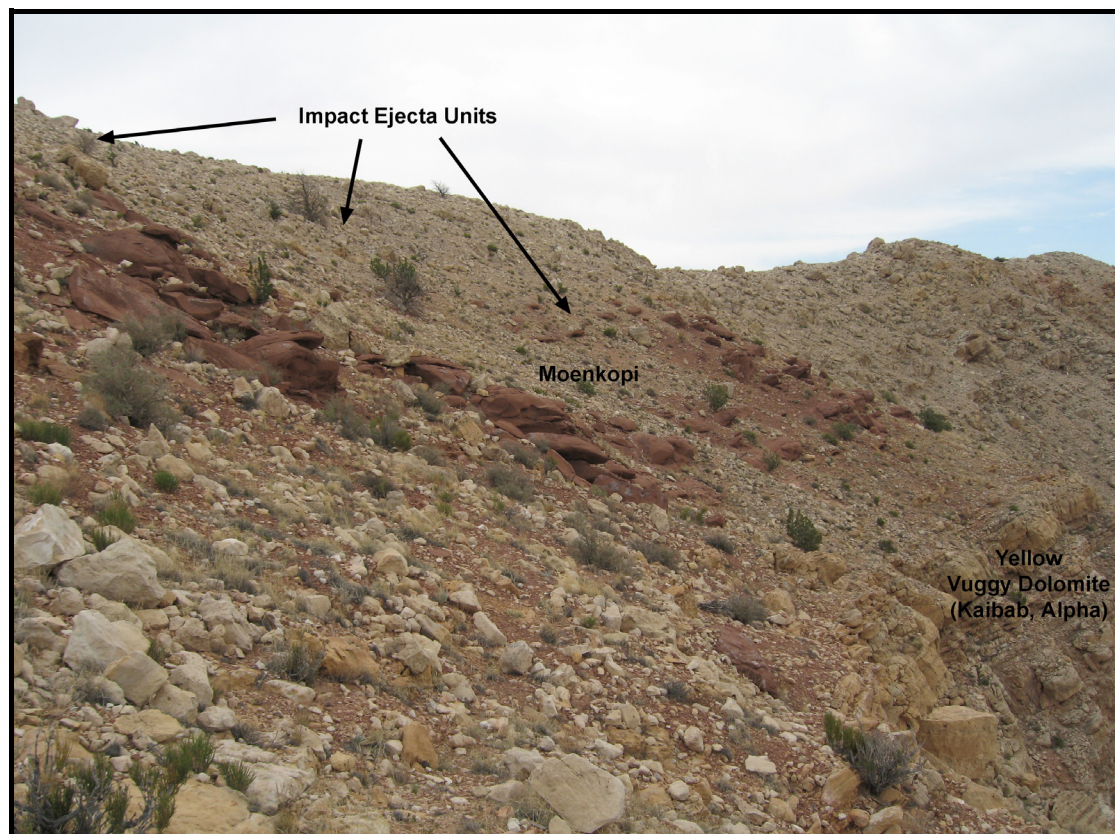


Fig. 14.4. A sequence of Moenkopi units with cross-bedded laminae that can be used to demonstrate the overturned sequence that characterizes the ejecta units at the crater. In this particular view to the east, the stratigraphic sequence begins with normal Kaibab-Alpha (including the yellow vuggy dolomite marker bed), normal Moenkopi, overturned Moenkopi, and overturned Kaibab at the top.

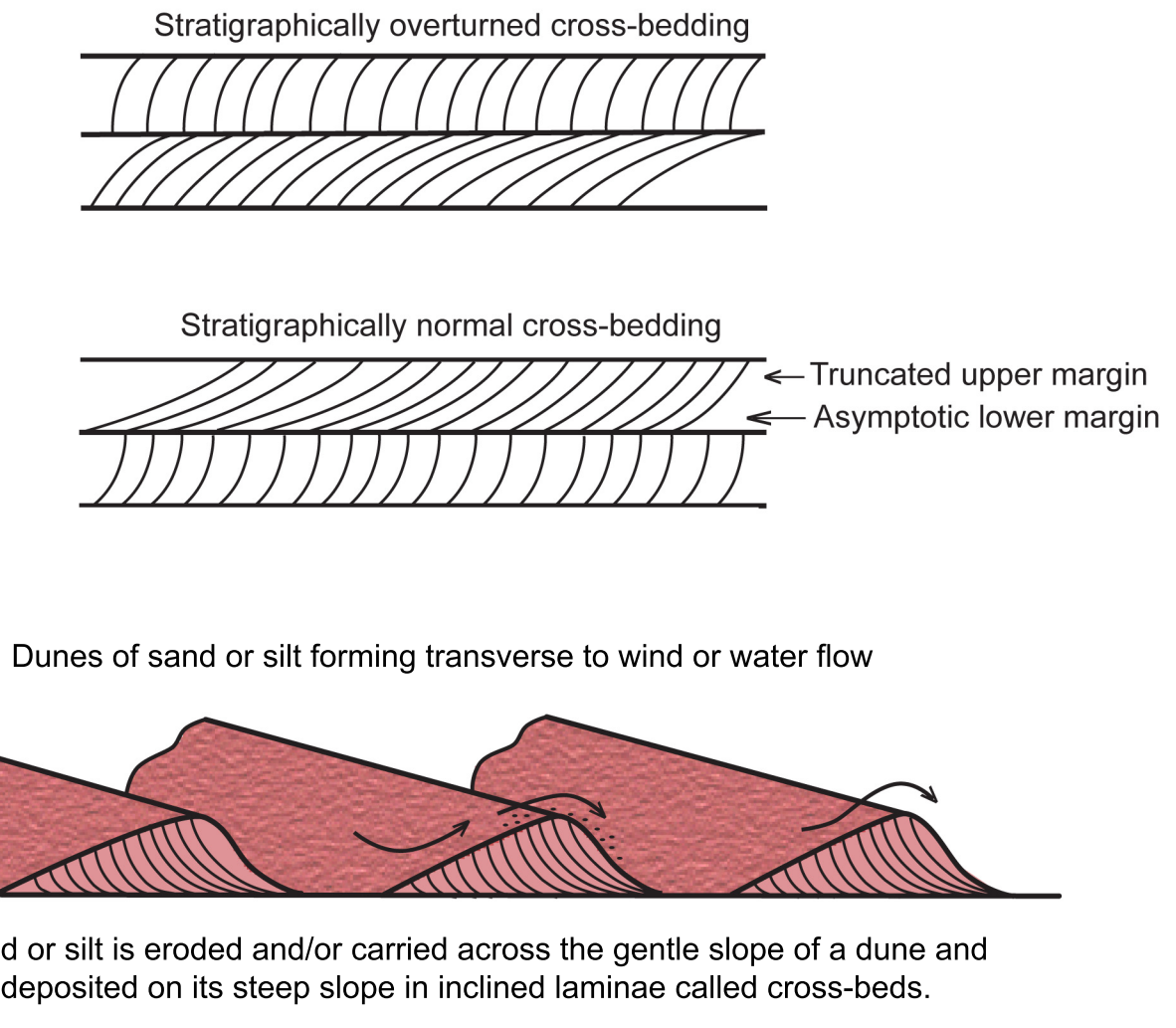


Fig. 14.5. Schematic diagram illustrating the formation of cross-bedded laminae in the Wuptaki Member of the Moenkopi Formation. The geometry of the cross-bedded laminae can be used to determine the orientation of the Moenkopi strata in the rim of Barringer Crater. When the strata are in their normal orientation, the cross-bedded laminae asymptotically approach the lower margin of each set and are truncated at the top of each set. In the overturned part of the crater rim, the truncated margin of a set is below the asymptotic margin. This is an illustration of simple cross-bedding. Within the Moenkopi one can find more complex forms of cross-bedding (like trough cross-bedding), which can also be used to determine the orientation of strata. However, some silt was deposited in higher velocity currents, producing horizontal laminae. In these cases, one has to find other geopetal features (like mud cracks) to determine the orientation of strata.



Fig. 14.6. View towards the southeast corner of the crater. The Gamma Mbr of the Kaibab Fm is outlined to help show tear fault displacements along the east crater wall. A very large displacement occurs in the southeast corner of the crater. On this side of that large tear fault, the Coconino Fm is visible. It is the thickest sequence of Coconino exposed in the crater wall. The crater wall farther to the west (right) is shown in Fig. 14.1.

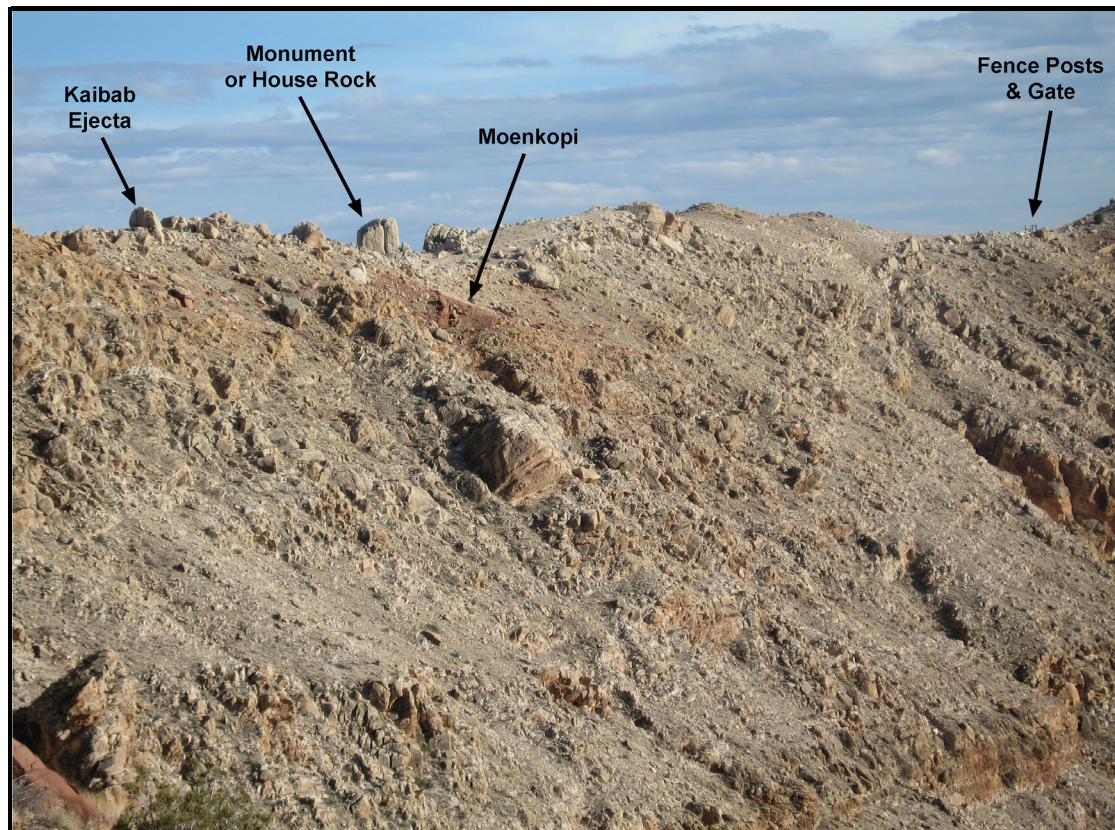


Fig. 14.7. Zooming in on the east rim of the crater, one can spy Monument Rock within a boulder field of Kaibab ejecta that was deposited above normally-bedded and overturned Moenkopi. We will be hiking along the crater rim and will eventually stop within that boulder field. We will then continue towards the south and turn around near the fence posts and gate. We will backtrack along the inner crater wall.

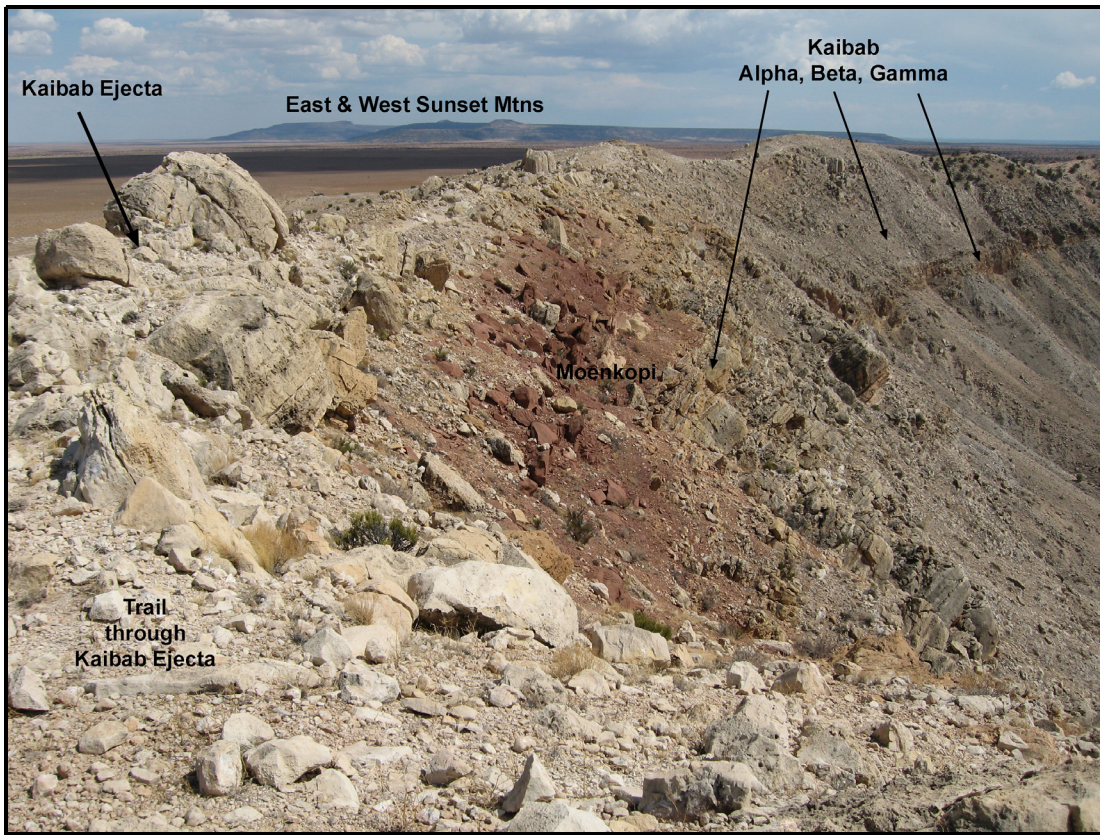


Fig. 14.8. View of upper crater wall from a trail along the rim of the crater. The trail is winding through Kaibab ejecta. Lower on the crater slopes, one can see the outward dipping normally-bedded strata of the Kaibab Fm, including all three members of that formation (Alpha, Beta, and Gamma). If one looks carefully, small thrust faults that thicken the Kaibab sequence will be visible from this location. The bedded and ejected Kaibab units sandwich the red Moenkopi. Farther to the south, the Quaternary volcanics of East and West Sunset Mountains are visible.

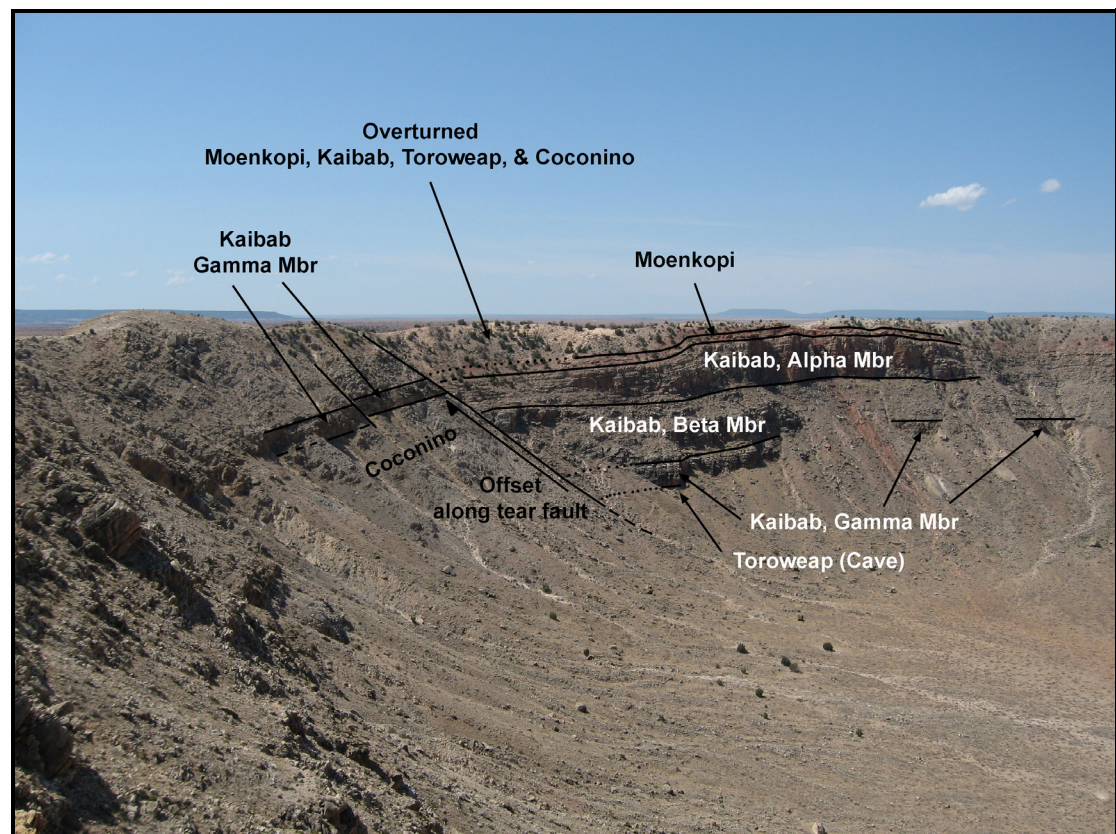


Fig. 14.9. This is a closer view of the stratigraphy and one of the fault displacements that were previously seen in Fig. 14.4 and 14.6. The total displacement along the tear fault is more than 45 m. On this side of the fault, ~90 m of the upper Coconino Fm are exposed.

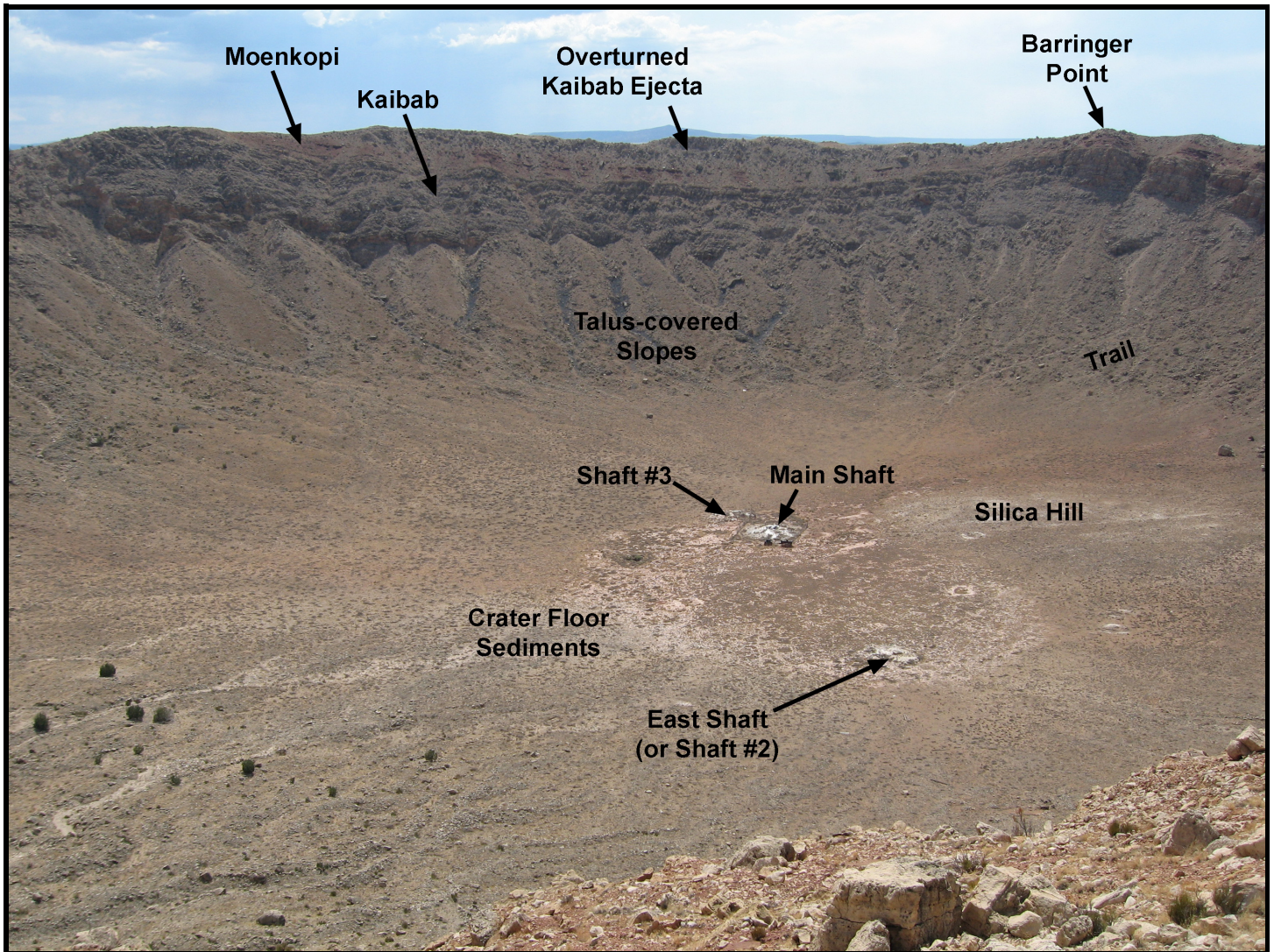


Fig. 14.10. View of the west crater wall and the crater floor from the trail on the east rim of the crater. The stratigraphy of the upper west crater wall is similar to that on the east crater wall. The highest point along the rim of the crater is visible on the horizon. Thrust faults have thickened the Beta Mbr of the Kaibab Fm beneath Barringer Point, creating an anticline. A trail from the northwest crater rim to the crater floor traverses talus-covered slopes. On the floor of the crater, one can see a topographic high (Silica Hill) surrounded by playa sediments. Several exploration shafts were sunk into the crater floor, three of which are identified in the image. The Main Shaft and East Shaft penetrated ~30 m of lake sediments, ~10 m of fall-back breccia, and bottomed in an ~175 m thick alloigenic breccia lens that is dominated by blocks of Coconino sandstone, including one slab with an area of 20,000 square meters.



Fig. 14.11. Monument or House Rock is one of the largest boulders that is visible in the ejecta blanket. It is a large block of Kaibab within a boulder field of ejected Kaibab. A small, dark green tree is growing at the base of the rock in the foreground. Over 7,000 metric tons of rock are exposed in the block above erosional surface at the base of the exposure. This is one of the blocks used to determine a cosmogenic exposure age and, thus, an approximate age for the crater. (See Chapter 11 for details.)

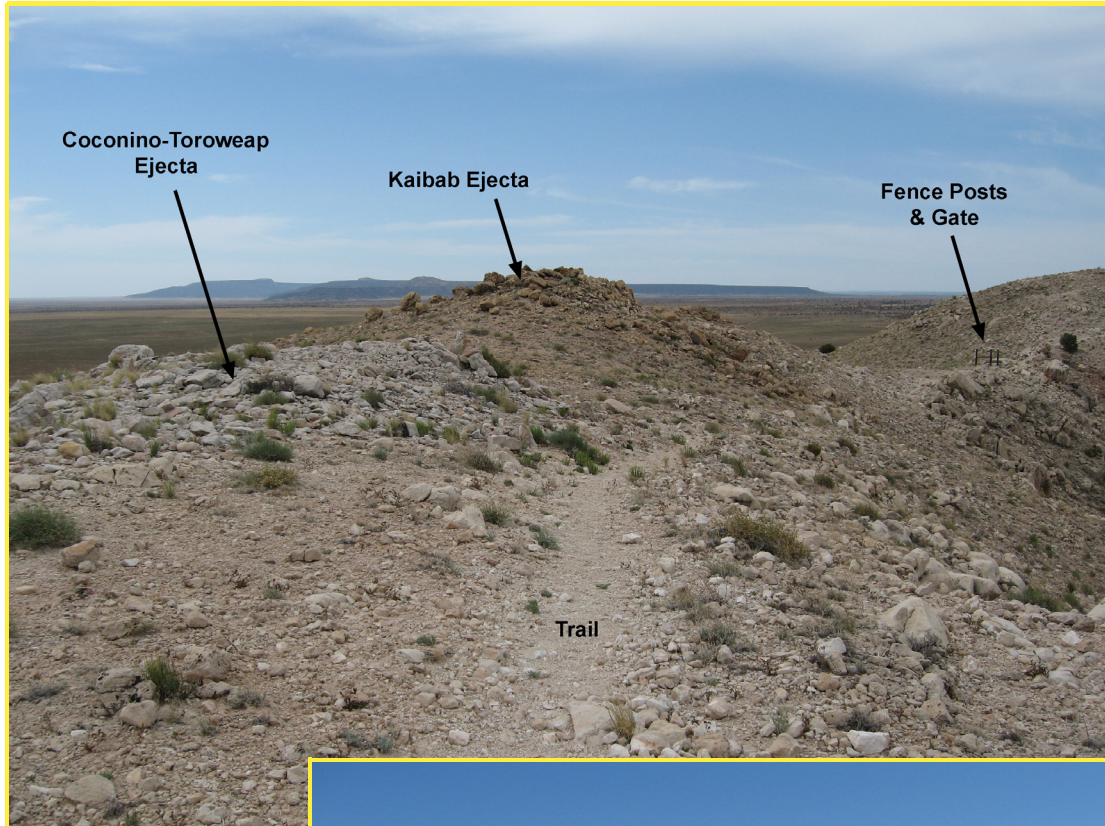


Fig. 14.12. Trailside outcrops of co-mingled Kaibab and Coconino-Toroweap ejecta deposits. The Coconino-Toroweap deposit was first mapped by Barringer (1910) as a ray of debris. There are two potential sources for this type of juxtaposition: (a) Coconino debris fills depressions in a hummocky surface on the ejected Kaibab debris unit (as shown in Fig. 7.3) or (b) material drapes a rim sequence with differential uplift (e.g., on either side of a tear fault), which may be modified further by differential rates of erosion (as shown in Fig. 6.4).



Fig. 14.13. View from southeast crater "corner" of the Barringer Point anticline in the west-northwest portion of the crater wall and rim. Thrust fault(s) within the Kaibab-Beta have thickened that part of the sequence, creating additional uplift of the overlying Kaibab-Alpha, Moenkopi, and ejected debris. Barringer Point is the highest topographic point on the crater rim.



Fig. 14.14. A winch on the crater rim is a reminder of the mining exploration that once occurred at the crater. This winch was probably mule-driven and transported supplies down a slide raised above the rocky crater wall below. The winch is at the top of a large tear fault in the crater wall and rim (which is not visible in the photograph). In the middle distance, one can see blocks and mounds of Kaibab ejecta.



Fig. 14.15. Structurally and stratigraphically overturned Kaibab and Moenkopi, with an exposed hinge within the Moenkopi. Crater center is to left and the ejecta blanket lies beyond the top of the crater rim on the right. As can be seen in the lower left (above), the crater wall rocks have been uplifted so that they have an outward dipping slope. The top of the Kaibab reaches near vertical dips. The hinge within the Kaibab is eroded, but a trace of the fold is indicated with a dashed line. At the upper far right, the Kaibab is overturned. Within that Kaibab fold is a Moenkopi fold. Erosion has exposed the hinge in the Moenkopi fold. The location of the hinge within the overturned rim is shown above and a close-up of that hinge is shown to the right. The hinge is visible within the fissile Moqui Member of the Moenkopi. The orbicular Wupatki Member is visible between the Moqui and Kaibab (right).





Fig. 14.16. A field of Kaibab boulders is strewn across the east flank of the crater. Finer-grained ejecta has probably been eroded from the ejecta blanket, exposing larger blocks within the shattered and overturned sequence. Subtle mounds of additional ejecta are visible in the middle distance, including a mound of Coconino-Toroweap debris (near bushes and a pole in the upper left corner).



Fig. 14.17. A mixture of large blocks and finer-grained debris within the ejecta blanket is accentuated among the erosional remnants of distant mounds of Kaibab ejecta. The light-colored soil in the fore- and middle-ground is dominated by Kaibab detritus. A transition to red Moenkopi-derived material is visible in the distance.

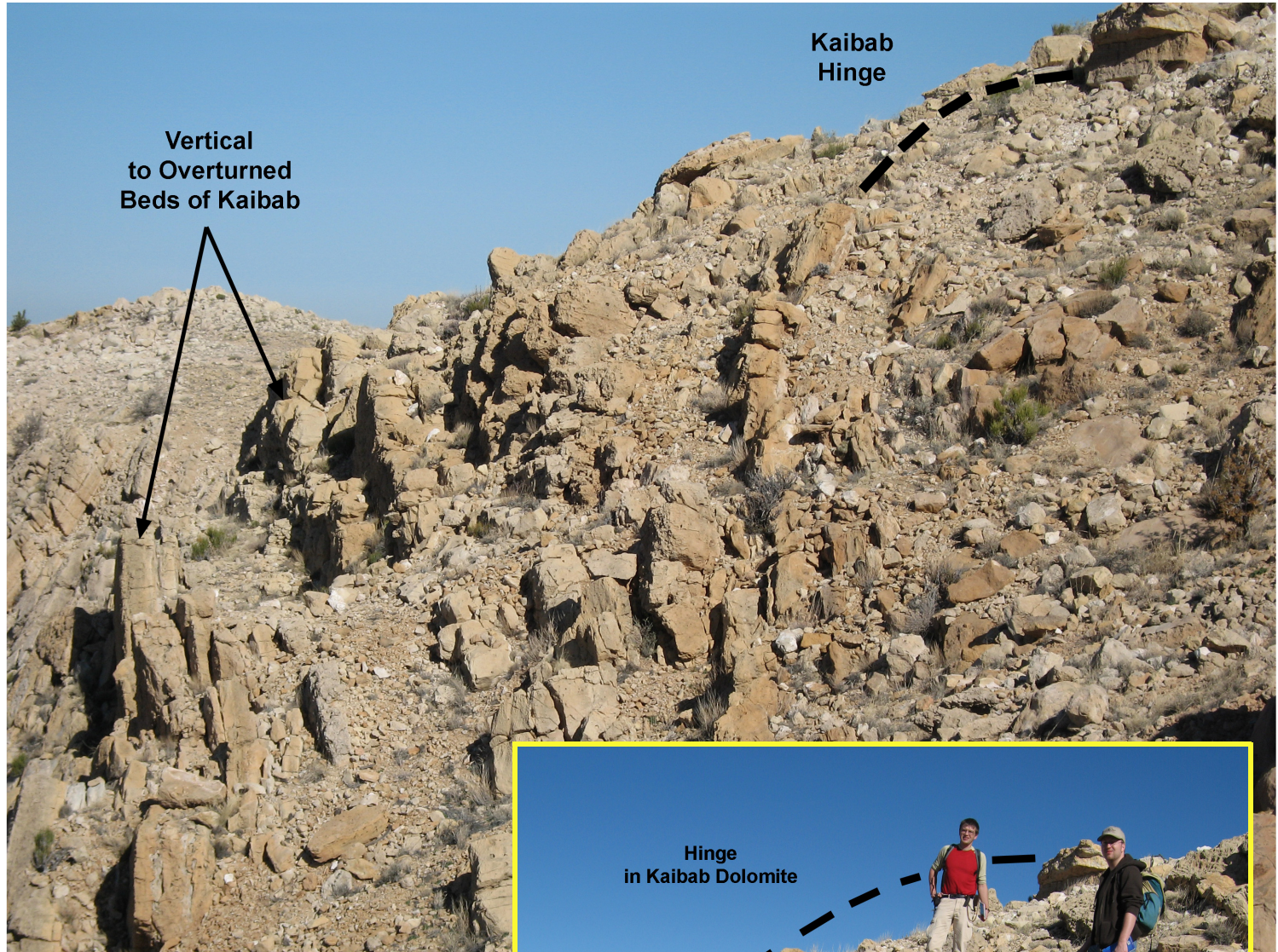


Fig. 14.18. Uplifted and overturned portion of the Kaibab Formation in the crater rim. In a context view (above), the dip of Kaibab in the upper crater wall is near vertical (e.g., left side of image). It is then overturned (center and upper right). Erosion has exposed the fold hinge. Thomas Kenkmann and Michael Poelchau appear for scale in a close-up view of the core of that fold hinge (right).

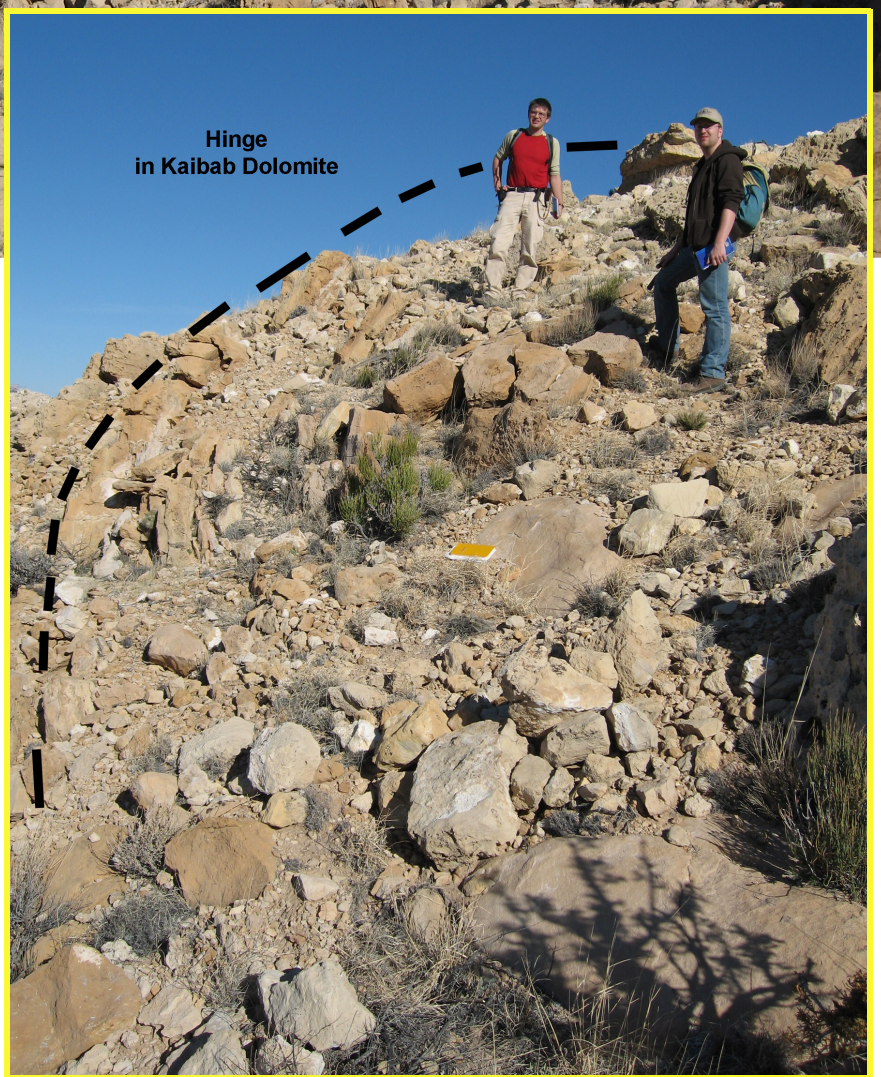
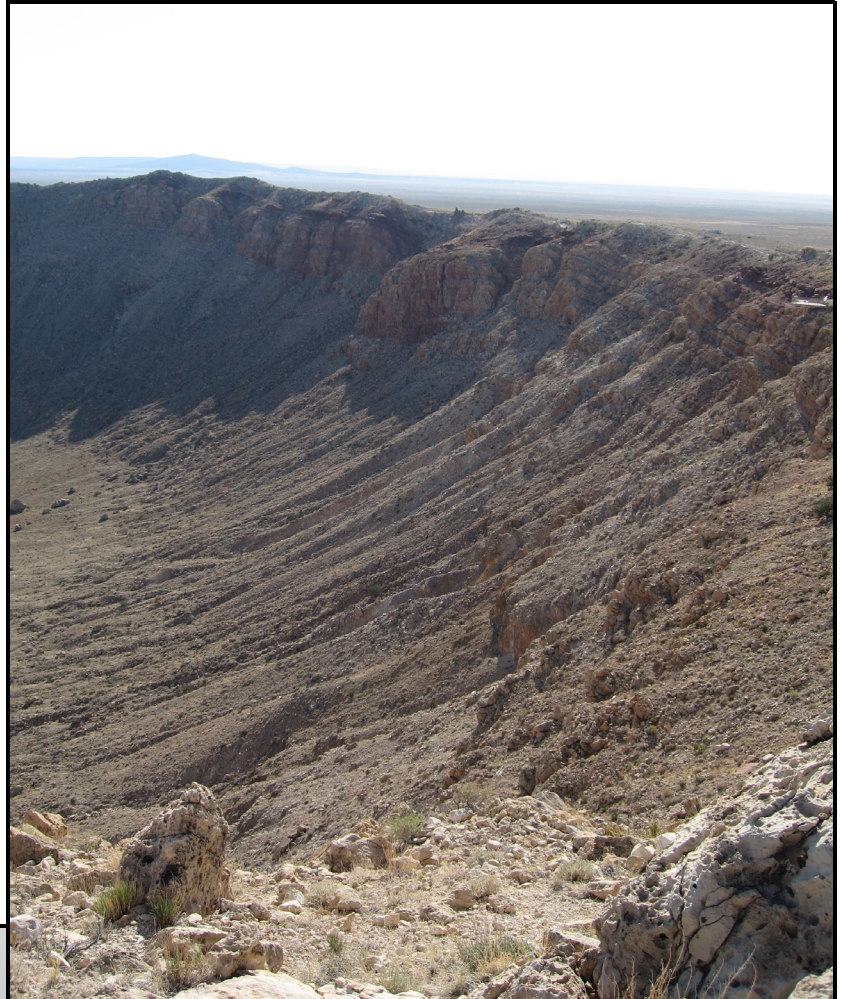


Fig. 14.19. Impact debris coats the interior wall of the crater (right). Within the shallower-sloping deposits on the lower crater walls, an allogenic breccia is draped over bedrock. The allogenic breccia is draped, in turn, by fall-out breccia. Both are mantled by Pleistocene talus that eroded from the steep upper crater walls. The allogenic breccia is dominated by Coconino and Kaibab debris, whereas the fall-out breccia has a large Moenkopi component. Lechatelierite and meteoritic debris are found within the fall-out breccia. A final view towards the northeast (below) reveals the Hopi Buttes and several mesas. The mesas are carved from Triassic, Jurassic, and Cretaceous sandstones and shales. The Hopi Buttes are the erosional remnants of Tertiary dia-tremes.



15. Trail Guide 2: Crater Floor



To reach the trail-head for the crater floor excursion, we exit the museum and hike west along a trail on the north rim of the crater. This is the same trail that the public uses when guided by museum staff to the northwest corner of the crater. When we reach the northwest corner, however, we will be stepping off that trail so that we can hike down to the crater floor. Permission to leave the public trail must be obtained from museum staff. Once off the public trail, I ask that you walk softly. Try to avoid stepping on vegetation and do not unnecessarily disturb the soil. After we descend below the ejecta blanket, we will reach and follow a 100-year-old trail into the crater that was developed by the Standard Iron Company. You will see a lot of debris from those mining operations while we descend. A decision was made several years ago to leave those artifacts in place for historical purposes, rather than discard them. Please do not disturb the artifacts. The trail-head is also marked by the remnants of a building constructed of red Moenkopi (Fig. 15.1). That building is the original crater museum.

Coconino and Kaibab Ejecta

This excursion begins in a gap along the crater rim. The gap represents the top of a tear fault through the crater wall that has facilitated erosion, providing an excellent cross-section through the rim sequence. At the top of the gap, just a few feet from the public trail, an incredibly white outcrop is visible (Fig. 15.2). The material in the outcrop is weakly consolidated. It is a mass of shocked and ejected sandstone that is transitional to a type of rock flour that was described by Barringer (1905). The material in the outcrop is heterogeneously damaged. Cores of surviving Coconino with traces of cross-bedding can be found in it. Outcrops like this one also contain his Variety A shock-metamorphosed sandstone, which has a higher density than normal sandstone.

This sandstone deposit is in the midst of Kaibab dolomite ejecta. A patchy distribution of both lithologies occur along this portion of the crater rim, in part because there is a hummocky surface to the Kaibab ejecta blanket. Coconino-Toroweap ejecta fill depressions in that surface. En route to the trail-head, we passed a classic example of this hummocky structure (Fig. 7.3). There is a sharp contrast between the level of impact-induced damage in the Kaibab dolomite and this outcrop of sandstone. Several multi-meter-diameter Kaibab boulders are resting on the rim around us and seem to be completely unaffected by the impact event (albeit upside down), yet the sandstone in the outcrop at our feet is almost pulverized. The same contrast exists in the crater walls beneath the ejecta. Kaibab maintains good bedding and is cross-cut with few fractures, whereas the Coconino is often shattered into angular blocks that are only a few centimeters to decimeters in size.

Continue to descend along the tear fault until you reach the Standard Iron Company's trail and a nice bench in the red Moenkopi.

Crater Rim Uplift and Overturning Along a Tear Fault

From this vantage point, we can easily see that the target strata were uplifted by the impact blast and now have a steep outward dipping orientation (Fig. 15.3). Dips of strata in the crater walls are often 30 to 40°. At the top of the normally-bedded portion of the sequence is red Moenkopi siltstone. Below the Moenkopi is Kaibab dolomite and some minor sands. The Kaibab is a buff to yellow-colored rock, but its surface in the cliff is stained red from the overlying Moenkopi. The Moenkopi and Kaibab are overturned on the upper part of the slope.

Offset along the tear fault is also visible from this location. The rock in the cliff on the far side of the fault were uplifted farther than the rocks on this side of the fault. Tear faults around the wall of the crater have given it a pseudo-square shape in plan view (*e.g.*, Fig. 3.1). Shoemaker (1960) suggested the tear faults were activated along pre-existing sets of joints. In this portion of the Colorado Plateau, there is a strong SE-NW trending set of joints and a weaker SW-NE trending set of joints. Some of the joints that cut through the Kaibab have been accentuated by carbonate dissolution, creating cavernous seams that extend all the way to the underlying Coconino-Toroweap. Several of these large crevices can be found within a few kilometers of the crater.

The tear fault in front of us is not a simple fault plane. The fault surface curves as it climbs up the crater wall and is actually composed of multiple fault surfaces (Fig. 15.4). Drag along the tear fault folded the bedrock on the far side of the fault. Although not shown in the figure, there are also two small thrust faults in the Kaibab-Alpha sequence that are roughly orthogonal to the tear fault. These types of thrust faults contributed to rim uplift and can be found in both the Kaibab-Alpha and Kaibab-Beta units. One of the largest thrust fault systems is below Barringer Point, which is slightly farther to the west along the crater wall. It thickened the Kaibab-Beta, producing an anticline in the Kaibab-Alpha and overlying units. The anticline is the highest topographic point around the crater rim. We will have a good view of the Barringer Point anticline from the crater floor and southeast crater rim later in our excursion.

This tear fault, plus the regional distribution of joints and dissolution through the Kaibab, led Hager (1953) to propose an alternative origin for the crater. He envisioned the crater was originally an anticlinal mound. That is, the dipping strata in the cliffs once arched over the crater in a broad dome of rock. He argued that the dome was cross-cut with fractures similar to those visible in Kaibab today. Water infiltrated those fractures and dissolved subsurface lithologies. The dome then collapsed downward along faults (the tear faults), forming a graben that was subsequently been modified by erosion. Like Gilbert (1896), he argued the meteoritic debris was coincidental. He also argued silica glass found around the crater is the erosional remnant of a pure silica volcanic lava flow.

Continue down the trail towards the crater floor where we will re-assemble. As you hike down the trail, you will encounter a landslide. Climb over the landslide with care. Do not descend directly above another person, in case a rock is dislodged. The first time this trail washed out occurred over 100 years ago in September 1906. An interesting report of the event survives (Fairchild, 1907): A “cloudburst” opened up over the crater and the “northern trail leading down the crater wall was obliterated and trains of boulders were swept far out on the floor of the crater, while the shaft-house, tool-house, and other buildings in the middle of the pit had their floors buried in mud.” If you look to the crater floor below, you can still see some of those boulders.

Once we reach the crater floor, we will hike to the north wall of the crater and climb up to an outcrop of impact breccias. Be careful when hiking across the crater floor, because the soft sediments have been burrowed by animals. You may fall through the roof a burrow system and find yourself knee-deep in the soil. If you move too quickly, you risk breaking a leg.

Allogenic and Fall-out Impact Breccias

A gully dissects debris on the crater wall, exposing two types of impact breccia and a layer of Pleistocene talus (Fig. 15.4). The best view of the units is on the west wall of the gully. The lowest unit is Shoemaker’s allogenic breccia. Patches of this material are found scattered around the crater (Fig. 3.3) and form the thick breccia lens on the floor of the crater. Depending on location, allogenic breccia is composed of Coconino, Kaibab, or a mixture of those two lithologies. It tends to be dominated by Kaibab on the crater walls and Coconino in the breccia lens. At this locality, Kaibab dominates the breccia.

Shoemaker and Kieffer (1974) identified most of the clasts as being from the Beta Mbr of the Kaibab Fm. Clasts within the breccia are angular and have irregular surfaces.

Draping the allogenic breccia is a fall-out or fall-back breccia unit that is up to 1 ½ m thick where it fills a local depression on the surface of the allogenic breccia. This unit has a mixture of target lithologies, including bright red fragments of Moenkopi and brilliant white fragments of shocked Coconino sandstone. Lechatelierite and meteoritic debris occurs in this unit and have been recovered from this particular outcrop.

The impact breccias are buried beneath Pleistocene talus. Elsewhere along the gully, the talus rests directly on allogenic breccia. The fall-out breccia appears to have been eroded from those surfaces prior to the deposition of talus.

From this vantage point, we also have a good view of the east and southeast walls of the crater (Fig. 15.5). The Gamma Mbr of the Kaibab Fm forms a cliff that can be traced around the crater wall. Several displacements of the Gamma Mbr are visible, including a huge displacement along a tear fault in the southeast corner. This tear fault is similar to the one that occurs in the northwest corner, but the displacement is greater. The units on the left (north) side of the tear fault were uplifted 45 m higher than those on the right side of the fault, which exposed 90 m of Coconino sandstone.

Return to the crater floor and hike towards a covered shaft on the east side. Stop at the mid-point.

Sedimentation on the Lower Crater Wall and Crater Floor

Looking east, we see two sedimentary units on the lower crater wall (Fig. 15.6). The oldest debris occurs in triangular patches that begin near the base of Gamma Mbr of the Kaibab Fm (or at the top of the Coconino-Toroweap Fms) and descends towards the crater floor. The Toroweap Fm is only 1 ½ m thick at the crater, so most of the sandstone visible near the patches of talus is Coconino sandstone. Shoemaker and Kieffer (1974) correlated soil profiles within the talus with soil profiles in the Hopi Buttes region northeast of the crater. They determined that the talus formed at the same time as the late Pleistocene Jeddito Fm. They surmised that the talus was deposited during a pluvial episode during the Wisconsin glacial period. After the talus was deposited, the slope stabilized and a soil formed before the deposits were cut by deep gullies.

Coarse alluvium pours through those gullies and onto the crater floor. This deposit also has a soil of late Pleistocene age and corresponds to the highest soil within the Jeddito Fm (Shoemaker and Kieffer, 1974). The alluvial fans were produced in another pluvial episode during the Wisconsin glacial period. The flow of material through the fans produced levied channels that are still preserved. Although erosion has been modest since the alluvial fans were deposited, it has consumed the lower margins of the fans. Small alluvium-filled channels are dissecting the alluvial fans where they interface with playa sediments on the crater floor.

If we turn around and look west, we see a small hill protrudes from the crater floor (Fig. 15.7). This feature is called Silica Hill. It is composed of Pleistocene lake beds, which imply the level of a lake in the crater was once higher than the hill. The top of the lake sediment is 69 m above the current water table, indicating the water table has fallen dramatically since the late Pleistocene.

Several exploration shafts surround Silica Hill and one of them penetrates the hill. Most of the shafts have been filled in, but Shoemaker was able to examine the walls of the shafts before they were lost. In four shafts (I, II, IV, and V) around Silica Hill, he found three basaltic volcanic ash layers about 5

m below the surface. These are late Pleistocene ashes that were deposited during eruptions in the San Francisco Volcanic Field near Flagstaff, possibly from Saddle Mountain. In contrast, he did not find any ash in Shaft VI on the top of Silica Hill, which suggests the lake level had fallen below the summit of Silica Hill prior to the volcanic eruptions. Any ash that fell on the island was eroded into the surrounding lake.

Shoemaker correlated lake sediments in Silica Hill with the lower to middle stratigraphic levels of lake sediments elsewhere on the crater floor, implying that the base of the lake sediments of Silica Hill is 15 m higher than elsewhere in the crater. Based on this correlation, Shoemaker and Kieffer (1974) suggested the lake sediments of Silica Hill were deposited on top of a topographic high or off-centered “central peak” on the original crater floor. Structural uplift of underlying bedrock is not expected in a crater this small, nor is there evidence of it in exploration boreholes and geophysical surveys. However, observations of lunar craters suggest uneven topography can form on the surface of the breccia lens during collapse of that debris from the walls of the transient crater.

Silica Hill is surrounded by playa sediments that were deposited after the lake disappeared. They are beneath our feet (Fig. 15.8). In the walls of the Main Shaft, Shoemaker measured a total thickness of 1.8 m. The playa sediments are composed of pink aeolian silt that blows in from outside the crater. In a trench cut into the playa beds, he found two volcanic ash layers that he correlated with the eruption of Sunset Crater. Using that ash as a chronometer, he determined that 30 cm of playa sediments have been deposited since the eruption. The eruption occurred ~900 years ago, possibly in 1064 or 1065 (Smiley, 1958).

Continue hiking across the crater floor towards the southeast corner of the crater, where we will begin our hike up to the crater rim. En route, we will pass several remnants from mining operations. We will stop at Shaft II on the east side of the crater floor. If time allows, one can also detour to the Main Shaft in the crater center.

Probing the Crater Floor in 100-Year-Old Exploration Shafts

A large steam boiler and winch sits in the center of the crater floor (Fig. 15.9), immediately east of the Main Shaft, which is enclosed by a safety fence. (Do not enter this fenced area.) The Main Shaft is a large 2-compartment shaft suitable for commercial production of meteoritic ore. Unfortunately, water was encountered at a depth of 210 ft (63 m). Pumps were installed, but they could not mitigate the flow of water and work ceased at a level of 230 ft (69 m) when the walls at the bottom collapsed. A building used to stand over the main shaft (Fig. 15.10). Shaft III is adjacent to the Main Shaft and also surrounded by a safety fence.

Shaft II is on the east side of the crater floor and now covered by a set of doors (Fig. 15.9). The shaft is 43.3 m (145 ft) deep. The upper 30 m (100 ft) of the shaft is composed of lake sediments with the volcanic ash described above. Below the lake sediments is 10.3 m (35 ft) of fall-out breccia. The unit is generally massive, but there is a subtle grading upwards from coarse debris at the bottom to finer-grained debris at the top of the unit. The basal 1.3 m (5 ft) is particularly coarse. The shaft penetrates 3 m (10 ft) into the allogenic breccia lens on the crater floor, where it bottoms. The allogenic breccia is composed entirely of Coconino sandstone. Some of the blocks are more than a meter in size. Superficially, the blocks look like they represent several levels of shock, indicating that there was a lot of mixing on the walls of the transient crater before the material was deposited.

A dump around the top of the shaft contains debris from all levels in the shaft. Much of the dump has an inverted stratigraphy, because material removed from the bottom of the shaft was dumped on

material previously removed from the top of the shaft. However, the miners also dumped material on different sides of the shaft as they plunged deeper. Fall-out breccia dominates the surface on the east side of the dump. Allogenic breccia dominates the surface on the southwest side of the dump. Lacustrine sediments dominate the northwest side of the dump.

Material from the fall-out unit contains severely shocked Coconino sandstone, including vesicular silica glass. Shocked Coconino is also found in material from the allogenic breccia, but shock levels are less severe. Microscopic examination might be needed to classify the shock level. The lacustrine sediments are dominated by thinly-laminated, calcareous siltstones with fossils of the organisms that lived in the lake. Although not apparent in the dump, the lake sediments also contain shock-metamorphosed debris. In the shaft, the lower 1.5 m (5 ft) of lake sediments contain many blocks of lechatelierite. Shoemaker measured one block of lechatelierite that was 30 cm across. These low density materials were able to float while water flooded the crater and a lake grew. Eventually they became water-logged, sank, and were buried by the first lake sediments. Lechatelierite blocks may have floated up directly from fall-out breccia deposited on the crater floor, but some of them may have also been washed into the lake from the crater walls.

The contact between the fall-out breccia and lacustrine sediments is sharp. There is no intervening alluvium. Based on this observation, Shoemaker and Kieffer (1974) concluded the lake formed immediately after the impact event and, thus, that the water table was at least 30 m higher in the Coconino sandstone than it is today.

Unfortunately, the cribbing in this shaft is no longer safe and work in it has been suspended. Before the shaft was closed, however, I was able to sample the first horizon of lake sediments deposited on top of the fall-out breccia on the original crater floor. Pollen in that sample was used to improve an environmental reconstruction of the vegetation at the time of impact. (See Chapter 12 for more details). Plans have been made to replace the cribbing, so that we have a permanent research and educational facility that provides access to both the impact breccia lens and overlying lake sediments. We are still working to acquire the necessary funds for the project.

Continue hiking towards the southeast corner and begin climbing out of the crater along an old mule trail. The trail will switch back and forth across Pleistocene alluvium. We will stop when we reach the base of the cliffs along the southern wall of the crater.

Toroweap Cave

The Toroweap Fm is much thinner at the crater than it is in the Grand Canyon. Only 1.5 m is found between the underlying Coconino Fm and overlying Kaibab Fm. A small cavernous exposure is visible to the right (southwest) of the trail (Fig. 15.11). Large fractures in the Gamma Mbr of the Kaibab Fm feed water into the boundary region, enhancing erosion of the Toroweap. The dissolution of Toroweap appears to be a post-impact phenomenon. However, elsewhere in the region, large subsurface caverns have been found immediately below the Kaibab-Toroweap contact. Thus, caverns may have existed in the target sequence prior to impact.

Continue hiking up the trail. Three stops are planned for the remainder of the climb to the crater rim.

Hauling supplies

During mining operations, a lot of supplies had to be transported into the crater. Mules carried some of that material on the trail we are following. Material was also winched to and from the crater floor along a slide that was built on the crater walls. Remnants of the wooden staging can still be seen on the slope (Fig. 15.12). A mule-driven winch sits at the top of the slide on the crater rim. The primitive elevator is no longer in service.

Mining activity within the crater was widely followed by newspapers across the country. In 1906, The Arizona Republican published a summary of the operations and Barringer's impact hypothesis after the first four holes had been drilled in the crater floor and concluded: "It is fortunate indeed for Arizona, that this wonder came into the possession of the men who became deeply interested in it and who at the time had the money and pluck enough to exploit it (February 26, 1906)." Newspaper stories sometimes had a few facts wrong or were intentionally exaggerated. For example, based on the presence of diamonds in Canyon Diablo meteorites, The Indianapolis Star reported (October 6, 1912) that the mining syndicate was trying to recover a half-mile thick diamond.

Thrust Faults and Anticlines in Crater Walls

Looking towards the northwest corner of the crater (Fig. 15.13), we can see the tear fault that we utilized in our earlier descent to the crater floor. The drag fold on the west side of the fault is easily visible from this perspective. Scanning around the crater wall to the west, we see Barringer Point, which is the highest point on the crater rim. The Beta Mbr of the Kaibab Fm is unusually thick beneath Barringer Point because of one or more thrust faults. The thickened sequence contributes to the uplift of the crater wall and has created an anticline.

Another thrust fault can be seen beneath Moon Mountain (Fig. 15.13). In this case, a section of the Alpha Mbr of the Kaibab Fm has been duplicated, forming another anticline and topographic high.

These types of faults occur in several locations around the crater, in both the Alpha and Beta Mbrs of the Kaibab, and are responsible for a significant portion of crater rim uplift. They occur on the west, north, and east sides of the crater. The thrusts are often small, but can occur multiple times, producing a cumulative effect. Bedding within the Kaibab (particularly the Beta Mbr) is often indistinct, so the amount of bedding repetition cannot always be measured quantitatively. Nonetheless, most of the uplift in the largest anticlines appears to be a direct consequence of the thrusts. Shoemaker and Kieffer (1974) suggested that a concentration of thrust faults in the northwest wall of the crater indicates the impacting asteroid was moving from southeast to northwest. I concur, although I worry that we may be biased by what we can observe. If thrust faulting occurs at depth, lower in the crater walls, it is hidden from us and not factored into our analysis. For that reason, new studies of other structural indicators are underway to further test the trajectory.

Breccia at the (Permian-Triassic) Kaibab-Moenkopi Boundary

In some parts of the crater, a breccia occurs at the Kaibab-Moenkopi boundary. An example is visible along the trail (Fig. 15.14). The breccia is often dominated by Kaibab clasts, as is the lower portion of the outcrop here. Another outcrop of this breccia occurs along the north wall of the crater (Fig. 15.15) where it can be traced for over 100 m. Several other outcrops occur on the south wall of the crater near our present location. The matrix is often sandy and weathers differently than enclosed dolomite clasts.

There are three possible origins for the breccia: (1) the breccia is a karst product that existed at the top of the Kaibab before impact; (2) the breccia was formed by shear between the Kaibab and Moenkopi during the impact; and (3) the breccia was produced when debris on the transient crater wall was injected between the Kaibab and Moenkopi during impact.

Shoemaker and Kieffer (1974) described a similar unit adjacent to the museum complex. At that locality, the uppermost unit of Kaibab has irregular to chaotic bedding with clasts of sandstone and sandy dolomite. They interpreted the unit to represent a karst surface that developed during the late Permian and/or early Triassic. Breccias in the uppermost interval of Kaibab have been described elsewhere on the Colorado Plateau, particularly in Utah. Paul Knauth (personal communication, 2007) told me that several examples also occur in the Grand Canyon region. Those breccias, however, are dominated by chert pebbles.

The breccia may be more complex than previously appreciated and is currently being re-investigated. The study is not complete, but a description of some of the observations will be provided for our discussion.

Although the outcrop described by Shoemaker and Kieffer (1974) is composed entirely of Kaibab clasts, some outcrops elsewhere in the crater contain red clasts. These are sometimes red-stained Kaibab clasts, but in many cases are true Moenkopi clasts (Fig. 15.16), which is inconsistent with scenario (1). The sand matrix does not appear to be a simple sediment deposit, infiltrating and burying karst dolomite cobbles. Rather, it sometimes appears to be injected through fractures in clasts (Fig. 15.15). The unit is sometimes compressed into small folds, whose limbs can be sheared (Fig. 15.17). Fractures and displacements also occur within Kaibab-dominated outcrops of the breccia unit (Fig. 15.18 and 15.19). Elongated clasts are sometimes aligned, as if part of a flow (Fig. 15.20). The presence of Moenkopi and Kaibab clasts, injection textures, and internal shearing of clasts seems to point to scenarios (2) and (3). The folding of breccia horizons, however, suggests the breccia unit already existed. That either points to scenario (1) or requires formation and lithification of the breccia early in the cratering process and then folding late in the cratering process. Finally, a block of Kaibab-dominated breccia was found on the rim of the crater. If it was not moved during earlier exploration phases at the crater and is a part of the ejecta blanket, then it points to scenario (1) or the special circumstance of formation and lithification of an impact breccia early in the cratering process. Alternatively, there may be two types of breccias at the Kaibab-Moenkopi boundary, one that existed in the target sequence and another that was generated during the impact. The outcrop in front of us hints at a two-step formation process.

Continue hiking towards the crater rim.

Coconino-Toroweap Impact Ejecta

When we reach the rim of the crater, the ground will be paved with ejected debris from the Coconino-Toroweap Fms (Fig. 15.21). These sandstones dominate the surface of the ejecta blanket on the south side of the crater. Only small patches of that type of debris are found on other sides of the crater.

The sandstone ejecta is dominated by cobble- to small boulder-size fragments. These fragments are much smaller than the immense boulders of Kaibab that we observed at the beginning of our excursion. Immediately after the impact event, this Coconino debris was probably covered with a layer of fall-out debris. Erosion removed it.

The Coconino is formed from an aeolian sand. The blocks of debris on the surface are laminated,

but it is sometimes difficult to determine if the laminae are cross-beds. Rare examples of the truncated interface of a cross-bed can be found, however (Fig. 15.21 inset). Appropriately, the sandstone is being eroded to produce another generation of aeolian sands. The new sand forms small dunes on the southern flank of the crater. Long wind streaks of sand stretch from the crater towards the northeast, reflecting the prevailing southwest wind. The sand dunes lap up against two-needle pinyon pine and juniper trees. The latter were examined by Barringer's team. Tree-rings indicated some of the trees are more than 700 years old (in 1905), or more than 800 years old now. This is the minimum age of the crater.

A short distance to the west is the top of the 1,376 ft deep borehole that was drilled through the crater wall and into a fractured and/or brecciated sequence contaminated with meteoritic debris. (See Chapter 3 for details.) Even farther to the west are the "Silica Pits," which are composed of finely comminuted Coconino. At that location, fractured versions of the blocks at our feet occur in a massive and brilliantly white matrix of "rock flour."

That deposit is covered with a breccia that contains red Moenkopi fragments. Because the only outcrops of Moenkopi on the south side lie below the crater rim on the interior crater wall, those Moenkopi-bearing deposits are candidates for surviving fall-out breccia. Shoemaker (1960), however, mapped them as post-impact alluvium. Although they may be secondary deposits, they contain many of the eroded remnants of fall-out debris, including Class 4 and 5 shock-metamorphosed Coconino sandstone.

To examine hinges in overturned Moenkopi and Kaibab, however, we need to follow the rim trail towards the east. We will use the Crater Rim East trail guide for the remainder of the hike back to the museum.



Fig. 15.1. The remnants of a stone building sit at the top of a tear fault through the crater rim. The building was the original museum at the crater. It sits on top of the impact ejecta blanket, which has an inverted Moenkopi, Kaibab, and Coconino sequence.

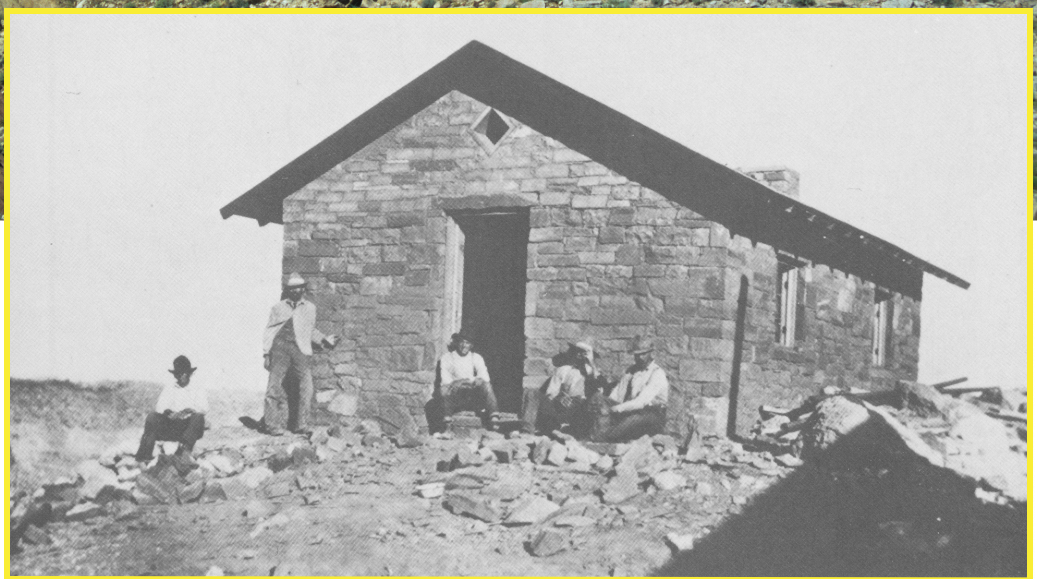




Fig. 15.2. Outcrop of shocked and ejected Coconino sandstone. The sample is transitional to "rock flour" and may contain remnant cores of relatively unshocked Coconino sandstone. Shock may have created a slatey cleavage within these types of units that is distinct from pre-existing target cross-bedding. This outcrop of Coconino debris was deposited in a depression on a hummocky surface of Kaibab ejecta. The Coconino debris in this outcrop is more severely damaged than Kaibab material in the area.

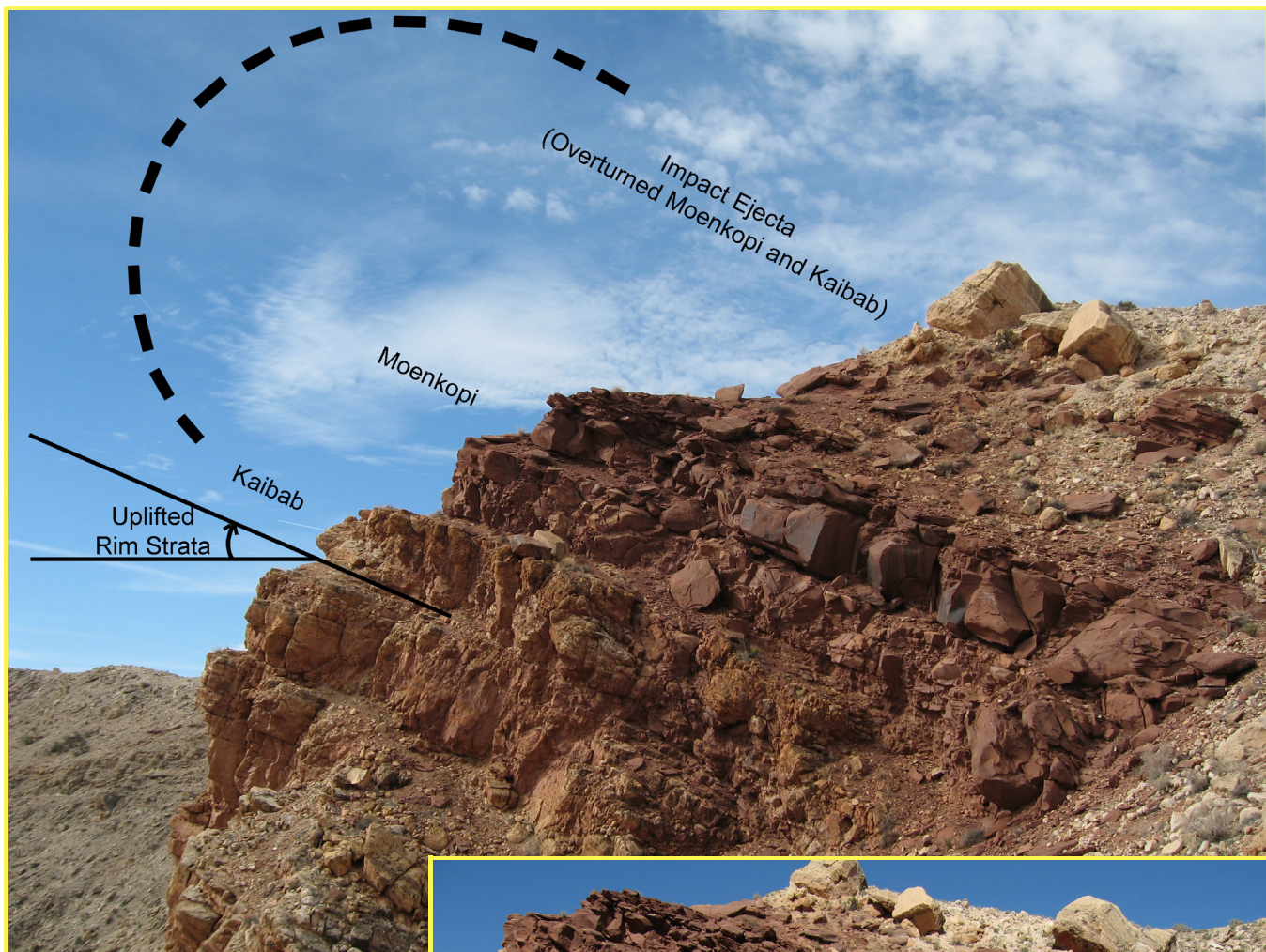


Fig. 15.3. View of structure in the crater wall. Strata that had a horizontal pre-impact orientation were uplifted during crater excavation (above). Dips are often 30 to 40 degrees. The strata were also overturned and ejected. This further enhanced rim height and distributed debris over the surrounding landscape. Crater wall uplift was not uniform. Differential uplift was accommodated (or facilitated) by tear faults (right) that may have been produced along pre-existing joints. Offsets along these tear faults range from meters to several tens of meters. The structure illustrated (right) is simplified. Small thrust faults, for example, also occur in this part of the crater, but are not easily seen in this image.





Fig. 15.4. Outcrop of allogenic breccia, fall-back breccia, and Pleistocene talus (upper left). Close-up views of allogenic breccia (bottom left), fall-back breccia (above), and fragment of impacting asteroid eroding out of fall-back breccia (left center). Fall-back breccia contains Moenkopi, whereas allogenic breccia is dominated by Kaibab and Coconino.

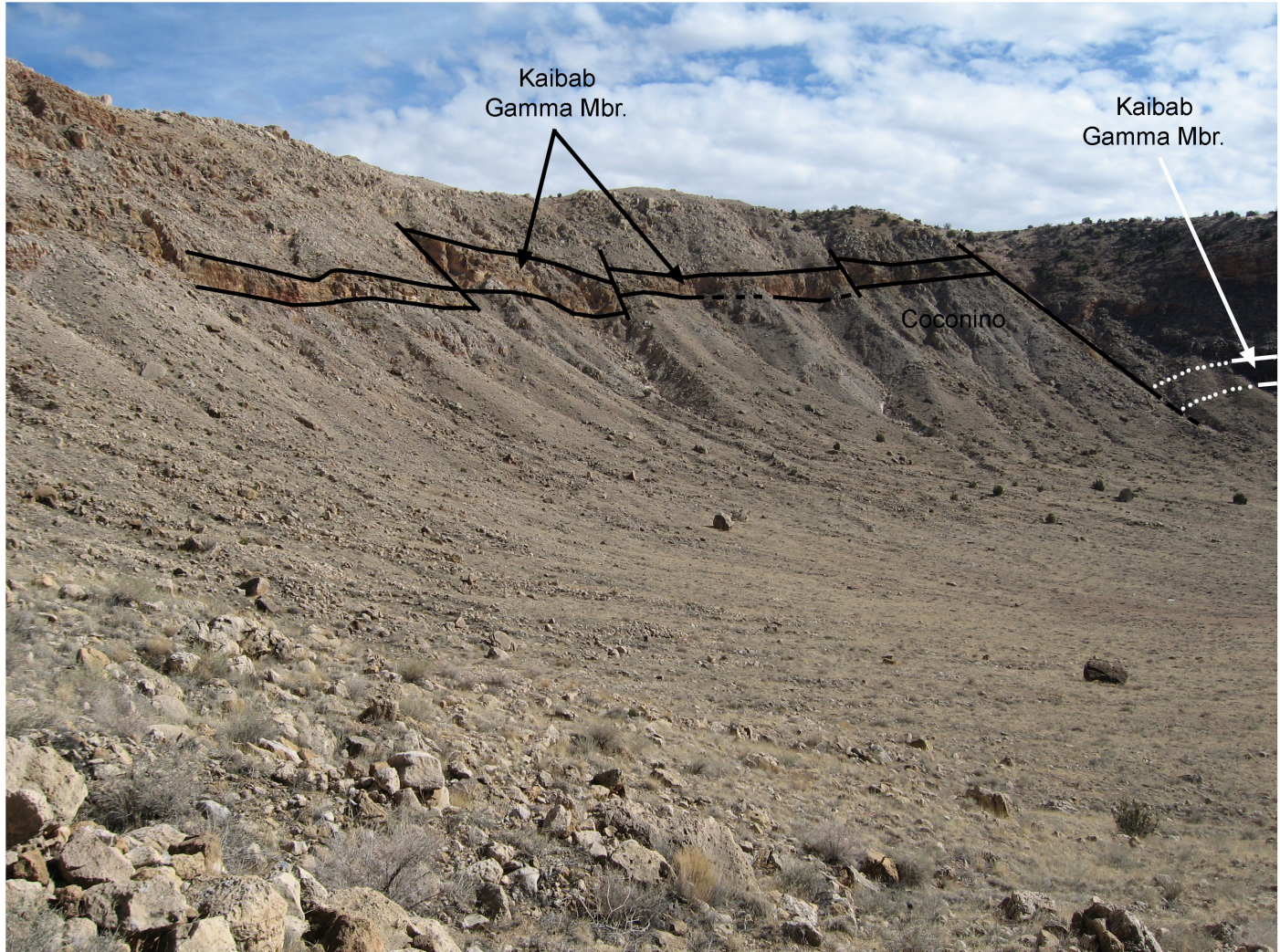


Fig. 15.5. From this vantage point we can trace the Gamma Mbr of the Kaibab Fm along the east crater wall, into the southeast corner of the crater, and part way across the south crater wall. The unit is off-set by several faults, including a large tear fault in the corner. The displacement along that tear fault is 45 m. On the north side of the tear fault, 90 m of Coconino sandstone is exposed. Coconino is not exposed on the southside of fault and only traces of Coconino and Toroweap can be found along the south crater wall. Those units along the south crater wall were buried by alloigenic and fall-out breccia (like the deposits examined in the previous figure) and Pleistocene talus (like that in the foreground of this photograph).



Fig. 15.6. The lower walls of the crater are covered by Pleistocene sediments. Talus derived from the upper crater walls was produced first (Qpt) and then dissected, so that only small remnants survive. A younger alluvium (Qp) spilled through the dissecting gullies and flowed towards the center of the crater. Two periods of wetter climatic conditions than we have today are implied. The margins of the younger alluvium deposit are now being dissected and overlapped by recent playa deposits. View is to the east from the crater floor.

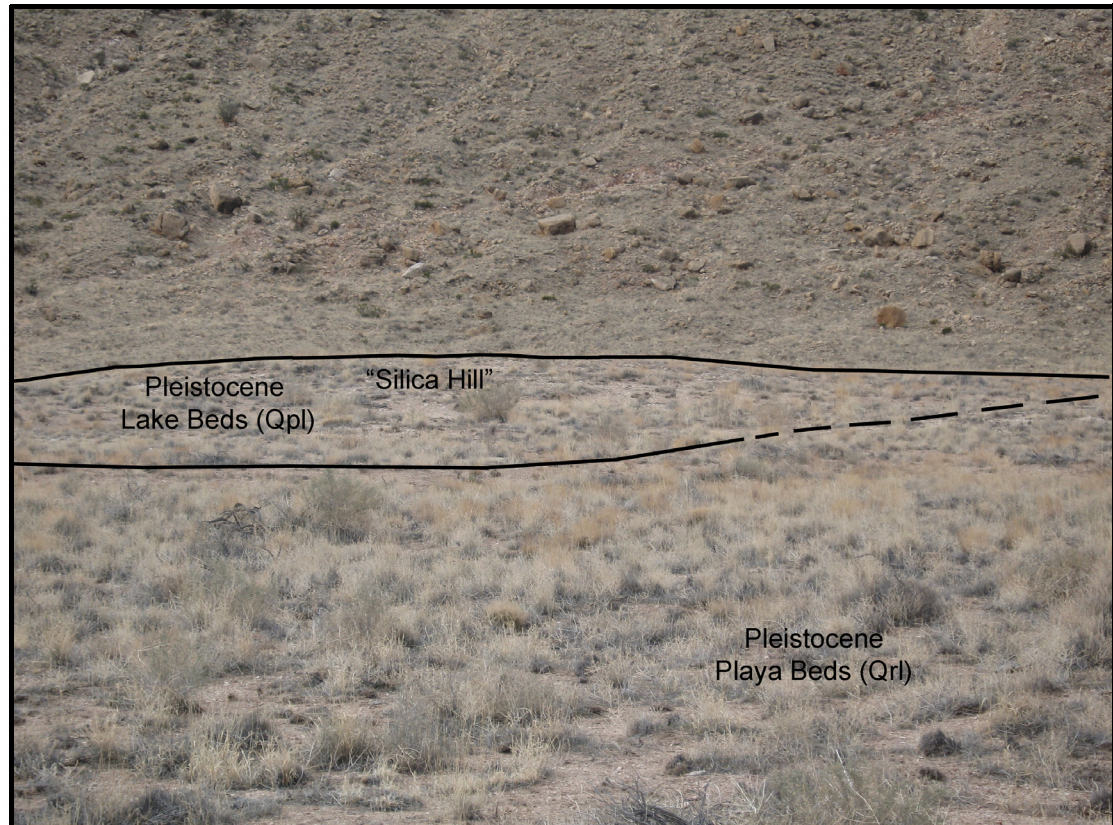


Fig. 15.7. A hill composed of Pleistocene lake sediments rises on the north side of the crater floor and is surrounded by recent playa sediments. The lake sediments imply at least one period of wetter climatic conditions, sufficient to raise the water table >69 m above its current level. The lake sediments are nearly 30 m thick and cover the original floor of the crater. View is looking west. The trail that descends from the northwest corner of the crater rim cuts across the slope in the background.



Fig. 15.8. Desiccation polygons or mud cracks occur on the crater floor, reflecting current arid conditions and intermittent rainfall. These features are found in playa sediment, new fine-grained alluvium, and remnants of drilling mud generated during mining operations. These recent, relatively soft-sediment features are similar to lithified features in the Triassic Moenkopi Fm in the upper crater walls (e.g., Fig. 2.4).



Fig. 15.9. The Main Shaft and Shaft III (#3) are enclosed by safety fences (middle panel). A steam boiler and winch sit east of the Main Shaft (middle and bottom panels). Shaft II (#2) is on the east side of the crater floor and covered with a set of doors (top panel).

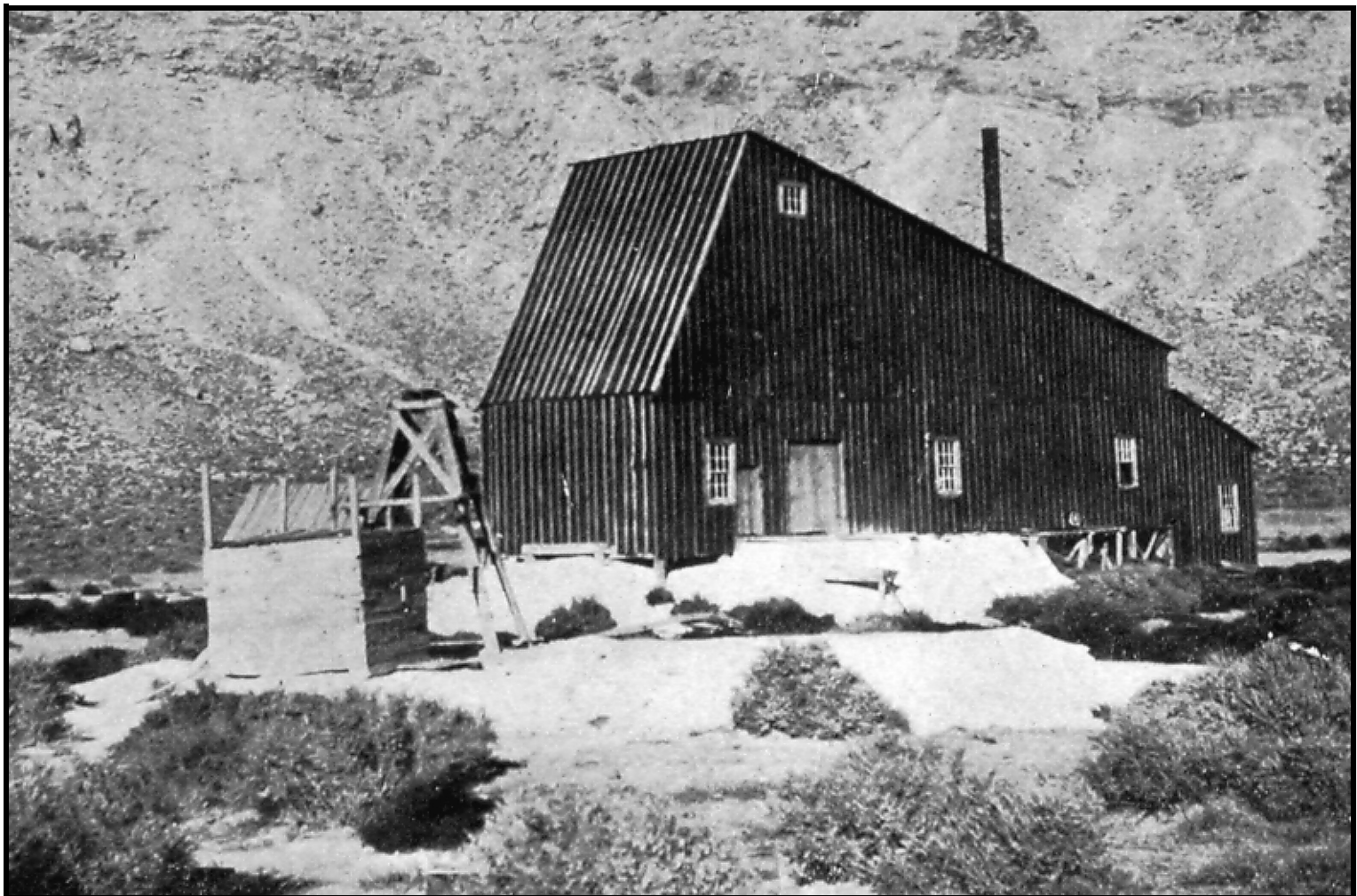
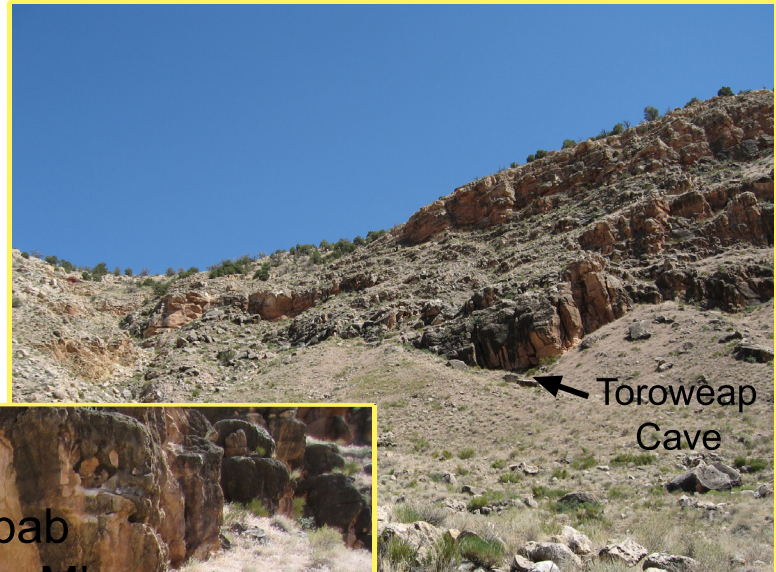


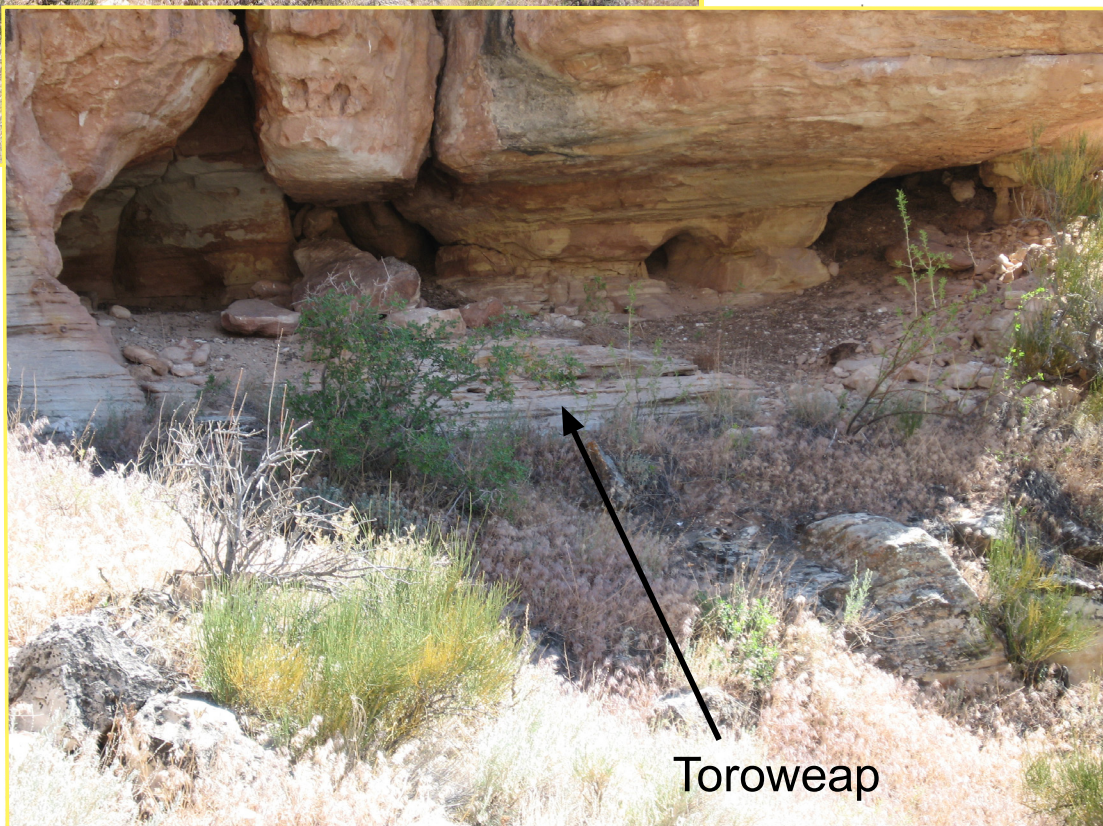
Fig. 15.10. Main Shaft house in the center of the crater floor. The shaft is very wide so that it would be suitable for two compartments. Excavation in the shaft reached a depth of ~230 ft, which was ~20 ft beneath the water table. Pumps were installed, but the bottom of the shaft collapsed and the effort to descend farther was abandoned. (Bottom panel of Plate XI in Barringer, 1910.)

Fig. 15.11. A cave in the Toroweap Formation is visible from the trail while hiking out of the crater (right). Water flows from the rim of the crater down through vertical fractures in the crater wall (middle and bottom panels). Water is then flushed into the crater at the Kaibab-Toroweap contact and through the Toroweap, causing preferential erosion of Toroweap sand. This sequence is a potential analogue for some local hydrological and erosional features on Mars.



Kaibab
Gamma Mbr.

Note: This and other niches around the crater contain pack-rat middens. Please do not disturb the middens, because they will be analyzed to better determine the age of the crater and how climate has changed since the crater formed. The middens may also harbour the deadly Hanta-virus Pulmonary Syndrome.



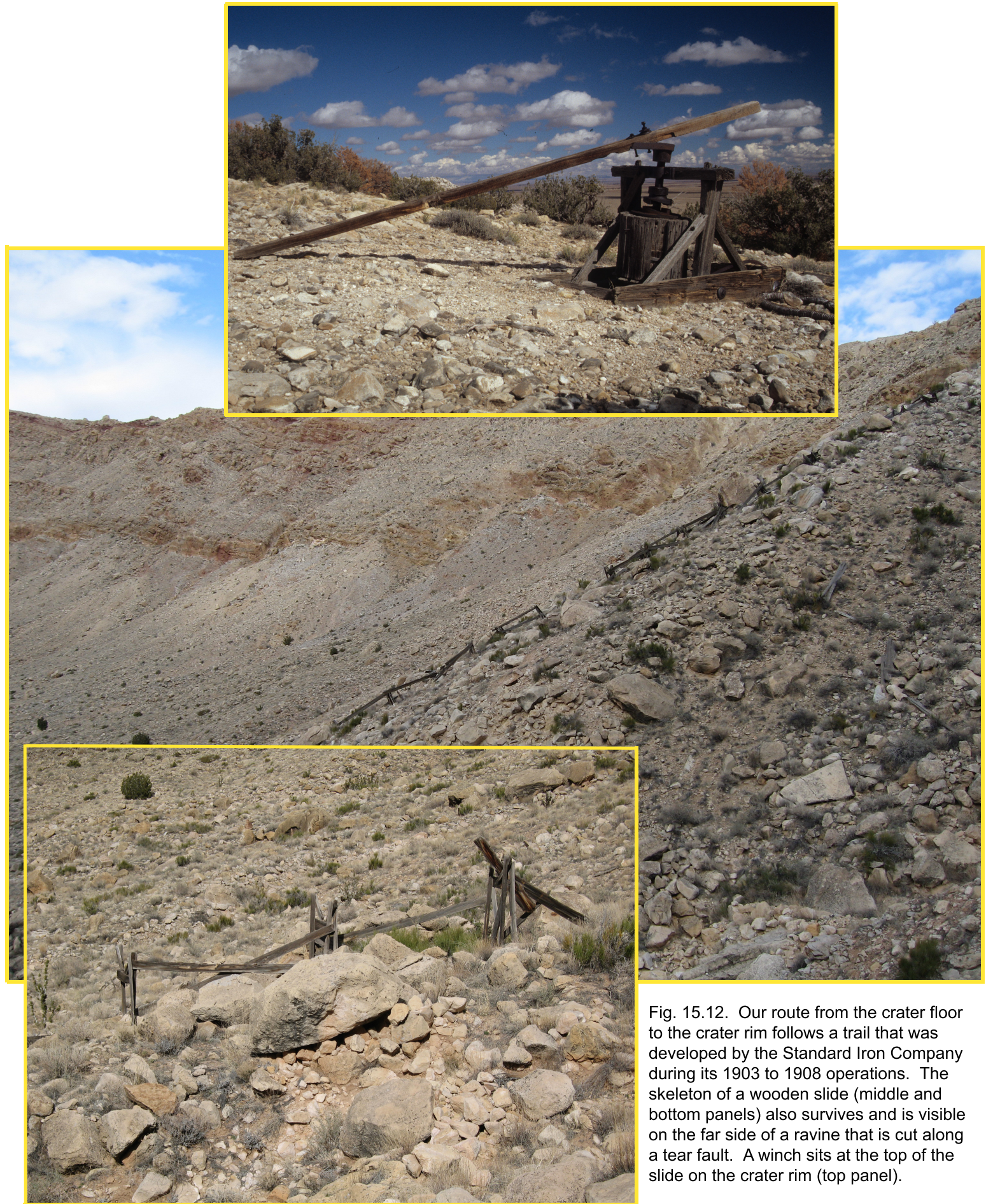


Fig. 15.12. Our route from the crater floor to the crater rim follows a trail that was developed by the Standard Iron Company during its 1903 to 1908 operations. The skeleton of a wooden slide (middle and bottom panels) also survives and is visible on the far side of a ravine that is cut along a tear fault. A winch sits at the top of the slide on the crater rim (top panel).

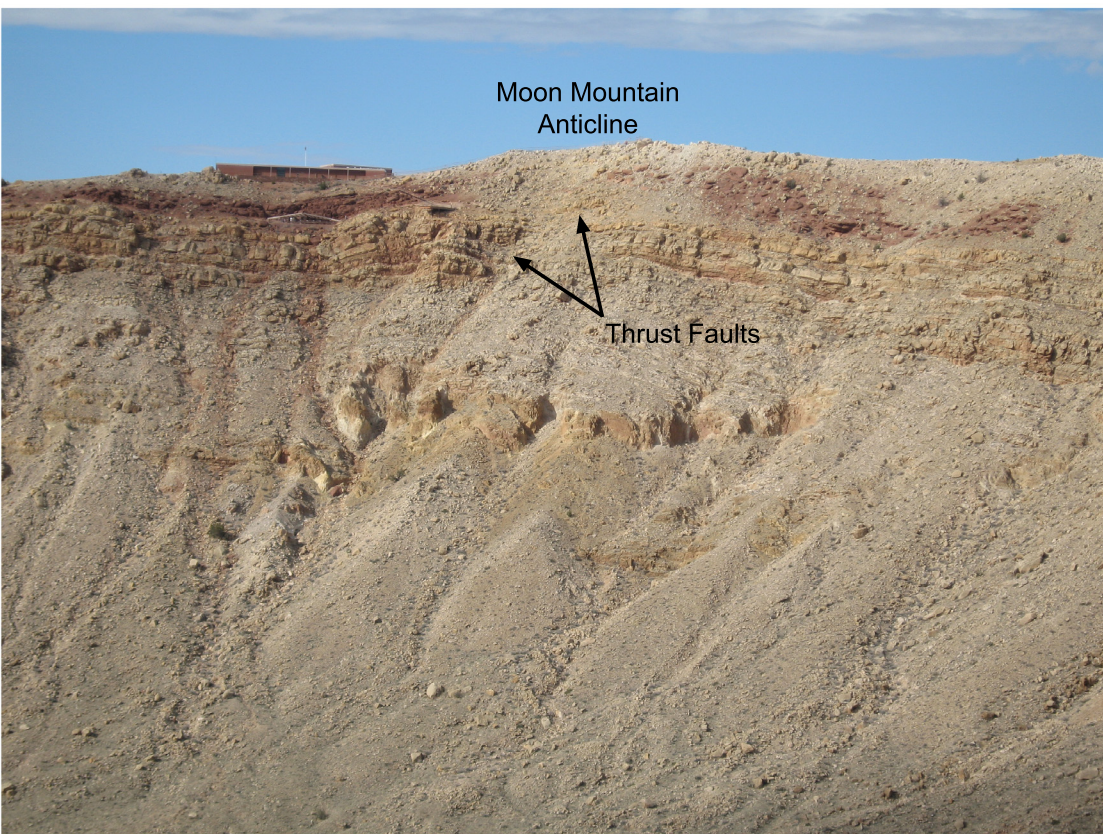
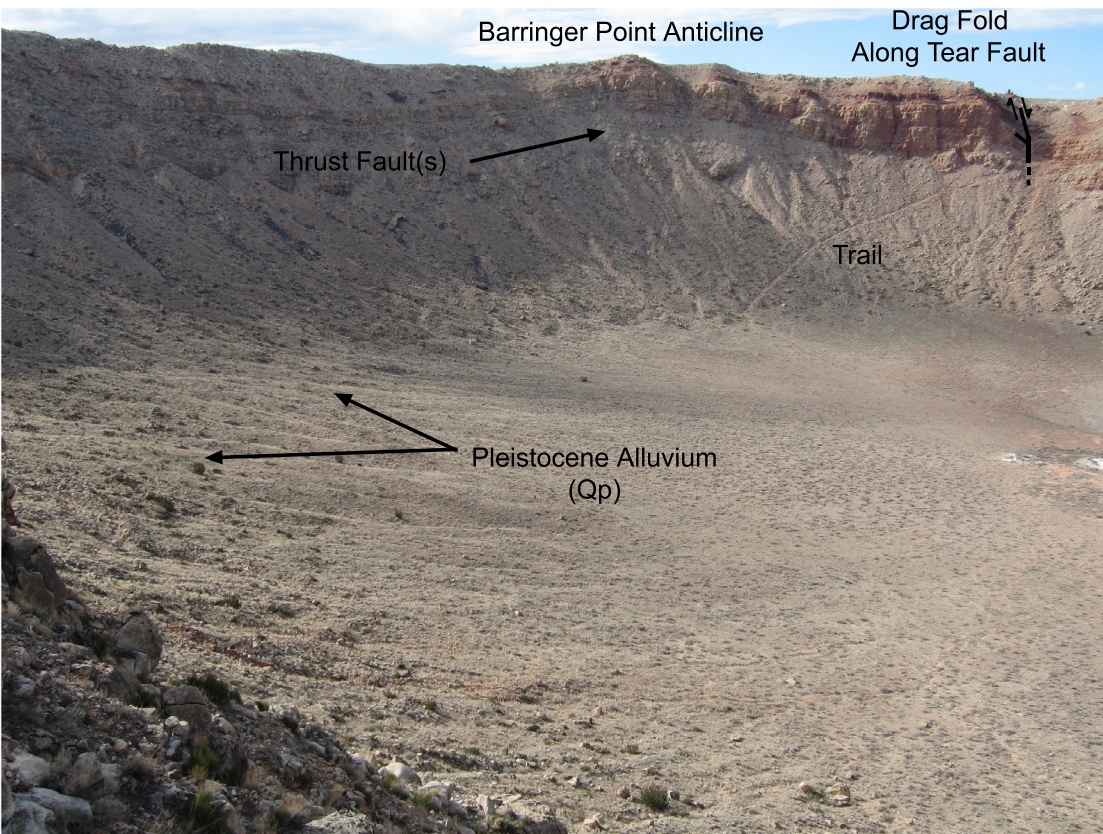


Fig. 15.13. Structural features associated with crater rim uplift are visible in distant crater walls. To the west-northwest (top panel) the Barringer Point anticline is visible; it is uplifted by one or more thrusts in the Beta Mbr of the Kaibab Fm. Moving clockwise around the crater rim, a complex tear fault is visible in the northwest “corner” of the crater. Drag along that fault is apparent to the left of the fault, near the trail we descended. Pleistocene alluvium that was shed from the crater walls is also visible in that same view. To the north, adjacent to the museum complex (bottom panel), the Moon Mountain anticline is visible. It is uplifted by thrust faults within the Alpha Mbr of the Kaibab Fm.



Fig. 15.14. The trail rises through Moenkopi (upper left). Slightly below trail level is the Kaibab-Moenkopi boundary (left center). Here, and at a few other locations around the crater, a breccia occurs at this boundary. Portions of the breccia are dominated by Kaibab clasts (lower right), although some portions contain Moenkopi clasts (upper right), including blocks with pre-existing desiccation cracks.



Fig. 15.15. Outcrop of breccia at the Kaibab-Moenkopi boundary. Clasts of dolomite are being etched by acidic water. The matrix is sandy and probably calcareous. The matrix appears to flow through a fracture separating a Kaibab cobble (upper center). Differential weathering of the sandy matrix and carbonate clasts accentuate the texture of the breccia. This outcrop is part of an extensive bed that can be traced along the north wall of the crater.

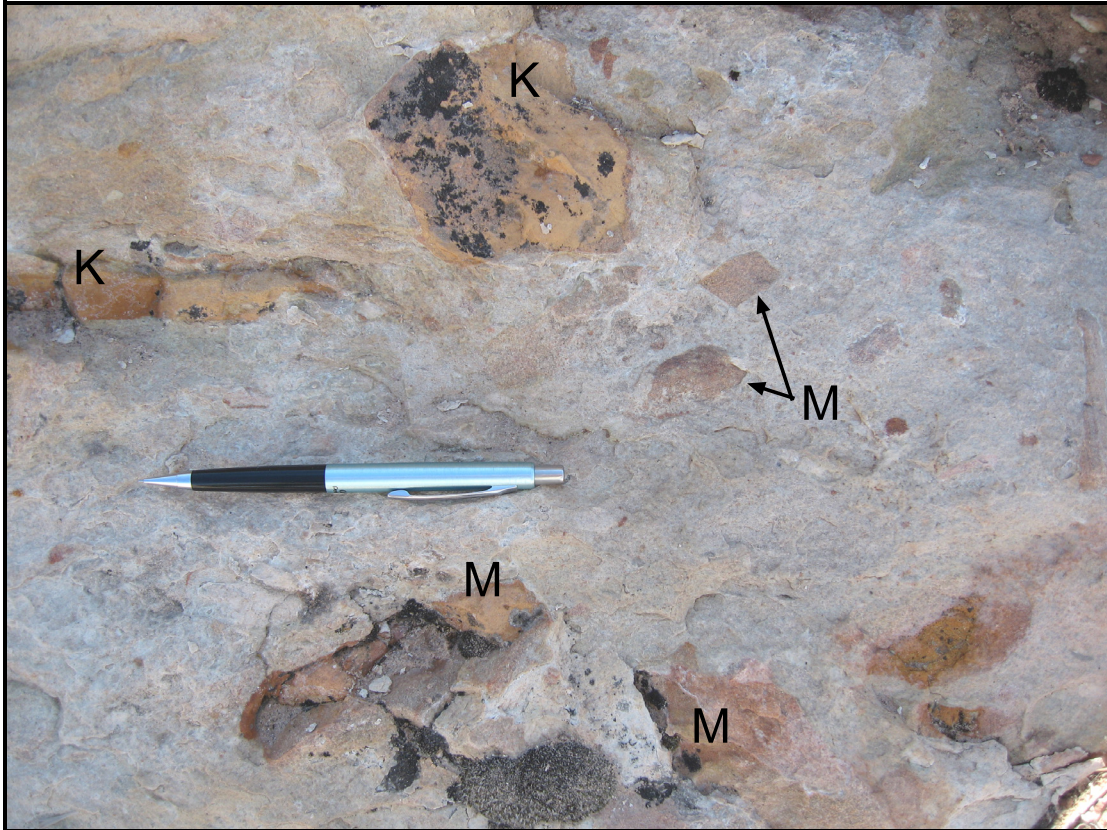


Fig. 15.16. Breccia along Kaibab-Moenkopi boundary that contains clasts from both units. Kaibab clasts are yellow and Moenkopi clasts are red. In case color reproduction is poor, they are labeled K and M, respectively. This outcrop is located in the southeast corner of the crater.



Fig. 15.17. Beds along the Kaibab-Moenkopi boundary have been compressed, forming folds whose limbs are sometimes sheared along small off-set faults. This outcrop is located in the southeast corner of the crater.



Fig. 15.18. Clasts or remnant beds within the breccia at the Kaibab-Moenkopi boundary have been fractured, displaced, and rotated. This outcrop is along the north wall of the crater.



Fig. 15.19. Large clast or remnant bed that has been fractured and displaced. Smaller clasts populate the breccia above and to the right of the large sheared clast. Intermediate-size clasts are at the top of the view (upper right). This outcrop is along the north wall of the crater.

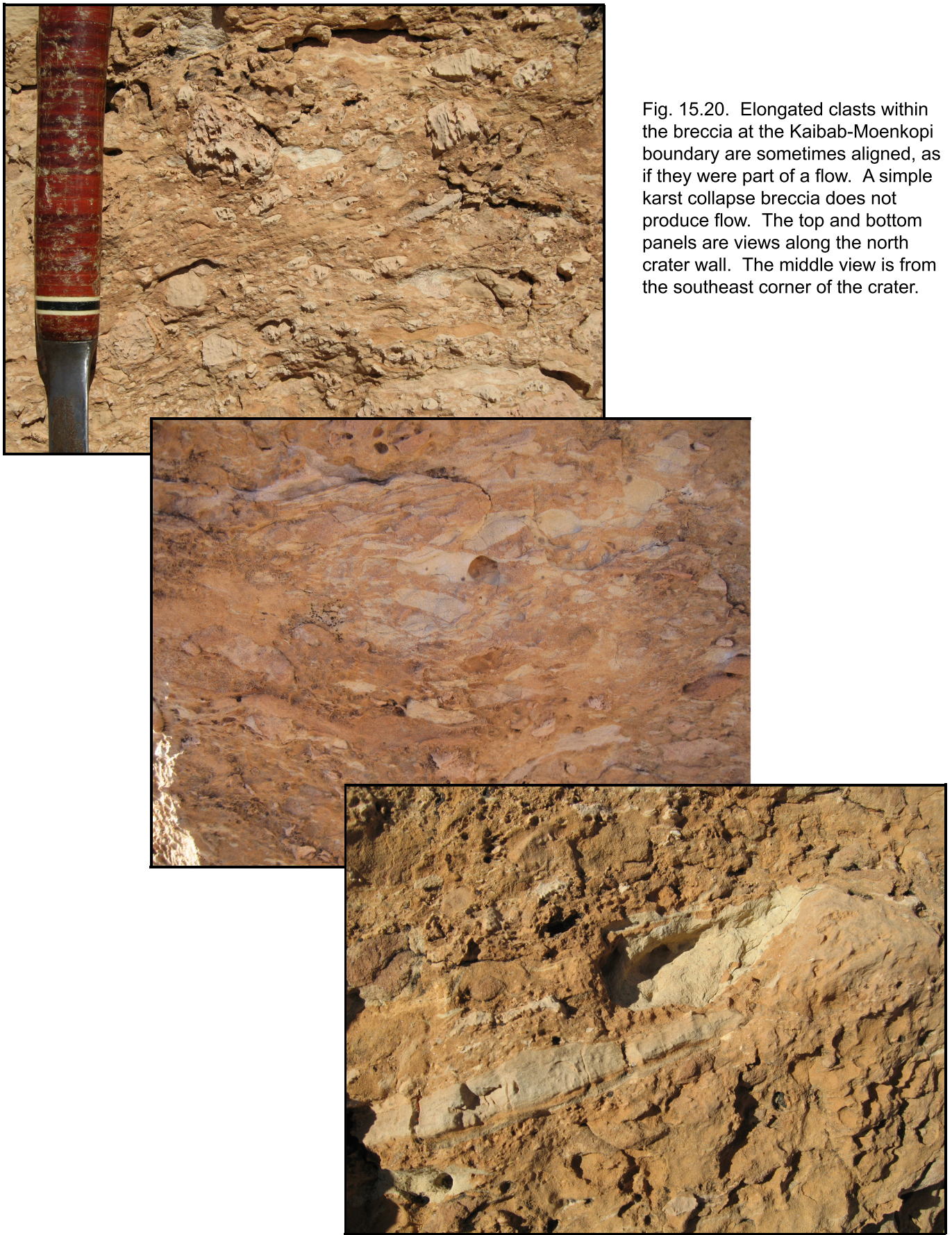


Fig. 15.20. Elongated clasts within the breccia at the Kaibab-Moenkopi boundary are sometimes aligned, as if they were part of a flow. A simple karst collapse breccia does not produce flow. The top and bottom panels are views along the north crater wall. The middle view is from the southeast corner of the crater.



Fig. 15.21. Most of the south rim of the crater is covered with debris from the Toroweap and Coconino formations. The aeolian Coconino sandstone is being eroded to produce a second generation of aeolian sands that now blanket portions of the south rim. Most blocks appear to have fractured along cross-bed contacts, because there are very few blocks with any hint of cross-bedding. An exception is shown above.

❖ Bibliography

Note: This bibliography contains the sources used in the text above. To assist readers with other projects, it also includes a broader list of publications that have been involved in the developing story of the crater.

Ackermann, H.D. and Godson, R.H. (1966) P-wave velocity and attenuation summary, FY-66. In Investigation of in situ physical properties of surface and subsurface site materials by engineering geophysical techniques, annual report, fiscal year 1966, edited by J.S. Watkins. NASA Contractor Report (CR)-65502 and USGS Open-File Report 67-272, pp. 305-317.

Ackermann, H.D., Godson, R.H., and Watkins, J.S. (1975) A seismic refraction technique used for subsurface investigations at Meteor crater, Arizona. *Journal of Geophysical Research*, v. 80, pp. 765-775.

Ahrens, T.J. and Gregson, V.G. Jr. (1964) Shock compression of crustal rocks; data for quartz, calcite, and plagioclase rocks. *Journal of Geophysical Research*, v. 69, pp. 4,839-4,874.

Ai, H.-A. and Ahrens, T.J. (2004) Dynamic tensile strength of terrestrial rocks and application to impact cratering. *Meteoritics and Planetary Science*, v. 39, pp. 233-246.

Alexander, E.C. Jr. and Manuel, O.K. (1958) Isotopic anomalies of krypton and xenon in Canyon Diablo graphite. *Earth and Planetary Science Letters*, v. 2, pp. 220-224.

Anders, E. and Lipschutz, M.E. (1966) Critique of paper by N.L. Carter and G.C. Kennedy, 'Origin of Diamonds in the Canyon Diablo and Novo Urei meteorites.' *Journal of Geophysical Research*, v. 71, pp. 643-674.

Artemieva, N.A. (2006) Size and velocity of Canyon Diablo meteorite - models comparison (abstract). *Meteoritics and Planetary Science*, v. 41, p. A17.

Barnes, W.C. (1934) The "discovery" of Meteor crater. Museum Northern Arizona (Flagstaff). *Museum Notes*, v. 7, pp. 5-8.

Barringer, B. (1964) Daniel Moreau Barringer (1860-1929) and his crater (The beginning of the Crater Branch of Meteoritics). *Meteoritics*, v. 2, pp. 183-199.

Barringer, B. (1967) Historical notes on the Odessa Meteorite Crater. *Meteoritics*, v. 3, pp. 161-168.

Barringer, D.M. (1905) Coon Mountain and its crater. *Proceedings of the Academy of Natural Sciences of Philadelphia*, v. 57, pp. 861-886.

Barringer, D.M. (1910) Meteor Crater (formerly called Coon Mountain or Coon Butte) in northern central Arizona. Paper presented at the National Academy of Sciences, Princeton University, Nov. 16, 1909. 24 p. (plus 18 plates, and 3 maps).

Barringer, D.M. (1914) Further notes on Meteor Crater, Arizona. *American Journal of Science*, v. 39, pp. 482-483.

Barringer, D.M. (1924) Further notes on Meteor crater in northern central Arizona (No. 2). Proceedings Academy of Natural Sciences of Philadelphia, v. 76, pp. 275-278.

Beaty, J.J. (1966) The great crater controversy. *Frontiers*, v. 30, pp. 112-117.

Bennett, J.H. and Manuel, O.K. (1967) On the origin of noble gas anomalies in Canyon Diablo graphite. *Earth and Planetary Science Letters* 3, 95-100.

Bingham, W.F. (1937) Summary of findings from exploration, geophysical survey, and test-drilling at Meteor crater, Arizona. *Pan-American Geologist*, v. 68, pp. 196-198.

Bjork, R.L. (1961) Analysis of the formation of Meteor crater, Arizona: A preliminary report. *Journal of Geophysical Research*, v. 66, pp. 3,379-3,387.

Blackwelder, E. (1932) The age of Meteor Crater. *Science*, v. 76, pp. 557-560.

Blau, P.J., Axon, H.J., and Goldstein, J.I. (1973) Investigation of the Canyon Diablo metallic spheroids and their relationship to the breakup of the Canyon Diablo meteorite. *Journal of Geophysical Research*, v. 78, pp. 363-374.

Boone, J.D. and Albritton, C.C. Jr. (1938) The impact of large meteorites. *Field and Laboratory*, v. 6, pp. 57-64.

Brereton, R.G. (1965) Aeromagnetic survey of Meteor crater, Arizona. New York Academy Sciences, *Annals*, v. 123, pp. 1175-1181.

Brett, R. (1967) Metallic spherules in impactite and tektite glasses. *American Mineralogist*, v. 52, pp. 721-733.

Brett, R.G. (1968) Opaque minerals in drill cuttings from Meteor Crater, Arizona. U.S. Geological Survey Professional Paper 600-D, D179-D180.

Briley, D.J. and Moore, C.B. (1976) A checklist of published references to Barringer meteorite crater, Arizona, 1891-1970. Center for Meteorite Studies, Arizona State University, 71 p.

Brown, F.M. (1933) The Age of Meteor Crater. *Science* 77, 239-240.

Brown, D.E. and Lowe, C.H. (1980) Map of Biotic Communities of the Southwest. U.S. Government Printing Office, Washington, DC. (Also published as a supplementary map to Biotic Communities: Southwestern United States and Northwestern Mexico, edited by D.E. Brown, University of Utah Press, Salt Lake City, 1994).

Bryan, J.B. (1978) Meteorite impact cratering on a digital computer: A simulation of the formation of Meteor (Barringer) Crater, Arizona. *Meteoritics*, v. 13, pp. 399-402.

Bryan, J.B., Burton, D.E., Cunningham, M.E., and Lettis, L.A. Jr. (1978) A two-dimensional computer simulation of hypervelocity impact cratering: Some preliminary results for Meteor crater, Arizona. *Proceedings Lunar and Planetary Science Conference* 9th, pp. 3,931-3,964.

Buchwald, V.F. (1975) Handbook of iron meteorites. University of California Press, Berkeley, v. 3, pp. 937-942.

Buddhue, J.D. (1948) A sieve analysis of crushed sandstone from the Canyon Diablo, Arizona, meteorite crater. *Popular Astronomy*, v. 56, pp. 387-389.

Bunch, T.E. and Cohen, A.J. (1964) Shock deformation of quartz from two meteorite craters. *Geological Society of America Bulletin*, v. 75, pp. 1,263-1,266.

Busch, M.W., Giorgini, J.D., Ostro, S.J., Benner, L.A.M., Pravec, P., Kusnirak, P., Ireland, M.J., Scheeres, D.J., Broschart, S.B., Magri, C., Nolan, M.C., and Hine, A.A. (2007) Physical modeling of near-Earth asteroid (29075) 1950 DA. *Icarus*, submitted.

Carlson, R.H. and Roberts, W.A. (1963) Project Sedan: Mass Distribution and Throwout Studies. U.S. Atomic Energy Commission, Report PNE-217F, 143 p.

Camp C.L., Colbert E.H., McKee E.D., and Welles S.P. (1947) A guide to the continental Triassic of northern Arizona. *Plateau*, v. 20, pp. 1-9.

Carter, N.L. (1965) Basal quartz deformation lamellae--a criterion for recognition of impactites. *American Journal of Science*, v. 263, pp. 786-806.

Carter, N.L. and Kennedy G.C. (1964) Origin of diamonds in the Canyon Diablo and Novo Urei meteorites. *Journal of Geophysical Research*, v. 69, pp. 2,403-2,421.

Carter, N.L. and Kennedy G.C. (1966) Origin of diamonds in the Canyon Diablo and Novo Urei meteorites — A reply. *Journal of Geophysical Research*, v. 71, pp. 663-672.

Chamberlin, T.C. (1890) The method of multiple working hypotheses. *Science*, vol. XV, no. 366, pp. 92-96.

Chao, E.C.T. (1967) Impact metamorphism. In *Researches in Geochemistry*, v. 2, edited by P.H. Abelson, pp. 204-233. John Wiley and Sons, New York.

Chao, E.C.T., Shoemaker, E.M., and Madsen, B.M. (1960) First natural occurrence of coesite. *Science*, v. 132, pp. 220-222.

Chao, E.C.T., Fahey, J.J., Littler, J., and Milton, D.J. (1962) Stishovite, SiO₂, a very high pressure new mineral from Meteor crater, Arizona. *Journal of Geophysical Research*, v. 67, pp. 419-421.

Chao, E.C.T. (1966) Impact metamorphism. U.S. Geological Survey, Astrogeologic Studies Annual Progress Report, pp. 135-168.

Cook, C.S. (1964) Mass of the Canyon Diablo meteoroid. *Nature*, v. 204, p. 867.

Crocket, J.H. (1972) Some aspects of the geochemistry of Ru, OS, Ir and Pt in iron meteorites. *Geochimica et Cosmochimica Acta*, v. 36, pp. 517-535.

Crowson, H.L. (1971) A method for determining the residual meteoritical mass in the Barringer meteor crater. *Pure and Applied Geophysics*, v. 85, pp. 38-68.

Darton, N.H. (1910) A reconnaissance of parts of northwestern New Mexico and northern Arizona. *USGS Bulletin* 435, 88 p. and 17 pl. (including 3 folded maps).

Davis, O. and Kring, D.A. (200) Preliminary analysis of the late Pleistocene lake sediments deposited in Barringer Crater, Coconino County, Arizona (abstract). Abstract volume for the Annual Meeting of the Arizona-Nevada Academy of Sciences.

Davison, J.M. (1910) A contribution to the problem of Coon Butte. *Science*, v. 32, pp. 724-726.

Derby, O.A. (1895) Constituents of the Canyon Diablo Meteorite. *American Journal of Science*, v. 49, pp. 101-110.

Dietz, R.S. (1963) Astroblemes: Ancient meteorite-impact structures on the Earth. Middlehurst, B.M. and Kuiper, G.P., eds., *The Moon, Meteorites and Comets*, University of Chicago Press, Chicago, v. IV, pp. 285-300.

Elston, W.E. (1990) How did impact processes on Earth and Moon become respectable in geological thought? *Earth Sciences History*, v. 9, pp. 82-87.

Elwood Madden, M.E., Kring, D.A., and Bodnar, R.J. (2006) Shock reequilibration of fluid inclusions in Coconino sandstone from Meteor Crater, Arizona. *Earth and Planetary Science Letters*, v. 241, pp. 32-46.

Fahey, J.J. (1964) Recovery of coesite and stishovite from Coconino sandstone of Meteor Crater, Arizona. *American Mineralogist*, v. 49, pp. 1643-1647.

Fairchild, H.L. (1907) Origin of Meteor Crater (Coon Butte), Arizona. *Geological Society of America Bulletin*, v. 18, pp. 493-504.

Fairchild, H.L. (1930) Nature and fate of the Meteor crater bolide. *Science*, v. 72, pp. 463-467.

Farrington, O.C. (1906) Analysis of 'iron shale' from Coon Mountain, Arizona. *American Journal of Science*, v. 22, pp. 303-309.

Fletcher, L.A. (1906) A search for a buried meteorite. *Nature*, v. 74, pp. 490-492.

Foote, A.E. (1891) Geological features of the meteoric locality in Arizona. *Academy of Natural Sciences Philadelphia Proceedings*, v. 40, p. 407.

Foote, A.E. (1892) A new locality for meteoric iron with a preliminary notice of discovery of diamonds in the iron. *Proc. American Association of Advanced Science*, v. 40, pp. 279-283.

Forester, R.M. (1987) Late Quaternary paleoclimate records from lacustrine ostracodes. In Ruddiman, W.F. and Wright, H.E. Jr. (eds.), *North America and Adjacent Oceans During the Last Glaciation*, v. K-3, pp. 261-276. *The Geology of North America*. Geological Society of America, Boulder.

Foster, G.E. (1953) Arizona's Meteorite Crater. Meteor Crater Publications, Winslow, Arizona, 28 pp.

Foster, G.E. (1957) The Barringer (Arizona) meteorite crater. Meteor Crater, Ariz., Published Privately, 31 p.

Foster, G.E. (1964) The Meteor Crater Story. Meteor Crater Enterprises, Inc., Winslow, Arizona, 32 pp.

Frandsen, A.D. (1967) Project Pre-Schooner II: Postshot geologic and engineering properties investigations. U.S. Army Engineer Nuclear Cratering Group, Final Report PNE-516, 63 pp.

- Gilbert, G.K. (1896) The origin of hypotheses, illustrated by the discussion of a topographic problem. *Science*, v. 3, pp. 1-13 (plus 1 plate).
- Grady, M.M. (2000) Catalogue of Meteorites (Fifth edition). Cambridge University Press, Cambridge, 689 p. (plus CD-ROM).
- Grant, J.A. and Schultz, P.H. (1993) Erosion of ejecta at Meteor Crater, Arizona. *Journal of Geophysical Research*, v. 98, pp. 15,033-15047.
- Greenwood, W.R. and Morrison, D.A. (1969) Genetic significance of the morphology of some impact bombs from Meteor crater, Arizona. *Meteoritics*, v. 4, pp. 182-183.
- Grieve, R.A.F. (1982) The record of impact on Earth: Implications for a major Cretaceous/Tertiary impact event. *Geological Society of America, Special Paper* 190, pp. 25-37.
- Grieve, R.A.F. (1991) Terrestrial impact: The record in the rocks. *Meteoritics*, v. 26, pp. 175-194.
- Grieve, R.A.F. and Garvin, J.B. (1984) A geometric model for excavation and modification at terrestrial simple impact craters. *Journal of Geophysical Research*, v. 89, pp. 11,561-11,572.
- Grieve, R.A.F., Garvin, J.B., Coderre, J.M., and Rupert, J. (1989) Test of a geometric model for the modification stage of simple impact crater development. *Meteoritics*, v. 24, pp. 83-88.
- Grieve R., Rupert J., Smith J., and Therriault A. (1995) The record of terrestrial impact cratering. *GSA Today*, v. 5(10), pp. 189 and 194-196.
- Hager, D. (1953) Crater Mound (Meteor crater), Arizona, a geologic feature. *American Association of Petroleum Geologists, Bulletin*, v. 37, pp. 821-857.
- Hager, D. (1954) Notes on Crater Mound in answer to some points raised by H.H. Nininger. *American Journal of Science*, v. 252, pp. 695-697.
- Haines, D.V. (1966) Petrography of Meteor Crater Core 4, Meteor Crater, Arizona. In: Investigation of in situ physical properties of surface and subsurface site materials by engineering geophysical techniques, annual report, fiscal year 1966, edited by J.S. Watkins. NASA Contractor Report (CR)-65502 and USGS Open-File Report 67-272, pp. 171-194.
- Hall, R.A. (1965) Secondary meteorites from the Arizona crater. *Meteoritics*, v. 2, pp. 337-348.
- Hargraves, R.B. and Perkins W.E. (1969) Investigations of the effect of shock on natural remanent magnetism. *Journal of Geophysical Research*, v. 74, pp. 2,576-2,589.
- Heymann, D. (1964) Origin of the Canyon Diablo No. 2 and No. 3 meteorites. *Nature*, v. 204, pp. 819-820.
- Heymann, D., Lipschutz, M.E., Nielsen, B., and Anders, E. (1966) Canyon Diablo meteorite: Metallographic and mass spectrometric study of 56 fragments. *Journal of Geophysical Research*, v. 71, pp. 619-641.
- Hodge P.W. and Wright F.W. (1970) Meteoritic spherules in the soil surrounding terrestrial impact craters. *Nature*, v. 225, pp. 717-718.

Holliday, V.T., Kring, D.A., Mayer, J.H., and Goble, R.J. (2005) Age and effects of the Odessa meteorite impact, western Texas, USA. *Geology*, v. 33, pp. 945-948.

Hörz, F., Ostertag, R., and Rainey, D.A. (1983) Bunte breccia of the Ries: Continuous deposits of large impact craters. *Reviews of Geophysics and Space Physics*, v. 21, pp. 1667-1725.

Hörz, F., Mittlefehldt, D.W., See, T.H., and Galindo, C. (2002) Petrographic studies of the impact melts from Meteor Crater, Arizona, USA. *Meteoritics and Planetary Science*, v. 37, pp. 501-531.

Hoyt, W.G. (1987) Coon Mountain Controversies: Meteor Crater and the Development of the Impact Theory. The University of Arizona Press, Tucson, 442 p.

Ivanov, B.A. and Basilevsky, A.T. (1985) Meteorite craters (in Russian). *Priroda*, v. 10, pp. 23-35.

Ives P.C., Levin B., Robinson R.D., and Rubin M. (1964) U. S. Geological Survey radiocarbon dates VII. *Radiocarbon*, v. 6, pp. 37-76.

Jakosky, J.J., Wilson, C.H., and Daly, J.W. (1932) Geophysical examination of Meteor crater, Arizona. American Institute of Mining, Metallurgical, and Petroleum Engineers, Transactions, v. 97, pp. 63-98.

Jakosky, J.J. (1932) Geophysical methods locate meteorite. *Engineering and Mining Journal-Press*, v. 133, pp. 392-393.

Johnson G.W. (1960) Note on estimating the energies of the Arizona and Ungava meteorite craters. California Univ., Livermore, Lawrence Radiation Lab. Report UCRL-6227, 18 pp. (Report prepared for the U.S. Atomic Energy Commission)

Kaputskina, I.G. and Fel'dman, V.I. (1988) Fractionation of meteoritic material in the impact process (in Russian). *Geokhimiya*, v. 11, pp. 1547-1557.

Kargel, J.S. Coffin, P., Kraft, M., Lewis, J.S., Moore, C., Roddy, D., Shoemaker, E.M. and Wittke, J.H. (1996) Systematic collection and analysis of meteoritic materials from Meteor crater, Arizona (abstract). *Lunar and Planetary Science*, v. XXVII, pp. 645-646.

Kelley, V.C. and Clinton, J.N. (1960) Fracture Systems and Tectonic Elements of the Colorado Plateau. University of New Mexico Publications in Geology, No. 6, University of New Mexico Press, Albuquerque, 104 p.

Kelly, W.R., Holdworth, E., and Moore, C.B. (1974) The chemical composition of metallic spheroids and metallic particles within impactite from Barringer meteorite crater, Arizona. *Geochimica et Cosmochimica Acta*, v. 38, pp. 533-543.

Kieffer, S.W. (1971) Shock metamorphism of the Coconino sandstone at Meteor crater, Arizona. *Journal of Geophysical Research*, v. 76, pp. 5449-5473.

Kieffer, S.W. (1974) Shock metamorphism of the Coconino sandstone at Meteor Crater. In: Guidebook to the Geology of Meteor Crater, Arizona, edited by E.M. Shoemaker and S.W. Kieffer. Center for Meteorite Studies Publication No. 17, Arizona State University, pp. 12-19.

Kieffer, S.W. (1976) Shock processes in porous quartzite: Transmission electron microscope observations and theory. *Contributions to Mineralogy and Petrology*, v. 59, pp. 41-93.

- Kieffer, S.W. and Simonds, C.H. (1980) The role of volatiles and lithology in the impact cratering process. *Reviews of Geophysics and Space Physics*, v. 18, pp. 143-181.
- Koeberl, C., Reimold, W.U., and Shirey, S.B. (1995) Saltpan impact crater, South Africa: Geochemistry of target rocks, breccias, and impact glasses, and osmium isotope systematics. *Geochimica et Cosmochimica Acta*, v. 58, pp. 2893-2910.
- Koeberl, C., Reimold, W.U., and Shirey, S.B. (1998) The Aouelloul crater, Mauritania: On the problem of confirming the impact origin of a small crater. *Meteoritics and Planetary Science*, v. 33, pp. 513-517.
- Kreins, E.R. (1953) Results of a systematic study of the ratio of meteorite to oxidite at the Barringer Meteorite Crater of Arizona. *Meteoritics*, v. 1, pp. 29-30.
- Kring, D.A. (1997) Air blast produced by the Meteor Crater impact event and a reconstruction of the affected environment. *Meteoritics and Planetary Science*, v. 32, pp. 517-530
- Kring, D.A. (1999) Calamity at Meteor Crater. *Sky and Telescope*, vol. 98, no. 5, pp. 48-53.
- Kring, D.A. (2003) Meteor Crater & An Asteroid's Impact on Floral Ecosystems; with sidebar 'Megafauna & Dietary Flora.' *Wildflower*, v. 19(4), pp. 16-17 and 29.
- Kring, D.A. (2005) Hypervelocity collisions into continental crust composed of sediments and an underlying crystalline basement: Comparing the Ries (~24 km) and Chicxulub (~180 km) impact craters. *Chemie der Erde*, v. 65, pp. 1-46.
- Kring, D.A. (2006) Blast from the Past. *Astronomy*, v. 34(8), pp. 46-51.
- Kring, D.A., Jull, A.J.T., McHargue, L.R., Bland, P.A., Hill, D.H., and Berry, F.J. (2001) Gold Basin meteorite strewn field, Mojave Desert, northwestern Arizona: Relic of a small late Pleistocene impact event. *Meteoritics and Planetary Science*, v. 36, pp. 1057-1066.
- Krinov, E.L. (1966) The Arizona (Barringer) meteorite crater. Beynon, M.M., ed., *Giant Meteorites*, Pergamon Press, New York, pp. 78-124.
- Ksanda, C.J. and Henderson, E.P. (1939) Identification of diamond in the Canyon Diablo iron. *American Mineralogist*, v. 24, pp. 677-680.
- Kunz, G.F. and Huntington, E.P. (1939) On the diamond in the Canyon Diablo meteoric iron, and on the hardness of carborundum. *American Journal of Science*, v. 46, pp. 470-473.
- LaPaz, L. (1953) The discovery and interpretation of nickel - iron granules associated with meteorite craters. *R.A.S.C. Journal*, v. 47, pp. 191-194.
- Leonard, F.C. (1950) The name of the Barringer meteorite crater of Arizona. *Popular Astronomy*, v. 58, p. 469.
- Leya, I., Wieler, R., Ma, P., Schnabel, C., and Herzog, G.F. (2002) Pre-atmospheric depths and thermal histories of Canyon Diablo spheroids. *Meteoritics and Planetary Science*, v. 37, pp. 1015-1025.
- Lipschutz, M.E. and Anders, E. (1961a) The record in the meteorites, 4, Origin of diamonds in iron meteorites. *Geochimica et Cosmochimica Acta*, v. 24, pp. 83-105.

Lipschutz, M.E. and Anders, E. (1961b) On the mechanism of diamond formation. *Science*, v. 134, pp. 2095-2099.

Magie, W.F. (1910) Physical notes of Meteor Crater, Arizona. *Proceedings of the American Philosophical Society*, v. 49, p. 41.

Marvin, U.B. (1990) Impact and its revolutionary implications for geology. In: *Global Catastrophes in Earth History, An Interdisciplinary Conference on Impacts, Volcanism, and Mass Mortality*, V.L. Sharpton and P.D. Ward (eds.), Special Paper 247, Geological Society of America, Boulder, pp. 147-154.

McKee, E.D. (1934) The Coconino Sandstone – Its history and origin. *Contributions to Paleontology*, Carnegie Institution of Washington Publication 400, pp. 78-115.

McKee, E.D. (1938) The environment and history of the Toroweap and Kaibab Formations of northern Arizona and southern Utah. *Carnegie Institution of Washington Publication* 492, 221 p.

McKee, E.D. (1951) Triassic deposits of the Arizona-New Mexico border area. *New Mexico Geological Society Guidebook, 2nd Field Conference*, San Juan Basin, pp. 85-92.

McKee, E.D. (1954) Stratigraphy and history of the Moenkopi Formation of Triassic age. *Geological Society of America Memoir* 61, 133 p.

Mead, C.W., Littler, J., and Chao, E.C.T. (1965) Metallic spheroids from Meteor crater. *American Mineralogist*, v. 50, pp. 667-681.

Melosh, H.J. and Collins, G.S. (2005) Meteor Crater formed by low-velocity impact. *Nature*, v. 434, p. 157.

Merrill, G.P. (1908) The Meteor Crater of Canyon Diablo, Arizona; its history, origin, and associated meteoric irons. *Smithsonian Miscellaneous Collections*, v. L, no. 1789, pp. 461-498 (with multiple plates).

Michlovich, E.S., Vogt, S., Masarik, J., Reedy, R.C., Elmore, D., and Lipschutz, M.E. (1994) Aluminum 26, ^{10}Be , and ^{36}Cl depth profiles in the Canyon Diablo iron meteorite. *Journal of Geophysical Research*, v. 99, pp. 23,187-23,194.

Moore, C.B., Birrell, P.J., and Lewis, C.F. (1967) Variations in the chemical and mineralogical composition of rim and plains specimens of the Canyon Diablo meteorite. *Geochimica et Cosmochimica Acta*, v. 31, pp. 1,885-1,892.

Niermeyer, J.F. (1949) A new type of magnetometer survey of Barringer meteorite crater. *Popular Astronomy*, v. 57, pp. 1-5.

Nininger, H.H. (1949) Oxidation studies at Barringer Crater, Metal-center pellets and oxide droplets. *American Philosophical Society Yearbook*, pp. 126-130.

Nininger, H.H. (1951) Condensation globules at Meteor Crater. *Science*, v. 113, pp. 755-756.

Nininger, H.H. (1954) Impactite slag at Barringer crater. *American Journal of Science*, v. 252, pp. 277-290.

Nininger, H.H. (1956) Arizona's Meteorite Crater. American Meteorite Museum, Sedona, 232 p.

Nishiizumi, K., Kohl, C.P., Shoemaker, E.M., Arnold, J.R., Klein, J., Fink, D., and Middleton, R. (1991) In situ ^{10}Be - ^{26}Al exposure ages at Meteor Crater, Arizona. *Geochimica et Cosmochimica Acta*, v. 55, pp. 2,699-2,703.

Noble, L.F. (1914) The Shinumo Quadrangle. U.S. Geological Survey Bulletin 549, 100 p.

Öpik, E.J. (1958) Meteor impact on solid surface. *Irish Astronomical Journal*, v. 5, pp. 14-33.

Öpik, E.P. (1936) Researches on the Physical Theory of Meteor Phenomena. I. Theory of the formation of meteor craters. *Publications of the Astronomical Observatory of the University of Tartu*, v. 28, pp. 3-12.

Ostro, S.J., Campbell, D.B., Chandler, J.F., Hine, A.A., Hudson, R.S., Rosema, K.E., and Shapiro, I.I. (1991) Asteroid 1986 DA: Radar evidence for a metallic composition. *Science*, v. 252, pp. 1,401-1,404.

Peabody F.E. (1948) Reptile and amphibian trackways from the Lower Triassic Moenkopi Formation of Arizona and Utah. *University of California Publications, Bulletin of the Department of Geologocial Sciences*, v. 27, pp. 295-468.

Phillips, F.M., Zreda, M.G., Smith, S.S., Elmore, D., Kubik, P.W., Dorn, R.I., and Roddy, D.J. (1991) Age and geomorphic history of Meteor Crater, Arizona, from cosmogenic ^{36}Cl and ^{14}C in rock varnish. *Geochimica et Cosmochimica Acta*, v. 55, pp. 2,695-2,698.

Pilon, J.A., Grieve, R.A.F., and Sharpton, V.L. (1991) The subsurface character of Meteor Crater, Arizona, as determined by ground-probing radar. *Journal of Geophysical Research*, v. 96, pp. 15,563-15,576.

Pilon, J.A., Grieve, R.A.F., Sharpton, V.L., Coderre, J., and Kennedy, J. (1992) Reconnaissance ground penetrating radar survey of the interior of Meteor Crater, Arizona. Pilon, J.A., ed., *Geological Survey of Canada Paper 90-4, Ground Penetrating Radar*, Canada Communications Group, Ottawa, Canada, pp. 177-186.

Ramsey, M.S. (2002) Ejecta distribution patterns at Meteor Crater, Arizona: On the applicability of lithologic end-member deconvolution for spaceborne thermal infrared data of Earth and Mars, *Journal of Geophysical Research*, v. 107, no. E9, 5059, doi: 10.1029/2001JE001827.

Read, C.B. (1950, reprinted 1996) Stratigraphy of the outcropping Permian rocks around the San Juan Basin. *New Mexico Geological Society Guidebook of the San Juan Basin, New Mexico and Colorado*, 152 pp., edited by V.C. Kelley, E.C. Beaumont, and C. Silver, pp. 62-66.

Regan, R.D. and Hinze, W.J. (1975) Gravity and magnetic investigations of Meteor crater, Arizona. *Journal of Geophysical Research*, v. 80, pp. 776-778.

Regan, R.D. (1967) Technical letter: Astrogeology 29. Preliminary geophysical report on selected geologic test sites. United States Department of the Interior Geological Survey, pp. 1-22.

Reger, R.D. and Batchelder G.L. (1971) Late Pleistocene molluscs and a minimum age of Meteor Crater, Arizona. *Journal of the Arizona Academy of Science*, v. 6, pp. 190-195.

Reiche, P. (1938) An analysis of cross-lamination of the Coconino sandstone. *Journal of Geology*, v. 46, no. 7, pp. 905-932.

Rinehart, J.S. (1957) A soil survey around the Barringer crater. *Sky and Telescope*, v. 16, pp. 366-369.

Rinehart, J.S. (1958) Distribution of meteoritic debris about the Arizona meteorite crater. *Smithsonian Contributions to Astrophysics*, v. 2, pp. 145-160.

Roberts, W.A. (1965) Genetic stratigraphy of the Meteor crater outer lip. *Icarus*, v. 4, pp. 431-433.

Roberts, W.A. (1968) Shock crater ejecta characteristics. In *Shock Metamorphism of Natural Materials*, B.M. French and N.M. Short (eds.), Mono Book Corp., Baltimore, MD, pp. 101-114.

Roddy, D.J. (1977) Large-scale impact and explosion craters: Comparisons of morphological and structural analogs. In: *Impacts and Explosion Cratering*, D.J. Roddy, R.O. Pepin, and R.B. Merrill (eds.), Pergamon Press, New York, pp. 185-246.

Roddy, D.J. (1978) Pre-impact geologic conditions, physical properties, energy calculations, meteorite and initial crater dimensions and orientations of joints, faults and walls at Meteor Crater, Arizona. *Proc. Lunar Planetary Science Conf. 9th*, pp. 3,891-3,930.

Roddy, D.J. and Shoemaker, E.M. (1995) Meteor crater (Barringer meteorite crater), Arizona: Summary of impact conditions (abstract). *Meteoritics*, v. 30, pp. 567.

Roddy, D.J., Boyce, J.M., Colton, G.W., and Dial A.L. Jr. (1975) Meteor Crater, Arizona, rim drilling and thickness, structural uplift, diameter, depth, volume, and mass-balance calculations. *Proc. Lunar Science Conf. 6th*, pp. 2,621-2,644.

Roddy, D.J., Schuster, S.H., Dreyenhagen K.N., and Orphal, D.L. (1980) Computer code simulations of the formation of Meteor Crater, Arizona: Calculations MC-1 and MC-2. *Proc. Lunar Planetary Science Conf. 11th*, pp. 2,275-2,308.

Rogers, A.F. (1928) Natural history of the silica minerals. *American Mineralogist*, v. 13, pp. 73-92.

Rostoker, N. (1953) The formation of craters by high-speed particles. *Meteoritics*, v. 1, pp. 11-27.

Ryabenko, V.A. and Val'ter, A.A. (1977) Meteorite explosion craters as an object of study in modern geology (in Russian). *Visnyk*, v. 1-6, pp. 7-16.

Schmidt, R.M. (1980) Meteor Crater: Energy of formation-implications of centrifuge scaling. *Proceedings Lunar and Planetary Science Conference 11th*, pp. 2,099-2,128.

Schnabel, C., Pierazzo, E., Xue, S., Herzog, G.F., Masarik, J., Cresswell, R.G., di Tada, M.L., Liu, K., and L.K. Fifield (1999) Shock melting of the Canyon Diablo impactor: constraints from nickel-59 contents and numerical modeling. *Science*, v. 285, pp. 85-88

Schuchert, C. (1918) On the Carboniferous of the Grand Canyon of Arizona. *American Journal of Science*, v. XLV (4th Series), pp. 347-434.

See, T.H., Hörz, F., Mittlefehldt, D.W., Varley, L., Mertzman, S., and Roddy, D. (2002) Major element analyses of the target rocks at Meteor Crater, Arizona. *NASA Technical Memorandum (TM)-2002-*

210787, 31 p.

Shipman, F.H. and Gregson, V.G., and Jones, A.H. (1971) A shock-wave study of Coconino sandstone. NASA Contractor Report (CR)-1842, 46 p.

Shoemaker, E.M. (1959) Impact mechanics at Meteor crater, Arizona, U.S. Atomic Energy Commission Open File Report, 55 p.

Shoemaker, E.M. (1960) Penetration mechanics of high velocity meteorites, illustrated by Meteor crater, Arizona. International Geological Congress, 21st, Copenhagen, pp. 418-434.

Shoemaker, E.M. (1963) Impact mechanics at Meteor crater, Arizona. In: The Moon, Meteorites and Comets, edited by Middlehurst, B.M. and Kuiper, G.P., University of Chicago Press, Chicago, v. IV, pp. 301-336.

Shoemaker, E.M. (1983) Asteroid and comet bombardment of the Earth. Annual Review of Earth and Planetary Sciences, v. 11, pp. 461-494.

Shoemaker, E.M. (1987) Meteor Crater, Arizona. Geological Society of America Centennial Field Guide - Rocky Mountain Section, pp. 399-404.

Shoemaker, E.M. and Kieffer, S.W. (1974) Guidebook to the geology of Meteor crater, Arizona. Meteoritical Society, 37th Annual Meeting, Arizona State University Centre for Meteorite Studies, Tempe, Arizona, 1974 (66 pp.) Reprinted in 1988.

Skinner, B.J. and Fahey, J.J. (1963) Observations on the inversion of stishovite to silica glass. Journal of Geophysical Research, v. 68, pp. 5,595-5,604.

Skrynnik, G.V. (1977) Meteorite craters on the Earth (in Russian). Astronomicheskii Vestnik, v. 11, pp. 198-210.

Smiley, T.L. (1958) The geology and dating of Sunset Crater, Flagstaff, Arizona. In Guidebook of the Black Mesa Basin, Northeastern Arizona, R.Y. Anderson and J.W. Harschbarger (eds.), New Mexico Geological Society, Ninth Field Conference, pp. 186-190.

Southgate, N. and F. Barringer (2002) A Grand Obsession: Daniel Moreau Barringer and His Crater. The Barringer Crater Company, Flagstaff, Arizona, 78 p.

Spencer, L.J. (1933) Meteorite craters as topographical features on the Earth's surface. Geographical Journal (London), v. 81, pp. 227-248.

Stöffler, D. (1972) Deformation and transformation of rock-forming minerals by natural and experimental shock processes: I. Behavior of minerals under shock compression. Fortschr. Mineral., v. 49, pp. 50-113.

Sutton, S.R. (1985) Thermoluminescence measurements on shock-metamorphosed sandstone and dolomite from Meteor Crater, Arizona. 1. shock dependence of thermoluminescence properties. Journal of Geophysical Research, v. 90, pp. 3683-3689.

Sutton, S.R. (1985) Thermoluminescence measurements on shock-metamorphosed sandstone and dolomite from Meteor Crater, Arizona. 2. Thermoluminescence age of Meteor crater. Journal of Geophysical Research, v. 90, pp. 3,690-3,700.

Tilghman, B.C. (1905) Coon Butte, Arizona. Proceedings of the Academy of Natural Sciences of Philadelphia, v. 57, pp. 887-914.

Urey, H.C. (1956) Diamonds, meteorites, and the origin of the solar system. *Astrophysics Journal*, v. 124, pp. 623-637.

Val'ter, A.A. and Gurov, E.P. (1978) The system of mineralogical indicators in factors of shock metamorphism in granitoid rocks (in Russian). *Kosmicheskaya mineralogiya*, v. 11, pp. 92-102.

Walters, L.A. (1966) In situ physical properties measurements. In *Investigation of in situ physical properties of surface and subsurface site materials by engineering geophysical techniques, annual report, fiscal year 1966*, edited by J.S. Watkins. NASA Contractor Report (CR)-65502 and USGS Open-File Report 67-272, pp. 7-24.

Wasson, J.T. (1967) Concentrations of Ni, Ga, and Ge in a series of Canyon Diablo and Odessa meteorite specimens. *Journal of Geophysical Research*, v. 72, pp. 721-730.

Wasson, J.T. (1968) Concentrations of nickel, gallium, germanium, and iridium in Canyon Diablo and other Arizona octahedrites. *Journal of Geophysical Research*, v. 73, 3,207-3,211.

Wasson, J.T. and Ouyan, X. (1990) Compositional range in the Canyon Diablo meteoroid. *Geochimica et Cosmochimica Acta*, v. 54, pp. 3,175-3,183.

Watkins, J.S., ed. (1966) Annual Report, Investigation of in situ physical properties of surface and subsurface site materials by engineering geophysical techniques. NASA Contract T-25091(G). Also catalogued as NASA Contractor Report (CR)-65502 and USGS Open-File Report 67-272. 373 p.

Watkins, J.S. and Walters, L.A. (1966) Laboratory physical property measurements on core and surface samples from six lunar analog test sites. In: *Investigations of in situ physical properties of surface and subsurface site materials by engineering geophysical techniques, annual report, fiscal year 1966*, edited by J.S. Watkins, NASA Contractor Report (CR)-65502 and USGS Open-File Report 67-272, pp. 259-267.

Watkins, J.S., Roach, C.H., and Christian, R.P. (1966) Correlation of physical properties – from laboratory measurements and from in situ measurements. In: *Investigation of in situ physical properties of surface and subsurface site materials by engineering geophysical techniques, annual report, fiscal year 1966*, edited by J.S. Watkins. NASA Contractor Report (CR)-65502 and USGS Open-File Report 67-272, pp. 25-35.

Welles S.P. and Cosgriff J. (1965) A revision of the Labyrinthodont family Capitosauridae. University of California Publications in Geological Sciences, v. 54, 148 p. (plus 1 plate).

Wylie, C.C. (1943a) Calculations on the probable mass of the object which formed Meteor Crater. *Popular Astronomy*, v. 51, pp. 97-99.

Wylie, C.C. (1943b) Second note on the probably mass of the object which formed Meteor Crater. *Popular Astronomy*, v. 51, pp. 158-161.

Xue, S., Herzog, G.F., Hall, G.S., Klein, J., Middleton, R., and Juenemann, D. (1995) Stable nickel isotopes and cosmogenic beryllium-10 and aluminum-26 in metallic spheroids from Meteor crater, Arizona. *Meteoritics*, v. 30, pp. 303-310.